Conference Proceedings of the Society for Experimental Mechanics Series

Bonnie Antoun · H. Jerry Qi · Richard Hall · G.P. Tandon
Hongbing Lu · Charles Lu *Editors*

Challenges in Mechanics of Time-Dependent Materials and Processes in Conventional and Multifunctional Materials, Volume 2

Proceedings of the 2012 Annual Conference on Experimental and Applied Mechanics

SEM Springer

Conference Proceedings of the Society for Experimental Mechanics Series

For further volumes:
http://www.springer.com/series/8922

Bonnie Antoun • H. Jerry Qi • Richard Hall • G.P. Tandon
Hongbing Lu • Charles Lu
Editors

Challenges in Mechanics of Time-Dependent Materials and Processes in Conventional and Multifunctional Materials, Volume 2

Proceedings of the 2012 Annual Conference on Experimental and Applied Mechanics

Springer

Editors
Bonnie Antoun
Sandia National Laboratories
Livermore, CA, USA

Richard Hall
AirForce Research Laboratory
Wright-Patterson Air Force Base, OH, USA

Hongbing Lu
University of Texas-Dallas
Dallas, TX, USA

H. Jerry Qi
University of Colorado
Boulder, CO, USA

G.P. Tandon
University of Dayton Research Institute
Dayton, OH, USA

Charles Lu
University of Kentucky
Paducah, KY, USA

ISSN 2191-5644 ISSN 2191-5652 (electronic)
ISBN 978-1-4614-4240-0 ISBN 978-1-4614-4241-7 (eBook)
DOI 10.1007/978-1-4614-4241-7
Springer New York Heidelberg Dordrecht London

Library of Congress Control Number: 2012952717

Printed on acid-free paper

Springer is part of Springer Science+Business Media (www.springer.com)

Preface

Challenges in Mechanics of Time-Dependent Materials and Processes in Conventional and Multifunctional Materials, Volume 2: Proceedings of the 2012 Annual Conference on Experimental and Applied Mechanics represents one of seven volumes of technical papers presented at the Society for Experimental Mechanics SEM 12th International Congress and Exposition on Experimental and Applied Mechanics, held at Costa Mesa, California, June 11–14, 2012. The full set of proceedings also includes volumes on Dynamic Behavior of Materials, Imaging Methods for Novel Materials and Challenging Applications, Experimental and Applied Mechanics, Mechanics of Biological Systems and Materials, MEMS and Nanotechnology, and Composite Materials and Joining Technologies for Composites.

Each collection presents early findings from experimental and computational investigations on an important area within experimental mechanics. The Challenges in Mechanics of Time-Dependent Materials and Processes in Conventional and Multifunctional Materials conference track was organized by Bonnie Antoun, Sandia National Laboratories; H. Jerry Qi, University of Colorado; Richard Hall, Air Force Research Laboratory; G.P. Tandon, University of Dayton Research Institute; Hongbing Lu, University of Texas-Dallas; Charles Lu, University of Kentucky, and sponsored by the SEM Time Dependent Materials and Composite, Hybrid and Multifunctional Materials Technical Divisions.

This volume includes chapters which address constitutive, time (rate)-dependent constitutive and fracture/failure behavior of a broad range of materials systems, including prominent researches in both applied and experimental mechanics. Solicited chapters involve nonnegligible time-dependent mechanical response in cases incorporating nonmechanical fields. The sessions are as follows:

- Time-Dependent Model Validation
- Small-Scale and Dissipative Mechanisms in Failure
- Thermomechanics and Coupled Phenomena I
- Strain-Rate and Frequency Effects
- Process Models and High-Temperature Polymers
- Shape Memory Materials
- Time-Dependent Nanoscale Testing
- Time-Dependent and Small-Scale Effects in Biocomposites
- Viscoelastoplasticity and Damage
- Composites, Hybrids, and Multifunctional Materials

Chapters in the following general technical research areas are included:

- Effects of interfaces and interphases on the time-dependent behaviors of composite, hybrid, and multifunctional materials
- Effects of inhomogeneities on the time-dependent behaviors of metallic, polymeric, and composite materials
- Environmental and reactive property change effects on thermomechanical and multifunctional behaviors
- Challenges in time-dependent behavior modeling in metallic and polymeric materials at low, moderate, and high strain rates, and effects of frequency and hysteretic heating
- Challenges in time-dependent behavior Modeling in composite, hybrid, and multifunctional materials – viscoelasto-plasticity and damage
- Modeling and characterization of fabrication processes of conventional and multifunctional materials
- Time-dependent and small-scale effects in micro/nanoscale testing

The organizers thank the presenters, authors, and session chairs for their participation in this symposium.
The opinions expressed herein are those of the individual authors and not necessarily those of the Society for Experimental Mechanics, Inc.

Livermore, CA, USA — Bonnie Antoun
Boulder, CO, USA — H. Jerry Qi
Wright-Patterson Air Force Base, OH, USA — Richard Hall
Dayton, OH, USA — G.P. Tandon
Dallas, TX, USA — Hongbing Lu
Paducah, KY, USA — Charles Lu

Contents

Chapter 1
Elastomeric Polymers for Shockwave Mitigation and Extreme Loading Conditions

Roshdy George S. Barsoum

Abstract Recent investigations into blast resistant properties of polymers with high rate sensitivity, have shown that they interact with the underlying substrates in quite different manner than any ballistic material known to the shock community. We are going to discuss in this paper that these polymers have a profound effect on the failure (fracture) mechanism of the substrate: suppression or delay of shear localization (or penetration) mechanisms, and delay of necking instability in ductile metals, in addition to dissipating large amounts of energy through wave reflections. The intrinsic property of the polymer under blast/ballistic/ shock, in addition to its high strain rate sensitivity, is a very large increase of its shear properties, both modulus and strength, under very high pressure and loading rate, which exists under extreme loading conditions. In addition, because these elastomeric polymers are multi-phase of hard and soft domains, at the nano scale, they can dissipate broad bands of frequencies such as those encountered in blast events. We will discuss also research in the development of polymers-by-design to divert and dissipate shockwaves from the head and thus prevent Traumatic Brain Injury—TBI, using molecular dynamics, polymer synthesis and high strain rate testing of shock properties for constitutive models, and the continuum analysis of shockwave propagation.

Building on successful testing of elastomeric polymers in demonstrating its effect on the blast, ballistics performance of steel, ONR initiated efforts to understand the mechanisms involved in extreme loading conditions. The fundamental property of these polymers is *high strain rate sensitivity*, which was shown to be essential in the suppression of shear localization in high strain rate events [1], such as those encountered in blast and penetration mechanics [2]. To fully illustrate the delay or suppression of shear localization, Fig. 1.1 shows the failure mechanism of large scale of uncoated and coated thick steel plates subject to underwater high rate loading. Examination of the fracture in the uncoated plates, show the failure to be the result of shear localization. On the other hand, Fig. 1.2, of small (thin steel) specimens also subject to intense high rate loading, the failure of the uncoated specimens was ductile. It is instructive to know that the % increase in pressure associated with the coated plates vs. uncoated plates was much higher in the case of the shear localization case, than in the ductile failure case. What is more interesting, is that in the case of thick plates, where the failure is governed by shear localization, it did not matter whether the coating is, on the side of the loading (front) or the back side. While in the case of thin plates, the coating was only effective when the coating was on the backside. In Ref. [3], it is argued that the polymer on the front side, focuses the shock, while in the backside it attenuates the shock. No computation was done to prove these arguments, because of the difficulty in performing large deformation nonlinear plasticity combined with shockwave propagation in extremely thin layers. This type of analysis was recently resolved by Fish [4], using multi-scale computational approach with solitons to compute the shockwave

R.G.S. Barsoum (✉)
Office of Naval Research, Arlington, VA 22203, USA
e-mail: roshdy.barsoum@navy.mil

B. Antoun et al. (eds.), *Challenges in Mechanics of Time-Dependent Materials and Processes in Conventional and Multifunctional Materials, Volume 2*, Conference Proceedings of the Society for Experimental Mechanics Series 37,
DOI 10.1007/978-1-4614-4241-7_1,

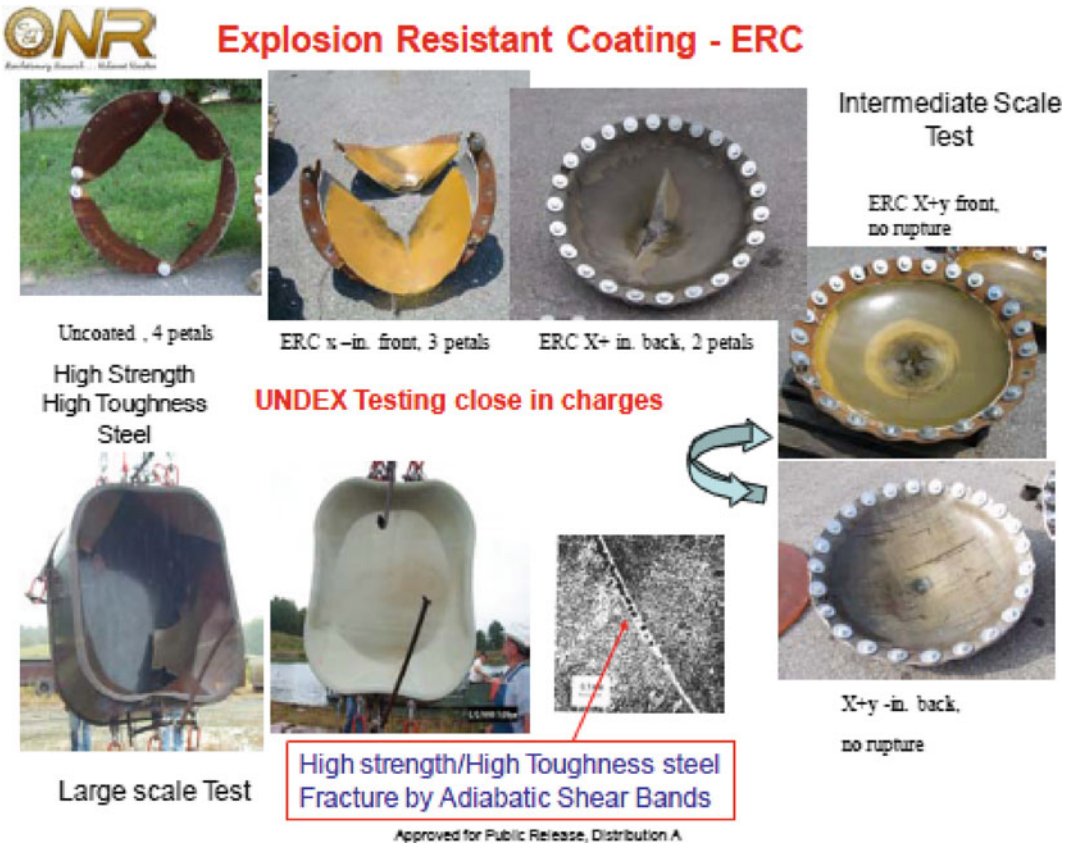

Fig. 1.1 Thick-high strength steel plates coated with ERC subject to intense underwater high rate loading

propagation and its reflections at interfaces, which provides another mechanism of dissipation. Therefore there are three mechanisms associated with these polymers: (1) in the case of thin plates, as the strain rate increases the polymer hardens significantly, and thus reduces the plastic deformation; (2) in the case of thick plates the thick plates the polymer hardens similarly, but it spreads the localization to neighboring areas and delays shear localization; and (3) the polymer dissipates the shockwave and attenuates it, as shown by the analysis [4] of experiments done earlier at NSWC. The mechanisms of how the high strain rate sensitive polymer can result in delay in shear-localization or ductile fracture and shockwave propagation/dissipation, can be further deployed to further improvements in multi-layered hybrid plates with different materials. ONR is pursuing a new computational approach to perform shear localization analysis of thick high strength, high toughness steel plates.

To further exploit these polymers in a highly complex and formidable problem facing the warfighter, ONR is leading a Basic Research Challenge and applied S&T effort, to develop polymers-by-design to divert and dissipate shockwaves from the head and thus prevent Traumatic Brain Injury—TBI [6].

Protection against TBI is one of the most challenging problems in mechanics, because the brain is the most sensitive instrument we know of, and helmets requires lightweight materials, so that they are worn all the time. Elastomeric polymers, if designed accordingly, can both address shockwaves and ballistic effects. Tests and theoretical developments on polymers, indicate that these polymers can provide the necessary protection against TBI. Investigations into blast resistant properties of polyureas and other multi-phase polymeric elastomers, indicate that they can dissipate broad bands of frequencies such as those encountered in blast events. Recent experiments and multi-scale computations of polymers with underlying substrates, have been shown that polymers absorb shock loading in quite a different manner than any ballistic material known to the armor community.

Fig. 1.2 Thin-high strength steel plates coated with ERC

In this presentation we will discuss efforts on the multi-scale approach addressing constitutive modeling, analysis, and tests of various extreme loading events. To understand interaction between materials and wave propagation at extreme high rate requires multi scale computation, which are in the nano scale space and time. Molecular dynamics, coarse scale modeling, continuum modeling, high rate load testing, and constitutive modeling and large scale computations simulating biofidel models of the head and brain are used in addressing the Traumatic Brain Injury problem [5–8].

Figures 1.3 and 1.4, illustrate the multi-scale computational effort of atomistic-to-continuum behavior of polymers subject to shockwaves and its impending dissipation and diversion of shock energy.

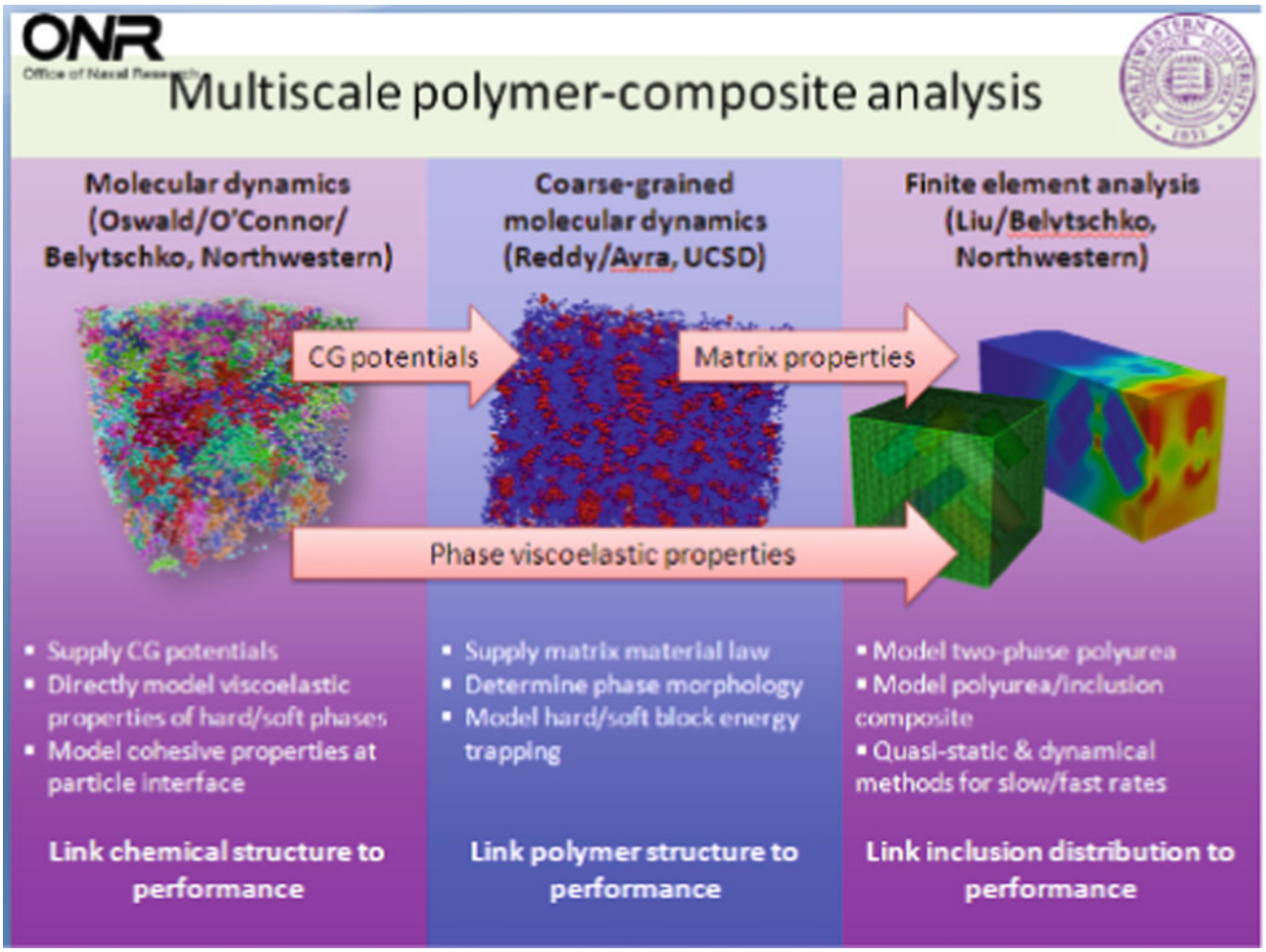

Fig. 1.3 Multi-scale modeling of polymers with nano and micro inclusions to divert shockwaves

1.1 Why Polymers for TBI?

- Polymers are the best hope for protection against TBI for the following reasons:
  - Lightweight and can both improve blast and ballistic protection
  - When combined with other materials, have proven to offer increased protection against blast, shockwave, and fragments.
  - Highly strain rate sensitive and shear mechanical properties increase significantly under combined pressure and high rate.
- Under shock loading, brain tissue is weak in shear, while polymers increase in strength and modulus (both direct and shear stresses).
- Polyureas have multi-scale structures from the nano to the micro and continuum level with complex interactions with all frequencies of shockwaves, thus, in principle, have the potential for absorbing/dissipating harmful effects that result in mTBI.
- Polymers can be design from the molecule up. But what is the design criteria in the case of shock-
- Nano- and micro- particles, and shaped interfaces and layers can be included to dissipate and divert shock-

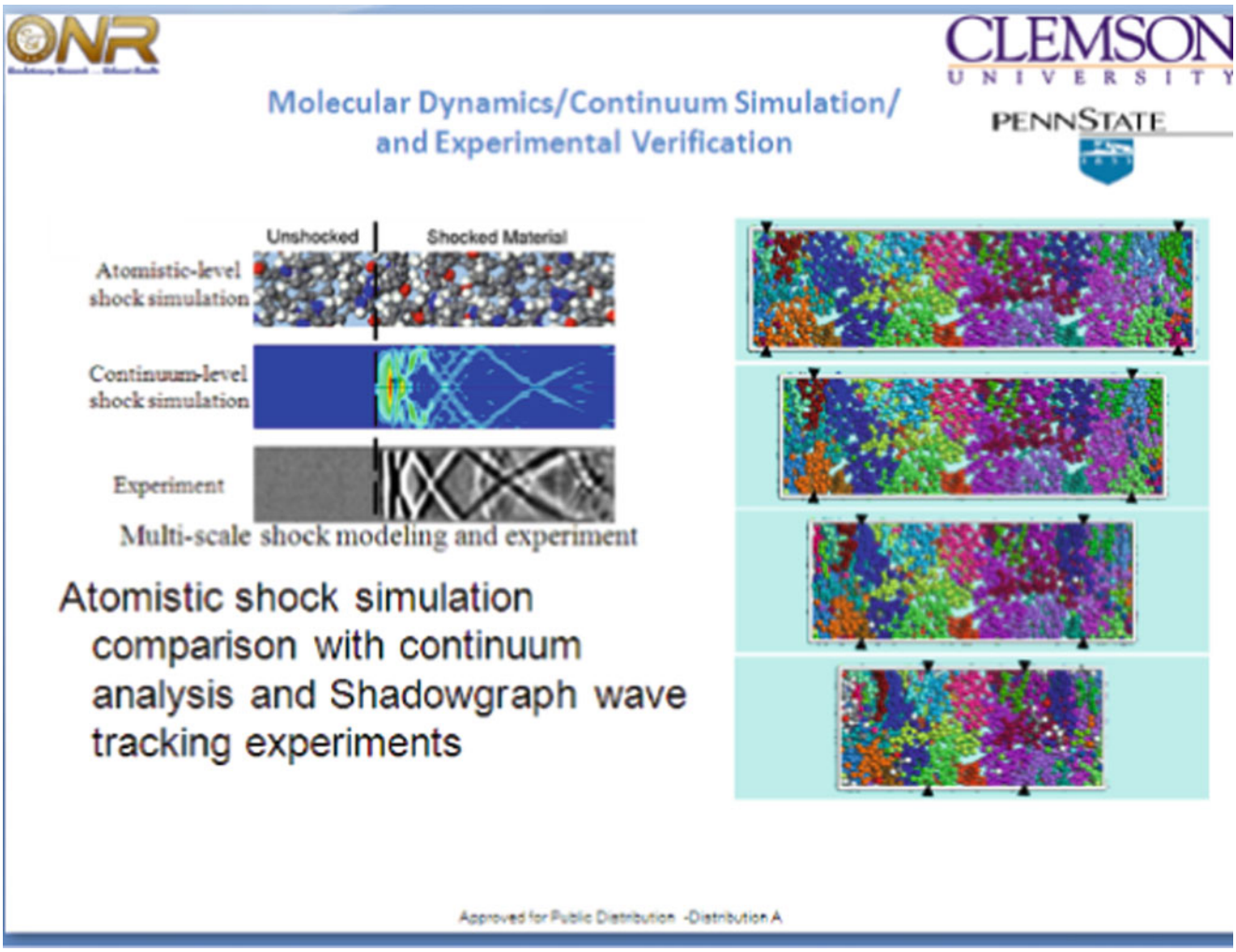

Fig. 1.4 Multi-scale modeling of shockwave reflections at boundaries—comparison between molecular dynamics, continuum mechanics computations and shock testing

References

1. Barsoum RSG (2007) Shear localization and the possibility of its suppression or delay. In: Proceedings of the international symposium on plasticity 2007, Alyeska, Alaska
2. Barsoum RG, Dudt P (2009) The fascinating behaviors of ordinary materials under dynamic conditions. AMMTIAC Quart 4(4)
3. Samiee A, Amirkhizi A, Nemat-Nasser S, Numerical study of the effect of polyurea on the performance of steel plates under blast loads (submitted to Mechanics of Materials)
4. Fish J (2011) The role of dispersion on energy absorption of metal-high density polyethylene. ONR Review, July 11–12, 2011
5. Runt J (2011) Elastomeric polymer-by-design to protect the warfighter against traumatic brain injury. PSU, ONR Review, 11–12 July 2011
6. Barsoum RG (2011) Protection against TBI using polymers for shock mitigation. In: Proceedings – NATO/RTO-MP-HFM-207 A survey of blast injury across the full landscape of military science, Halifax, Canada, 3–5 Oct 2011
7. Nemat-Nasser S (2011) Elastomeric polymer by-design for blast induced shack wave management. UCSD, ONR Review, 11–12 July 2011
8. Radovitzky R (2011) Large scale simulation of polymer-by-design systems for blast-induced TBI mitigation. MIT, ONR Review, 11–12 July 2011

Chapter 2
Temperature Dependent Ductile Material Failure Constitutive Modeling with Validation Experiments

J. Franklin Dempsey, Bonnie R. Antoun, Vicente J. Romero, Gerald W. Wellman, William M. Scherzinger, and Spencer Grange

Abstract A unique quasi-static temperature dependent low strain rate constitutive finite element failure model is being developed at Sandia National Laboratories (Dempsey JF, Antoun B, Wellman G, Romero V, Scherzinger W (2010) Coupled thermal pressurization failure simulations with validation experiments. Presentation at ASME 2010 international mechanical engineering congress & exposition, Vancouver, British Columbia, 12–18 Nov 2010). The model is used to predict ductile tensile failure initiation using a tearing parameter methodology and assessed for accuracy against validation experiments. Experiments include temperature dependent tensile testing of 304L stainless steel and a variety of aluminum alloy round specimens to generate true-stress true-strain material property specifications. Two simple geometries including pressure loaded steel cylinders and thread shear mechanisms are modeled and assessed for accuracy by experiment using novel uncertainty quantification techniques.

Keywords Finite element model • Validation testing • Temperature dependent constitutive model

2.1 Finite Element Material Characterization Modeling

Finite element (FE) analysis with validation testing is performed to predict quasi-static failure initiation of ductile materials when subjected to high pressures at elevated temperature. Two structure types are chosen to envelope load and displacement modes of failure. The structures include a simple stainless steel cylinder (pipe bomb) that that is pressurized and heated and an aluminum Acme thread geometry that is extended and heated to failure.

A unique FE quasi-static temperature dependent constitutive model [1] has been developed and uses a tearing parameter methodology for failure initiation. Model inputs require experimental derived tensile test hardening data taken at temperatures in the range of the desired failure prediction. The structural response is then validated by tests.

The elastic–plastic constitutive model incorporating temperature dependence was developed for use in Sandia's quasi-static finite element modeling software, Adagio [2]. The model requires a temperature dependent true stress-true strain hardening curve definition to failure plus temperature dependent elastic constant specifications. Elastic constants can be obtained in the open literature but the hardening curve data is characterized through experimental tensile tests at elevated temperature [3]. Pipe bomb tensile-test material samples were cut and machined from a common 304L stainless steel tubular stock. The resulting engineering stress strain curves are shown, Fig. 2.1.

Validation-experiment pipe vessels were machined from the same batch of tube stock material to match the tensile test data. As shown, the strength degrades with increasing temperature. From room temperature to 600°C, the ductility at failure decreases. After 600°C, it increases for this particular material.

For each measured stress–strain curve, an advanced optimization technique is used to solve an inverse finite element tensile necking problem to calculate true stress/true strain response and will later be used system model input. An example is presented in Fig. 2.2.

J.F. Dempsey (✉) • V.J. Romero • G.W. Wellman • W.M. Scherzinger • S. Grange
Sandia National Laboratories, Albuquerque, NM 87185, USA
e-mail: jfdemps@sandia.gov

B.R. Antoun
Sandia National Laboratories, Livermore, CA 94551-0969, USA

B. Antoun et al. (eds.), *Challenges in Mechanics of Time-Dependent Materials and Processes in Conventional and Multifunctional Materials, Volume 2*, Conference Proceedings of the Society for Experimental Mechanics Series 37,
DOI 10.1007/978-1-4614-4241-7_2,

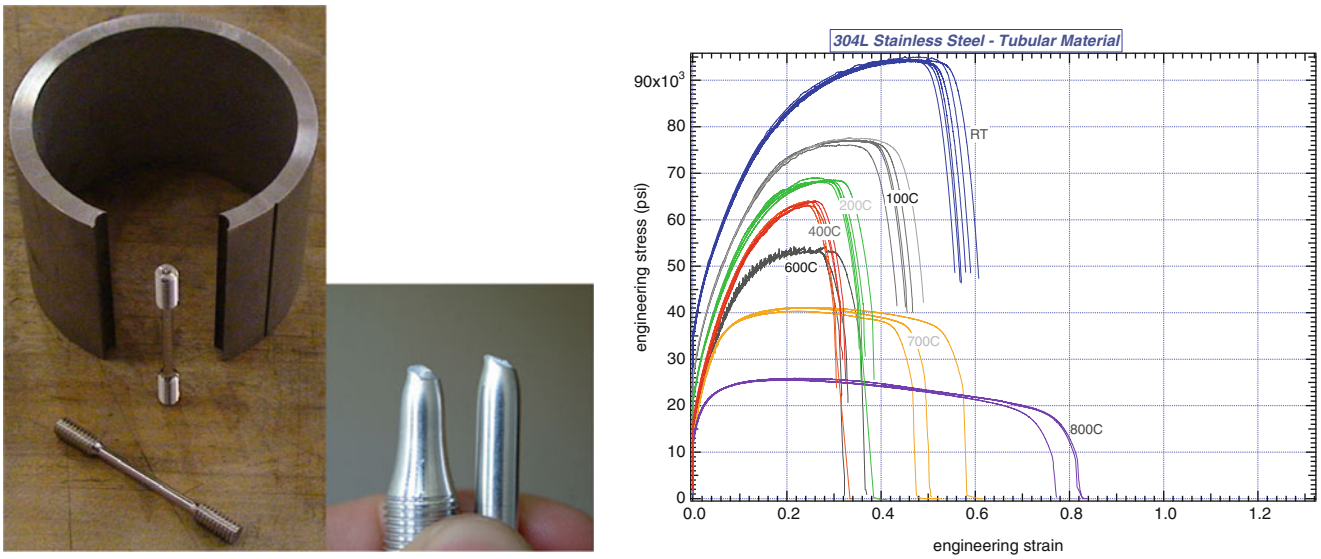

Fig. 2.1 Cylinder tensile-test material samples were cut and machined from the same 304L stainless steel tubular stock that the validation-experiment pipe vessels were machined from. Measured stress–strain response-to-failure curves plotted from cylinder pull-tests at a strain rate of 0.001/s for the labeled temperatures (note: *RT* in the plot stands for "room temperature", nominally 25°C)

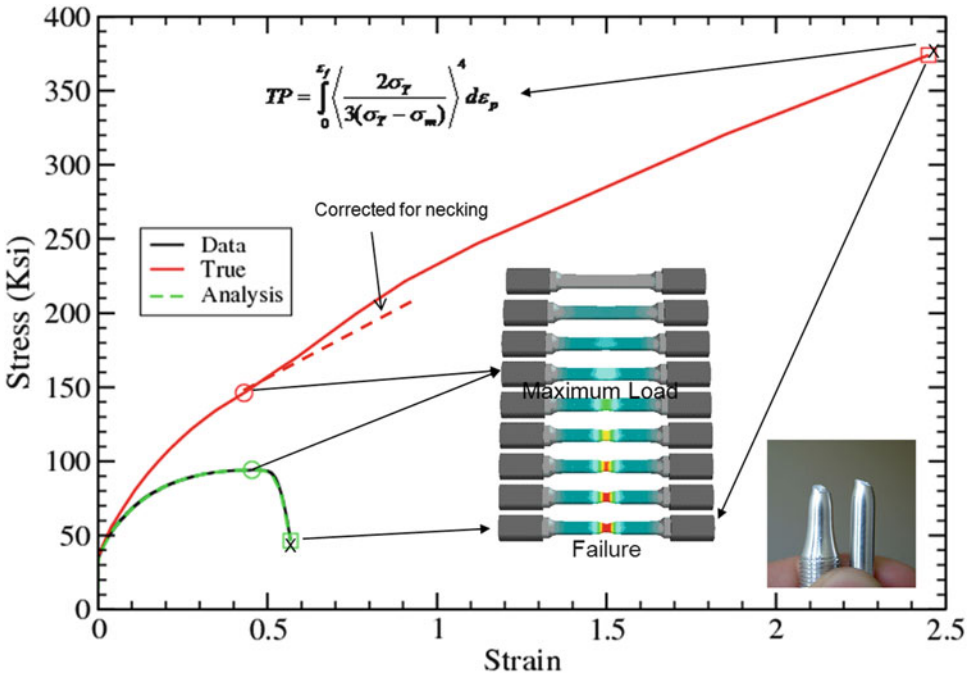

Fig. 2.2 Example of various stress–strain curves pertaining to experimental and modeled response in a given tensile-test. *True* curve is Cauchy-Stress/Logarithmic-Strain "True" curve conditioned to the constitutive model. The curve is inversely calculated using the constitutive model and a FE model of pulled cylinder such that when the curve is used with the constitutive model in the FE simulations the calculated *Analysis* stress–strain curve matches the experimentally measured *black* stress–strain curve from the pull test. See Ref. [8] for the set of derived curves at each temperature

Given the engineering stress strain response of a tensile test [3], the round tensile specimen is modeled using finite elements. A displacement controlled FE calculation is then performed to simulate the tensile test. The simulation predicts no necking through yield but as the specimen begins to harden, true stress/log strain necking response is estimated and checked against the original averaged engineering stress/strain. Iteratively, true stress and log strain can be computed to failure. This is referred to as solving the inverse problem. A tearing parameter method is used to track failure progress. At failure, a critical tearing parameter is calculated to be used in pipe bomb models. This procedure is repeated at every temperature. The inverse problem and solution procedures and results are more fully documented in Ref. [1].

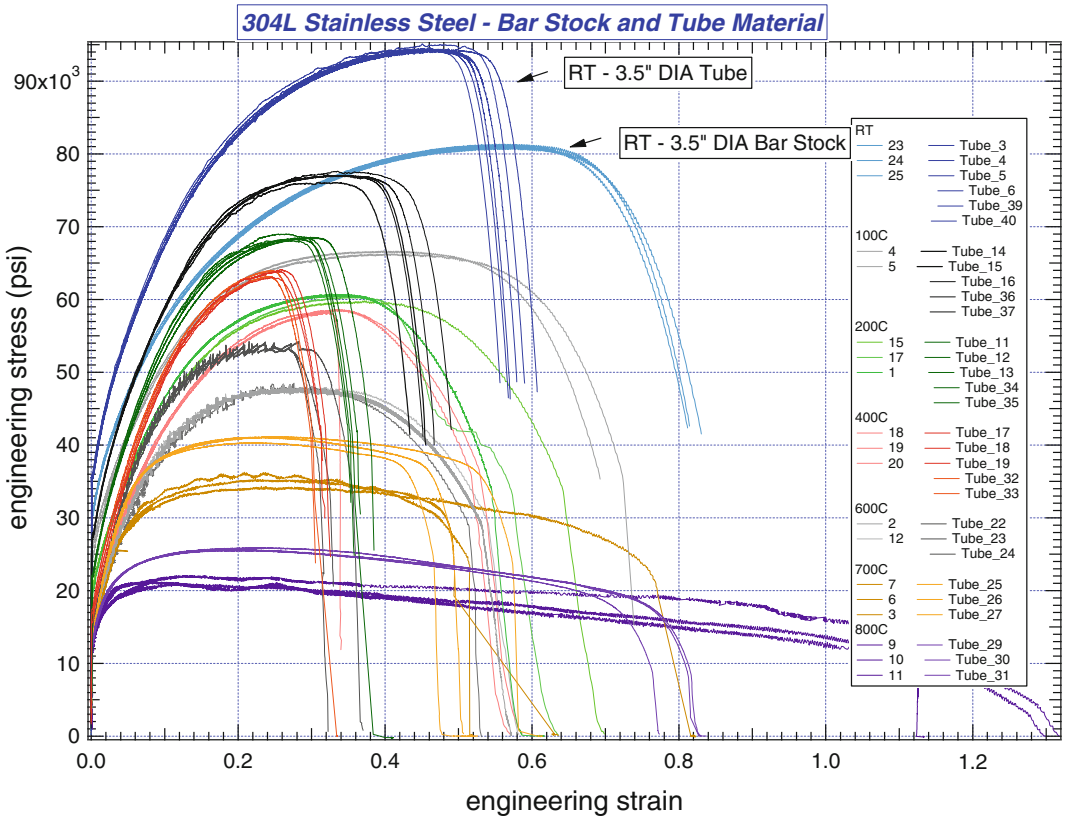

Fig. 2.3 Engineering stress/strain response of 304L bar stock tensile tests through elevated temperature and a comparison of bar stock and tube stock at room temperature

Once the material characterization has been defined for an applicable range of temperatures, it is formatted as input into a thermo-elastic plastic constitutive model and used to predict the failure response of a pressurized cylindrical steel vessel at high temperature. In this case, a critical tearing parameter is used to define a point in which the code will automatically delete elements, thus establishing the pressure, temperature and location of failure initiation.

True stress and log strain response for a given material at elevated temperatures is unique. For example, tensile tests have shown that extruded 304L bar stock has an ultimate strength of nearly 20% less than extruded tubing. It is also about 25% more ductile (Fig. 2.3). Additionally, some aluminum alloys including 6061-T651, 6061-T6, 7075-T651, 7075-T7351, 7079 and 7050-T74 have been tested and characterized to tensile failure at elevated temperature. The 304L tube stock is used for pipe bomb and aluminums for thread shear modeling and simulation.

2.2 Finite Element Validation Modeling

Two quasi-static verification models were created for validation to experiments. They include the pipe bomb pipe bomb and thread shear geometries. Figure 2.4 shows the pipe bomb geometry. Figures 2.5 and 2.6 show the pipe bomb and thread shear finite element models, respectively. Thread shear validation modeling is just beginning; therefore pipe bomb work will be discussed herein.

2.3 Finite Element Modeling to Validation Experiments

The pipe bomb consists of a 3″ O.D tube that is machined down to a 0.020″ wall thickness at the center (Fig. 2.4). Other thicknesses including 0.035 and 0.05 thicknesses are also investigated. It is 14″ in length.

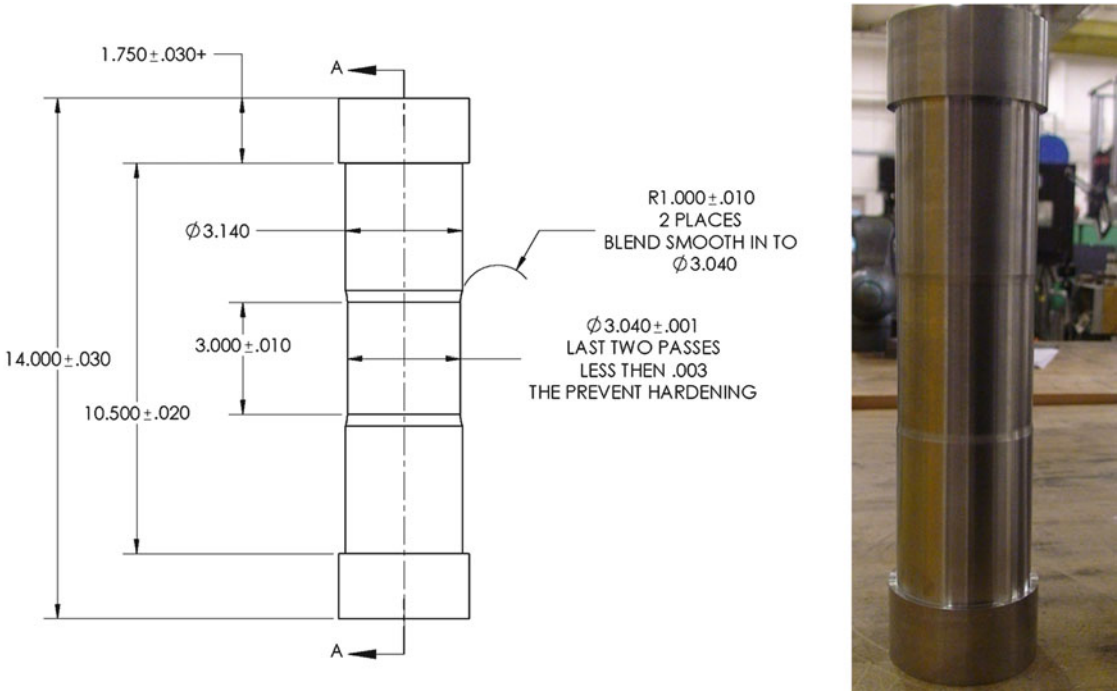

Fig. 2.4 Pipe bomb geometry and manufactured test article

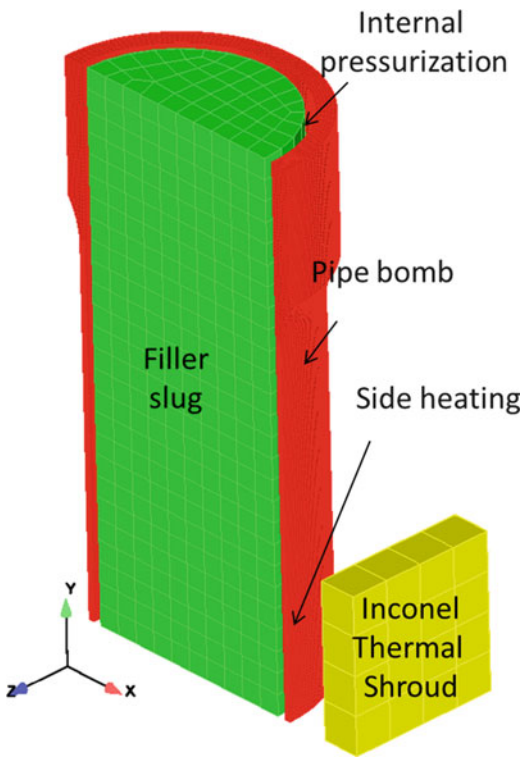

Fig. 2.5 Finite element model of the pipe bomb validation experiment, ¼ symmetry

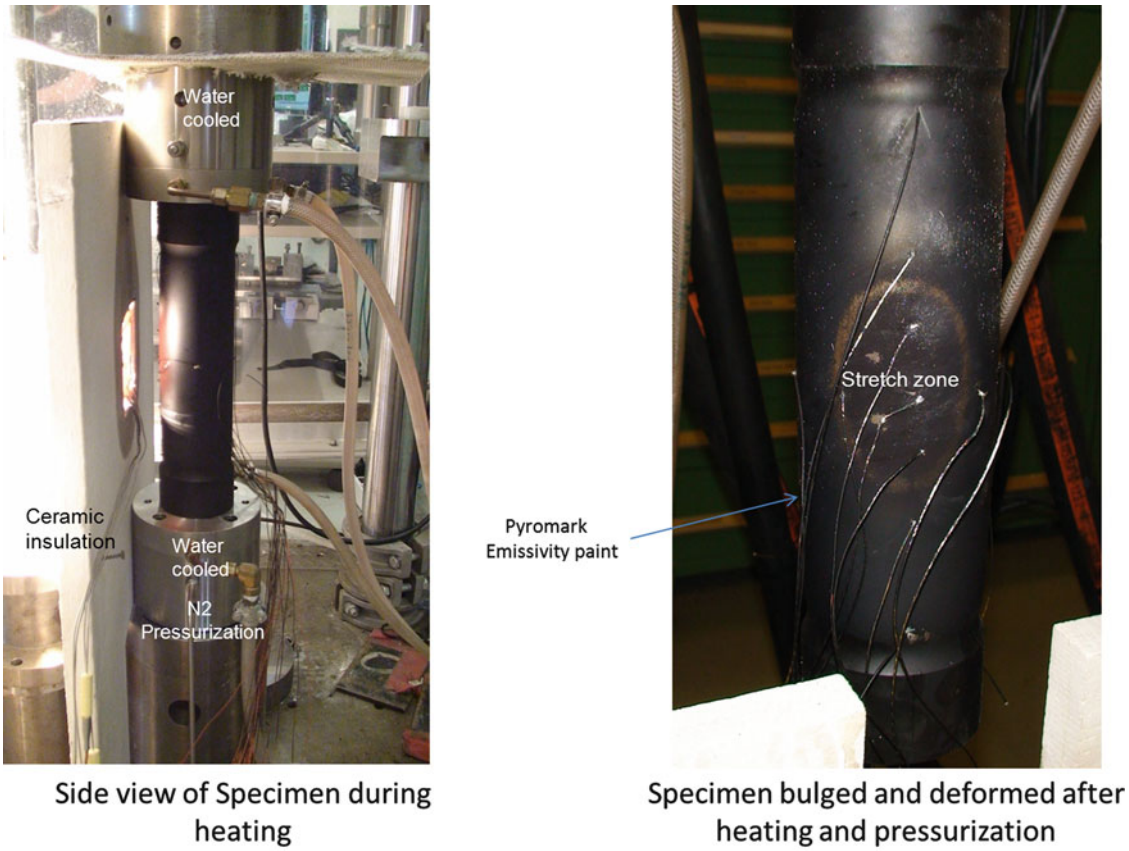

Fig. 2.6 Experimental setup and example specimen deformation during a pipe bomb validation test

A finite element model of the pipe bomb and thread shear validation experiments are shown in Figs. 2.5 and 2.6, respectively. In Fig. 2.5, a thermo-mechanical ¼ symmetric section of the experiment is modeled.

The ends are clamped and it is centrally heated by an external source. An internal steel slug is used to minimize gaseous energy due to pressurization for safety purposes. A variety of pressurization and temperature ramp rates were used to validate the model to experiment, however one particular scenario in which the tube is spot heated to 700°C, then pressurized to failure will be discussed.

Upon pressurization to failure, the material at the hot spot begins to displace toward the heat source. As it deforms, the wall thickness thins out and failure initiation occurs. Figure 2.6 shows the experimental setup and an example specimen during a pipe bomb validation test.

In quasi-statics [2], the model must be non-accelerating with no rigid body modes to be statically determinate. As the hot spot displaces toward the heating shroud, instability begins to develop and the model becomes ill conditioned, requiring a significant reduction in the solution time step to continue. Then, as the pressure incrementally increases, the equivalent plastic strain exponentially increases and the tearing parameter approaches critical. In these simulation calculations, adaptive time steps are typically driven to the nanosecond range or smaller in order to obtain convergent solutions with several hundred percent plastic strain and tearing parameters near ten. Given a set of code convergence tolerances, iteration limits and solution updates, the calculation will continue until static instability is reached. At this point, failure is assumed to have initiated. In some cases, element deletion occurs by exceeding the critical tearing parameter, however, in most cases failure is determined by an ill conditioning. Addition work is ongoing and has been demonstrated that failure propagation can be shown by restarting the calculation with an explicit dynamics solver (Presto) [4].

Figure 2.7 shows the experimental setup for a pipe bomb validation experiment. During an experiment, the center section is heated and pressurized, causing high deformation at the heated zone as shown. Failure initiation occurs at the hot spot and propagates axially, then circumferentially as shown, Fig. 2.8. Similarly, the pipe bomb models predict this response, but with 20–30% later failure times, as quasi-static finite element solutions are highly dependent on mesh quality, number of elements through the center thickness and a variety of code tolerance settings.

Fig. 2.7 Pressure loaded stainless steel "pipe bomb" validation experiment, resulting post-test failure and validation of repeated failure modes

Two iterative solvers can be used for pipe bomb pressurization breach at elevated temperature. These include the finite element tearing and interconnecting (FETI) [5] and conjugate gradient (CG) [6] solvers. The FETI solver is generally used for solving problems in the linear range whereas CG is best for non-linear solutions. Typically, CG can take two orders of magnitude more CPU time to find a solution that FETI. For typical pipe bomb solutions, FETI will tend to over predict failure by around 10% as compared to CG; however FETI has successfully predicted relative failure trends and is useful in screening calculations. For validation, CG is used. Table 2.1 lists suggested solver settings that should be used as a baseline for high temperature pressurization breach simulations.

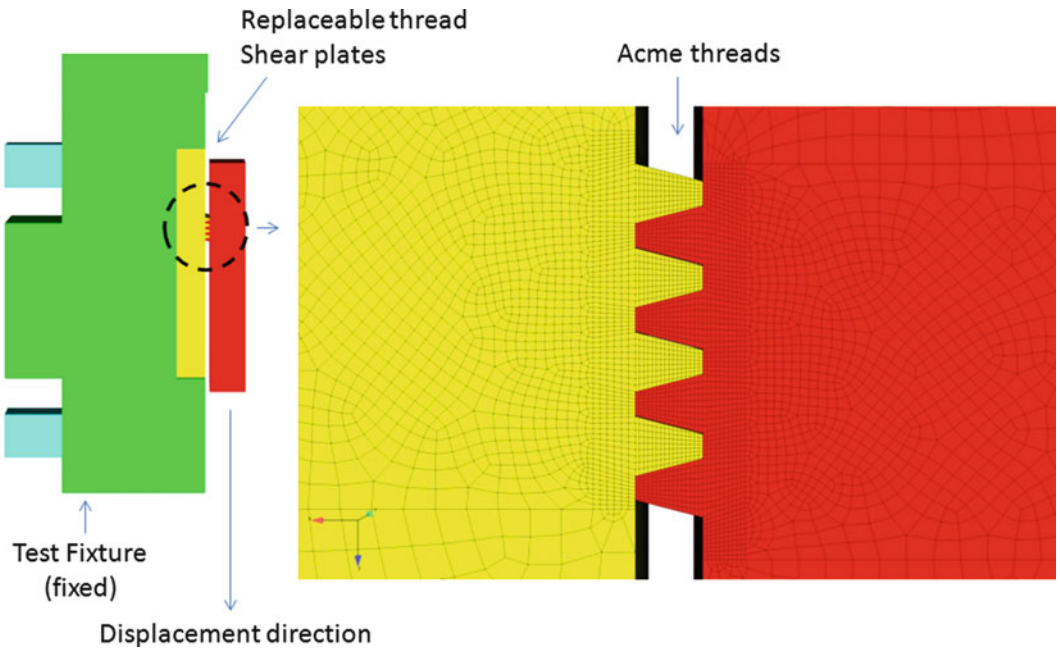

Fig. 2.8 Finite element model of the thread shear validation experiment

Table 2.1 Code settings that control simulation accuracies

Solver resolution settings	FETI	CG
Target relative residual	1.00E-06	1.00E-06
Acceptable relative residual	1.00E-04	1.00E-04
Max iterations	1,000	5,000
Min iterations	3	3
Adaptive time step settings		
Max cutback	10	10
cutback factor	0.5	0.5
Growth factor	1.5	1.1
Iteration window	100	1,000
Target iterations	400	35,000
Max multiplier	100	100
Min multiplier	1.00E-12	1.00E-09

Table 2.2 lists results of an isothermal pipe bomb screening simulation study used to rank tensile test data in terms of high and low material strengths. As shown, tensile test repeats were done at 20°C, 100°C, 200°C, 400°C, 600°C, 700°C and 800°C respectively. The failure pressures (Pmax) are listed for each simulation. For example, six sets of tensile tests were done at 20°C. Case try5-rt tensile test data produced a higher pipe bomb failure pressure than the other curves at this temperature. Case try40-rt produced the lowest failure pressure. Similarly, a status of high and low strength simulation runs were ranked for all of the tensile tests. Other quantities of interest include minimum simulation time step acquired for failure and maximum equivalent plastic strain (EQPS) and corresponding tearing parameter values.

The calculations were performed on Sandia's Red Sky [7] computer using 192 processors using a FETI [5] preconditioning solver with adaptive time stepping. Compute times were generally less than 0.4 h except as noted. Figure 2.9 shows a result of a fully coupled simulation.

Fully coupled thermo-mechanical and temperature mapped validation simulations are in progress to explore prediction extrapolations and temperature mapping techniques. Figure 2.9 depicts a result of a study to determine the effect of temperature mapping from a fully coupled simulation (or validation experiment) to an interpolated simulation. High/low material rankings were used to predict failure pressures at high temperature with variations in emissivities, an important step to quantify the error involved in temperature mapping from experiment to model [8, 9].

Table 2.2 Predicted pipe bomb pressurization failure results at isothermal temperature using 304L material characterization true stress/log strain tensile test data

Case	T_max	P_max (psi)	dt (s)	EQPS_max*	Tearing*	Status	# Procs	Cpu-hrs	Res	Adaptive
try3-rt	20	1484.5	1.60E-11	0.601	2.14		192	0.368	1.00E-06	FETI
try4-rt	20	1482.8	9.00E-13	0.571	2.03		192	0.308	1.00E-06	FETI
try5-rt	20	1485.2	9.00E-13	0.575	2.04	High	192	0.324	1.00E-06	FETI
try6-rt	20	1485	9.00E-13	0.549	1.54		192	0.348	1.00E-06	FETI
try39-rt	20	1483.9	9.00E-13	0.587	2.09		192	0.402	1.00E-06	FETI
try40-rt	20	1474.8	9.00E-13	0.555	1.96	Low	192	0.309	1.00E-06	FETI
try14-100	100	1227.1	1.00E-11	0.586	2.09	High	192	0.441	1.00E-06	FETI
try15-100	100	1208.7	9.00E-13	0.528	1.86	Low	192	0.546	1.00E-06	FETI
try16-100	100	1225.3	9.00E-13	0.561	1.99		192	0.31	1.00E-06	FETI
try36-100	100	1226.3	8.60E-12	0.559	1.98		192	0.335	1.00E-06	FETI
try37-100	100	1222.9	1.60E-08	0.549	1.95		192	0.284	1.00E-06	FETI
try11-200	200	1102.1	1.70E-09	0.529	1.66	High	192	0.335	1.00E-06	FETI
try12-200	200	1085.8	9.00E-13	0.426	1.26		192	2.62	1.00E-06	FETI
try13-200	200	1088.6	1.30E-06	0.469	1.43		192	2.26	1.00E-06	FETI
try34-200	200	1089.9	9.00E-13	0.442	1.32		192	0.453	1.00E-06	FETI
try35-200	200	1081.7	9.00E-13	0.402	1.17	Low	192	0.342	1.00E-06	FETI
try17-400	400	1010.3	1.00E-12	0.394	1.06		192	0.393	1.00E-06	FETI
try18-400	400	1007.2	1.00E-12	0.386	1.02		192	0.325	1.00E-06	FETI
try19-400	400	1005.7	3.00E-09	0.432	1.2		192	0.312	1.00E-06	FETI
try32-400	400	1001.9	1.00E-12	0.373	0.986	Low	192	2.479	1.00E-06	FETI
try33-400	400	1014	1.00E-12	0.384	1.03	High	192	0.369	1.00E-06	FETI
try22-600	600	869.2	1.00E-12	0.409	1.1	Low	192	0.361	1.00E-06	FETI
try23-600	600	880.1	4.00E-07	0.49	1.39		192	2.54	1.00E-06	FETI
try24-600	600	884.7	1.20E-09	0.523	1.52	High	192	0.359	1.00E-06	FETI
try25-700	700	705.1	1.00E-12	0.617	1.88	High	192	0.431	1.00E-06	FETI
try26-700	700	694.8	1.00E-12	0.605	1.84	Low	192	0.431	1.00E-06	FETI
try27-700	700	695.5	1.00E-12	0.606	1.83		192	0.443	1.00E-06	FETI
try29-800	800	448	3.50E-11	0.501	1.32		192	0.476	1.00E-06	FETI
try 30-800	800	440.8	1.00E-12	0.632	1.82	Low	192	0.431	1.00E-06	FETI
try31-800	800	448.8	1.00E-12	0.645	1.89	High	192	0.414	1.00E-06	FETI

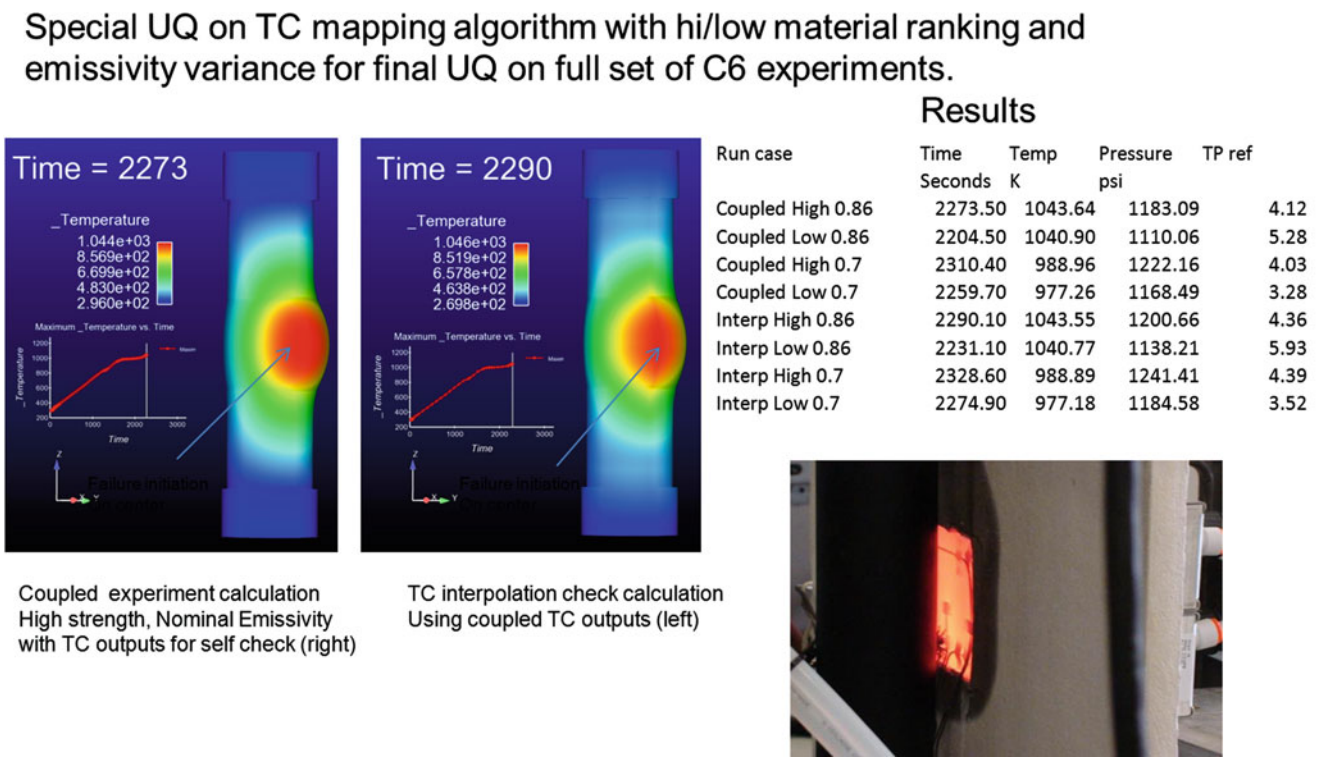

Fig. 2.9 Uncertainty on thermocouple mapping algorithm with hi/low material ranking and emissivity variance for the pipe bomb

Acknowledgements Sandia National Laboratories is a multi-program laboratory managed and operated by Sandia Corporation, a wholly owned subsidiary of Lockheed Martin Corporation, for the U.S. Department of Energy's National Nuclear Security Administration under contract DE-AC04-94AL85000.

References

1. Wellman GW. Modeling ductile failure, Sandia National Laboratories report in preparation
2. Adagio 4.24 User Guide, Sandia National Laboratories report SAND2011-1825, printed March 2011
3. Antoun B (2009) Material characterization and coupled thermal-mechanical experiments for pressurized, high temperature systems. Sandia National Laboratories C6 L3 Milestone Report, 11 Sep 2009
4. Presto 4.24 User Guide, Sandia National Laboratories report SAND2011-1825, printed March 2011
5. FETI, full tangent preconditioner for solid mechanics, Sandia National Laboratories, March 2011
6. CG, conjugate gradient solver for solid mechanics, Sandia National Laboratories, March 2011
7. Red Sky computing resource, Sandia scientific, engineering and high performance computing, ~505 Tflops peak, 2823 nodes, 22,584 cores, 2012
8. Romero V, Dempsey JF, Wellman G, Antoun B, Sherman M. Model validation and UQ techniques applied to temperature dependent stainless-steel constitutive model tested on heated pipes pressurized to failure, Sandia National Laboratories report in preparation
9. Romero V, Dempsey JF, Wellman G, Antoun B (2012). A method for projecting uncertainty from sparse samples of discrete random functions — example of multiple stress–strain curves. In: Proceedings of the 14th AIAA non-deterministic approaches conference, Honolulu, 23–26 Apr 2012

Chapter 3
Inverse Measurement of Stiffness by the Normalization Technique for *J*-Integral Fracture Toughness

Eric N. Brown

Abstract The single specimen normalization technique for *J*-integral fracture toughness has been successfully employed by several researchers to study the strongly non-linear fracture response of ductile semicrystalline polymers. As part of the normalization technique the load and the plastic component of displacement are normalized. The normalized data is then fit with a normalization function that approximates a power law for small displacements that are dominated by blunting and smoothly transitions to a linear relationship for large displacements that are dominated by stable crack extension. Particularly for very ductile polymers the compliance term used to determine the plastic displacement can dominate the solution and small errors in determining the elastic modulus can lead to large errors in the normalization or even make it ill posed. This can be further complicated for polymers where the elastic modulus is strong strain rate dependent and simply using a "quasistatic" modulus from a dogbone measurement may not equate to the dominant strain rate in the compact tension specimen. The current work proposes directly measuring the compliance of the compact tension specimen in the solution of *J*-integral fracture toughness and then solving for the elastic modulus. By comparison with a range of strain rate data the dominant strain rate can then be determined.

Keywords Fracture • Single specimen normalization technique • Viscoelastic polymers • Inverse method • Time-dependent materials

3.1 Introduction

The fracture toughness values of various polymers have been measured over the years employing techniques that have typically been developed for metals. While it is generally recognized that the value of fracture toughness for polymers—like many mechanical properties—are rate or time dependent, the implication of this rate dependence during the analysis is often overlooked. In linear elastic fracture mechanics (LEFM) the stress intensity factor K_i—the stress distribution at the crack tip corresponding to a given far-field load—for a compact tension specimen with an initial crack length of a_0 is given by

$$K_i = \frac{P_i}{b\sqrt{w}}\left[\frac{\left(2+\frac{a_0}{w}\right)\left(0.886+4.64\left(\frac{a_0}{w}\right)-13.32\left(\frac{a_0}{w}\right)^2+14.72\left(\frac{a_0}{w}\right)^3-5.6\left(\frac{a_0}{w}\right)^4\right)}{\left(1-\frac{a_0}{w}\right)^{3/2}}\right], \tag{3.1}$$

where P_i is the instantaneous load, w is the specimen width, and b is the specimen thickness. In this simple analysis, rate dependence can only enter through the independent measured critical load value P_c or dependent calculated critical stress intensity factor K_{Ic}. However, if fracture toughness is instead calculated in terms of strain energy release rate via

$$G_{Ic} = \frac{K_{Ic}^2}{E(\dot{\varepsilon})}, \tag{3.2}$$

E.N. Brown (✉)
Los Alamos National Laboratory, P-23, Mail Stop H803, Los Alamos, NM 87545, USA
e-mail: en_brown@lanl.gov

B. Antoun et al. (eds.), *Challenges in Mechanics of Time-Dependent Materials and Processes in Conventional and Multifunctional Materials, Volume 2*, Conference Proceedings of the Society for Experimental Mechanics Series 37,
DOI 10.1007/978-1-4614-4241-7_3,

strain rate dependence is explicitly introduced through the strain rate dependence of the Young's modulus E. In general the representative strain-rate dominating the compact tension specimen is not known and a generic "quasi-static" Young's modulus is employed. In the case of LEFM where K_{Ic} is determined, inaccurately accounting for the strain-rate dependence will simply introduce an error in the calculated value of G_{Ic}. Where as for metals the Young's modulus is strain-rate invariant [1], for polymers employing a Young's modulus for a strain-rate that is off by a few orders-of-magnitude can easily introduce errors well in excess of 10% [2, 3]. In the case of nonlinear elastic–plastic fracture mechanics—such as the single specimen normalization technique to measure J-integral fracture toughness—inaccuracy in E arising from uncertainty of the relevant strain-rate has been found to make the analysis ill posed. The current work proposes using the initial slope of the load displacement curve to measure compliance of the compact tension specimen to analytically solve for E. The normalization technique as proposed by Landes and Herrera [4] and included in ASTM Standard E1820 for elastic–plastic fracture toughness has been successfully applied for a variety of polymers [2, 3, 5–13].

3.2 Experimental Method and Results

Fracture toughness measurements performed using compact tension specimens as defined in ASTM Standard E1820 and shown in Fig. 3.1 are discussed, although the concept is applicable to any fracture specimen geometry. The geometry was modified to enable a crack opening displacement (COD) gage to be mounted along the loading line. The specimen notch was cut to have an inclusive angle of 40°, which was subsequently sharpened with a razor blade according to ASTM D5045. These specimens were tested using an MTS 880 load frame under constant crosshead displacement rates. Load-line displacements were measured with a MTS COD gage 632.03E-31. The single-specimen method for evaluating J-integral values of fracture toughness was elected due to the ability to limit the number of specimens required for multi-specimen methods and to avoid the visco-elastic nature of polymers that complicates loading-unloading methods. For the single specimen method, J-integral values corresponding to the ith data pair are given by

$$J_i = J_{el_i} + J_{pl_i} = \frac{K_i^2(1-\nu^2)}{E} + \frac{\eta_{pl} A_i^{pl}}{b(w-a_0)}, \tag{3.3}$$

where J_{el} and J_{pl} signify the division of energy into recoverable elastic deformation and permanent plastic deformation respectively. The Poisson ratio, ν, is taken from sound speed measurements, E is the Young's modulus, $\eta_{pl} = 2 + 0.522(w\text{-}a_{bi})/w$ is a dimensionless constant ($a_{bi} = a_0 + J_i/2\sigma_{ys}$ is the blunting corrected crack length correspond to the ith data point), A_i^{pl} is the area under the load displacement curve shown in Fig. 3.2. If the response is consistent with LEFM the plastic component is dropped.

The current work deviates from the standard method in proposing that values of E be determined on a specimen-by-specimen based from initial CT compliance C_i by

$$E = \frac{1}{C_i b}\left(\frac{w+a_i}{w-a_i}\right)^2\left[2.1630 + 12.219\left(\frac{a_i}{w}\right) - 20.065\left(\frac{a_i}{w}\right)^2 - 0.9925\left(\frac{a_i}{w}\right)^3 + 20.609\left(\frac{a_i}{w}\right)^4 - 9.9314\left(\frac{a_i}{w}\right)^5\right]. \tag{3.4}$$

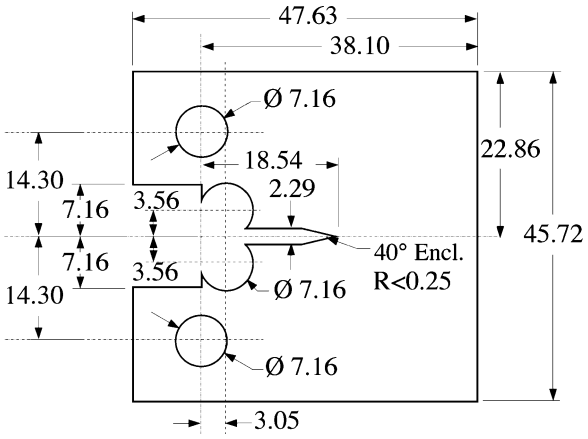

Fig. 3.1 Compact tension (CT-1/2) fracture specimen geometry with integrated load-line knife-edges for COD gage with dimensions in mm

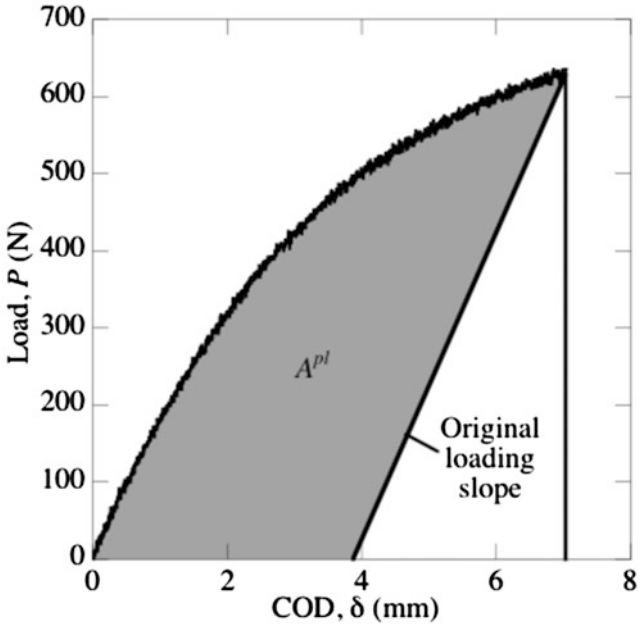

Fig. 3.2 Representative load–displacement curve

Values of the yield stress σ_{ys} must still be determined—nominally from tensile dog bone measurements—and are sensitive to the same strain-rate dependence as E. It is first worth noting that while errors in E have a first-order linear effect on the elastic fracture energy component, errors in σ_{ys} have a second-order effect on the plastic fracture energy component. Therefore, the error in J from ignoring the strain-rate dependence of σ_{ys} are small, particularly if the plastic component is small. Moreover, E is determined from the measured specimen compliance early in the test when the plastic component is negligible. The value of E can then be compared to experimental data taken over a range of strain-rates to determine the representative strain-rate. The value of σ_{ys} corresponding to this strain-rate can then be used in calculating J_{pl}.

To rigorously evaluate J_{IC}, J–R curve data are constructed with the critical fracture criterion, J_{IC}, defined as the fracture toughness of the material at fracture instability prior to the onset of significant stable tearing crack extension (the point of 0.2 mm of crack growth beyond crack tip blunting). The required data for application of the normalization technique consists of a record of load versus displacement P_i–δ_i, the initial crack length a_0, and the final crack length a_f. The final crack size is measured at nine equally spaced points centered about the specimen centerline. The two near surface measurements are averaged and then averaged with the remaining seven crack length measurements. The load data P_i up to the maximum load P_{max} is normalized by

$$P_{\mathrm{N}i} = \frac{P_i}{wb\left[\frac{w-a_{bi}}{w}\right]^{\eta_{pl}}}. \tag{3.5}$$

The final load–displacement data pair is normalized using the final measured crack length a_{f}. The plastic component of the load-line displacement is normalized as

$$\delta_i' pl = \frac{\delta_i^{pl}}{w} = \frac{\delta_i - P_i C_i}{w}, \tag{3.6}$$

where C_i is the specimen elastic load line compliance calculated with the instantaneous crack length,

$$C_i = \frac{1}{Eb}\left(\frac{w+a_i}{w-a_i}\right)^2\left[2.1630 + 12.219\left(\frac{a_i}{w}\right) - 20.065\left(\frac{a_i}{w}\right)^2 - 0.9925\left(\frac{a_i}{w}\right)^3 + 20.609\left(\frac{a_i}{w}\right)^4 - 9.9314\left(\frac{a_i}{w}\right)^5\right]. \tag{3.7}$$

Prior to crack extension C_i approximates the slope of the load–load line displacement curve. In this regime (3.6) very sensitive to the compliance and can in turn cause significant error in the calculated fracture toughness. To overcome this error and to incorporate the strain-rate, temperature, and sample-to-sample variation in E, (3.7) is set equal to the linear

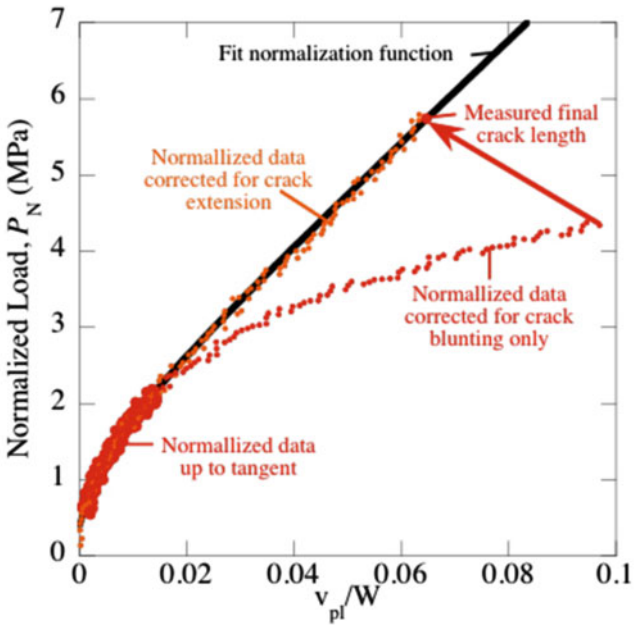

Fig. 3.3 Representative curve of normalized data

slope of the small-deformation section of the load–load line displacement curve to solve to E on a sample-by-sample basis. These values of E are compared well with those from dog-bone measurements over a reasonable range of strain-rates. A representative plot of the normalized data set corresponding to the data in Fig. 3.2 is given in Fig. 3.3. Normalized data corresponding to $\delta'^{pl}_i \leq 0.001$ is excluded. The normalized data is fit with a normalization function of the form

$$P_N = \frac{a + b\delta'_{pl} + c\delta'^{\,2}_{pl}}{d + \delta'_{pl}}, \tag{3.8}$$

where a, b, c, and d are fitting coefficients determined with Kaleidagraph (graphical data analysis software from Synergy Software, Reading, PA) while forcing the curve to intercept the final data point. This equation approximates a power law for small δ'_{pl} and smoothly transitions to a linear relationship for large δ'_{pl}. Because crack initiation generally occurs prior to the maximum load in ductile fracture, ASTM standard E1820 requires some manipulation of the normalized data to optimize the fit of the normalization function to the data. Once the normalization function is fixed, the previously excluded data is analyzed by determining the crack length—a value between the blunting corrected crack length and the final crack length—that forces each data pair to fall on the normalization function. These crack lengths give an accurate estimate of the crack tip position over the course of the test. The resulting J-integral–crack length data pairs are used to construct a J–R curve, shown in Fig. 3.4, which is subsequently used to determine J_{IC} values. The normalization technique is limited to cases of short crack extension (less than 15% of w-a).

3.3 Conclusions

The single specimen normalization technique for J-integral fracture toughness has been successfully employed to study the strongly non-linear fracture response of ductile semicrystalline polymers. Particularly for very ductile polymers the compliance term used to determine the plastic displacement can dominate the solution and small errors in determining theelastic modulus can lead to large errors in the normalization or even make it ill posed. This can be further complicated for polymers where the elastic modulus is strong strain rate dependent and simply using a "quasistatic" modulus from a dogbone measurement may not equate to the dominant strain rate in the compact tension specimen. By measuring the compact tension specimen compliance, the Young's modulus can be calculated on a specimen-by-specimen basis. This overcomes sample-to-sample variation and more importantly address the strain rate dependence of the Young's modulus.

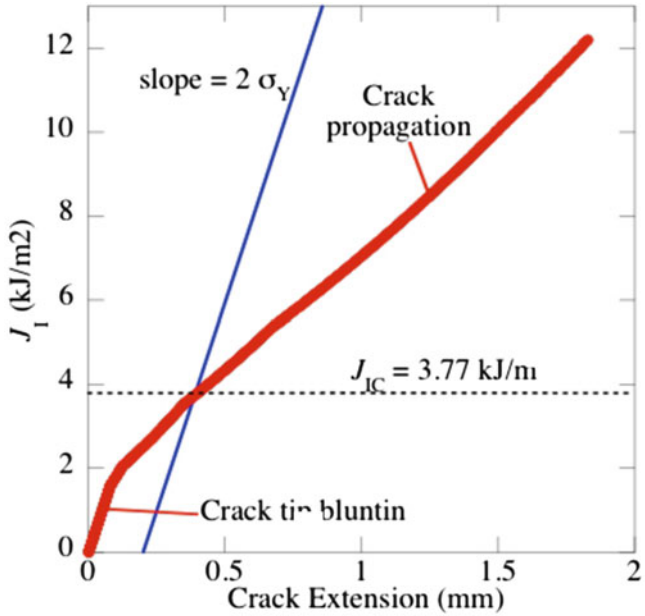

Fig. 3.4 Representative *J–R* curve obtained using the normalization technique

References

1. Rae PJ, Trujillo CP, and Lovato ML, in Shock Compression of Condensed Matter-2009, edited by M. L. Elert, W. T. Buttler, M. D. Furnish, W. W. Anderson, and W. G. Proud, AIP Press, Nashville, TN, 2009, pp 1119–1122.
2. Rae PJ, Brown EN (2007) On the mechanical properties of poly(ether-ether-ketone) (PEEK) with emphasis on the large compressive strain response. Polymer 48(2):598–615
3. Brown EN, Rae PJ, Orler EB (2006) The influence of temperature and strain rate on the constitutive and damage responses of Polychlorotrifluoroethylene (PCTFE, Kel-F 81). Polymer 47(21):7506–7518
4. Landes JD, Herrera R (1988) A new look at J–R analysis. Int J Fract 34:R9
5. Brown EN, Rae PJ, Orler EB, Gray GT III, Dattelbaum DM (2006) The effect of crystallinity on the fracture of polytetrafluoroethylene (PTFE). Mater Sci Eng C 26(8):1338–1343
6. Brown EN, Dattelbaum DM (2005) The role of crystalline phase on fracture and microstructure evolution of polytetrafluoroethylene (PTFE). Polymer 46(9):3056–3068
7. Bernal CR, Montemartini PE, Frontini PM (1996) The use of load separation criterion and normalization method in ductile fracture characterization of thermosetting polymers. J Polym Sci 34:1869
8. Che M, Grellman W, Seidler S, Landes JD (1997) Application of a normalization method for determining J-R curves in glassy polymer PVC at different cross head speeds. Fatigue Fract Eng Mater 20:119
9. Morhain C, Velasco JI (2001) Determination of J–R curve of polypropylene copolymers using the normalization method. J Mater Sci 36:1487
10. Landes JD, Bhambri SK, Lee K (2003) Fracture toughness testing of polymers using small compact specimens and normalization. J Test Eval 31:1
11. Joyce JA (2003) Fracture toughness evaluation of polytetrafluoroethylene. Polym Eng Sci 43:1702
12. Joyce PJ, Joyce JA (2004) Evaluation of the fracture toughness properties of polytetrafluoroethylene. Int J Fract 127:361
13. Joyce JA, Joyce PJ (2004) Toughness characterization of a metal filled PolyTetraFluoroEthylene using the J-integral. Eng Fract Mech 71:2513

Chapter 4
Energy Dissipation Mechanism in Nanocomposites Studied via Molecular Dynamics Simulation

Naida M. Lacevic and Shiv P. Joshi

Abstract Many military and industry applications increasingly require advanced materials that are able to simultaneous carry high load (stiffness) and dissipate energy upon impact (damping). Polymer nanocomposites are potentially excellent candidates for these applications since they offer tunability via advancements in nanoscale processing technology (e.g. layer-by-layer deposition). Understanding mechanisms for the simultaneous increase of stiffness and damping in polymer nanocomposites involves characterization of interactions at surfaces between nanoscale constituents and molecular-scale processes including the role of interphase regions and polymer ordering. This information is exceedingly difficult to obtain experimentally due to the small length and time scales and disorder of the system. Here, we perform molecular dynamics (MD) simulations to understand stress and strain heterogeneity responsible for increases in stiffness and dissipation on the nanoscale in a model polymer nanocomposite. We compute local stress and strain fluctuations at polymer-nanoparticle interfaces and identify polymer chain slippage as one of the mechanisms for energy dissipation.

Keywords Nanocomposites • Molecular dynamics simulations • Dissipation

4.1 Introduction

Molecular or nanoscale modeling is a characterization method that can be used in synergy with experiments to address nanoscale processes relevant to simultaneous enhancement of stiffness and damping in nanocomposites. Nanoparticles are characterized by their large surface to volume ratios, and consequently, the interactions that occur between the particle and the matrix within a few nm of the surface often dominate the behavior of nanocomposites. These interactions can drastically change the structure of the material in this region and control its mechanical properties. Furthermore, the small mass and size of the particles gives them unusually high mobility. These effects are generally difficult to predict a priori and require description at the atomistic level of detail.

Molecular dynamics simulations are ideal to understand stress and strain heterogeneity responsible for simultaneous increases in damping and stiffness on the nansoscale, since they explicitly express the interaction of individual (or small groups of) atoms and integrate their motions directly. This allows a highly accurate description of the nanoscale energy dissipation and stress distributions that occur in the vicinity and at the surfaces of nanoparticles. Similar information is difficult or impossible to obtain experimentally due to the small length scales and disorder of the system. The small timescales involved in energy dissipation involving nanoscale constituents are also difficult to probe experimentally. Using MD we can describe the surface and material properties and processes that are required to produce optimal composite microstructures at the atomistic level, and observe their behavior during extreme loading. MD focuses on the small length and timescales characteristic of atoms. This fine resolution is required to describe the roles of interaction at the surfaces between nanoscale constituents, interphase regions, and the molecular-scale processes such as polymer ordering in stiffness and energy dissipation.

In this work, we consider a model clay–polymer nanocomposite system, encompassing the reinforcement surface (clay) and matrix (polymer) interphase region in order to focus on the structure and processes resulting from interfacial effects.

N.M. Lacevic (✉) • S.P. Joshi
NextGen Aeronautics, Inc., 2780 Skypark Dr. Suite 400, Torrance, CA 90505, USA
e-mail: nlacevic@nextgenaero.com

B. Antoun et al. (eds.), *Challenges in Mechanics of Time-Dependent Materials and Processes in Conventional and Multifunctional Materials, Volume 2*, Conference Proceedings of the Society for Experimental Mechanics Series 37,
DOI 10.1007/978-1-4614-4241-7_4,

4.2 Computational Details

Our simulations need to address energy dissipation processes at polymer-clay interfaces, which depend strongly on the clay/polymer adhesion energy and the surface energy of clay fillers. We constructed a molecular model of a clay and polymer nanocomposite interphase shown in Fig. 4.1. Clay, $Al_4Ca_2H_{14}O_{24}Si_8$, is constructed using X-ray diffraction data for the crystal structure of montmorillonite (MTM) from Ref. [1]. The polymer modeled is polyurethane (PU) whose chemical structure is provided in Ref. [2]. This particular polyurethane has been used in Ref. [3] in applications demonstrating increase in stiffness approaching the theoretical maxima in layered polymer nanocomposites. The polymer modeled has chains with molecular weight ~90,000 g/mol and a bulk density ~1.02 g/cm^3 (Fig. 4.2).

Both polyurethane and clay are parameterized via the CVFF force field [4] fully utilizing all degrees of freedom of the polymer–clay interphase region (i.e. all intra- and inter molecular degrees of freedom are unconstrained). Since we are interested in characterizing interphase damping properties as a function of clay volume fraction, we constructed representative volume elements of the composite at four clay volume fractions (Table 4.1). The surface area of the clay (L_x*L_y) is kept constant at 27.86 nm^2 for all clay volume fractions while the length of the box normal to the clay surface (L_z) is changed to achieve the desired volume fractions.

Clay was incorporated into the polymer matrix via a multi-step process. Staring with a pure PU system, we (1) equilibrate the pure polymer with repulsive walls where the clay surface will be placed, (2) append the clay to the PU system, and (3) re-equilibrate the system to allow formation of the interphase region. Equilibration of the systems is performed under

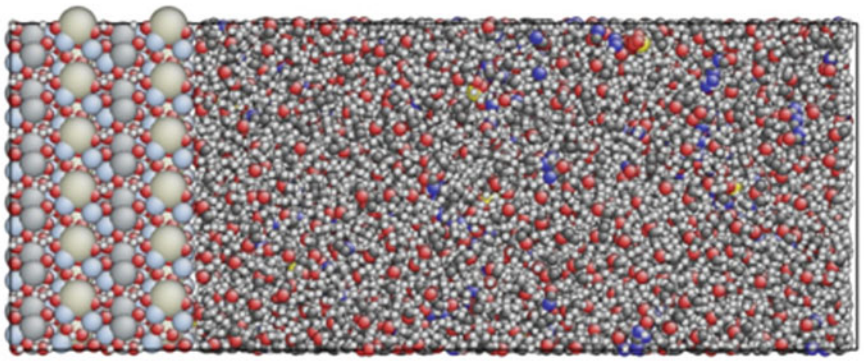

Fig. 4.1 Snapshot of the MD model of a clay–polymer system.

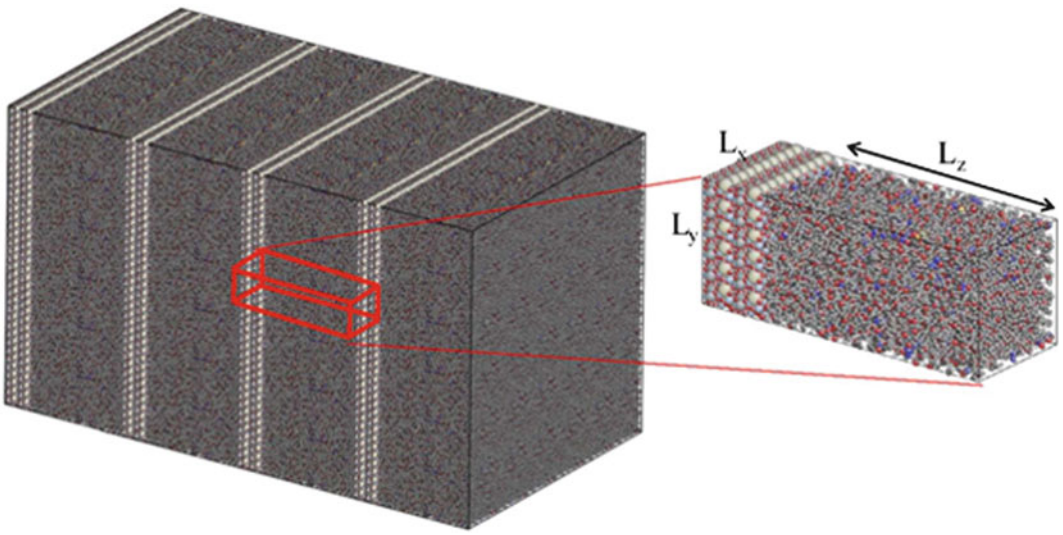

Fig. 4.2 (*Left*) Molecular model of layered nanocomposites, (*right*) representative molecular volume element treated via molecular dynamics

Table 4.1 Sample details

Clay volume fraction (%)	L_z (nm)	Number of PU chains	Total number of atoms
7	29	18	90,606
9	24	15	76,545
12	17	11	57,797
20	11	7	39,049

constant temperature and volume conditions (NVT) at room temperature and normal (atmospheric) pressure. Each system is equilibrated for at least 2 ns or until total energy of the system reaches a constant value. Periodic boundary conditions (PBC) are applied to mimic an infinitely large layered composite. All simulations are implemented and performed in LAMMPS [5].

4.3 Results and Discussions

Deformation simulations are carried out (at high strain rates as necessitated by MD) and used to localize and identify mechanisms for energy dissipation at the clay/polymer interface via density and local stress-stress autocorrelation calculations. The density profile as a function of distance from the clay particle surface is computed. We observe a strong first nearest neighbor peak in the case of oxygen atoms. Since the rigid parts of the polymer chains are oxygen rich compared to the soft parts, this may indicate that rigid segments have greater tendency accumulate closer to the clay surface and contribute to the increase in the stiffness of the interphase region observed in other nanocomposites [6]. In order to better understand the mechanical behavior of the composite, we characterize local shear stiffness based on variations in stress under a uniform shear strain. Figure 4.3 shows local stiffness distributions moving away from the clay surface as a function of the clay volume fraction. This demonstrates the inhomogeneity of stiffness in the interphase region where there is a significant increase close to the surface due to the effect of the polymer–clay interactions.

In addition to the static stiffness inhomogeneities, we are also interested in the variations of strain relaxation throughout the composite. To characterize the local strain distribution, we apply a uniform shear displacement schematically shown in Fig. 4.4. We output displacements of all atoms in the direction of applied shear as the system relaxes and then calculate the non-uniform strain as the derivate of shear displacement. During the relaxation process, per-atom stress and displacement are recorded periodically.

Figure 4.5 shows local strain distribution and strain gradient for a system that contains 7% clay. A sharp drop in the displacement is evident at the polymer–clay interface. This is attributed to chain slippage at the polymer clay interface. The ease of slippage at the interface suggests that the dissipation is dominated by relatively weak interactions between the polymer and the clay particle. The strain gradient in the polymer bulk (shown schematically in Fig. 4.5) is also important to understanding the mechanical behavior of the composite. Information from atomic level simulations such as these can inform continuum level calculations of the mechanical response of composites. Recent work has indicated the importance of matrix strain gradients in the stiffening action of polymer nanocomposites [7]. Strain gradients calculated in atomic level simulations can be applied in larger scale models such as strain gradient Mori-Tanaka to produce accurate predictions of large scale composite behavior.

4.4 Summary

We analyzed mechanisms of stiffening and stress relaxation in the polymer matrix of a clay-polymer nanocomposite and identified slip at the clay-polymer interface as an important energy dissipation mechanism. This analysis is based on correlations of atomic level stress and displacement values during shear relaxation, which allows mapping of inhomogenous dissipation of energy throughout the system. This finely resolved description of the mechanical behavior of the composite elements is available to continuum scale simulations of bulk composite behavior. These observations may be used to elucidate salient features leading to good performance and extrapolation of these to predict optimal combinations of nanoparticle, polymer matrix, and surface chemistry.

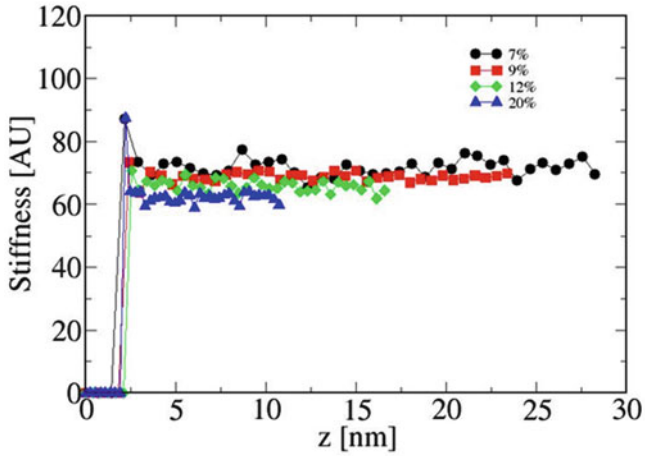

Fig. 4.3 Local stress distribution as a function of distance from clay

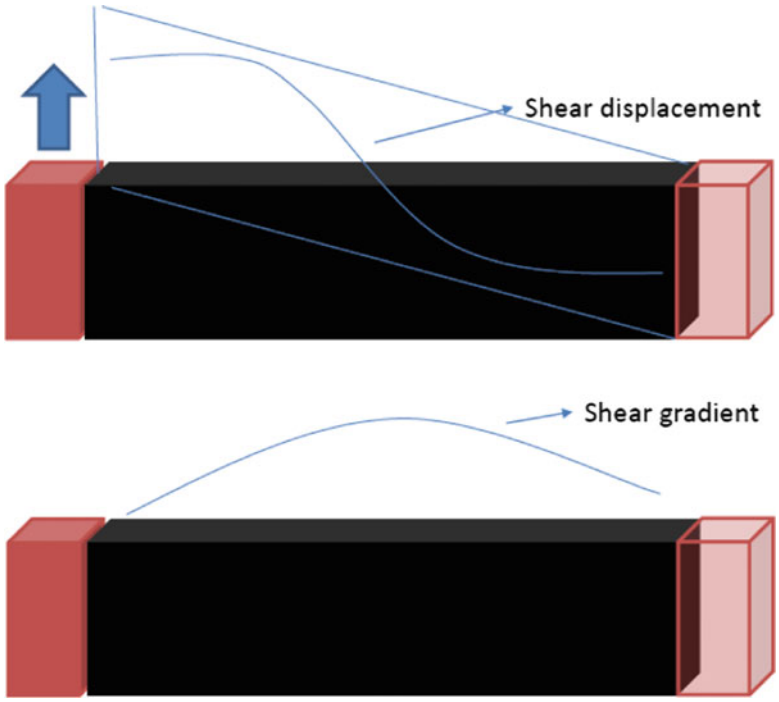

Fig. 4.4 Schematics of shear load application to a representative volume element of layered nanocomposite

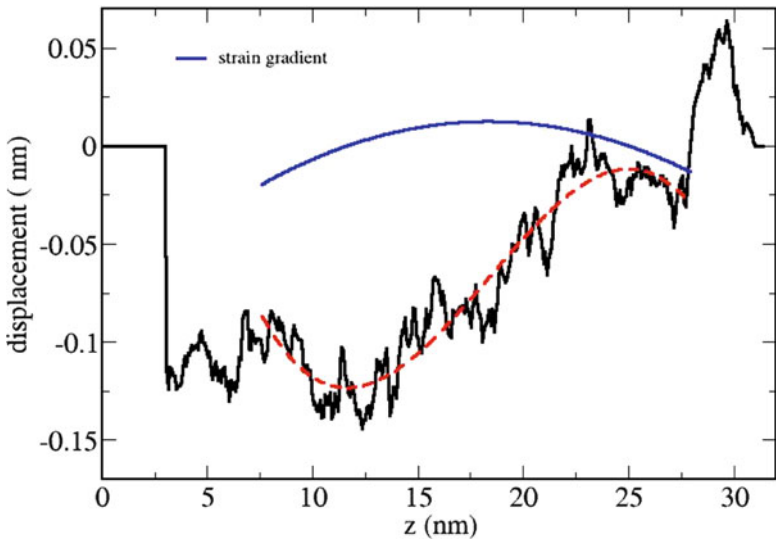

Fig. 4.5 Strain gradient

Acknowledgments This material is based upon work supported by DARPA under Contract No. HR0011-10-C-0192. The views and conclusions contained in this document are those of the authors and should not be interpreted as representing the official policies, either expressly or implied, of the Defense Advanced Research Projects Agency or the U.S. Government. Authors are thankful for useful discussions with Dr. Trisha Sain, Prof. Ellen Arruda, Dr. Bongjun Yeom, Prof. Tony Waas, and Prof. Nicholas Kotov of University of Michigan.

References

1. American Mineralogist Crystal Structure Database (http://rruff.geo.arizona.edu/AMS/amcsd.php)
2. Kaushik A (2010) Deformation mechanisms in polymer-clay nanocomposites. Ph.D. thesis, University of Michigan
3. Podsiadlo P et al (2007) Ultrastrong and stiff layered polymer nanocomposites. Science 318(5847):80–83
4. Dauber-Osguthorpe P et al (1988) Structure and energetics of ligand binding to proteins: *Escherichia coli* dihydrofolate reductase-trimethoprim, a drug-receptor system. Proteins 4(1):31–47
5. Plimpton S (1995) Fast parallel algorithms for short-range molecular dynamics. J Comput Phys 117:1–19
6. Sun L et al (2009) Energy absorption capability of nanocomposites: a review. Compos Sci Technol 69:2392–2409, and references therein
7. Li Y et al (2011) The effects of the interphase and strain gradients on the elasticity of layer by layer (LBL) polymer/clay nanocomposites. Int J Solids Struct 48:1044–1053

Chapter 5
Determination of Stresses in Drying Wood by Means of a Viscoelastic Relaxation Model

Omar Saifouni, Rostand Moutou Pitti, and Jean-François Destrebecq

Abstract Stress states caused in wood by drying periods are often the source of considerable structural disorders, when this material is used as structural material. The origin of these stresses is generally due to the viscoelastic behaviour of the wood combined with the dimensional variations (shrinkage) related to the moisture content. In order to better understand this phenomenon, a slice of green wood is submitted to natural drying in stable environmental conditions. The wood slice is placed on an electronic balance so as so to measure the moisture content variation during the drying period. Simultaneously, the displacements caused in the slice by the drying are captured by a video camera. An incremental relaxation model based on the generalized Maxwell's chain is used to analyze the evolution of the stresses induced by the drying process within the wood slice. Numerical results show the development of tensile stresses in the material. Analyzing these results leads to the conclusion that the stresses are due to the orthotropic behaviour of the wood material combined with anisotropic drying shrinkage. A tensile stress concentration is evidenced in a zone where a crack was finally observed during the test.

Keywords Green wood • Relaxation stresses • Drying process • Finite element method

5.1 Introduction

The natural or the artificial drying of wood is commonly responsible for large strain and can lead to the cracking and the final collapse of the timbers structures. These defects are much more marked on the wood pieces cut and stored outdoors the long periods ago [1]. The timber is composed of polymers sensitive to the temperature and the humidity, therefore, its drying involves dimensional changes due to the shrinkage. Hence, the behaviour of wood during drying depends strongly in the one part, of the geometry, the moisture content gradient, the temperature, the sorption of wood history, but also, of the heterogeneous character, the orthotropic behaviour, and the viscoelastic effects of this material. It appears that, the phenomenon of shrinkage and the mechanical behaviour of wood during drying play an important role in the development of wood defects. In this context, it is essential to understand the contribution of different processes in the strain of the green wood during the drying phase.

In the literature, various studies concerning the strain and the stress evolutions caused by drying of wood have been conducted. These works are generally based on complex analytical approaches solved by finite element models taking into account the changes of the mechanical properties of wood during the drying phase [2, 3]. In addition, several authors have presented drying models that can assess the distribution of moisture inside the wood during the shrinkage with moisture content near the fiber saturation point (FSP) [4]. Also, the mechanical behaviour of wood and tree has been proposed in order to know the impact of the biomechanical and the microstructures parameters in the old history [5]. Recently, the studies on the rheological behaviour of wood during growth phases have shown the effect of the viscoelastic effects in the recovery of the tree during its growth [6] without insist on the contribution of moisture content in the manifestation of this complex phenomenon.

O. Saifouni • R. Moutou Pitti (✉) • J.-F. Destrebecq
Clermont Université, Université Blaise Pascal, Institut Pascal, BP 10448, F-63000, Clermont-Ferrand, France

CNRS, Institut Pascal, UMR 6602, F-63171, Aubiere, France
e-mail: rostand.moutou.pitti@polytech.univ-bpclermont.fr

B. Antoun et al. (eds.), *Challenges in Mechanics of Time-Dependent Materials and Processes in Conventional and Multifunctional Materials, Volume 2*, Conference Proceedings of the Society for Experimental Mechanics Series 37,
DOI 10.1007/978-1-4614-4241-7_5,

In this work, an incremental viscoelastic relaxation model adapted to orthotropic material taking into account the hygroscopic variations of wood during the drying process is developed. The analytical model is based on the Boltzmann integral equations that can be solved by an incremental formulation expressed in term of creep [7] or relaxation [8, 9] approach. The first part describes the mechanism of drying stresses in wood and the experimental details considered in the numerical sample. Then, the incremental law applied to viscoelastic orthotropic material and the algorithm resolution implemented in the finite element code Cast3m, are detailed together. The numerical results, in terms of stress evolutions, with and without viscoelastic behaviour are compared are discussed.

5.2 Experimental Technique

5.2.1 Wood Drying Mechanical Behaviour and Experimental Setup

The objective of the drying process is to reduce the moisture content of wood avoiding in the same time the potential losses of quality caused by the different defects existing in the wood material [2]. For the wood species, it appears that above the fiber saturation point (FSP), the wood is not submitted to any dimensional changes. However, below the FSP until the anhydrous state, there is an almost linear relationship between moisture content and the dimensional changes [10]. The FSP rate is slightly variable and depends on the considered species. According to the cylindrical geometry of the tree, the circular path of the annual rings and the axial orientation of cells, an axisymmetric mechanical characteristics or cylindrical orthotropic material (longitudinal L, tangential T, and radial R directions) can be applied. In fact, the shrinkage is due to the dimensional changes during the variation of moisture content. Thus, each species is characterized by three coefficients of shrinkage (axial, radial and tangential shrinkages) that express the dimensional variations of a wood piece for a humidity change of 1% in the three directions mentioned above. The drying strain is highly anisotropic and the axial shrinkage can be neglected compared with the tangential and the radial shrinkage [10]. However, for some species, the radial and tangential shrinkage are almost identical, consequently, these species are less sensitive to drying cracks.

The experimental setup is based on the mark tracking method consisting of an acquisition system date recording the displacement of target posted on the wood slice during the drying phase, Fig. 5.1a. The diameter and thickness of the slice are about 10 and 2.5 cm respectively, and the environmental conditions of the room test are constant. Simultaneously, the sample is placed on an electronically balance providing the weight measure versus time, Fig. 5.1b.

5.2.2 Experimental Results

Figure 5.2 shows the evolution of the moisture content versus time obtained for a slice of green wood subjected to natural drying.

The slice was placed on a high-sensitivity weigh whose values were recorded every two hours until the stabilization of the internal moisture around 11% for a FSP of about 22%. The range time of observed hygroscopic variation is 14 h. According to the marked posted on the slice along the radius R_i, the displacements of the target 27 (see Fig. 5.3a) versus the moisture content are shown by Fig. 5.3b. It observed also that, the PSF is about 22% due to the low variation of displacements.

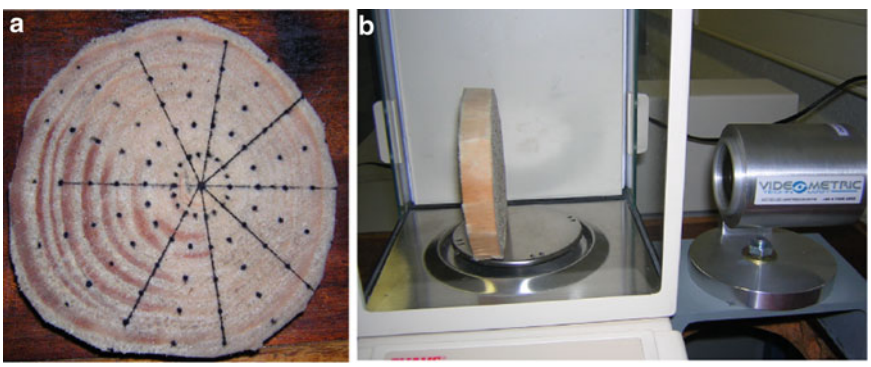

Fig. 5.1 (**a**) Green wood slice; (**b**) experimental device

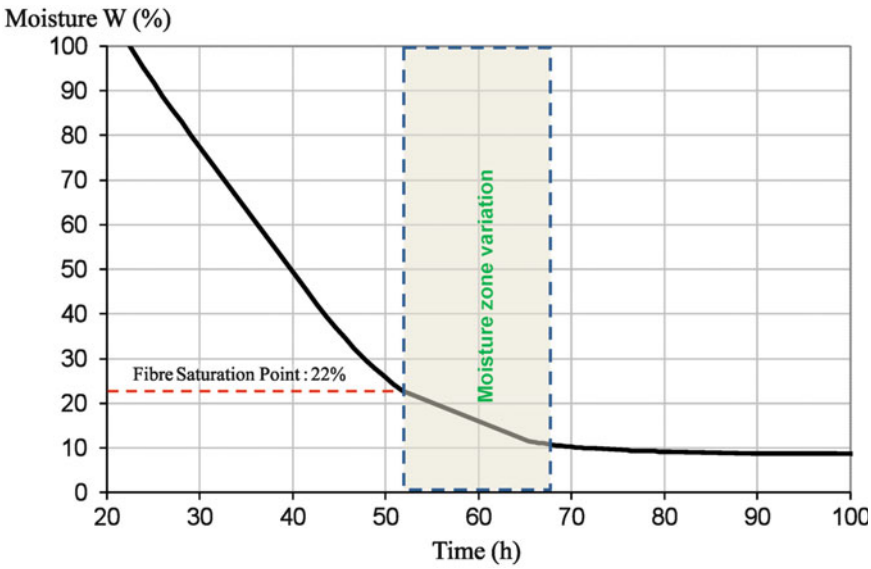

Fig. 5.2 Evolution of moisture versus time computed [11]

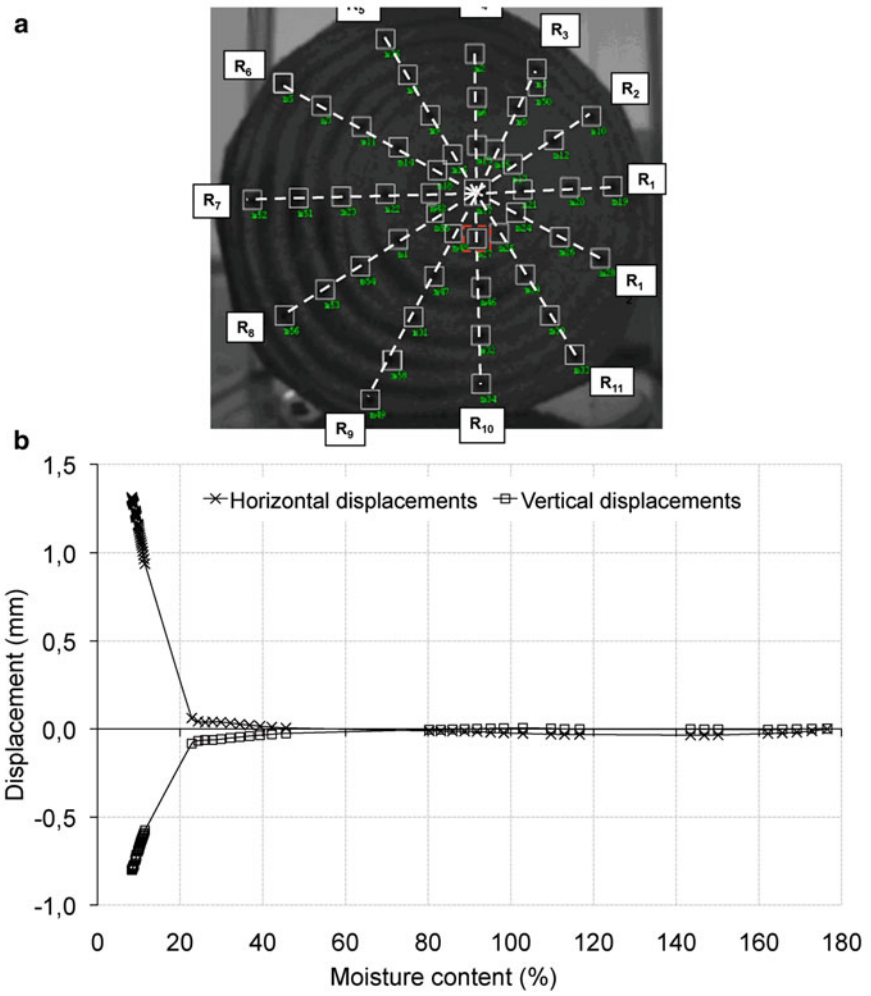

Fig. 5.3 (**a**) Target on wood slice; (**b**) displacement evolutions versus moisture content

5.3 Viscoelastic Formulation and Algorithm

5.3.1 Viscoelastic Incremental Approach

The behaviour of a viscoelastic solid material can be written in the course of time in the form of a Volterra's integral as follows: In the general orthotropic case, the viscoelastic relaxation matrix $[R(t,t_0)]$ depends on nine independent time functions t_0 (time loading application) and t (current time). This number is reduced to three in the one-dimensional case (plane stress or plane strain) if the creep or the relaxation takes place at constant Poisson's coefficient. According to the additional assumption that these quantities change proportionally to the same dimensionless relaxation function, the viscoelastic matrix relaxation is given by

$$[R(t,t_0)] = \rho(t,t_0)[K_0] \tag{5.1}$$

In this expression, $[K_0]$ is the orthotropic elastic stiffness matrix; $\rho(t,t_0)$ is a non-dimensional function that is expressed with a Dirichlet series (spectral representation equivalent to a generalized Maxwell model, Fig. 5.4):

$$\rho(t,t_0) = \gamma_0 + \sum_{\mu=1}^{r} \gamma_\mu \, e^{-\alpha_\mu (t-t_0)} \text{ with } \sum_{\mu=0}^{r} \gamma_\mu = 1 \text{ and } \rho(t,t_0) \in [1, \gamma_0[\tag{5.2}$$

The behaviour law of a viscoelastic material is given by the following Boltzmann constitutive equation written in the relaxation approach

$$\{\sigma(t)\} = [K_0] \int_0^t \rho(t,\tau) \, \{\dot{\varepsilon}^m(\tau)\} \, d\tau \tag{5.3}$$

Considering that the total strain is given by

$$\{\varepsilon(\tau)\} = \{\varepsilon^m(\tau)\} + \{\varepsilon^*(\tau)\} \tag{5.4}$$

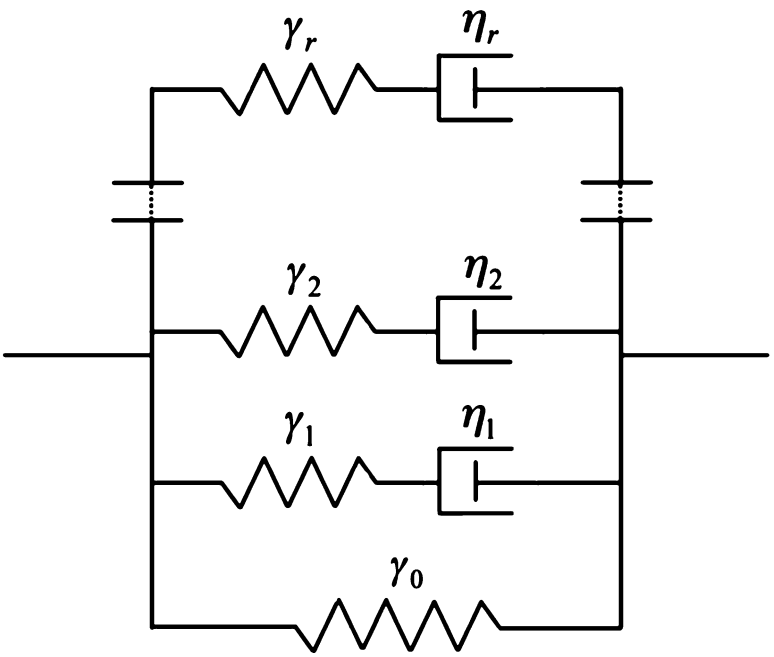

Fig. 5.4 Generalized Maxwell model

where$\{\varepsilon^m(\tau)\}$ is the origin mechanical strain,$\{\varepsilon^*(\tau)\}$ is the non dependent free strain of the material stress state (drying moisture). According to the (5.3), the stress increment $\{\Delta\sigma\}$ for a finite time interval $[t,\ t+\Delta t]$ takes the following form:

$$\{\Delta\sigma\} = [K_0]\left(\int_t^{t+\Delta t} \rho(t+\Delta t,\tau)\,\{\dot{\varepsilon}^m(\tau)\}d\tau + \int_0^t (\rho(t+\Delta t,\tau)-\rho(t,\tau))\,\{\dot{\varepsilon}^m(\tau)\}\,d\tau\right) \tag{5.5}$$

We suppose that the strain $\{\varepsilon^m(\tau)\}$ can be approached by a linear form during the time finite interval $[t,\ \ t+\Delta t]$ as follow:

$$\{\varepsilon^m(\tau)\} \cong \{\varepsilon^m(\tau)\} + \frac{\tau - t}{\Delta t}\{\Delta\varepsilon^m\} \text{ with } \{\dot{\varepsilon}^m(\tau)\} \cong \frac{\{\varepsilon^m\}}{\Delta t} \tag{5.6}$$

Finally, introducing the (5.6) and (5.4) in the relation (5.5), the orthotropic linear viscoelastic law takes the form of an incremental matrix equation:

$$\{\Delta\sigma\} = \left[\tilde{K}\right]\{\Delta\varepsilon\} + \left\{\sigma^{hist}(t)\right\} - \{\Delta\sigma^*\}\ \forall t, \Delta t \tag{5.7}$$

with

$$\begin{gathered}\left[\tilde{K}\right] = \left(\gamma_0 + \sum_{\mu=1}^{r}\tilde{\gamma}_\mu\right)[K_0] = \left(\gamma_0 + \sum_{\mu=1}^{r}\gamma_\mu\frac{1-e^{-\alpha_\mu\Delta t}}{\alpha_\mu\Delta t}\right)[K_0] \text{ and} \\ \left\{\sigma^{hist}(t)\right\} = \sum_{\mu=1}^{r}\left\{\sigma^{hist}{}_\mu(t)\right\} = -\sum_{\mu=1}^{r}\left(1-e^{-\alpha_\mu\Delta t}\right)\left\{\sigma_\mu(t)\right\} \quad \text{et} \quad \{\Delta\sigma^*\} = \left[\tilde{K}\right]\{\Delta\varepsilon^*\}\end{gathered} \tag{5.8}$$

where $\left[\tilde{K}\right]$ is the fictitious rigidity matrix. $\left\{\sigma^{hist}(t)\right\}$ is the term history witch summary the past loading effects until the first loading on the actual response. These values depends of the parameters α_μ, $\gamma_\mu$and of the time increment Δt; it depends also of the internal variables witch must be actualized at the end of each increment calculation:

$$\{\sigma\mu(t+\Delta t)\} = \{\sigma\mu(t)\} + [\tilde{K}\mu](\{\Delta\varepsilon\} - \{\Delta\varepsilon^*\}) + \{\sigma_\mu^{hist}(t)\} \qquad \forall\mu \in [1,r]: \tag{5.9}$$

The tensor $\{\Delta\varepsilon\}$ represents the strain increment for the step past time.

5.3.2 *Finite Element Implementation*

The proposed viscoelastic incremental model is implemented in the finite element software Cast3m following the routine presented in Fig. 5.5.

Each step viscoelastic calculation begins by the evaluation of the fictitious rigidity matrix $\left[\tilde{K}\right]$ and the hereditary stress $\left\{\sigma^{hist}(t)\right\}$. After, the precedent data are considered in the solving of the equivalent thermoelastic problem according to (5.7). Finally, the internal stresses regarding (5.8) are actualized before the following step.

5.4 Numerical Simulation and Discussion

5.4.1 *Wood Slice Viscoelastic Parameters*

The wood green slice (Douglas fir, see Fig. 5.4) is modelled with the finite element software Cast3M. Considering the Small thickness, the plane stress hypothesis is considered. The hygroscopic boundary conditions are free and the vertical displacements are zeroed at the bottom of the specimen. The modelling is conducted on the basis of the incremental formulation presented in the Sect. 5.3.1 by considering a Zener's model composed of two Maxwell's cells posted in Fig. 5.4.

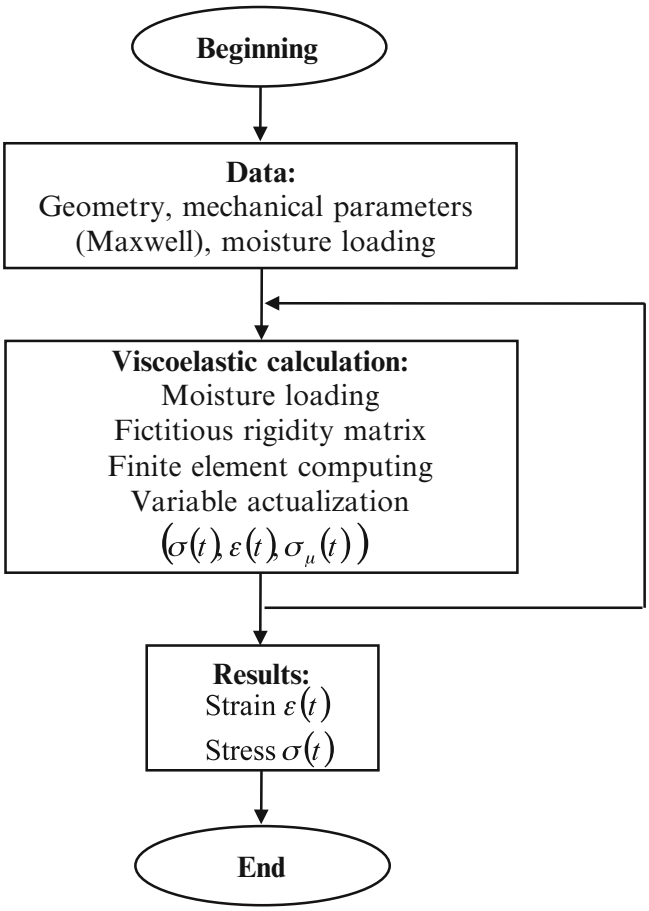

Fig. 5.5 Viscoelastic incremental routine

Table 5.1 Parameters of the relaxation function

E_r(GPa)	E_t(GPa)	G_{rt}(GPa)	υ_{rt}	α_r	α_t	γ_0	γ_1	$\alpha_1(h^{-1})$
1.125	0.730	0.096	0.3	0.17	0.31	0.75	0.25	0.5

The tree elastic moduli (E_r, $E_t$and G_{rt}), the Poisson's coefficient $\upsilon_{rt}$the radial and tangential shrinkage coefficients ($\alpha_r$and α_t) and the parameters of the non-dimensional relaxation function $\rho(t_0, t)$ are presented in the following Table 5.1.

5.4.2 Results and Discussion

The numerical simulation shows the stress onset during the development shrinkage by the heterogeneity of wood due to the orthotropic character or the shrinkage process

The stress analysis shows that the slice is compressed almost everywhere in the radial direction (Fig. 5.6a). In the circumferential direction (Fig. 5.6b), the sign of the stresses changes: there are tensile stresses at the periphery and compression stresses when approaching the center. We note also the existence of two zones of circumferential traction concentration stresses due to the asymmetry of the slice. For the further, we study the evolution of circumferential stresses versus the radius noted R, which connects the center of the slice around P1 at the point P4, where the circumferential stress is maximal.

Figure 5.7 shows that the circumferential stresses occur in a self-balanced manner along the radius R, the compressed zone at the center balancing the tension zone at the periphery.

Figure 5.8 shows the evolution of the circumferential stresses versus time for each point P1 to P4 in the case of elastic and viscoelastic behaviour. The both figures show that the stresses increase over time with the shrinkage increase until the time t = 14 h. In addition, the stresses stabilize and reduce due to relaxing effect (Fig. 5.8). The comparison between elastic and

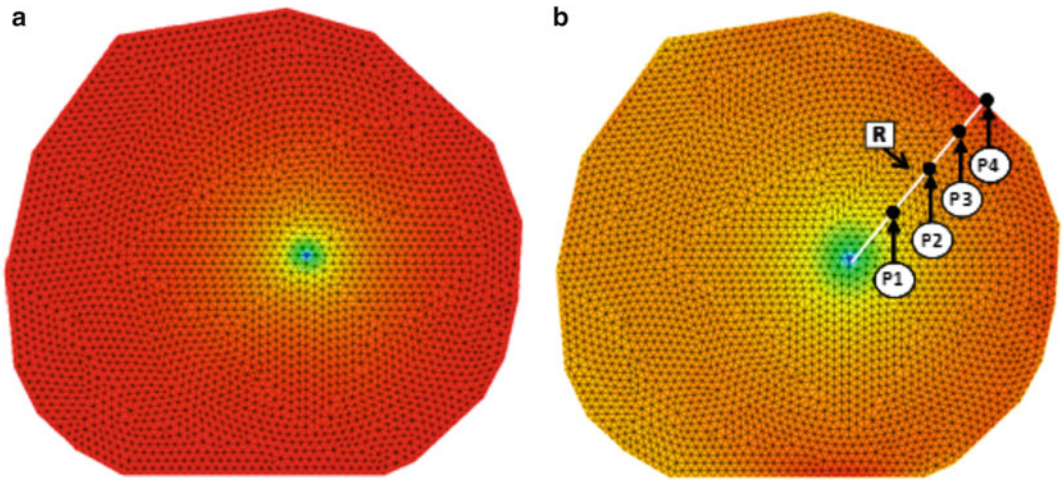

Fig. 5.6 Stress at the time $t = 14$ h: (**a**) radial stresses, (**b**) circumferential stresses

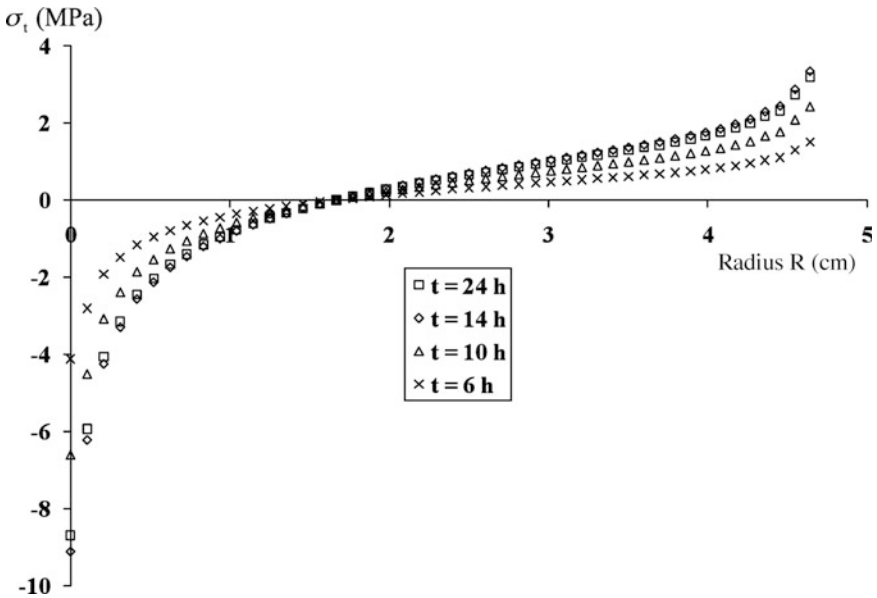

Fig. 5.7 Distribution of circumferential stresses along the radius R

viscoelastic calculations shows that the elastic calculation overestimates the stresses. In the viscoelastic case, the calculations yield stresses lower than in the elastic case.

5.5 Conclusion

The hydro-mechanical behaviour of wood during drying and the heterogeneous and orthotropic character of the material have been recalled. The experimental setup consisted of composed of a Douglas fir green wood slice, posted on a sensitively weigh, and a video camera recorded the displacements of targets have been used. The PSF around 22/% has been obtained by this technique. Then the decomposition of the relaxation tensor on the basis of a Dirichlet series has been introduced. This provided, according to the Boltzmann equation, to write the constitutive viscoelastic matrix under a free incremental strain. An algorithm incorporating the proposed incremental formulation, the humidity and the orthotropic behaviour of wood has been proposed and implemented using the finite element software Cast3m.

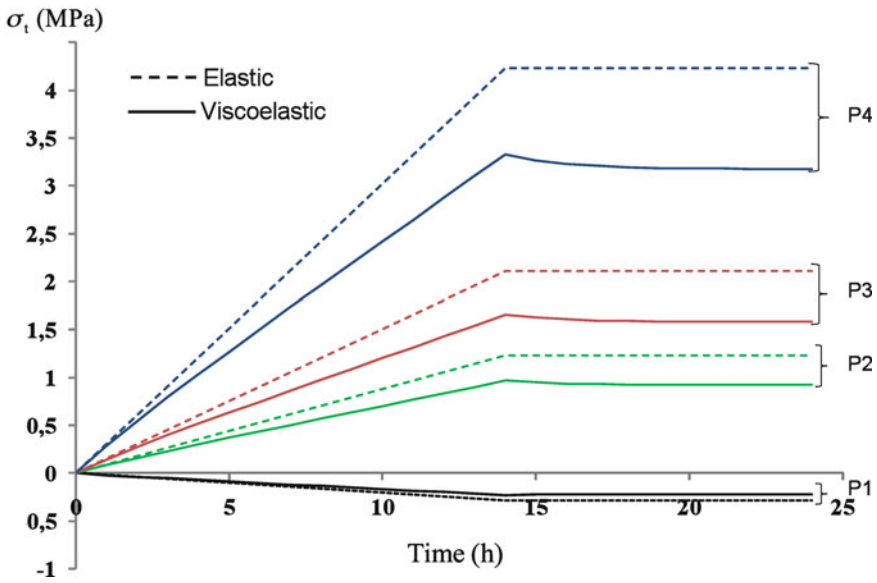

Fig. 5.8 Evolution of circumferential stresses along the radius (P1–P4)

This model was used to simulate a green wood slice subjected to natural drying. There is the appearance of stresses due to shrinkage and the wood orthotropic character. The combined effect of water loss and the viscoelasticity of wood gives stresses below those obtained by elastic calculation. The tensile stresses are observed in the circumferential direction with distance from the heart of the slice, the reaching peak values are observed at the slice boundary. These stresses can lead to radial cracking frequently observed in the drying phase. The characterization and the study of hydro-viscoelastic effects of wood are needed to predict its behaviour and avoid the risk of cracking during the drying process.

References

1. Ormarsson S, Dahlblom O, Petersson H (1998) Numerical study of the shape of Sawn timber subjected to moisture variation, part 1: theory. Wood Sci Technol 32:325–334
2. Moutee M (2006) Modélisation du comportement mécanique du bois au cours du séchage. Ph.D. thesis, Université Laval, Québec
3. Diawanich P, Matan N, Kyokong B (2010) Evolution of internal stress during drying, cooling and conditioning of rubberwood lumber. Eur J Wood Prod 68:1–12
4. Husson JM, Dubois F, Sauvat N (2010) Elastic response in wood under moisture content variations: analytic development. Mech Time-Depend Mater 14:203–217
5. Thibauta B, Gril J, Fournier M (2001) Mechanics of wood and trees: some new highlights for an old story, Mécanique du bois et biomécanique des arbres: nouveaux regards sur une vieille question. CR Mecanique 329:701–716
6. Coutand C, Mathias JD, Jeronimidis G, Destrebecq JF (2011) TWIG: a model to simulate the gravitropic response of a tree axis in the frame of elasticity and viscoelasticity, at intra-annual time scale. J Theor Biol 273:115–129
7. Chazal C, Moutou Pitti R (2011) Incremental constitutive formulation for time dependent materials: creep integral approach. Mech Time-Depend Mater. doi:10.1007/s11043-011-9135-z
8. Jurkiewiez B, Destrebecq JF, Vergne A (1999) Incremental analysis of time-dependent effects in composite structures. Comp Struct 73:425–435
9. Saifouni O, Moutou Pitti R, Destrebecq JF (2011) An incremental constitutive law for damaging viscoelastic materials. SEM annual conference & exposition on experimental and applied mechanics, Mohegan Sun, Uncasville. Springer, New York. DOI 10.1007/978-1-4614-0213-8
10. Navi P, Heger F (2005) Comportement thermo-hydromécanique du bois, Presses polytechniques et universitaires romandes, CH-1015 Lausanne.
11. Moutou Pitti R (2012) Mesure des déplacements par analyse d'images: déformations lors du sechage d'une rondelle de bois vert, Edition EUE, ISBN: 978-3-8417-9719-3

Chapter 6
Multiscale Modeling of Mechanoresponsive Polymers

Meredith N. Silberstein, Cassandra M. Kingsbury, Kyoungmin Min, Sharlotte B. Kramer, Brett A. Beierman, Narayan R. Aluru, Scott R. White, and Nancy R. Sottos

Abstract Mechanically-induced reactivity is a promising means for designing self sensing and autonomous materials. Mechanically sensitive chemical groups called mechanophores can be covalently linked into polymers in order to trigger specific chemical reactions upon mechanical loading. Here, glassy PMMA and rubbery PMA each linked with mechanochromic molecules, are used as representative polymer architectures for building both understanding and quantitative models of mechanophore activation in bulk polymers.

Keywords Mechanoresponsive polymers • Mechanopore activation • Activation modelling

6.1 Introduction

Mechanoresponsive polymers are created by covalently bonding force sensitive molecules, termed mechanophores, into bulk polymer architectures. Activation of the local chemical reaction (an electrocyclic ring opening converting spiropyran to its merocyanine form) is found to occur in response to macroscopic polymer deformation. The activation can be monitored via fluorescence associated with the merocyanine form of the mechanophore [1]. These mechanophores can therefore serve as probes into the local polymer environment and are ideal for determining design principles for smart materials based on alternative mechanophore chemistries. A microstructurally-based continuum model for the activation can help build quantitative understanding of the interaction between polymer architecture and molecular activation, and will set the groundwork for future mechanophore-based active material design.

6.2 Experiments

In order to build both the probe and predictive capability, we investigate two mechanophore linked representative polymer architectures: elastomeric linear polymethacrylate (PMA) and glassy crosslinked polymethylmethacrylate (PMMA). For the linear system a mechanophore is at the center of each polymer chain. For the crosslinked system, the mechanophores constitute 2% of the crosslinks. Full field fluorescence is collected during mechanical testing in order to obtain simultaneous information on stress, strain, time, and mechanophore activation. Specifically, the crosslinked PMMA is characterized via solid cylinder torsion and the linear PMA is characterized via uniaxial tension. As expected, the two materials have fundamentally different mechanical responses (Fig. 6.1a). PMMA is found to have an elastic-plastic mechanical behavior typical of glassy polymers with a linear elastic regime followed by a rate dependent yield peak which softens to a rate dependent minimum value and then exhibits moderate hardening. PMA is found to have a highly non-linear viscoelastic response typical of rubbery polymers. The two materials also have fundamentally different mechanophore activation responses (Fig. 6.1a). The onset of mechanophore activation in PMMA is found to occur following post-yield softening

M.N. Silberstein (✉) • C.M. Kingsbury • K. Min • S.B. Kramer • B.A. Beierman • N.R. Aluru • S.R. White • N.R. Sottos
Beckman Institute for Advanced Science and Technology, University of Illinois at Urbana-Champaign, 405 N. Mathews Avenue, Urbana, IL 61801, USA
e-mail: meredith.silberstein@gmail.com

B. Antoun et al. (eds.), *Challenges in Mechanics of Time-Dependent Materials and Processes in Conventional and Multifunctional Materials, Volume 2*, Conference Proceedings of the Society for Experimental Mechanics Series 37,
DOI 10.1007/978-1-4614-4241-7_6,

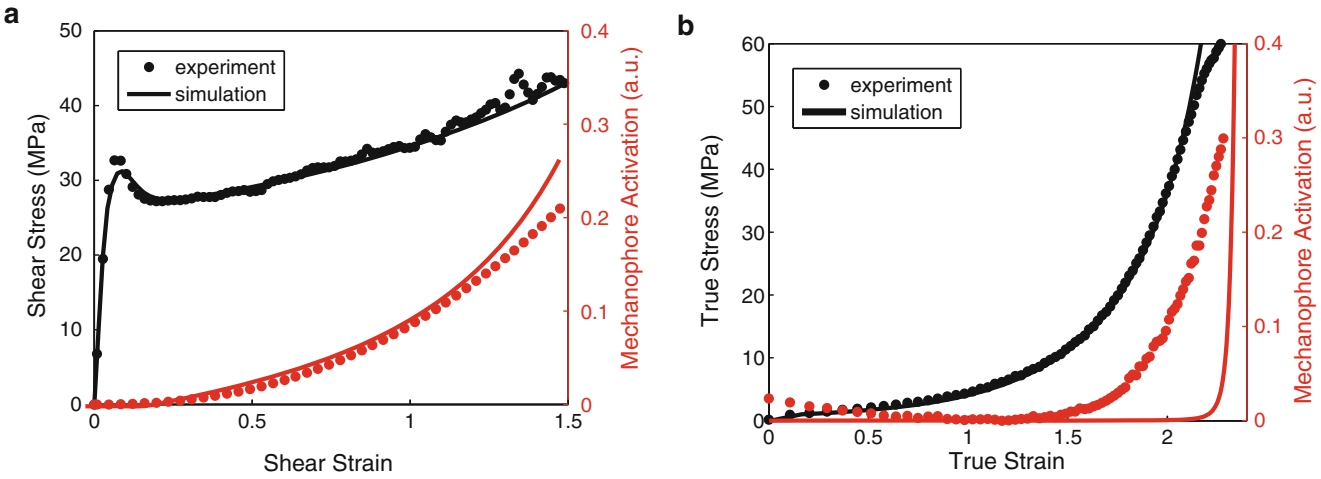

Fig. 6.1 Mechanical and fluorescence activation response of two different mechanophore-linked polymer architectures: (**a**) response of crosslinked PMMA to shear loading, (**b**) response of linear PMA to tensile loading

at a shear strain and stress of roughly 0.3 and 30 MPa respectively [2]. The activation then grows with strain with a gradually increasing slope. The onset of activation in PMA occurs at a significantly higher strain ($\sim$ 1.5) and significantly lower stress ($\sim$ 8 MPa). The activation then grows with an increasing slope that closely trails the shape of the stress-strain curve.

6.3 Model

A fully three dimensional continuum model is developed for the mechanical behavior and mechanophore activation in each polymer. These models take input from density functional theory (DFT) simulations of the spiropyran to merocyanine force-activated transformation, molecular dynamics simulations of the polymer architecture, polymer mechanics literature, and experimental data. The mechanical models are similar to those found in the literature and will not be discussed further here except to say they are sufficient to capture the rate dependent stress-strain response of each material over the range of conditions spanned experimentally.

The heart of the activation model is based on DFT simulations which reveal that the rate kinetics for conversion from the spiropyran to merocyanine form are strongly modified by the application of force across the mechanophore. In a bulk polymer, macroscopic stress provides the driving force for the spiropyran to merocyanine conversion. We therefore adopt a modified transition rate theory in which stress acts to reduce the spiropyran to merocyanine activation barrier with the form for the forward activation reaction given by Eq. 6.1:

$$\dot{\alpha} = \kappa \exp\left[-\frac{\Delta G}{R\theta}\left(1 - \frac{\sigma}{s_\alpha}\right)\right](1-\alpha) \tag{6.1}$$

where α is the fraction of activated mechanophores, κ is an attempt frequency, ΔG is the activation barrier to the stress-free spiropyran to merocyanine transition, R is the universal gas constant, θ is absolute temperature, σ is an effective stress measure, and s_α has units of stress and acts to scale the transmitted force. The simplest approximation would be to assume that all of the macroscopic stress is always available to contribute to activating the mechanophores. This assumption is however clearly contradicted by the PMMA data (Fig. 6.1a) in which activation only occurs after the yield peak. A constraint is therefore added to the activation equation which does not allow stress to be transmitted to the mechanophores until sufficient free volume evolution has occurred; free volume evolution has previously been closely tied with yield peak evolution [3, 4].

The activation model as given by Eq. 6.1 with the additional free volume constraint can be reasonably well fit to the monotonic PMMA data as shown in Fig. 6.1a. In order to highlight the differences in the polymer architectures, the identical activation equations and parameters are then used to simulate mechanophore activation within PMA (Fig. 6.1b). The model with these parameters predicts that the onset of activation occurs at a larger stress (and consequently strain) than seen experimentally. It also predicts that the material will reach full activation with minimal further increase in strain.

This comparison highlights the difference in stress transmission in the two polymer architectures. Interestingly, this rather simple exercise does pick up on the qualitative result that activation will increase with strain more drastically in PMA than PMMA due to the strong nonlinearity in mechanical stress.

More sophisticated versions of the activation model are then developed for each polymer as motivated by the underlying architecture of each. The successes and failures of these models in capturing the activation within each polymer under monotonic, stress relaxation, and creep loading are used to deduce the governing physics. The quantitative implementation of each physical idea is found to greatly simplify the comparison among polymer architectures and loading histories, in particular allowing decomposition of the mechanophore rate dependence from the polymer rate dependence.

6.4 Conclusions

Representative mechanochromically linked rubbery and glassy materials were used as model systems for understanding mechanophore activation in solid state polymers. Microstructurally based continuum models were used to determine the pertinent physics and parameters for activation. These models are now ready to be adapted to examine force distribution in other polymers and to guide design of mechanophore based smart materials.

Acknowledgements This material is based upon work supported in part by the U.S. Army Research Laboratory and the U.S. Army Research Office under contract/grant number W911NF-07-1-0409 and in part by an Arnold and Mabel Beckman Foundation postdoctoral fellowship.

References

1. Davis DA, Hamilton A, Yang JL, Cremar LD, Van Gough D, Potisek SL, Ong MT, Braun PV, Martinez TJ, White SR, Moore JS, Sottos NR (2011) Force-induced activation of covalent bonds in mechanoresponsive polymeric materials. Nature 21:8381–8388
2. Kingsbury CM, May PA, Davis DA, White SR, Moore JS, Sottos NR (2009) Shear activation of mechanophore-crosslinked polymers. J Mater Chem 459:68–72
3. Hossain D, Tschopp MA, Ward DK, Bouvard JL, Wang P, Horstemeyer MF (2010) Molecular dynamics simulations of deformation mechanisms of amorphous polyethylene. Polymer 51:6071–6083
4. Srivastava V, Chester SA, Ames NM, Anand L (2010) A thermo-mechanically-coupled large-deformation theory for amorphous polymers in a temperature range which spans their glass transition. Int J Plast 26:1138–1182

Chapter 7
An Identification Method for the Viscoelastic Characterization of Materials

David Yang

Abstract A driving point dynamic load non destructive test can be used to determine the modal stiffness, damping and mass of a structure. If the constitutive equations of viscoelasticity consist of a combination of time independent elastic behavior and time dependent viscous behavior and can be modeled as a collection of spring-dashpot arrangements then the modal stiffness can be used to determine the time independent elastic behavior and the modal damping to determine the time dependent viscous behavior. Using a simple spring and dashpot in parallel model (Kelvin-Voigt), solutions for the material properties of uniform beams in axial deformation, torsion and bending will be given. For non-uniform beams, the elastic properties can be identified by the finite element method which is used to derive the equilibrium equations. The modal stiffness is used to get the zero frequency response (equivalent static response) which determines a single point in the global system flexibility matrix. The identification becomes a problem in minimizing the error norm of the equilibrium equations. Several numerical examples are presented, one of varying geometry and one of varying rigidity.

Keywords Modal analysis • Structural dynamics • Nondestructive test • Viscoelasticity • Damping • System identification • Finite element method • Parameter estimation

7.1 Introduction

There are several methods to determine the coefficient of elasticity of a pavement's sub grade soil from dynamic load non destructive tests. The frequency sweep method [1] uses the driving point frequency response to correlate to the static response of a pavement from a plate load test. The frequency sweep method uses a weighted average of the driving point frequency response to determine the equivalent static response. A previous paper by this author [2] correlated the uniform beam response from a dynamic test to the static response from a conventional test but uses the zero frequency response of the dynamic test to compare to the static response of a conventional test. This paper shows that after introducing viscous damping into the equations of motion, the coefficient of elasticity remains constant but the dynamic response is dependent on two additional constants, a stiffness proportional constant and a mass proportional constant. The stiffness proportional constant is dependent on the material and the mass proportional constant is dependent on the system. Using the zero frequency response of the dynamic test as the equivalent static response, static data system identification methods are now possible.

7.2 Simple Models of Viscoelastic Behavior

In the simplest models of viscoelastic behavior, elastic behavior is represented by a spring while viscous behavior is represented by a dashpot. In the Kelvin-Voight model, the spring and dashpot are arranged in parallel so that under load, the same strain applies to both elements and the response is

D. Yang (✉)
Research Associate, Day Software Systems, Inc., 209 Shelter Rock Rd, Stamford, CT 06903, USA
e-mail: yandz@daysoftware.com

B. Antoun et al. (eds.), *Challenges in Mechanics of Time-Dependent Materials and Processes in Conventional and Multifunctional Materials, Volume 2*, Conference Proceedings of the Society for Experimental Mechanics Series 37,
DOI 10.1007/978-1-4614-4241-7_7,

$$\sigma = E\varepsilon + c\frac{d\varepsilon}{dt} \tag{7.1}$$

For the creep test, the strain is found by solving the ordinary differential equation with the boundary condition that the stress is constant for positive time.

$$\varepsilon = \frac{\sigma_0}{E}\left[1 - e^{-\frac{t}{t_1}}\right] \tag{7.2}$$

The retardation time is

$$t_1 = \frac{c}{E} \tag{7.3}$$

In the Maxwell model, the spring and dashpot are arranged in series so that under load, the same stress applies to both elements and the response is

$$\frac{d\varepsilon}{dt} = \frac{1}{E}\frac{d\sigma}{dt} + \frac{\sigma}{c} \tag{7.4}$$

For the relaxation test, the stress is found by solving the ordinary differential equation with the boundary condition that the strain is constant for positive time.

$$\sigma = E\varepsilon_0 e^{-\frac{t}{t_2}} \tag{7.5}$$

The relaxation time is

$$t_2 = \frac{c}{E} \tag{7.6}$$

For the generalized Kelvin-Voight model, where multiple parallel spring and dashpot are arranged in series, the total strain is

$$\sum \varepsilon_i = \sum \frac{\sigma - c_i\,\dot{\varepsilon_i}}{E_i} \tag{7.7}$$

The stress is

$$\sigma = \frac{1}{\sum \frac{1}{E_i}}\left[\sum \frac{1}{E_i}(E_i\varepsilon_i + c_i\,\dot{\varepsilon_i})\right] \tag{7.8}$$

For the creep test,

$$\varepsilon = \sum \frac{\sigma_0}{E_i}\left(1 - e^{-\frac{t}{t_{1i}}}\right) \tag{7.9}$$

For the generalized Maxwell model, where multiple series of spring and dashpot are arranged in parallel, the total stress is

$$\sum \sigma_i = \sum c_i\dot{\varepsilon} - \sum \frac{c_i}{E_i}\,\dot{\sigma_i} \tag{7.10}$$

The strain is

$$\dot{\varepsilon} = \frac{\sum c_i\left(\frac{1}{E_i}\,\dot{\sigma_i} + \frac{1}{c_i}\sigma_i\right)}{\sum c_i} \tag{7.11}$$

For the relaxation test,

$$\sigma = \sum E_i \varepsilon_0 e^{-\frac{t}{\tau_{2i}}} \tag{7.12}$$

More details are available in reference [3].

7.3 Uncoupled Axial Equations of Motion of Beam with Viscous Damping

The equilibrium of a differential beam element in axial deformation is

$$F + F_{inertial}\,dx - \left[F + \frac{\partial F}{\partial x}dx\right] + F_{damping}\,dx - F_{external}\,dx = 0 \tag{7.13}$$

$$F_{inertial} = m(x)\ddot{u} \tag{7.14}$$

$$F_{damping} = c(x)\dot{u} \;\text{ Generalized damping} \tag{7.15}$$

$$Let\ c(x) = t_0 m(x) \;\text{ Mass proportional damping} \tag{7.16}$$

$$F = \sigma A(x) = \left[u' + t_1 \dot{u}'\right] EA(x) \;\text{ Using Kelvin} - \text{Voight material model.} \tag{7.17}$$

$u(x,t)$ can be transformed from the geometric displacement coordinates to the modal amplitudes or normal coordinates.

$$u(x,t) = \sum_i^{\infty} \varnothing_i(x) U_i(t) \tag{7.18}$$

The $\varnothing_i(x)$ functions are orthogonal. Substituting the above equation into the force equilibrium and multiplying by $\varnothing_n(x)$ and integrating over the beam length gives the uncoupled axial equations of motion of beam with viscous damping.

$$M_n \ddot{U}_n + C_n \dot{U}_n + K_n U_n = \int_0^L \varnothing_n F_{external}\,dx \tag{7.19}$$

$$M_n = \int_0^L \varnothing_n^2 m(x) dx \tag{7.20}$$

$$K_n = -\int_0^L \varnothing_n \frac{\partial}{\partial x}\left[\varnothing_n' EA(x)\right] dx \tag{7.21}$$

$$C_n = t_0 M_n + t_1 K_n \tag{7.22}$$

t_0 *and* t_1 should be constant for all modes if the model is valid.

More details are available in reference [4].

7.4 Uncoupled Torsional Equations of Motion of Beam with Viscous Damping

The equilibrium of a differential beam element in torsion is similar to axial deformation

$$T + T_{inertial}\,dx - \left[T + \frac{\partial T}{\partial x}dx\right] + T_{damping}\,dx - T_{external}\,dx = 0 \tag{7.23}$$

$$T_{inertial} = m(x)J(x)\ddot{\theta} \tag{7.24}$$

$$T_{damping} = c(x)\dot{\theta} \text{ Generalized damping} \tag{7.25}$$

$$Let\ c(x) = t_0 m(x)J(x) \text{ Mass proportional damping} \tag{7.26}$$

$$T = \tau J(x) = \left[\theta' + t_1\dot{\theta}'\right]GJ(x) \text{ Using Kelvin} - \text{Voight material model.} \tag{7.27}$$

$$\theta(x,t) = \sum \varnothing_i(x)\bar{\theta}_i(t) \text{ Normal coordinate transformation} \tag{7.28}$$

$$M_n\ddot{\bar{\theta}}_n + C_n\dot{\bar{\theta}}_n + K_n\bar{\theta}_n = \int_0^L \varnothing_n T_{external}dx \tag{7.29}$$

$$M_n = \int_0^L \varnothing_n^2 m(x)J(x)dx \tag{7.30}$$

$$K_n = -\int_0^L \varnothing_n \frac{\partial}{\partial x}\left[\varnothing_n' GJ(x)\right]dx \tag{7.31}$$

$$C_n = t_0 M_n + t_1 K_n \tag{7.32}$$

7.5 Uncoupled Flexural Equations of Motion of Beam with Viscous Damping

The vertical force equilibrium of a differential flexural beam element is

$$\bar{V} - \bar{V}_{inertial}\,dx - \left[\bar{V} + \frac{\partial \bar{V}}{\partial x}dx\right] - \bar{V}_{damping}\,dx + \bar{V}_{external}\,dx = 0 \tag{7.33}$$

$$\bar{V}_{inertial} = m(x)\ddot{v} \tag{7.34}$$

$$\bar{V}_{damping} = c(x)\dot{v} \text{ Generalized damping} \tag{7.35}$$

$$Let\ c(x) = t_0 m(x) \text{ Mass proportional damping} \tag{7.36}$$

The moment equilibrium of a differential flexural beam element is

$$\bar{M} + \bar{V}\,dx - \left[\bar{M} + \frac{\partial \bar{M}}{\partial x}dx\right] = 0 \tag{7.37}$$

and ignoring rotational inertia

$$\bar{V} = \frac{\partial \bar{M}}{\partial x} and \frac{\partial \bar{V}}{\partial x} = \frac{\partial^2 \bar{M}}{\partial x^2} \tag{7.38}$$

Assuming normal strains vary linearly over the beam cross section and using the axial stress strain relationship from the Kelvin-Voight material model the moment curvature is

$$\bar{M} = EI(x)[v'' + t_1\dot{v}''] \tag{7.39}$$

$$v(x,t) = \sum \varnothing_i(x) V_i(t) \quad \text{Normal coordinate transformation} \tag{7.40}$$

As with the axial deformation the uncoupled flexural equation of motion is

$$M_n \ddot{V}_n + C_n \dot{V}_n + K_n V_n = \int_0^L \varnothing_n \bar{V}_{external} dx \tag{7.41}$$

$$M_n = \int_0^L \varnothing_n^2 m(x) dx \tag{7.42}$$

$$K_n = \int_0^L \varnothing_n \frac{\partial^2}{\partial x^2} \left[\varnothing_n'' EI(x) \right] dx \tag{7.43}$$

$$C_n = t_0 M_n + t_1 K_n \tag{7.44}$$

7.6 Dynamic Modal Model

The response of a multiple degree of freedom system under forced harmonic vibration [4–6], given by the general dynamic modal model is

$$x_s(t) = \sum_{n=1}^{N} \frac{\phi_{sn} \sum_{n=1}^{N} \phi_{dn} F_d}{K_n - \omega^2 M_n + i\omega C_n} e^{i\omega t} \tag{7.45}$$

For the special case when there is only one harmonic load at the sth degree of freedom and the mode shapes are normalized with respect to that location of the load, then $\phi_{sn} = 1$ for n = 1,2,. . .,N and $F_d = 0$ for all d <> s and $F_d = F$ when d = s. The driving point response is

$$x(t) = H(i\omega) F e^{i\omega t} \tag{7.46}$$

$$H(i\omega) = \sum_{n=1}^{N} H_n(i\omega) \tag{7.47}$$

$$H_n(i\omega) = \frac{1}{K_n - \omega^2 M_n + i\omega C_n} \tag{7.48}$$

The driving point response can be written as the sum of the magnitudes and phases of the individual modes

$$x(t) = \sum_{n=1}^{N} |H_n(i\omega)| e^{i(\omega t + \theta_n)} \tag{7.49}$$

$$|H_n(i\omega)|^2 = \frac{1}{(K_n - \omega^2 M_n)^2 + (\omega C_n)^2} \tag{7.50}$$

$$\theta_n = -\tan^{-1}\left(\frac{\omega C_n}{K_n - \omega^2 M_n} \right) \tag{7.51}$$

The driving point response can also be written directly as the total system magnitude and phase

$$x(t) = |H(i\omega)|Fe^{i(\omega t+\theta)} \tag{7.52}$$

$$|H(i\omega)|^2 = real(H(i\omega))^2 + imaginary(H(i\omega))^2 \tag{7.53}$$

$$\theta = \tan^{-1}\left(\frac{imaginary(H(i\omega))}{real(H(i\omega))}\right) \tag{7.54}$$

$$real(H(i\omega)) = \sum_{n=1}^{N} \frac{K_n - \omega^2 M_n}{(K_n - \omega^2 M_n)^2 + (\omega C_n)^2} \tag{7.55}$$

$$imaginary(H(i\omega)) = -\sum_{n=1}^{N} \frac{\omega C_n}{(K_n - \omega^2 M_n)^2 + (\omega C_n)^2} \tag{7.56}$$

When the load is harmonic, the response is harmonic and the magnitude and phase of the response has contributions from the individual modes. In theory, the magnitude of the frequency response at a frequency of zero corresponds to the static deflection due to a unit force. The zero frequency response [7] is defined as

$$H(0) = |H(0)| = \sum_{n=1}^{N} \frac{1}{K_n} \tag{7.57}$$

The zero frequency response is equivalent to the static deflection (flexibility) under a unit load of N springs in series where the spring constants, K_n, n = 1,2,. . .N, are the modal spring constants. The system stiffness is simply the inverse of the zero frequency response.

7.7 Static Response of Uniform Beam

The basic mechanical tension, compression, torsion and bending tests of uniform beams to determine the coefficient of elasticity are based on the following equations of static equilibrium [8].

Axial Tension/Compression

$$w = \frac{FL}{EA} \tag{7.58}$$

Torsion

$$\vartheta = \frac{TL}{GJ} \tag{7.59}$$

3 Point Bending at mid span

$$w = \frac{FL^3}{48EI} \tag{7.60}$$

Poisson's Ratio can be determined by the relation

$$v = \frac{E}{2G} - 1 \tag{7.61}$$

7.8 Dynamic Response of Uniform Beam in Bending

From the available frequency equation of a simply supported uniform beam bending at mid span [4–6]46

$$\omega_n^2 = \frac{K_n}{M_n} = \frac{n^4\pi^4 EI}{L^4 m} \tag{7.62}$$

$$M_n = \frac{mL}{2} \tag{7.63}$$

$$K_n = \frac{n^4\pi^4 EI}{2L^3} \tag{7.64}$$

$$\phi_n = \sin\left(\frac{n\pi x}{L}\right) \tag{7.65}$$

$$H(0) = \sum_{n=1}^{\infty} \frac{\phi_n^2}{K_n} \tag{7.66}$$

The static response is equal to the zero frequency response of the simply supported uniform beam in bending at mid span and can be expressed as a function of the first modal stiffness [2]

$$\frac{L^3}{48EI} = \frac{\pi^4}{96K_1} \tag{7.67}$$

The coefficient of elasticity as a function of the first modal stiffness is

$$E = \frac{2L^3 K_1}{\pi^4 I} \tag{7.68}$$

7.9 Dynamic Response of Uniform Beam in Axial Deformation

For axial deformation the available frequency equation [4–6]46 for a beam fixed at x = 0 and free at x = L is

$$\omega_n^2 = \frac{K_n}{M_n} = \frac{\pi^2(2n-1)^2 EA}{4mL^2} \tag{7.69}$$

$$M_n = \frac{mL}{2} \tag{7.70}$$

$$K_n = \frac{\pi^2(2n-1)^2 EA}{8L} \tag{7.71}$$

$$\phi_n = \sin\left((2n-1)\frac{\pi}{2}\frac{x}{L}\right) \tag{7.72}$$

The static response is equal to the zero frequency response of the beam and can be expressed as a function of the first modal stiffness

$$\frac{L}{EA} = \frac{\pi^2}{8K_1} \tag{7.73}$$

The coefficient of elasticity as a function of the first modal stiffness is

$$E = \frac{8LK_1}{\pi^2 A} \tag{7.74}$$

Dynamic Response of Uniform Beam in Torsion

For torsion the frequency equation [4–6]46 for a cylindrical beam fixed at x = 0 and free at x = L is similar to the axial frequency equation

$$\omega_n^2 = \frac{K_n}{M_n} = \frac{\pi^2(2n-1)^2 GJ}{4mL^2} \tag{7.75}$$

$$G = \frac{8LK_1}{\pi^2 J} \tag{7.76}$$

Knowing E and G, Poisson's ratio can be determined as

$$v = \frac{JK_{1axial}}{2AK_{1torsion}} - 1 \tag{7.77}$$

7.10 Uniform Beam in Bending Quarter Span

When $x_d = \frac{L}{2}$ and $x_s = \frac{L}{4}$ then the zero frequency response is

$$\sum_{n=1}^{\infty} \frac{\left(\frac{\sin\left(\frac{n\pi}{4}\right)}{\sin\left(\frac{n\pi}{2}\right)}\right)}{\left(\frac{K_n}{\sin\left(\frac{n\pi}{2}\right)^2}\right)} \tag{7.78}$$

and includes modes where $\sin\left(\frac{n\pi}{4}\right) <> 0$

When $x_d = x_s = \frac{L}{4}$ then the zero frequency response is

$$\sum_{n=1}^{\infty} \frac{1}{\left(\frac{K_n}{\sin\left(\frac{n\pi}{4}\right)^2}\right)} \tag{7.79}$$

$$\text{So measured } K_n = \frac{K_n}{\sin\left(\frac{n\pi}{4}\right)^2} \tag{7.80}$$

$$K_n\left(x_d = x_s = \frac{L}{4}\right) = \frac{K_n\left(x_d = x_s = \frac{L}{2}\right)}{\sin\left(\frac{n\pi}{4}\right)^2} \tag{7.81}$$

From statics [8], the quarter span elastic deformation is related to the mid span elastic deformation

$$w\left(x_d = x_s = \frac{L}{4}\right) = \frac{9}{16} w\left(x_d = x_s = \frac{L}{2}\right) \tag{7.82}$$

So

$$\sum_{n=1}^{\infty} \frac{\sin\left(\frac{n\pi}{4}\right)^2}{n^4} = \frac{\pi^4}{96}\frac{9}{16} \tag{7.83}$$

Reciprocity is valid because the zero frequency response when $x_d = \frac{L}{4}$ and $x_s = \frac{L}{2}$ is equal to the zero frequency response when $x_d = \frac{L}{2}$ and $x_s = \frac{L}{4}$

The zero frequency response is

$$\sum_{n=1}^{\infty} \frac{\left(\frac{\sin\left(\frac{n\pi}{2}\right)}{\sin\left(\frac{n\pi}{4}\right)}\right)}{\left(\frac{K_n}{\sin\left(\frac{n\pi}{4}\right)^2}\right)} = \sum_{n=1}^{\infty} \frac{\left(\frac{\sin\left(\frac{n\pi}{4}\right)}{\sin\left(\frac{n\pi}{2}\right)}\right)}{\left(\frac{K_n}{\sin\left(\frac{n\pi}{2}\right)^2}\right)} \tag{7.84}$$

From statics [8], the quarter span deformation due to the load at the mid span is related to the mid span elastic deformation.

$$w\left(x_d = \frac{L}{2}, x_s = \frac{L}{4}\right) = \frac{11}{16} w\left(x_d = x_s = \frac{L}{2}\right) \tag{7.85}$$

So

$$\sum_{n=1}^{\infty} \frac{\sin\left(\frac{n\pi}{2}\right)\sin\left(\frac{n\pi}{4}\right)}{n^4} = \frac{\pi^4}{96}\frac{11}{16} \tag{7.86}$$

7.11 Experimental Modal Analysis

From experimental modal analysis the frequency, damping, poles and residues can be estimated. From the damped frequencies and residues the zero frequency response can be determined. The partial fraction form of the frequency response function for a single force at x_d and the response at x_s

$$H_{sd}(i\omega) = \sum \frac{\varnothing_{sn}\varnothing_{dn}}{M_n(i\omega - s_n)\left(i\omega - s_n^*\right)} = \sum\left(\frac{A_n}{i\omega - s_n} + \frac{A_n^*}{i\omega - s_n^*}\right) \tag{7.87}$$

$$s_n = -\frac{C_n}{2M_n} + i\sqrt{\frac{K_n}{M_n} - \left(\frac{C_n}{2M_n}\right)^2} \tag{7.88}$$

$$A_n = \frac{\varnothing_{sn}\varnothing_{dn}}{i2M_n\sqrt{\frac{K_n}{M_n} - \left(\frac{C_n}{2M_n}\right)^2}} \tag{7.89}$$

Setting the frequency to zero, it can be shown that

$$H_{sd}(0) = \sum \left(\frac{A_n}{-s_n} + \frac{A_n^*}{-s_n^*} \right) = \sum \frac{\varnothing_{sn} \varnothing_{dn}}{K_n} \tag{7.90}$$

To get the stiffness proportional constant and mass proportional constant use the following equation. Since there are usually more modal frequencies than the two unknowns, the solution requires the pseudo inverse.

$$\phi_n = \frac{-real(s_n)}{\omega_n} = \frac{t_0}{2\omega_n} + \frac{t_1 \omega_n}{2} \tag{7.91}$$

Where $\omega_n = |s_n|$.

7.12 Element Stiffness Identification from Equivalent Static Test Data

The procedure for element stiffness identification follows that of [9] with a modification to use the complex variable semi-analytical method instead of the finite difference method in approximating the derivatives of the sensitivity matrix [10].

Using the zero frequency response as the equivalent static response, the global experimental stiffness matrix can be determined from inverting the flexibility matrix where

$$u(x = x_s = x_d) = \sum \frac{\varnothing_n^2}{K_n} \text{ and } u(x = x_s \neq x_d) = \sum \frac{\varnothing_{sn} \varnothing_{dn}}{K_n} \tag{7.92}$$

$$K^e = u^{-1} \tag{7.93}$$

The stiffness matrix derived from the finite element method matrix must be partitioned into four sub matrices.

$$\begin{bmatrix} F_m \\ F_u \end{bmatrix} = \begin{bmatrix} K_{mm} & K_{mu} \\ K_{um} & K_{uu} \end{bmatrix} \begin{bmatrix} U_m \\ U_u \end{bmatrix} \tag{7.94}$$

The m subscript indicates the degrees of freedom which represent the measured force, stiffness and displacement. The u subscript indicates the unmeasured degrees of freedom. The global analytical stiffness matrix is

$$K^a = K_{mm} - K_{mu} K_{uu}^{-1} K_{um} \tag{7.95}$$

By adjusting the experimental and analytical stiffness matrices into vectors that match the unknown parameters that are to be identified and minimizing the error norm between the two vectors, an estimate for the parameters can be made. Since the analytical stiffness vector of unknown parameters is non linear, a first order Taylor series expansion is used.

$$k^a(p + \Delta p) \cong k^a(p) + s(p)\Delta p \text{ where } s(p) = \frac{\partial}{\partial p} k^a(p) \tag{7.96}$$

$$S(p) = \frac{\partial}{\partial p} K^a(p) = \frac{\partial}{\partial p} K_{mm} - \left(\frac{\partial}{\partial p} K_{mu} \right) K_{uu}^{-1} K_{um} + K_{mu} K_{uu}^{-1} \left(\frac{\partial}{\partial p} K_{uu} \right) K_{uu}^{-1} K_{um} - K_{mu} K_{uu}^{-1} \left(\frac{\partial}{\partial p} K_{um} \right) \tag{7.97}$$

Placing the values of $S(p)$ into the vector $s(p)$.

$$J(\Delta p) = [e(\Delta p)]^T [e(\Delta p)] \text{ where } [e(\Delta p)] = k^e - k^a(p + \Delta p) = k^e - k^a(p) - s(p)\Delta p \tag{7.98}$$

$$\text{Setting } \frac{\partial J(\Delta p)}{\partial p} = 0 \text{ the relationship } s(p)\Delta p = \Delta k(p) \text{ can be derived where } \Delta k(p) = k^e - k^a(p). \tag{7.99}$$

An iterative procedure for parameter identification can now be used.

$$p^{i+1} = p^i + \Delta p \text{ where } \Delta p = \left[s(p)^T s(p)\right]^{-1} s(p)^T \Delta k(p) \tag{7.100}$$

The partial derivatives can be solved analytically, finite differences, or by complex variable semi analytical method. The CVSAM has several numerical advantages and a brief description follows.

A Taylor series expansion of a function in the complex plane is

$$f(x + i\Delta x) = f(x) + i\Delta x f^{'}(x) - \frac{\Delta x^2 f^{''}(x)}{2!} - \frac{i\Delta x^3 f^{'''}(x)}{3!} + \ldots \tag{7.101}$$

Grouping the real and imaginary parts, the first order derivative can be obtained as

$$f^{'}(x) = \frac{imag(f(x + i\Delta x))}{\Delta x} + O(\Delta x^2) \tag{7.102}$$

Note the calculation of the first order derivative does not involve the subtraction of two numbers and using the above approximation avoids the subtractive cancellation errors that plague the finite difference approach.

7.13 A 2 Node Isotropic Beam Element

Considering the well known 2 node, 6 degree of freedom isotropic beam element, the analytic stiffness matrix for a cantilever beam element is as follows, where the free end is at x = 0 and the fixed end at x = L and there are 2 degrees of freedom which are considered to be measured, the axial and flexural at x = 0 and where the unknown parameter is the coefficient of elasticity.

$$K_{mm} = \begin{bmatrix} \frac{AE}{L} & 0 \\ 0 & \frac{12EI}{L^3} \end{bmatrix} \text{ and } \frac{\partial K_{mm}}{\partial E} = \begin{bmatrix} \frac{A}{L} & 0 \\ 0 & \frac{12I}{L^3} \end{bmatrix} \tag{7.103}$$

$$K_{um} = \begin{bmatrix} 0 & \frac{6EI}{L^2} \end{bmatrix} \text{ and } \frac{\partial K_{um}}{\partial E} = \begin{bmatrix} 0 & \frac{6I}{L^2} \end{bmatrix} \text{ and } K_{mu} = K_{um}^T \text{ and } \frac{\partial K_{mu}}{\partial E} = \frac{\partial K_{um}^T}{\partial E} \tag{7.104}$$

$$K_{uu} = \frac{4EI}{L} \text{ and } \frac{\partial K_{uu}}{\partial E} = \frac{4I}{L} \text{ and } K_{uu}^{-1} = \frac{L}{4EI} \tag{7.105}$$

Using CVSAM, the first derivative approximation for this element is equal to the analytic first derivative.

$$\frac{\partial K_{mm}}{\partial E} = \frac{imag\begin{bmatrix} \frac{A(E+i\Delta E)}{L} & 0 \\ 0 & \frac{12(E+i\Delta E)I}{L^3} \end{bmatrix}}{\Delta E} = \begin{bmatrix} \frac{A}{L} & 0 \\ 0 & \frac{12I}{L^3} \end{bmatrix} \tag{7.106}$$

$$S(E) = \begin{bmatrix} \frac{A}{L} & 0 \\ 0 & \frac{3I}{L^3} \end{bmatrix} \text{ and } K^a = \begin{bmatrix} \frac{AE}{L} & 0 \\ 0 & \frac{3EI}{L^3} \end{bmatrix} \tag{7.107}$$

After some manipulation,

$$E^{i+1} = E^i + \frac{\frac{A}{L}\left(k_x - \frac{AE^i}{L}\right) + \frac{3I}{L^3}\left(k_y - \frac{3E^iI}{L^3}\right)}{\left(\frac{A}{L}\right)^2 + \left(\frac{3I}{L^3}\right)^2} \tag{7.108}$$

7.14 A 2 Node Orthotropic Beam Element

Considering the 2 node, 6 degree of freedom orthotropic beam element [11], the analytic stiffness matrix for a cantilever beam element is as follows, where the free end is at x = 0 and the fixed end at x = L and there are 2 degrees of freedom which are considered to be measured, the axial and flexural at x = 0 and where the unknown parameter is the fiber angle.

The stress strain relations for an orthotropic material in plane stress are as follows

$$\frac{\partial u}{\partial x} = \varepsilon_x = a_{11}\sigma_x + a_{12}\sigma_y + a_{16}\sigma_{xy} \tag{7.109}$$

$$\frac{\partial v}{\partial y} = \varepsilon_y = a_{12}\sigma_x + a_{22}\sigma_y + a_{26}\sigma_{xy} \tag{7.110}$$

$$\frac{\partial u}{\partial y} + \frac{\partial v}{\partial x} = \varepsilon_{xy} = a_{16}\sigma_x + a_{26}\sigma_y + a_{66}\sigma_{xy} \tag{7.111}$$

$$m = cos\theta \text{ and } n = sin\theta$$

$$S_{11} = \frac{1}{E_1} \text{ and } S_{12} = -\frac{v_{12}}{E_1} \text{ and } S_{22} = \frac{1}{E_2} \text{ and } S_{66} = \frac{1}{G_{12}} \tag{7.112}$$

$$a_{11} = S_{11}m^4 + (2S_{12} + S_{66})m^2n^2 + S_{22}n^4 \tag{7.113}$$

$$a_{12} = S_{12}(m^4 + n^4) + (S_{11} + S_{22} - S_{66})m^2n^2 \tag{7.114}$$

$$a_{22} = S_{11}n^4 + (2S_{12} + S_{66})m^2n^2 + S_{22}m^4 \tag{7.115}$$

$$a_{16} = (2S_{11} - 2S_{12} - S_{66})nm^3 - (2S_{22} - 2S_{12} - S_{66})n^3m \tag{7.116}$$

$$a_{26} = (2S_{11} - 2S_{12} - S_{66})mn^3 - (2S_{22} - 2S_{12} - S_{66})m^3n \tag{7.117}$$

$$a_{66} = 2(2S_{11} + 2S_{22} - 4S_{12} - S_{66})n^2m^2 - S_{66}(n^4 + m^4) \tag{7.118}$$

The deflection equation in the symmetry axis of the beam, y = 0 is

$$v = \frac{P}{I}\frac{a_{11}}{6}\left(x^3 - 3L^2x + 2L^3\right) \text{ and } v(x=0) = \frac{P}{I}\frac{a_{11}L^3}{3} \tag{7.119}$$

$$When\ \theta = 0^0, v(x=0) = \frac{PL^3}{3E_1I} \text{ and when } \theta = 90^0, v(x=0) = \frac{PL^3}{3E_2I} \tag{7.120}$$

$$K_{mm} = \begin{bmatrix} \frac{A}{La_{11}} & 0 \\ 0 & \frac{12I}{L^3a_{11}} \end{bmatrix} \tag{7.121}$$

$$K_{um} = \begin{bmatrix} 0 & \frac{6I}{L^2a_{11}} \end{bmatrix} \text{ and } K_{mu} = K_{um}^T \text{ and } \frac{\partial K_{mu}}{\partial E} = \frac{\partial K_{um}^T}{\partial E} \tag{7.122}$$

$$K_{uu} = \frac{4I}{La_{11}} \text{ and } K_{uu}^{-1} = \frac{La_{11}}{4I} \tag{7.123}$$

Using CVSAM requires evaluating

$$\frac{\partial a_{11}}{\partial \theta} \cong \frac{imag[S_{11}\cos^4(\theta + i\Delta\theta) + (2S_{12} + S_{66})\cos^2(\theta + i\Delta\theta)\sin^2(\theta + i\Delta\theta) + S_{22}\sin^4(\theta + i\Delta\theta)]}{\Delta\theta} \tag{7.124}$$

7.15 Summary

When the frequency equation is known, the elastic properties of uniform beams can be determined from knowledge of the first modal stiffness. If the frequency equation is not known then the elastic properties can be determined by inverse identification methods using finite elements with the zero frequency response as the equivalent static response. The modal stiffness is derived from parameter estimation using experimental modal data [12]. The experimental modal data can be from any dynamic test using a time domain or frequency domain parameter estimation technique. After introducing viscous damping into the equations of motion, the coefficient of elasticity remains constant but the dynamic response is dependent on two additional constants, a stiffness proportional constant and a mass proportional constant. The stiffness proportional constant is dependent on the material and the mass proportional constant is dependent on the system. The two constants can be estimated by the pseudo inverse of a matrix based on the modal frequency and damping.

References

1. Yang NC (1972) Design of functional pavements. McGraw-Hill, New York
2. Yang D (2010) An identification method for the elastic characterization of materials. In: Proceedings of IMAC XXIX Jacksonville, FL
3. Christensen RM (1982) Theory of viscoelasticity. Academic, New York
4. Clough RW, Penzien J (1993) Dynamics of structures. McGraw-Hill, New York
5. Biggs JM (1964) Introduction to structural dynamics. McGraw-Hill, New York
6. Warburton GB (1976) The dynamical behaviour of structures. Pergamon Press, Oxford/New York
7. Yang D (1978) Response of multi-frequency pavement systems. Masters' thesis, MIT
8. Roark RJ (1954) Formulas for stress and strain. McGraw-Hill, New York
9. Sanayei M, Scampoli SF (1991) Structural element stiffness identification from static test data. J Eng Mech, ASCE. 117(5):1021–1036.
10. Dennis BH, Jin W, Dulikravich GS, Jaric J (2011) Application of the finite element method to inverse problems in solid mechanics. Int J Struct Changes Solids 3(2):11–21
11. Aktas A (2001) Determination of the deflection function of a composite cantilever beam using theory of anisotropic elasticity. Math Comput Appl 6:67–74
12. Richardson MH, Formenti DL (1982) Parameter estimation from frequency response measurements using rational fraction polynomials. In: Proceedings of the 1st international modal analysis conference, Orlando, FL, 8–10 Nov 1982

Chapter 8
Experimental Investigation of Failure in Viscoelastic Elastomers Under Combined Shear and Pressure

Maen Alkhader, Wolfgang Knauss, and Guruswami Ravichandran

Abstract An experimental approach, based on Split Hopkinson Pressure Bar (SHPB) apparatus, is developed to elucidate failure of viscoelastic elastomers under combined shear and high pressures such as are encountered in explosive and/or armor-impact scenarios. In this experimental arrangement, thin cylindrical polyurea specimens with an aspect ratio (Diameter to thickness) greater or equal to 15 are tested, up to failure, using Split Hopkinson Pressure Bar (SHPB). Specimens with large aspect ratio are used to guarantee the close approximation of a triaxial state of stress in the specimen upon loading; hence the measured normal stress would be approximately equal to the hydrostatic pressure in the specimen. Friction at the loading interfaces forces the stress state to deviate from uniformity, restrict both the circumferential and radial displacements and lead to the development of shear stresses and strains. Hence, induced failure occurs under conditions combining high-strain-rate, high pressure and shear stresses. By using this setup, repeatable failure modes were detected and elucidated using finite element simulations.

Keywords Failure • Viscoelastic elastomers • Combined loading • High-strain-rate

8.1 Introduction

Viscoelastic elastomers have gained substantial importance in engineering applications requiring the mitigation of the adverse effects resulting from impact or shock loadings. In particular, the viscoelastic elastomer polyurea has proved effective in enhancing the impact energy absorption capacity as well as the penetration and fragmentation resistance of armor when applied as armor coating. In this role viscoelastic elastomers experience large deformations, high strain-rates and complex states of stress that combine shear and high pressures. Because the totality of potential situations during impact is extremely large, failure of materials involved in impact needs to be understood and well characterized under complex loadings combining high rates, elevated pressures and shear stresses.

Inducing failure in polyurea specimens under conditions dominated by shear stress and elevated hydrostatic pressure in a controlled laboratory environment while permitting access for acquiring experimental measurements is not a simple task. To this end, we envision using an experimental arrangement in which thin cylindrical polyurea specimens with an aspect ratio (Diameter to thickness) greater or equal to 15 are placed between two parallel surfaces as shown in Fig. 8.1a. These parallel surfaces are made to move relative to each other at high rates to generate high-strain-rate compressive strains in the polyurea specimens. During the deformation process both displacements and forces acting on the parallel surfaces are acquired to compute the state of stress and strain in the specimen. Specimens with large aspect ratio were used to guarantee the close approximation of a triaxial state of stress in the specimen; hence the computed normal stress would be approximately equal to the hydrostatic pressure in the specimen. Ideally, and by assuming the existence of frictionless conditions at the specimen-surface interface, one predicts the development of uniform stresses without the development of any shear stresses, as illustrated in Fig. 8.1b. However, friction at the loading interfaces forces the stress to deviate from uniformity, as

M. Alkhader (✉)
Department of Mechanical Engineering, Stony Brook University, Light Engineering Bld. Room 137, Stony Brook, NY 11776, USA
e-mail: maen.alkhader@stonybrook.edu

W. Knauss • G. Ravichandran
Graduate Aerospace Laboratories, California Institute of Technology, 1200 E. California Blvd., Pasadena, CA 91125, USA

B. Antoun et al. (eds.), *Challenges in Mechanics of Time-Dependent Materials and Processes in Conventional and Multifunctional Materials, Volume 2*, Conference Proceedings of the Society for Experimental Mechanics Series 37,
DOI 10.1007/978-1-4614-4241-7_8,

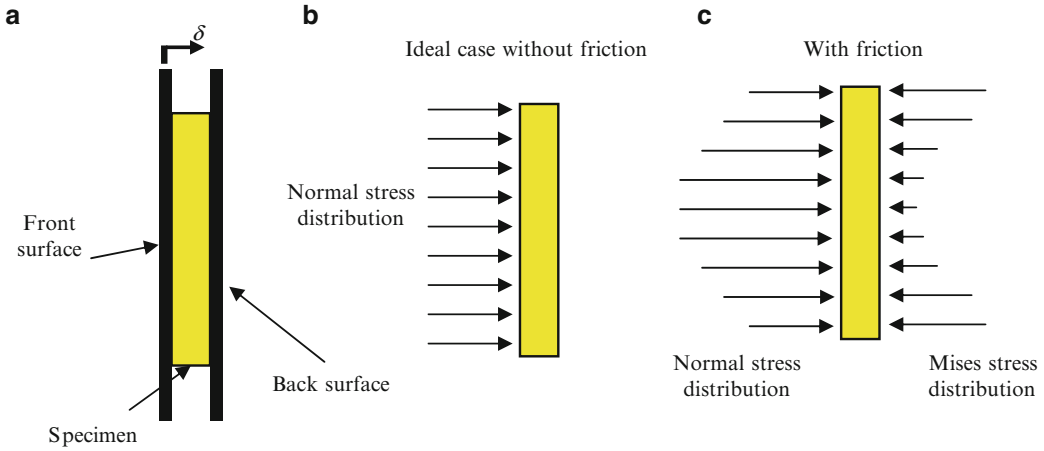

Fig. 8.1 (**a**) Schematic of the experimental arrangement concept, showing the normal stress and shear stress distributions for: (**b**) an ideal case with no friction and (**c**) an actual case with friction

in Fig. 8.1c. Friction forces restrict both the circumferential and radial displacements and lead to the development of shear stresses and strains. Ideally, the normal stress would have a maximum value at the center of the specimen, and would decrease in the outward radial direction, while the shear stress (Mises) would follow an opposite trend with a maximum at the perimeter of the specimen, see Fig. 8.1c. Accordingly, a thin specimen would be subjected to a state of stress that combines both shear stresses and elevated pressures. If deformation continues to the onset of failure, this failure would be induced under elevated pressures and permits investigating the effect of different pressures and loading scenarios on failure. Ultimately, meaningful quantitative data describing the stress and strain at the onset of failure can be determined, after the experimental conditions leading to failure are introduced into an identical model for a finite element simulation. "Identical conditions" include boundary conditions and constitute response. For polyurea, multiple experimentally driven constitute models exist but each guarantees the model response accuracy within the range in which model calibration was performed. A few of such experimentally based models have been reported in the work of [1, 2]. However, the experimental nature of these models does not permit a simple extension or extrapolation of the constitute description to arbitrary complex loading conditions that combines high-strain-rate, large strains, pressure and shear stresses. In the following we provide a detailed description of the experimental arrangement and the finite element simulations performed to explain the observed experimental results.

8.1.1 Experimental Arrangement

The conceptual experimental methodology described in the previous section is simply and naturally realized by means of the well established Split Hopkinson Pressure Bar (SHPB) apparatus. The apparatus used in this work employs precision ground high-strength C350 maraging steel bars. The incident and transmission bars are 1,215 and 1,020 mm in length, respectively. All bars and strikers had a common diameter of 19.05 mm. Strikers with varying lengths were used to achieve stress pulses of varying durations, thereby achieving various strain levels.

8.1.2 Specimens

Isocynate under the commercial brand Isonate 134L from Dow Chemicals mixed with the curative Versalink P1000 from Airproducts, provide the polyurea samples. A 4-to-1 ratio (curative-to-Isocyante) by weight is used. Mixing and casting are accomplished in a custom built dry box in which the moisture content is controlled with the aid of silica gel. Upon introducing the silica gel, a waiting period of 30 min is required before the moisture content in the dry box drops to 8%.

Both the Isocynate and the curative were placed under vacuum for an hour before mixing. The mix was also placed under vacuum for a few minutes prior to casting to eliminate air-bubbles introduced during mixing. Before casting, all air-bubbles were forced out to the point that none were visible to the unaided eye. Casting was accomplished using two transparent

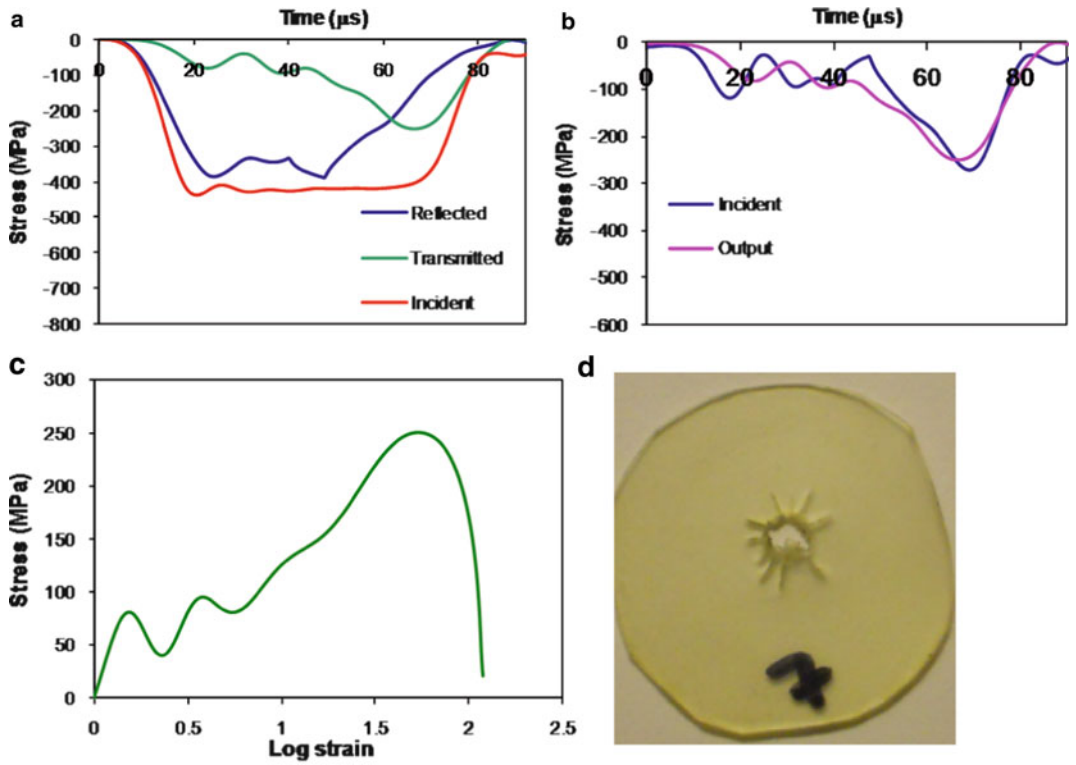

Fig. 8.2 Data acquired from a typical test, showing (**a**) incident, reflected and transmitted signals, (**b**) stresses at both surfaces of the specimen (confirming dynamic equilibrium), and (**c**) the stress and strain response, (**d**) post mortem picture of the specimen

polycarbonate plates and thin steel strips that were used as spacers. One polycarbonate plate was used as a substrate to which the steel spacers were attached. Once polyurea was poured on the polycarbonate substrate, a clear transparent foil was carefully placed on the cast so as to minimize the introduction of air-bubbles. The second polycarbonate plate was then placed on top of the transparency and a weight was placed on top to force out all excess material. After curing, the transparency and polyurea layers are pealed, as a group, from the substrate, and then the transparency is peeled off the polyurea layer. This approach was followed as we found that polycarbonate substrate allowed us to fabricate specimens with better surface finish. Moreover, the compliance of the transparency facilitated manipulating the peeling angle, which, in turn, helped in peeling the polyurea specimen from the substrate without exerting any significant force.

8.1.3 Experimental Details and Measurements

For each test, the incident, reflected and transmitted signals are registered and used to compute the state of stress and strain in the specimen. One of the most important issues to check, given the compliance and low impedance of the tested specimens, is dynamic equilibrium. Accordingly, during our analysis we always used all three signals (incident, reflected and transmitted) to determine the stress and strain in the specimen and to check for dynamic equilibrium. Often, within the SHPB users community, dynamic equilibrium is assumed to be satisfied and only the reflected signal is used to compute the strain in the specimen. Out of caution this practice was avoided here because the sound speed in elastomeric materials is low compared to that in metals. A specimen thickness around 1 mm was found to facilitate achieving dynamic equilibrium at small impacting speeds. More importantly, we are using steel bars and significant stress has to be transmitted to the output bar for the strain gage to register a strain signal with a desirably low noise-to-signal ratio. After multiple iterations it was found that 1 mm is well suited to relax all the mentioned restrictions. Moreover, we found that specimens of 1 mm thickness were thin enough for failure to occur during the deformation process.

A typical test would produce data similar to those presented in Fig. 8.2. For this particular test, a specimen was subjected to an incident stress wave which moved the front face of the specimen at a nominal speed of 16 m/s which led to a relative

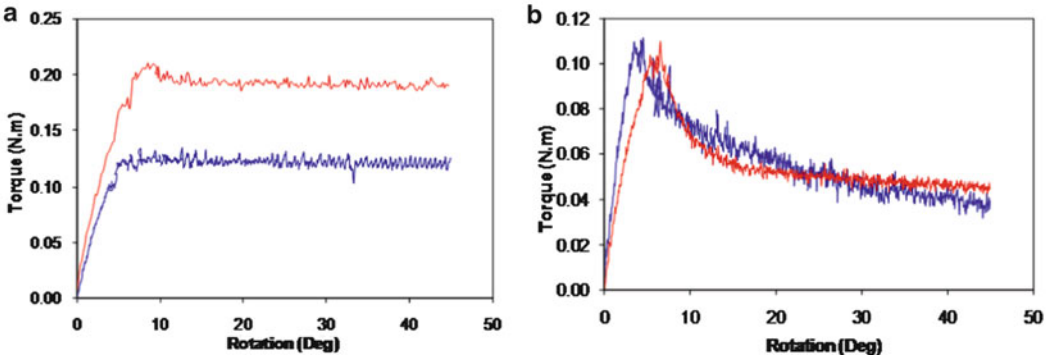

Fig. 8.3 Torque due to friction, showing the effect of friction on torque for: (**a**) without lubricant, (**b**) with lubricant

velocity of 14 m/s. Generating such loading required setting the pressure in the gas gun to 40 psi. This pressure represents 40% of the maximum pressure achievable by our gas gun.

One of the illusive parameters to determine relate to the friction forces at the interfaces. In this regard, we opted to utilize the simple Coulomb model, to represent and investigate the effect of friction and the amplitude of friction forces at the polyurea-steel bars interfaces. Characterizing the level of friction forces acting on the polyurea specimens during impact is instrumental for the finite element modeling process and for determining the conditions preceding specimen failure.

To estimate friction forces, the coefficient of friction (COF) between polyurea and steel had to be determined first. A simple experiment was performed via an MTS system capable of both compression and torsion. In this test a cylindrical specimen with a height and diameter of 1 mm is glued to the loading rod attached to the MTS cross-head. The specimen is then compressed against a steel plate attached to the load cell. Once a predetermined compressive force is achieved, torsional deformation is imposed on the specimen. From the torque measured by the load cell, and by utilizing the Coulomb model, one can compute the coefficient of friction. This methodology is repeated for scenarios employing multiple types of lubricants and for cases without lubricant. Friction forces without the use of lubricant were seen to vary from test to test, even while maintaining the same normal force, see Fig. 8.3a; in other words, the coefficient of friction between polyurea and steel is not a constant. So, although in our dynamic tests, we favor the existence of friction forces to induce significantly high Mises stress, the lack of lubricant at the interface came at the expense of having variable coefficients of friction with no means to control it. Variations in COF from test to test would add difficulties to any computational work intended to mimic the experimental results. On the other hand, tests with Silicon-Teflon based lubricant, available commercially under the brand name (DuPont™ Teflon™ Silicone Lubricant), led to reasonably repeatable coefficients of friction as can be seen in Fig. 8.3b. Hence, for all dynamic tests, the same Silicon-Teflon-based lubricant was used.

8.2 Results

Thin polyurea specimens were tested at impact velocities ranging from low to large velocities (22 m/s) that are sufficiently high to induce failure in the specimens. For each of the specimens the stress–strain response was computed and is presented in Fig. 8.4. The behavior illustrated in this figure represents the approximate bulk compressive response of the specimens. As the strain rate was increasing during each test, Fig. 8.4 does not include a legend to distinguish the strain rate at which each test was performed.

With increasing the impact speed (increasing the gas gun pressure) through-thickness fractures were observed. We note that the shape of the perforations and the dependence between their shape on pressure and impact speed is not straightforwardly predicted. However, at significantly high impact speeds severe failures are observed, in which a through-hole is formed and a large number of radial cracks propagate outwardly from the center; see Fig. 8.5. This type of failure was also observed in thicker specimens but at higher impact speeds.

It was clear in all failure-inducing tests that material was lost, possibly in the form of minute fragments, from the center of the specimens. To better understand this evolution of failure we provided an enclosure during the tests to collect all debris produced and found that the shape of the debris did not follow a universal trend: For a few samples the failed region (missing parts) was retrieved and found to be almost intact with few fragments. For other specimens the failed region was fragmented into extremely small pieces. The later case is more consistent with the fragmentation of brittle materials under impact. Comprehending the aforementioned observations and understanding the mechanisms behind them requires knowing the stress

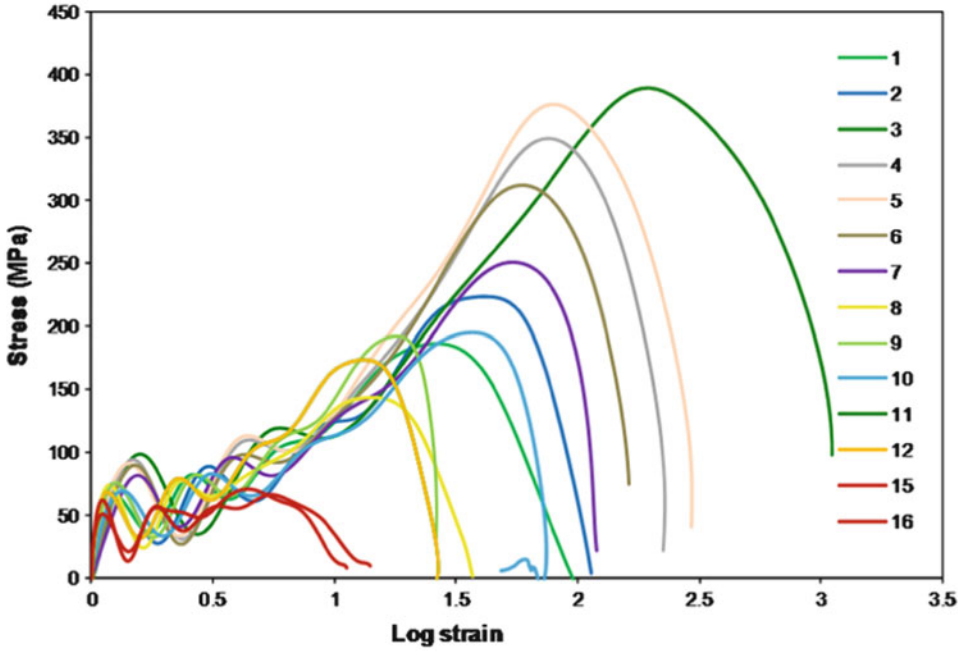

Fig. 8.4 True stress–strain response measured using the SHPB apparatus. It should be noted that this figure represents the approximate bulk response of polyurea since the specimens are subjected to a triaxial state of stress, due to the geometry of the specimens (large diameter to height ratio)

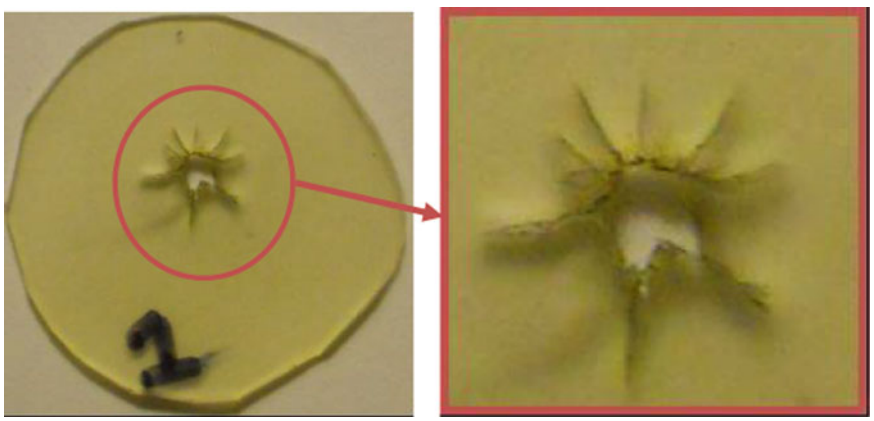

Fig. 8.5 Post mortem images of a specimen

and strain distributions in the specimens. Since our experimental procedure did not have the capability of providing such data directly, we employed, in the sequel, finite element analysis to deduce the stress and strain distribution during our tests.

8.3 Modeling

The finite element software ABAQUS is used to perform all the simulations in this study. Symmetry was used and only one quarter of a cylindrical disk was needed to model the test specimens. Loading was applied via displacement controlled boundary conditions imposed on two rigid surfaces representing the steel interfaces in the experiments. The default contact algorithm provided by the software is employed to resolve all impact forces. Whenever friction was included, the Coulomb

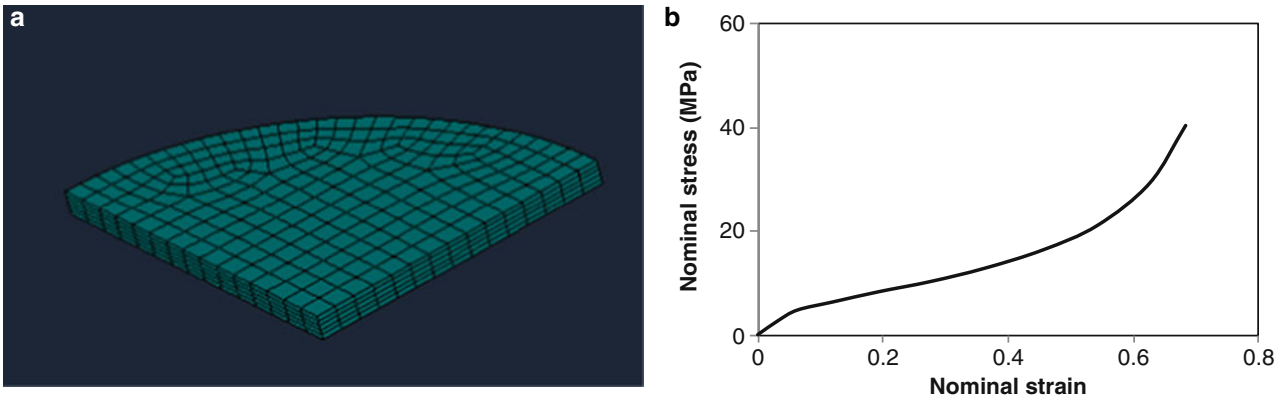

Fig. 8.6 (**a**) Finite element model after invoking symmetry, (**b**) Quasi-static response of polyurea used in the simulations and is based on the measurements reported in [4]

model was utilized. The coefficient of friction was varied between 0.0 and 0.15. Figure 8.6a presents the finite element model with a thickness of 1 mm and a diameter of 19 mm. The rigid surfaces are not present in Fig. 8.6a, which is shown merely for visualization reasons.

Defining a proper constitutive response to describe the behavior of polyurea at large strains, strain rates and pressure is still a major hurdle. Based on the current understanding of the large strain behavior of polyurea, we decided to utilize the viscoelstic material model with finite elasticity. This is a predefined model, included in the material library of ABAQUS. In this model the hereditary integral is constructed as a multiplication of a time dependent stiffness with the time derivative of the green strain tensor. The time dependent component of the model (time constants) follows linear viscoelasticity and hence the time constants are calibrated against the master curve reported in [3]. On the other hand, the hyperelastic component constitutive model was calibrated using the quasi-static stress–strain data for polyurea reported in [4]. The Ogden model was used to present the hyperelastic potential because we found that it represents the stress–strain data reported in [4] well. Figure 8.6b represents the hyperelastic response used to model the elastomeric specimens in the simulations.

Displacement boundary conditions prescribed on the two rigid surfaces were made to follow the relative velocity experienced by the polyurea specimens during the tests. Accordingly, for all the simulations included in this work, the back rigid surface was fixed and the front rigid surface had a prescribed velocity. This velocity increases linearly from 0 to a plateau value of 10,000 m/s in 15 μs. This relative velocity profile is an idealized representation of the relative velocity experienced by the specimens.

8.4 Computations Versus Measurements

Results from the finite element analysis are reported next for models with identical parameters, except for the coefficient of friction, the value of which is varied between 0.0 and 0.15. In Figs. 8.7 and 8.8, the distribution of stress or strain is probed along the radial direction. Stress and strain distributions are obtained and plotted every 10 μs to investigate how they evolve with time. The legends in the following figures represent the times at which the data is probed. Figure 8.7 presents the stress distribution for the case with frictionless interfaces. This figure illustrates that in the absence of friction forces, von Mises and pressure stress distributions within the specimen evolve uniformly. It is worth mentioning that simulations confirmed that stresses and strains do not vary through the specimen thickness, and this was anticipated since the specimens are relatively thin. Although, the figures cover 90 μs, we focus on the first 60 μs, since in all tests fracture or damage occurred within a time window of 60 μs. In passing from the frictionless situation to experiencing a coefficient of friction of 0.15 a remarkable change is apparent, as illustrated in Fig. 8.8. Stresses and strains are relatively uniform only during the first 10 μs. At later times, the strains in the neighborhood of the specimen perimeter tend to evolve faster than strains near the center of the specimen. This observation is consistent with the distribution of friction forces which have a maximum in areas with the highest pressure (i.e. the center of the specimen). A 0.15 coefficient of friction resulted in frictional forces that effectively developed two distinctive distributions which become more pronounced at the later stages of deformation. Figure 8.8 presents the stress and strain distributions resulting from the simulation implementing a 0.15 coefficient of friction. In this figure, in illustrations

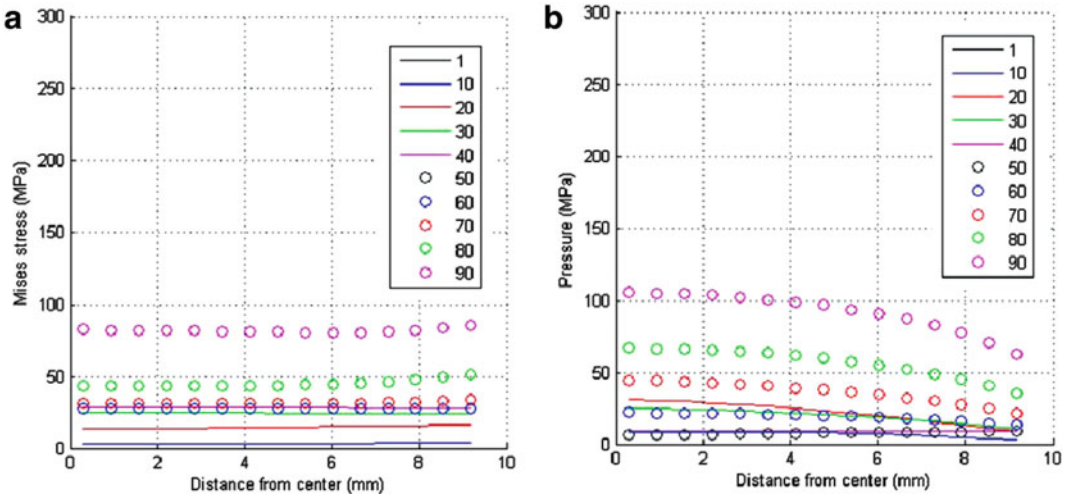

Fig. 8.7 Results of simulations employing COF = 0.0. Showing the distribution of (**a**) Mises stress, (**b**) pressure

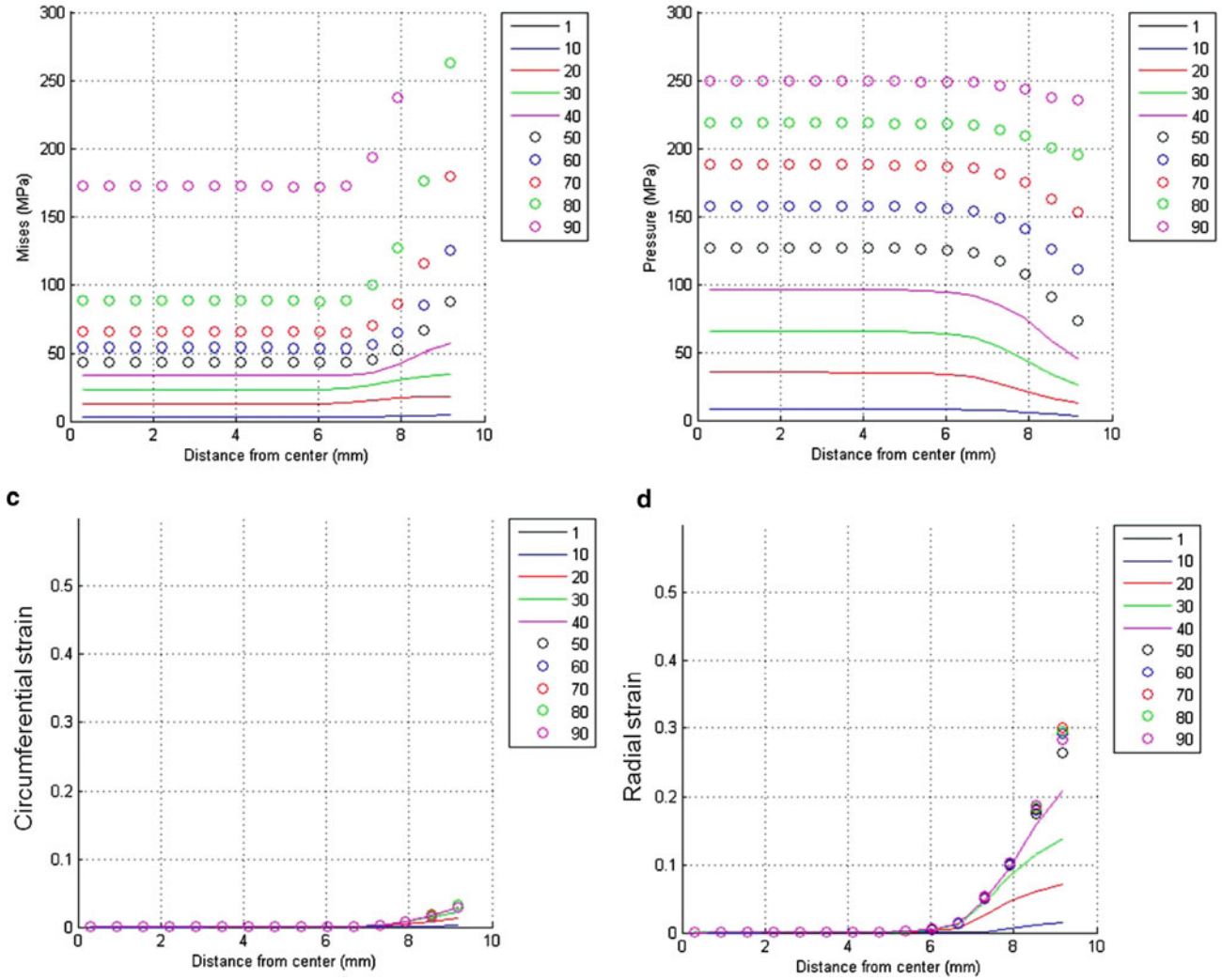

Fig. 8.8 Results of simulations employing COF = 0.15. Showing the distribution of (**a**) Mises stress, (**b**) pressure, (**c**) circumferential strain, (**d**) radial strain; insert numbers represent time in μs

a and b, one observes that stresses are uniform in the neighborhood of the center of the specimen, within 7 mm radius. Moreover, stresses inside the 7 mm radius area remain uniform during the whole deformation process. Beyond the 7 mm radius, stresses (von Mises and pressure stresses) deviate from uniformity with time. The development of a central area with uniform pressure and low shear stresses is anticipated when frictional forces are significant enough to prevent radial and circumferential strains from developing in the central area (7 mm disk). Figure 8.8c, d which presents the tangential and radial strains for the case employing a coefficient of friction of 0.15 clearly shows the existence of a central disc with approximately zero strains. The size of this field can be controlled by the amplitude of frictional forces, which in turn, is controlled by pressure and the coefficient of friction, assuming, of course, that friction is described accurately by Coulomb forces. Larger a coefficient of friction results in larger frictional forces, which restricts deformations in a larger area.

This observation brings attention to the effect of pressure on the constitutive response of polyurea. Increasing pressure is known to have an effect similar to reducing temperatures for viscoelastic materials. The central region experiences the maximum pressure and thus relaxation processes are slowest in this area. By slowing the relaxation processes, the material is closer to its glassy state, or possibly in the glassy state. As the material is closer to its glassy state, it partially loses its ability to stretch, especially at high deformation rates. Accordingly, once the tensile strain wave, traveling from the specimen perimeter towards the center, arrives at the perimeter of the central area with maximum pressure, it exerts a high rate tensile strain on the part of the specimen with the slowest stress relaxation processes. As the material at the perimeter of the central region with maximum pressure cannot accommodate sudden deformation, the major failure (failed region) occurs in this location. Beyond this point, few cracks radiate from the perimeter of the failed region to release more energy; accordingly, tests conducted at higher pressures, which deliver more energy to the specimen resulted in specimens with a higher number of radial cracks. Based on the computations exemplified by Fig. 8.8, we note first that the radial strain outside of the "pinned region" increases at rate of about three times that of the circumferential strain. It would stand to reason, then, that failure results first along a circumferential direction. After that event, the "outer ring" is more free to move and the subsequent expansion causes the radial cracks. This scenario would explain the experimentally observed failure modes. However, we must not forget that under high pressure the material acts more like a rigid polymer rather than like a rubber; consequently, we must think of the failure behavior more in terms of a rigid polymer rather than as a highly extensible solid.

8.5 Conclusions and Future Work

We have proposed an experimental approach and implemented it to investigate the failure of viscoelastic elastomers in general and polyurea in particular under conditions combining high rates, shear and elevated pressure. The principles behind this experimental approach were discussed in detail. Finite element simulations were used to analyze and characterize the deformations during the impact history. Results showed the ability of the approach to induce failure in polyurea specimens while under high rates, shear and elevated pressures. A repetitive failure pattern was observed at high rates; specimens had a failed region along with radially expanding cracks. Ultimately, this combined experimental-computational approach can be used to elucidate a failure criterion for polyurea and viscoelastic polymers in general which would be of great value for engineers and designers aiming to utilize viscoelastic polymers in engineering applications, in particular where they might be subjected to a combination of high rates, shear and elevated pressures.

Aknowledgement The authors wish to thank Dr. Roshdy Barsoum of the Office of Naval Research through his guidance and cooperation and for the sustained support of this difficult effort under Grant ONR N00014-07-1-0624.

References

1. Amirkhize A, Isaacs J, Mcgee J, Nemat-Nasser S (2006) An experimentally-based viscoelastic constitutive model for polyurea, including pressure and temperature effects. Philos Mag 86(36):5847–5866
2. Li C, Lua J (2009) A hyper-viscoelastic constitutive model for polyurea. Mater Lett 63:877–880
3. Zhao J, Knauss WG, Ravichandran G (2009) A new shear-compression-specimen for determining quasistatic and dynamic polymer properties. Exp Mech 49(3):427–436
4. Sarva SS et al (2007) Stress–strain behavior of a polyurea and a polyurethane from low to high strain rates. Polymer 48(8):2208–2213

Chapter 9
Hybrid Polymer Grafted Nanoparticle Composites for Blast-Induced Shock-Wave Mitigation

K. Holzworth, G. Williams, Z. Guan, and S. Nemat-Nasser

Abstract In this work, we seek to create elastomeric nano composites for blast-induced shock-wave management. There are three main elements of nano composite structure, namely the particle (hard), the matrix (soft), and the interfacial chemistry connecting these two. For compositing, the blending approach allows for superb control of particle size, shape, and density; however, the hard/soft interface is typically weak for simple blends. Here we develop hybrid polymer grafted nanoparticle composites, which allow for tuning of the interface to overcome this deficiency. These nanoparticles have tethered polymer chains that can interact with their surrounding environment and provide a method to control enhanced nano-composites. We have established a "grow-from" method to covalently link polymers of variable molecular weight and chemical functionality to the surface of silica nanoparticles. The resulting nano-composite consists of homogeneously dispersed silica nanoparticles with tethered polymer chains within a bulk elastomeric matrix. Such a composite can manage shock-wave energy via dissipation and resonant trapping. The work described here is part of an ongoing effort to develop and verify rules and tools for creating elastomeric composites with optimally designed compositions and characteristics to manage blast-induced shock-wave energy.

Keywords Elastomeric nano composite • Shock-wave management • Interfacial chemistry

9.1 Introduction

Polyurea elastomer exhibits excellent properties including high thermal stability, insensitivity to humidity, abrasion resistance, and superior mechanical properties. In light of these properties, polyurea has been widely utilized in coating applications as well as to enhance impact resistance. It has been demonstrated that a polyurea coating is capable of improving the energy absorption and dynamic performance of structures.

Blast-mitigating applications utilize polyurea due to its excellent thermo-mechanical properties. While polyurea offers a useful starting point for dissipating and managing blast-induced shock-wave energy, control over crystallite size and morphology is limited. For compositing, the blending approach allows for superb control of particle size, shape, and density; however, the particle/matrix interface is typically weak for such simple blends.

Here, we develop hybrid polymer grafted nanoparticles, which have adjustable exposed functionality to control the location and tune the interface, in order to overcome the common compositing limitations. These nanoparticles have tethered polymer chains that can interact with their surrounding environment and provide a method to control enhanced nano composites.

These efforts are part of an ongoing initiative to develop elastomeric composites with optimally designed compositions and characteristics for blast-induced stress-wave energy management.

K. Holzworth (✉) • S. Nemat-Nasser
Department of Mechanical and Aerospace Engineering, Center of Excellence for Advanced Materials, University of California, 9500 Gilman Drive, La Jolla, San Diego, CA 92093-0416, USA
e-mail: kristin.holzworth@gmail.com

G. Williams • Z. Guan
Department of Chemistry, University of California, Irvine, CA 92697, USA

B. Antoun et al. (eds.), *Challenges in Mechanics of Time-Dependent Materials and Processes in Conventional and Multifunctional Materials, Volume 2*, Conference Proceedings of the Society for Experimental Mechanics Series 37,
DOI 10.1007/978-1-4614-4241-7_9,

9.2 Experimental Details

9.2.1 Materials

Polyurea is synthesized by reacting a difunctional amine, Versalink P-1000 [1], with Isonate 143L [2], which is a mixture of difunctional and trifunctional isocyanates. The reaction occurs at room temperature forming a lightly cross-linked block copolymer. Block copolymers are a unique subset of copolymers that have the ability to microphase separate. Phase separation occurs because of the chemical dissimilarity of the soft and hard phases resulting in a hard phase that is dispersed in a soft matrix. The hard phase not only reinforces the soft matrix, but also creates a cross-linked backbone, both of which lead to enhanced mechanical properties (Fig. 9.1).

A "grow-from" method is established to covalently link polymers of variable molecular weight and chemical functionality to the surface of silica nanoparticles, which gives rise to hybrid polymer grafted nanoparticles. The method is readily scalable and can be used with particles in the size range of 15–200 nm.

9.2.2 Composite Preparation

In order to integrate the hybrid polymer grafted nanoparticles into polyurea, they are first dispersed in a solvent. Then the solution is mechanically mixed into the Versalink P-1000 component. Following solvent evaporation from the mixture, the Isonate 143L component is added. Given the rapid reaction rate of Versalink P-1000 and Isonate 143L, the components are mixed for 5 min. Ultimately, the hybrid polymer grafted nanoparticle reinforced polyurea composite is cast in the desired geometry (Fig. 9.2).

9.3 Results and Discussion

Preliminary efforts to synthesize and characterize the hybrid polymer grafted nanoparticle reinforced polyurea composites demonstrate substantial enhancement of the dynamic mechanical properties, both storage and loss moduli, of polyurea through the incorporation of hybrid polymer grafted nanoparticles. A parametric study focusing on the effect of particle size, polymer graft length, and polymer graft density is currently in progress in order to illuminate a basic understanding of the mechanisms involved.

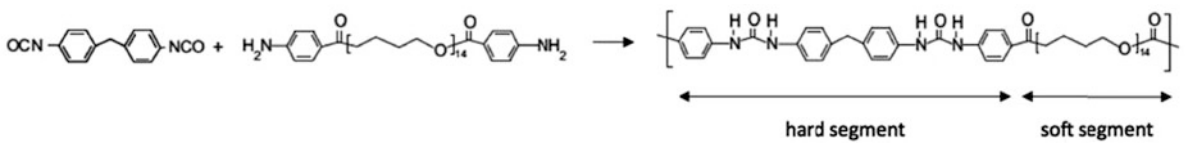

Fig. 9.1 Representative reaction between isocyanate and amine to form polyurea. [3]

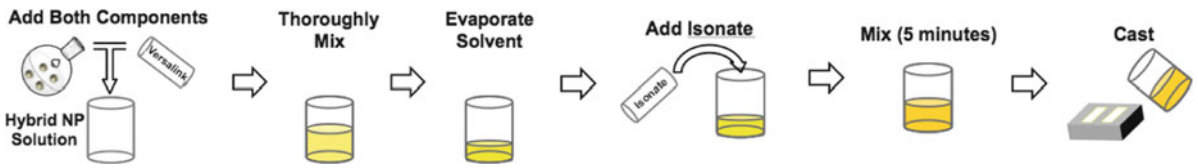

Fig. 9.2 Synthesis protocol for hybrid polymer grafted nanoparticle reinforced polyurea composites

Acknowledgements This work has been supported by the Office of Naval Research (ONR) grant N00014-09-1-1126 to the University of California, San Diego.

References

1. Air Products Chemicals, Inc. (2003) Polyurethane specialty products. Air Products and Chemicals, Allentown
2. The Dow Chemical Company (2001) Isonate 143L, modified MDI. Dow Chemical, Midland
3. Fragiadakis D, Gamache R, Bogoslovov RB, Roland CM (2010) Segmental dynamics of polyurea: effect of stoichiometry. Polymer 51:178–184

Chapter 10
Large-Strain Time-Temperature Equivalence and Adiabatic Heating of Polyethylene

J. Furmanski, E.N. Brown, and C.M. Cady

Abstract Time-temperature equivalence is a well-known phenomenon in time-dependent material response, where rapid events at a moderate temperature are indistinguishable from some occurring at modest rates but elevated temperatures. However, there is as-yet little elucidation of how well this equivalence holds for substantial plastic strains. In this work, we demonstrate time-temperature equivalence over a large range in a previously studied high-density polyethylene formulation (HDPE). At strain-rates exceeding 0.1/s, adiabatic heating confounds the comparison of nominally isothermal material response, apparently violating time-temperature equivalence. Strain-rate jumps can be employed to access the instantaneous true strain rate without heating. Adiabatic heating effects were isolated by comparing a locus of isothermal instantaneous flow stress measurements from strain-rate jumps up to 1/s with the predicted equivalent states at 0.01/s and 0.001/s in compression. Excellent agreement between the isothermal jump condition locus and the quasi-static tests was observed up to 50% strain, yielding one effective isothermal plastic response for each material for a given time-temperature equivalent state. These results imply that time-temperature equivalence can be effectively used to predict the deformation response of polymers during extreme mechanical events (large strain and high strain-rate) from measurements taken at reduced temperatures and nominal strain-rates in the laboratory.

Keywords Adiabatic heating • Large strain • Polymer mechanics • Time-temperature superposition

10.1 Introduction

Time-temperature equivalence is a widely recognized property of many time-dependent material systems, where there is a clear predictive link relating the deformation response at a nominal temperature and a high strain-rate to an equivalent response (i.e., stiffness or flow stress) at a depressed temperature and nominal strain-rate. This is often attributed, in metals and polymers alike, to the deformation response being governed by a local activation process which is a function of the temperature, the applied stress, and the activation energy for the particular activated process, due to Eyring [1, 2]. In metals, the time-temperature equivalent state has been widely related using activation models that are adaptations of the Eyring approach, for example, Zener and Holloman [3], and Zerilli and Armstrong [4, 5]. There have been numerous modeling attempts to capture time-temperature equivalence in polymers, and perhaps the most well-known is the Williams-Landel-Ferry (WLF) formula, which has been extremely successful for predicting small-strain deformations for a moderate window of temperatures in a variety of amorphous polymers [6]. Furthermore, such studies of viscoelasticity are typically confined to the small-strain regime, whether the intended application is time-temperature equivalence or creep modeling, which is problematic for the prediction of large deformations using equivalency approaches. Notably, Zerilli and Armstrong applied their adaptation of the Eyring equation obtained from their work in plasticity of metals to activated flow in polymers [7].

Recent work has investigated time-temperature equivalence in a number of polymers substantially beyond the small-strain regime. Siviour and coworkers examined uniaxial deformations at a wide range of temperatures and strain-rates in

J. Furmanski (✉) • C.M. Cady
Los Alamos National Laboratory, MST-8, Mail Stop G755, Los Alamos, NM 87545, USA
e-mail: jevan@lanl.gov

E.N. Brown
Los Alamos National Laboratory, P-23, Mail Stop H803, Los Alamos, NM 87545, USA

B. Antoun et al. (eds.), *Challenges in Mechanics of Time-Dependent Materials and Processes in Conventional and Multifunctional Materials, Volume 2*, Conference Proceedings of the Society for Experimental Mechanics Series 37,
DOI 10.1007/978-1-4614-4241-7_10,

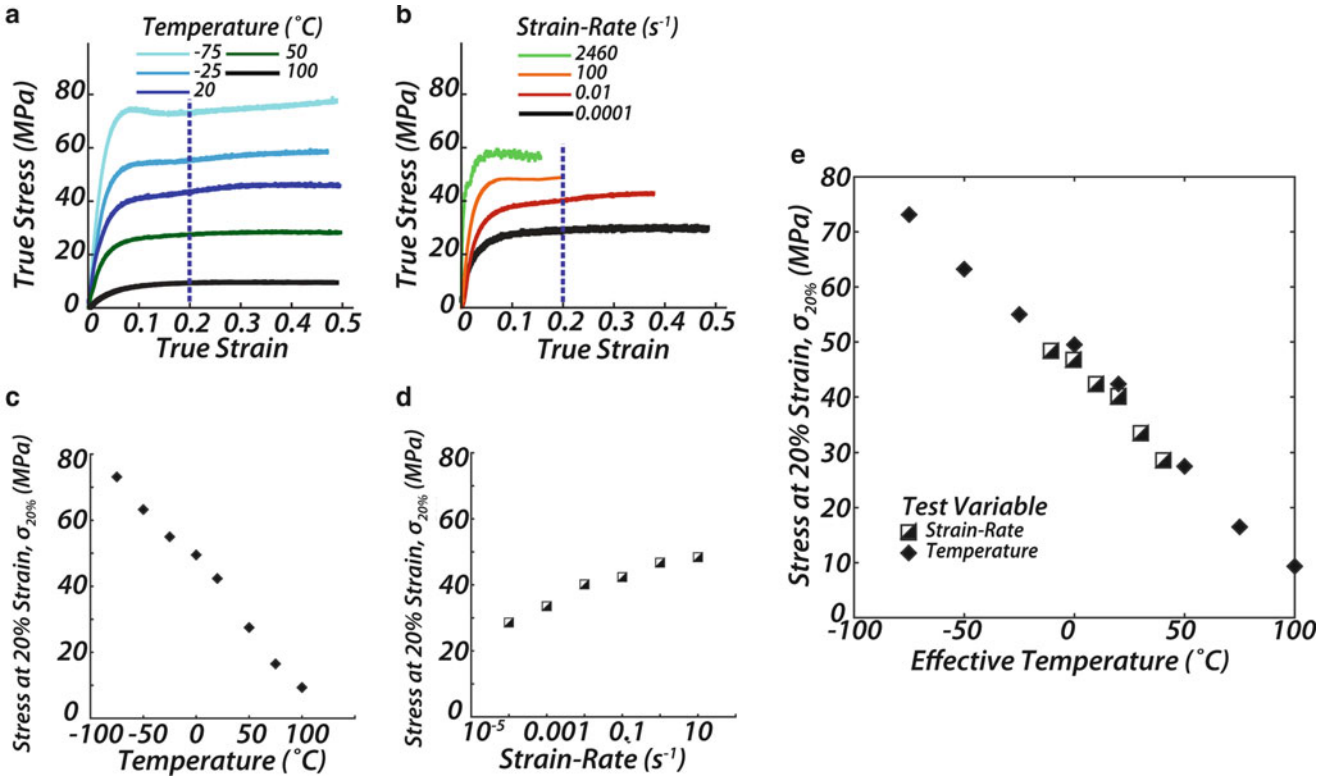

Fig. 10.1 (**a**) Stress-strain response of HDPE with varied temperature and (**b**) strain-rate. (**c-d**) Flow stress at 20 % strain from (**a-b**) respectively. (**e**) Equation 10.1 applied to collapse (**c-d**) to a single equivalent response locus (After [8])

polycarbonate, and polyvinyl-difluoride (PVDF), and proposed an empirical linear formula for relating these that agreed well with the data (Fig. 10.1) [9, 10].

$$T_{Eq} = T_{Test} + A\left[Log_{10}\left(\dot{\varepsilon}_{Eq}\right) - Log_{10}\left(\dot{\varepsilon}_{Test}\right)\right] \tag{10.1}$$

This model has a single free parameter (A), here termed the temperature/strain-rate equivalence parameter, which relates the temperature and strain-rate sensitivities of the stress state. When comparing measurements of the yield strength, their results showed that with a single free parameter in the model virtually all experimentally accessible states in temperature and strain-rate collapsed to a single trend in a given polymer. The agreement was even more remarkable when the test matrix spanned a glass transition, and a sharp inflection was observed in the temperature dependence of the yield strength, and the model nevertheless fit the data at temperatures both above and below the glass transition with a single value for the model equivalence parameter.

Brown and coworkers examined time-temperature equivalence in PTFE, PCTFE, and reported similar agreement with the formula employed by Siviour [11]. In another study, the finite strain time-temperature equivalence behavior of high density polyethylene (HDPE) and ultrahigh molecular weight polyethylene (UHMWPE) were studied and found to agree considerably with one another. It was also found that the temperature dependence of the yield strength exhibited no inflection over a large range of temperatures, in contrast to other polymers so investigated [12]. Their work reported the time-temperature equivalence of the yield strength, as defined as the onset of plasticity, which was observed to occur at 7.5% strain. An important finding of their work showed that one decade of increased strain-rate in that HDPE formulation was equivalent to a 10.2 K reduction in temperature. It is also important to note that their results also revealed substantial adiabatic heating and softening of the materials at strain-rates above 0.1/s. This work also tracked the time-temperature equivalence of the flow stress at 20% strain, $\sigma_{20\%}$, corresponding to the onset of fully-developed plasticity, for a wide range of temperatures and applied true strain-rates. The deformation response for HDPE at these conditions (Fig. 10.1a, b), can be represented directly as the temperature and strain-rate dependence of $\sigma_{20\%}$ can be represented (Fig. 10.1c, d) and they collapse to one equivalent response when (10.1) is applied with A = 10.2 K/Decade (Fig. 10.1e).

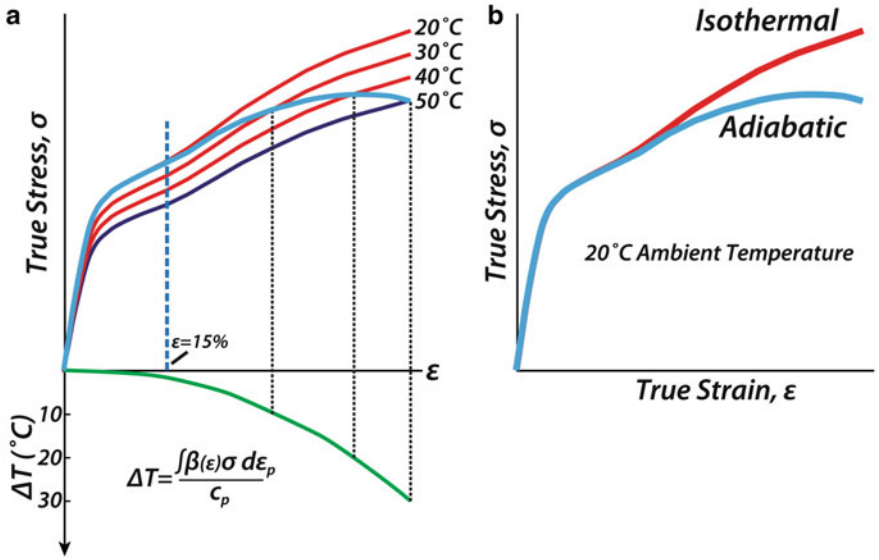

Fig. 10.2 Isothermal stress–strain curves for polyethylene for a range of temperatures (*dark gray*) are qualitatively similar. Specimen temperature rises (ΔT) due to accumulated plastic work converted into heat, dependent on the heat capacity (C_p) and the effective strain-dependent thermal plastic work conversion factor (β). If the test is rapid enough to effectively prevent heat conduction, then the test is adiabatic and the maximum specimen heating takes place. In this case, (**a**, *gray*) the observed flow stress follows the isothermal stress–strain for the current specimen temperature. (**b**) The resulting stress–strain curve in the adiabatic case is qualitatively different than the isothermal curve in the same ambient conditions

Special attention is paid to $\sigma_{20\%}$ here because the deformation beyond 15% strain in monotonic loading is apparently pure plastic deformation, as the recoverable viscoelastic deformation is exhausted at that point and does not contribute to further deformation [13]. At intermediate strains where both recoverable and plastic deformation are active, the two mechanisms are confounded and could have distinct activation energies and time-temperature equivalence behaviors.

While the wide agreement of time-temperature equivalence in a number of disparate polymers with a single-parameter empirical model is remarkable, one limitation of that work is that only a single locus of stress at a particular strain is used to generate the equivalency. That is, there is no direct reporting of the correspondence of the full deformation response, i.e., the collapsing of the full stress–strain curves of multiple distinct equivalent states. A verification of the correspondence of the entire response is critical to the proper thermomechanical constitutive modeling of the material. From a more pragmatic point of view, point-by-point correspondence over the entire deformation response is necessary if equivalent controlled laboratory-generated stress–strain curves are to be used in place of measurements made at extreme equivalent states that are experimentally inaccessible. In the present work, time-temperature equivalence of the same HDPE studied by Brown and coworkers [12] is extended to the continuous stress–strain curve in compression, beyond yield and beyond 50% logarithmic strain, where the reliability of compression tests becomes tenuous.

Another potential limitation to time-temperature equivalence lies in the difficulty in maintaining a constant specimen temperature at elevated strain-rates. The conversion of plastic work to heat during deformation is well-documented, where the fraction of the plastic work converted to heat often exceeds 90% [13, 14]. The temperature rise in a specimen during a test is determined by the total plastic work done, the effective thermal plastic work conversion factor ($\beta_{(\varepsilon)}$), and the heat capacity, C_p (10.2).

$$\Delta T = \frac{\int \beta_{(\varepsilon)} \sigma d\varepsilon_p}{c_p} \tag{10.2}$$

When the test is sufficiently rapid heat transfer cannot dissipate the thermal load from plastic work and the test is adiabatic. In this case heat energy cannot escape the specimen during the test and the effective β is maximized. The resulting flow stress follows the deformation response for the instantaneous temperature in the specimen, which manifests as thermal softening (Fig. 10.2).

Non-isothermal stress–strain curves are not unique, and therefore have limited interpretability for material characterization. Adiabatic heating therefore frustrates attempts to study time-temperature equivalence between non-isothermal states. Haward and coworkers investigated adiabatic heating in large tensile deformations in HDPE, and found the plastic work at large

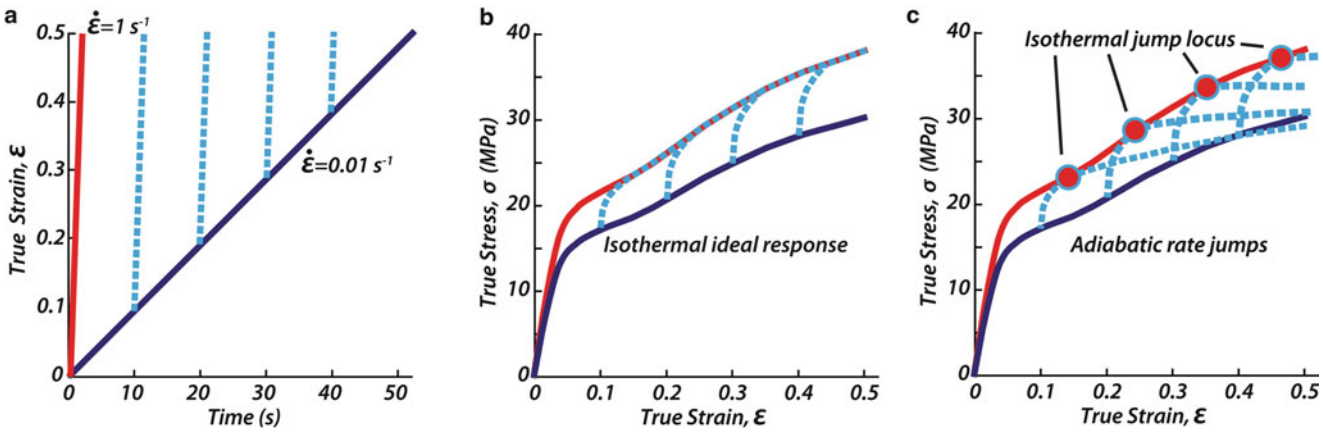

Fig. 10.3 (**a**) Strain program for constant strain-rate compression testing (*solid*) and rate-jumps from the lower bound to the upper bound strain-rate. (**b**) The expected result for ideal viscoplastic behavior, where the response after the strain-rate jump is indistinguishable from the isothermal response at that strain-rate. All responses are drawn in (**b**) here with the ideal isothermal response, i.e., without specimen heating from plastic work. (**c**) Adiabatic heating progressively lowers the flow stress after an increment of plastic work has been done, leaving the initial portion of the rate jump response in agreement with the isothermal response at that rate. The corresponding experimental data are then in the form of the isothermal locus of points on the jump response just prior to specimen softening

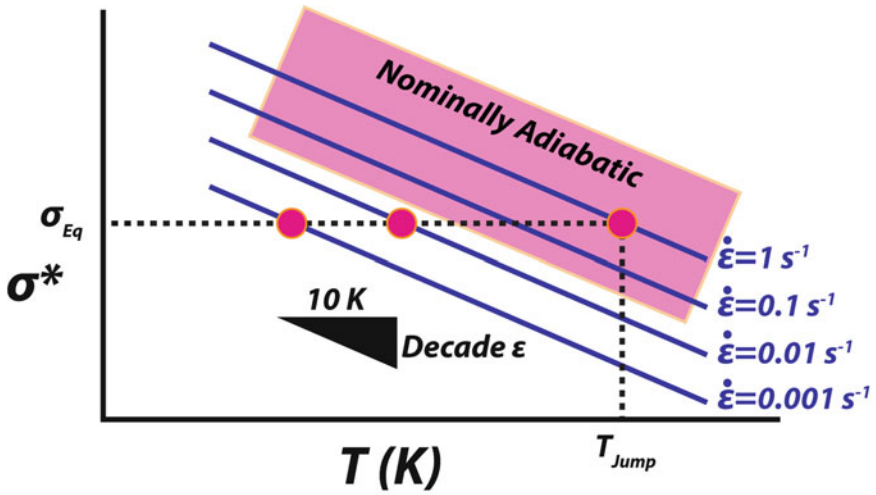

Fig. 10.4 Flow stress dependence on absolute temperature, with multiple strain-rates shown obeying the time-temperature equivalence in (10.1). Data are represented by the flow stress at a given state, often at a certain strain (e.g., 20 %). To check for equivalence from the prediction of (10.1), multiple tests are run at strain-rate/temperature states that are predicted to exhibit the same flow stress. For strain-rates greater than 0.01/s, isothermal conditions are not guaranteed, and specimen heating can confound the comparison, unless strain-rate jump tests are employed

strains to be nearly completely converted to heat, i.e., β~1 [13]. Other work has found the conversion to heat of inelastic strains below 10% in polymers to be considerably less complete, owing to the reversibility of the strain through viscoelastic recovery [15–17]. However, the potential effect of adiabatic heating at small or intermediate strains has a diminishing effect on the overall deformation response, as the overall strain energy is still limited at those strains. Thus, while the specimen geometry plays a role in heat dissipation, plastic work heating generally needs to be considered at strain-rates exceeding 0.01/s and strains in excess of 15%.

In the present work, the confounding effect of adiabatic heating on the presumed test temperature was accounted for at large strains by employing sudden strain-rate jumps to access an instantaneous value of the flow stress for elevated strain-rates at a given jump strain, which is therefore obtained prior to measurable adiabatic heating from further plastic work (Fig. 10.3).

Several of these rate-jump measurements were then synthesized to form a locus of the isothermal plastic deformation response (Fig. 10.3c) up to large compressive strains at a constant supplied temperature and elevated (nominally adiabatic) strain-rate. Thus, multiple equivalent states resulting in an identical flow stress at an arbitrary strain can be directly compared though a construction of an experiment with a suitable interchanging of test temperature and strain-rate via the equivalence relation (10.1, Fig. 10.4).

The purpose of the present work is to identify whether the empirical time-temperature formula (10.1) employed point-wise in the literature is sufficient to enable prediction of the full isothermal stress–strain response at large strains and high strain-rates in HDPE from equivalent quasi-static tests at suitably depressed temperatures. Further, this comparison was undertaken over a wide range of temperatures to ensure that a single model fit is suitable for all equivalent temperature/strain-rate conditions of interest.

10.2 Materials and Methods

Compression tests were conducted with cylindrical specimens 6.2 mm in diameter and height on an MTS 880 servohydraulic load frame (MTS, Eden Prarie MN). The test specimens were machined from the same original stock employed in previous work by the authors [12]. All specimens were measured with a micrometer prior to testing. The specimens were preloaded in load control at 20 N. The tests were conducted in strain control at a computed true strain rate, and the strain was measured by an extensometer during the test mounted directly on the compression stage. Load, displacement, and strain were recorded both at regular time increments and at displacement increments of 0.001 mm. Data were computed as true stress and strain assuming uniform incompressible deformation.

The test temperature was controlled through compression platens cooled by nitrogen exhaust from a liquid nitrogen filled Dewar, and the temperature was controlled within +/−0.5 K of the target temperature through manual adjustment of the gas flow rate. The specimens were loaded between optically flat tungsten carbide platens and were unlubricated. The lateral surfaces of the specimen were insulated from the environment with a foam sleeve. Temperature equilibrium was achieved by delaying testing until the displacement rate under a constant preload of 50 N was negligible (<1 μm/min). The temperatures employed during testing were 20°C and −50°C for a maximum strain-rate of 1/s; test temperature was 20 K or 30 K depressed for comparison isothermal quasi-static conditions at strain-rates of 0.01/s and 0.001/s, respectively. A limited number of quasi-static tests were also conducted below −100°C on the cold platens. Additionally, quasi-static tests were conducted immersed in a liquid nitrogen bath to challenge the modeled linearity of the temperature dependence of the strength at extremely low temperatures.

The tests employed strain-rates of 0.01/s and 0.001/s for baseline isothermal quasi-static conditions (with the latter 10 K cooler in each temperature condition) (Figs. 10.3 and 10.4). Lower strain-rates are impractical for the manual temperature control scheme employed and added little insight to the experiment. A comparison of the deformation response between these two presumably equivalent quasi-static conditions was used as an additional test for isothermality in these tests, as a rate-dependent thermal softening would present as a divergence in the plastic hardening. To assess higher rate isothermal conditions, strain-rate jumps from 0.01 up to a 1/s were conducted, at strains of 10%, 20%, 30%, and 40% (Fig. 10.3a). The maximum strain-rate in a test was held until a true strain of 100% was achieved to prevent machine deceleration from affecting the data at strains less than 50%. Care was taken to tune the load frame response to ensure that the strain-rate jump occurred with negligible acceleration lag or error, which required the use of a 6 GPM servohydraulic valve in the system.

10.3 Results

Using the time-temperature equivalence relation noted above (10.1) and the equivalence parameter found from previous work for each material (10.2 K/decade strain-rate), quasi-static near-equivalent conditions for both materials can be directly compared to the results of the rate-jump tests by depressing the temperature by 20 K or 30 K for constant true strain-rates of 0.01/s and 0.001/s, respectively (Fig. 10.4). A direct comparison of these quasi-static equivalent states and the rate-jump loci shows generally good agreement for strains exceeding 10%. Thus, by isolating adiabatic heating from the large strain deformation response through the use of strain-rate jumps, excellent agreement is obtained between the isothermal quasi-static equivalent state and the isothermal rate-jump flow stress locus at 1/s without apparent overshooting or undershooting of the isothermal response. Overshoot or undershoot of the jump condition (under isothermal conditions)

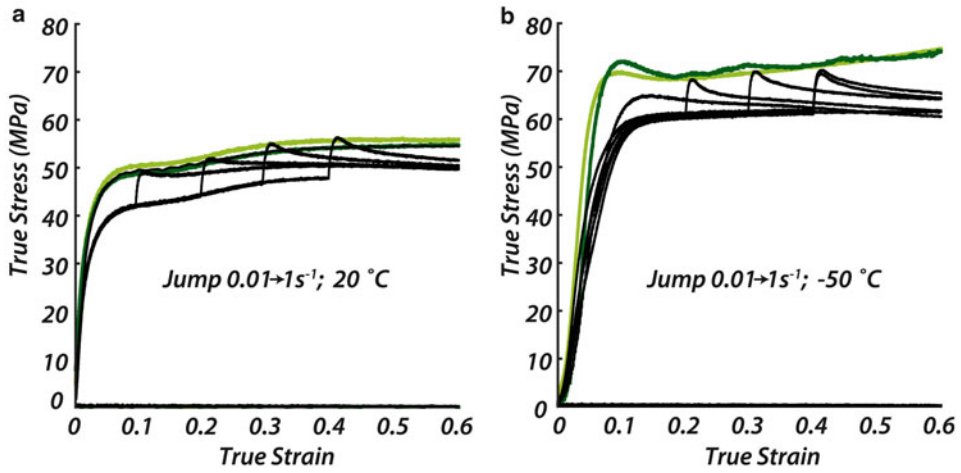

Fig. 10.5 Deformation response of HDPE at a nominal temperature of (**a**) 20 °C and (**b**) −50 °C, including strain-rate jumps from 0.01/s to 1/s. In *gray* are the predicted isothermal states equivalent to the nominal temperature at 1/s, with strain-rates of 0.01/s and 0.001/s. Good agreement between the equivalent states and the isothermal jump locus is obtained

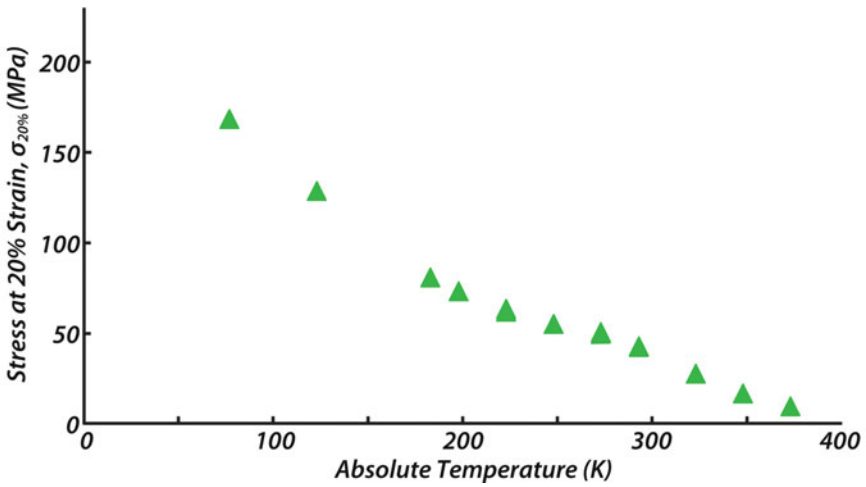

Fig. 10.6 The flow stress in HDPE at 20% strain is exponential with absolute temperature with a high degree of correlation for temperatures substantially below the melting temperature (410 K). However, there is apparently a breakdown in the exponential fit above room temperature (293 K) where the flow stress decreases linearly and drops to zero near the melt temperature. Note that for temperatures between 200 K ($T_m/2$) and 300 K, a linear relation is approximate for many applications of interest, though this observation obscures a good interpretation of the overall data

has been identified as evidence of history dependence of the process, effectively breaking the presumption of general time-temperature equivalence.

At 20°C, the deformation response in HDPE underwent thermal softening at a strain-rate of 1/s; the flow stress was depressed by 3–5 MPa between 20% and 50% strain (Fig. 10.5a). The agreement between the equivalent quasi-static tests is good. The jump locus also agrees well with the quasi-static isothermal equivalent states. The response at −50°C in HDPE exhibits considerable softening, with the flow stress dropping approximately 10 MPa after each rate jump (Fig. 10.5b). The 1/s response softens to the point that the flow stress is lower at large strains than that at 0.01/s—a hallmark of adiabatic heating effects (Fig. 10.3c).

To test for increased temperature sensitivity of the flow stress below −80°C, quasi-static tests were conducted at further reduced temperatures, including immersion in liquid nitrogen (Fig. 10.6). The temperature dependence of the strength is clearly non-linear when taken to low temperatures, with the deviation occurring around −90°C (180 K).

10.4 Discussion

The agreement of the isothermal deformation response at quasi-static and elevated strain-rates in HDPE, over a wide range of plastic strains, extends the applicability of time-temperature equivalence techniques in these materials into the large strain regime. This significantly improves the efficacy of time-temperature equivalence relations by enabling the translation of continuous stress–strain curves obtained in the laboratory at quasi-static isothermal conditions into dynamic regimes of behavior at substantially elevated strain-rates. The ability to shift experimental stress–strain curves is extremely valuable in the development or evaluation of rate-dependent constitutive models, where model predictions of difficult-to-test extreme mechanical conditions (e.g., large strains at high strain-rates) can be directly compared to time-temperature equivalent conditions from laboratory data. Time-temperature equivalence holding over a wide range of strains and temperatures also implies that one mechanism of temperature-dependence is active in general, which is also useful information for model development.

It is also of note that the jump locus coincides directly with the equivalent state, apparently without substantial overshoot or undershoot. In metals, such a disagreement is linked to the pinning or accumulation of dislocations (respectively), making the rate-sensitivity a history dependent phenomenon. The rate-sensitivity in HDPE, and hence its time-temperature equivalence, appears to be history-independent and therefore generally applicable. We had hypothesized that there would be a history dependence in HDPE, as HDPE has thick crystal lamellae that are likely dominated by dislocation half-loops [18] that are likely to interact and perhaps tangle than pure screw dislocations during dynamic loading, resulting in a path- or history-dependence in plasticity. More work is warranted to elucidate the path-independence of the time-temperature equivalence in polyethylenes, with attention to activation phenomena, while employing more complicated strain histories.

It has been observed in many materials that adiabatic heating effects are exacerbated at depressed temperatures, and the results of this work are consistent with those observations. To hedge against this phenomenon, which could potentially lead to heating even at 0.01/s, equivalent conditions at 0.01/s and 0.001/s both were compared to the isothermal rate-jump locus and to one another. The agreement of both quasi-static strain-rates with the rate-jump locus strengthens the claim of equivalence by collapsing three equivalent states, and clarifies that heating effects do not confound the 0.01/s data above $-80°$C.

The linear strength dependence on temperature implied by the equivalence relation (for log-linear strength—strain-rate dependence) is likely sufficient for most mechanical conditions that could occur in the service of components, as extremely low temperatures correspond to extremely high strain-rates. For instance, for a loading at a depressed temperature of -20 C to be affected by the observed deviation from linearity of the strength, according to the non-linear strength model fit, the strain-rate would have to exceed 10^5/s. Such a high strain-rate is unlikely to occur in most applications, making the distinction largely academic. However, even if such conditions were a concern, strain-rates substantially exceeding 10^5/s the response must also take into account shock wave and compressibility phenomena, and thus a refinement of the model would be necessary to accurately predict such a deformation. Still, there is an indication that a general non-linear treatment of the temperature dependence of the flow stress could be more consistent and physically motivated than the treatment in the empirical equivalence model employed here and elsewhere.

10.5 Conclusion

This work demonstrated that the empirical time-temperature equivalence model proposed by Siviour [9, 10] is suitable for the prediction the continuous deformation response of HDPE at elevated strain-rates from quasi-static data at depressed temperatures above $-80°$C. Further, the effect of adiabatic heating, which was clearly evident at substantially depressed temperature and strain-rates above 0.1/s, was successfully accounted for by assessing the isothermal deformation response at elevated strain-rates by employing strain-rate jumps. Thus, the results of this work enable the predictive translation of quasi-static stress–strain curves into equivalent dynamic mechanical conditions for a wide range of temperatures. Such a translation enables the comparison of advanced constitutive model predictions of dynamic deformation response directly with well-controlled laboratory data (with adiabatic heating taken into account), as experimental measurement of the deformation response at large strains and high strain-rates is typically not feasible. Further work is warranted to clarify large strain time-temperature equivalence for all temperatures in polyethylene and other polymers, with attention to the non-linear dependence of flow stress on temperature and the mechanisms of temperature- and time-dependence implied by such relationships.

References

1. Eyring H (1935) The activated complex in chemical reactions. J Chem Phys 3(2):107–115
2. Eyring H (1936) Viscosity, plasticity, and diffusion as examples of absolute reaction rates. J Chem Phys 4(4):283–291
3. Zener C, Hollomon JH (1944) Effect of strain rate upon plastic flow of steel. J Appl Phys 15(1):22–32
4. Zerilli FJ, Armstrong RW (1987) Dislocation-mechanics-based constitutive relations for material dynamics calculations. J Appl Phys 61(5):1816–1825
5. Zerilli FJ, Armstrong RW (1992) The effect of dislocation drag on the stress-strain behavior of Fcc metals. Acta Metallurgica Et Materialia 40(8):1803–1808
6. Williams ML, Landel RF, Ferry JD (1955) Mechanical properties of substances of high molecular weight.19. The temperature dependence of relaxation mechanisms in amorphous polymers and other glass-forming liquids. J Am Chem Soc 77(14):3701–3707
7. Zerilli FJ, Armstrong RW (2007) A constitutive equation for the dynamic deformation behavior of polymers. J Mater Sci 42(12):4562–4574
8. Brown EN et al (2007) Influence of molecular conformation on the constitutive response of polyethylene: a comparison of HDPE, UHMWPE, and PEX. Exp Mech 47(3):381–393
9. Siviour CR et al (2005) The high strain rate compressive behaviour of polycarbonate and polyvinylidene difluoride. Polymer 46 (26):12546–12555
10. Siviour CR et al (2006) Mechanical behaviour of polymers at high rates of strain. Journal De Physique Iv 134:949–955
11. Brown EN, Rae PJ, Gray GT (2006) The influence of temperature and strain rate on the tensile and compressive constitutive response of four fluoropolymers. Journal De Physique Iv 134:935–940
12. Brown EN et al (2007) Soft recovery of polytetrafluoroethylene shocked through the crystalline phase II-III transition. J Appl Phys 101 (2):024916
13. Hillmansen S, Haward RN (2001) Adiabatic failure in polyethylene. Polymer 42(22):9301–9312
14. Hillmansen S et al (2000) The effect of strain rate, temperature, and molecular mass on the tensile deformation of polyethylene. Polym Eng Sci 40(2):481–489
15. Brooks NW, Duckett RA, Ward IM (1992) Investigation into double yield points in polyethylene. Polymer 33(9):1872–1880
16. Salamatina OB et al (2011) Thermodynamics of inelastic deformation of amorphous and crystalline phases in linear polyethylene. Polym Sci Ser A 53(9):775–786
17. Shenogin SV, Hohne GWH, Oleinik EF (2002) Thermodynamics of the pre-yield deformation behavior of glassy polymers: measurements with new deformation calorimeter. Thermochimica Acta 391(1–2):13–23
18. Argon AS, Galeski A, Kazmierczak T (2005) Rate mechanisms of plasticity in semi-crystalline polyethylene. Polymer 46(25):11798–11805

Chapter 11
New Thermo-Mechanical Modelling for Visco Elastic, Visco Plastic Polymers

Noëlle Billon

Abstract A 3D Visco hyperelastic model is discussed and validated using a rich and rigorous data base obtained on PMMA above Tg. Inelastic phenomena are accounted for as an evolution of internal variables assumed to be related to entanglements. Inelastic strain-rate is deduced from energy balance between elastic and dissipative phenomenon. The concept allowing introducing time effects in any rubber elasticity theory, is used with Edward-Vilgis' model. Extended model allows reproducing most of the visco-elastic phenomena in polymer: strain rate dependence, hysteretic effects and relaxation. An accounting for temperature and strain-rate by an "a priori" uses of time temperature superposition principle is also proposed. The three concepts result in an original and attractive model of high efficiency. This is demonstrated in the case of PMMA.

Keywords Time-dependent behaviour • Large-strain • Polymers • Inelasticity • PMMA

11.1 Introduction

Modelling the mechanical behaviour of polymers is a nontrivial task due to its nonlinearity and the combination of visco-elastic, visco-plastic, strain-hardening and damaging processes sometimes ruled by discrete relaxations and a high sensitivity to temperature and strain-rate.

Usual macroscopic approaches that arbitrary decompose global deformation into three elementary components (reversible-instantaneous (elastic part), or irreversible-not dependent upon strain-rate (plastic part) or irreversible-dependent upon strain-rate (viscous part), respectively) whose contributions to global behaviour are combined, either in a parallel, or in a serial manner, was extensively applied in that field. Mathematical writings were built up, either on the basis of 1D-model, further extended to 3D case, or in the continuum thermodynamics frame [1, 2], in which global behaviour is ruled by energy potentials and dissipation pseudo-potentials. Whatever the route is, basic assumptions were equivalent in the most rigorous of those studies, despite of some mathematical differences. Nonlinearity was addressed at two levels:

- Important strain-hardening, often reproduced introducing various hyper-elastic reversible elements [3–17].
- Nonlinear viscous effects introduced through "non Newtonian pseudo plastic, Eyring or Carreau"—like elements or through phenomenological accountings for disentanglement [17–23].

Coupled with the dependence upon strain-rate and temperature (in example [24, 25]), those approaches resulted in numerous parameters that are not that easy to identify without specific protocol that pre-allocates one element or another to one macroscopic phenomenon.

This study deals at promoting another concept thanks to the fact that it is possible to combine the general rubber hyper elastic theory and some evolution of internal variables, potentially induced by microstructure alteration [26, 27], to model time effects in the constitutive model. General goal is to model visco-hyper-elasticity of polymers above Tg without arbitrary decomposition into "viscous" and "elastic" stresses or strains. Therefore, a hyper elastic model is extended to

N. Billon (✉)
Mines-ParisTech, CEMEF, UMR 7635, BP 207, 06904, Sophia Antipolis cedex, France
e-mail: noelle.billon@mines-paristech.fr

B. Antoun et al. (eds.), *Challenges in Mechanics of Time-Dependent Materials and Processes in Conventional and Multifunctional Materials, Volume 2*, Conference Proceedings of the Society for Experimental Mechanics Series 37,
DOI 10.1007/978-1-4614-4241-7_11,

account for inelastic processes. Those latter are assumed to result in a kinetics of variation of internal variables that have to be accounted for in the energy balance at any time and induce time effects in the writing.

Model is validated in its 1-D form using experimental observations on PMMA. However, it was developed in a much more general 3D form, consistent with the large strain mechanical approach and with continuum thermodynamics [28, 29].

11.2 Theoretical

Let's assume that above glass transition temperature any polymer can be modelled as an equivalent entangled network. So, core of the behaviour is a hyper-elastic body whose energy is ruled by a strain energy density, W. As a first approach, an incompressible material, being initially isotropic was considered. Then, the principal stresses, σ_i (i = 1, 2, 3), are related to the principal elastic extension ratios, λ_i^e, through (11.1).

$$\sigma_i = \lambda_i^e \frac{\partial W}{\partial \lambda_i^e} - P \quad (i = 1, 2, 3) \tag{11.1}$$

where P is an arbitrary pressure that is introduced due to incompressibility.

Additionally, W-potential depends on internal variables, among which temperature, T, some variables that reflect the microstructure of the material (m_1, m_2, …, m_n) and elastic extension ratios, λ_i^e or the three elastic invariants ($I_1^e = \lambda_1^{e2} + \lambda_2^{e2} + \lambda_3^{e2}; I_2^e = \lambda_1^{e2}\lambda_2^{e2} + \lambda_1^{e2}\lambda_3^{e2} + \lambda_2^{e2}\lambda_3^{e2}; I_3^e = \lambda_1^{e2}\lambda_2^{e2}\lambda_3^{e2} = 1$).

During loading, microstructure of the material can vary due to disentanglement, crystallisation or crystalline reorganisation etc., which results in evolution of associated m-variables. This represents a change in the energy of the material that has to be compensated for thermodynamics principles to be obeyed. This is achieved partly by some local elastic recovery in the network, $\partial\lambda_i^{re}/\partial t$, which is the source of inelastic strain-rate, $\partial\lambda_i^a/\partial t$, in our model, i.e., the fraction of elastic extension that has to be released to compensate change in energy due to microstructure processes. Assuming $\partial m_j/\partial t$ to be the kinetics of the evolution of variable m_j the concept is summarised in (11.2) assuming that principal elastic extension ratios and principal inelastic extension ratios are collinear.

$$\sum_{j=1}^{n} \frac{\partial W}{\partial m_j}\frac{\partial m_j}{\partial t} = -\frac{1}{\beta'}\sum_{i=1}^{3} \frac{\partial W}{\partial \lambda_i^e}\frac{\partial \lambda_i^{re}}{\partial t} = \frac{1}{\beta'}\sum_{i=1}^{3} \frac{\partial W}{\partial \lambda_i^e}\left(\frac{\lambda_i^e}{\lambda_i^a}\frac{\partial \lambda_i^a}{\partial t}\right) \quad with \quad \beta' \geq 1 \tag{11.2}$$

β′-parameter, express the fact that part of the released energy could be dissipated into heat (thermo mechanical coupling) or stored via some permanent changes in the microstructure (plastic-like phenomenon). Model was derived totally in its 3D form [28, 29] but in the case of uniaxial tension parallel to 1-axis, (11.2) is reduced to (11.3):

$$\sum_{j=1}^{n} \frac{\partial W}{\partial m_j}\frac{\partial m_j}{\partial t} = \frac{1}{\beta'}\sigma\frac{\partial \varepsilon^a}{\partial t} \quad with \quad \beta' \geq 1 \tag{11.3}$$

where $\frac{\partial \varepsilon^a}{\partial t}$ is the so-called inelastic strain-rate.

Due to its proved efficiency [10–16], we chose Eswards-Vilgis' model as primary network (11.4). This model is based on a Ball's statistical approach. Chains are assumed to have a finite extensibility, ultimately controlled by one positive parameter α, being 0 in the case of a Gaussian chain. Chains are linked by permanent nodes of density N_c per unit volume and slip links (entanglements) of density N_s per unit volume. A positive "slipperiness factor", η, is ultimately defined and related do the degree of mobility of slip links. A zero η-value corresponds to permanent nodes. Initial η-value is chosen close to 0.2343 following [7].

$$\begin{aligned} W &= \frac{N_s^{\sim}}{2}\left(\frac{A_{\alpha\eta}}{X_{\alpha\lambda}Y_{\eta\lambda}}Z_{\eta\lambda} + \ln\left(Y_{\eta\lambda}\right) + \ln\left(X_{\alpha\lambda}\right)\right) + \frac{N_c^{\sim}}{2}\left(\frac{\left(1-\alpha^2\right)}{X_{\alpha\lambda}}I_1^e + \ln\left(X_{\alpha\lambda}\right)\right) \\ Y_{\eta\lambda} &= 1 + \eta I_1^e + \eta^2 I_2^e + \eta^3; X_{\alpha\lambda} = 1 - \alpha^2 I_1^e; Z_{\eta\lambda} = I_1^e + 2\eta I_2^e + 3\eta^2; A_{\alpha\eta} = (1+\eta)\left(1-\alpha^2\right) \end{aligned} \tag{11.4}$$

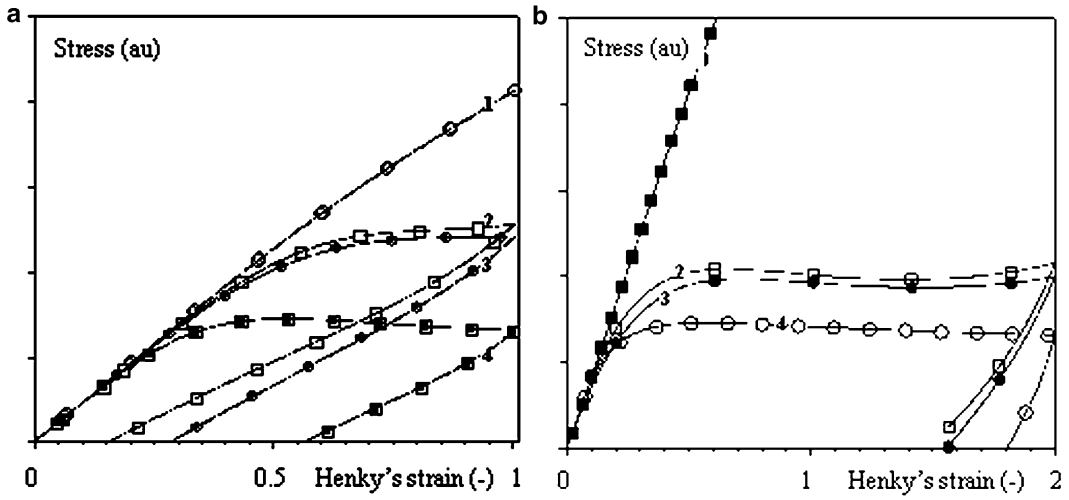

Fig. 11.1 Efficiency of the model (11.5, 11.6 and 11.7) compared to initial Edward Vilgis' (EV's) model for uploading-unloading cycles at a constant strain-rate 0.01 s^{-1}. (**a**) $N_c = 0.1\ N_s$, $\alpha^2 = 0$ and $\Psi = 0$: (*1*) EV's model; (*2*) $\xi = 0.01$, $\beta' = 1°$; (*3*) $\xi = 0.01$, $\Psi = 0$, $\beta' = 0.5°$; (*4*) $\xi = 0.1$, $\beta' = 1$. (**b**) 0.01 s^{-1}, $N_c = 0.1\ N_s$, $\alpha^2 = 0.001$: (*1*) Initial potential; (*2*) $\xi = 0.03$, $\Psi = 0.01$, $\beta' = 1$; (*3*) $\xi = 0.03$, $\Psi = 0$, $\beta' = 1$; (*4*) $\xi = 0.03$, $\Psi = 0.01$, $\beta' = 0.5$. (**b**) $N_c = 0.1\ N_s$, $\alpha^2 = 0$ and $\Psi = 0$: (*1*); (*2*) $\xi = 0.01$, $\beta' = 1°$; (*3*) $\xi = 0.01$, $\Psi = 0$, $\beta' = 0.5°$; (*4*) $\xi = 0.1$, $\beta' = 1$

where $N_s^{\sim}$ and $N_c^{\sim}$ are $N_s kT$ and $N_c kT$, respectively, with k the Boltzmann's constant and T, the absolute temperature. Obviously, this model only allows reproducing hyper-elastic behaviours but is rather powerful despite of a few numbers of parameters.

Time dependent effects can be introduced through the alteration of parameters. In example disentanglement could result in an increase in η. Hence, according to (11.3):

$$\frac{\partial \varepsilon^a}{\partial t} = \frac{\beta'}{\sigma}\left(\frac{\partial W}{\partial \eta}\frac{\partial \eta}{\partial t}\right) \quad with \quad \beta' \geq 1 \tag{11.5}$$

Obviously, rate of microstructure changes must be related to the energy that is available in the material. If one focus on disentanglements, one can assume that the more stressed the slip-links the faster the processes. In consequence, this means that that kinetics should probably depend on the elementary energy of the slip-link due to extension, f_s (11.6).

$$f_s = \left(\frac{A_{\alpha\eta}}{X_{\alpha\lambda}Y_{\eta\lambda}}Z_{\eta\lambda} + \ln\left(Y_{\eta\lambda}\right) + \ln\left(X_{\alpha\lambda}\right)\right) - 3\left[\frac{(1-\alpha^2)}{(1-3\alpha^2)} + \ln(1+\eta)\right] + \ln\left(1-3\alpha^2\right) \tag{11.6}$$

Than, if one assumes that disentanglement could result in: $\frac{\partial \eta}{\partial t} = \Im(f_s) > 0$, behaviour is ruled by the functions $\Im$. Once those functions are defined, an explicit scheme is adopted to calculate the evolution of the stress as a function of the strain-rate. Figures 11.1 and 11.2 depict results obtained in two fictitious 0.01 and 0.001 s^{-1} uploading-unloading cycles and allow illustrating and comparing effects of alteration of parameters. In those cases $\Im$-functions are arbitrary simple to give an example of potential of the approach accounting for the fact that alteration kinetics is faster when energy increases, using as less numerous parameters as possible (one to two, (11.7)).

$$\begin{aligned} \Im &= \xi\,(\exp(f_s - \psi) - 1) \quad if \quad fs > \psi \\ \Im &= 0 \quad if \quad fs \leq \psi \end{aligned} \tag{11.7}$$

Figure 11.2b, for its part, demonstrates that, introducing the kinetics of microstructure modification makes it possible to predict some sensitivity to strain-rate.

One has to emphasize that only a few numbers of parameters (5 to 6 per conditions) were necessary to obtain such a pretty good efficiency in introducing time effects in constitutive model, which makes this model unique.

Following is devoted to a validation using experimental results obtains on a PMMA.

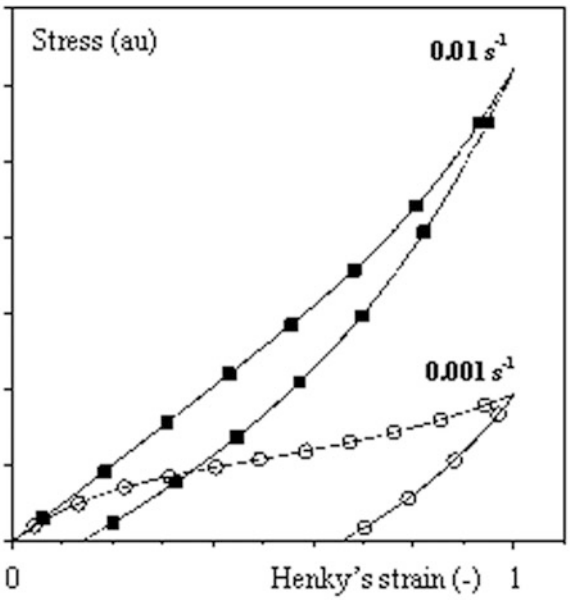

Fig. 11.2 Efficiency of the model (11.5, 11.6 and 11.7) compared to initial Edward Vilgis' model (EV's model). Uploading-unloading cycles for two constant strain-rates, 0.0001 and 0.01 s^{-1}. $N_c = N_s$, $\alpha^2 = 0.001$, $\xi = 0.013$, $\Psi = 0$, $\beta' = 1$

11.3 Experimentals

The material a poly methyl methacrylate (PMMA) ALTUGLAS V 825T provided by Arkema of average molar masses, M_n and M_w, 40,434 and 93,000 g/mol, respectively. Material was processed as 4 mm-thick injection moulded plaques of dimensions 10 cm $\times$ 10 cm. Gate was a through-the-width lateral gate and processing conditions were chosen according to the state of the art. Resulting mechanical anisotropy in the plane of the plaques was found to be negligible.

DMTA analyses were performed in tension on 5 mm $\times$ 1 mm bars, to characterise the linear visco-elastic domain of the material (maximum strain of 2×10^{-3}). The α-transition temperature (chosen at the maximum value of the tangent of the loss angle) ranged from 128°C to 146°C, for loading frequencies ranging from 0.3 to 31 Hz (132°C for a 1 Hz-frequency). Despite of some discrepancy for higher frequencies, the time-temperature superposition principle could be applied.

Uploading (up to different levels of strain)-unloading or uploading (up to different levels of strain)-relaxation experiments were performed in tension, exploring temperatures ranging from 100°C to 160°C and strain rates ranging from 0.0001 to 0.01 s^{-1}. Strain rates were chosen to reduce heat dissipation and overall experimental data base was designed to characterise the material above but close to Tg. Experiments were conducted at constant strain rates. DIC allowed 3D strain field analysis and, in consequence, measurements of local true strains in the necking zone. This 3D extensometer allowed also concluding that the plaques were totally isotropic and that the volume strain remained close to zero in any case. Consequently, this PMMA is an isotropic and incompressible material and can be modelled using our model.

In parallel, as expected, behaviour of PMMA exhibited a huge dependence upon strain-rate and temperature in the range that was considered in this study. In a less classical manner, it was observed that equivalent strain-rate at reference temperature was a relevant parameter to refer to experimental conditions.

11.4 Validation of the Model

The model described in the above sections could reproduce those experimental data, including uploading-unloading, uploading- relaxation and DMTA results. Parameters of the model could be identified as a whole set, using inverse analysis based on a "mean square" cost function between experimental and calculated stresses. Minimisation relied on the simplex algorithm of the "fminsearch" MATLAB® function.

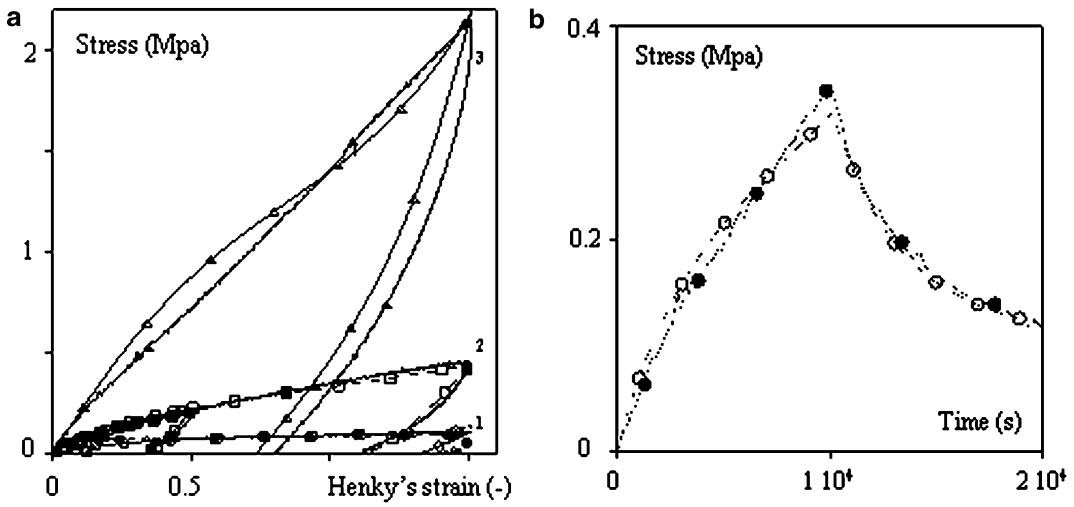

Fig. 11.3 Comparison between experiment (*plain symbols*) and model (*hollow symbols*) in the case of (**a**) uploading-unloading experiments: (*1*) 150°C and 10^{-3} s^{-1}; (*2*) 130°C and 10^{-4} s^{-1}; (*3*) 120°C and 2×10^{-4} s^{-1} and (**b**) uploading at 0.0001 s^{-1} relaxation at 130°C

To model the increase in η, i.e., disentanglement, a purely phenomenological approach was chosen (11.8).

$$\frac{\partial \eta}{\partial t} = \xi\left(\exp\left(f_s^p\right) - 1\right) \tag{11.8}$$

where ξ and p are parameters.

To introduce dependences upon temperature and strain-rate in a combined manner the classical WLF's approach was used to estimate one unique parameter per experimental condition, namely the equivalent strain-rate at a reference temperature (chosen at 130°C), after experimental validation for such a route. It was then chosen to assume that $N_s^{\sim}, N_c^{\sim}, \xi$ and β' depend upon average equivalent strain-rate, according to the same type of equation (11.9).

$$\begin{Bmatrix} N_s^{\sim} \\ N_c^{\sim} \\ \xi \\ \beta' \end{Bmatrix} = \begin{Bmatrix} N_{s0}^{\sim} \\ N_{c0}^{\sim} \\ \xi_0 \\ 1 \end{Bmatrix} + 2\begin{Bmatrix} N_{s1}^{\sim} \\ N_{c1}^{\sim} \\ \xi_1 \\ \beta_1' \end{Bmatrix} \frac{1}{1 + \left(\tau_1\, a_{T/T_0}\, \dot{\varepsilon}\right)^{-2m_1}} + 2\begin{Bmatrix} N_{s2}^{\sim} \\ N_{c2}^{\sim} \\ \xi_2 \\ \beta_2' \end{Bmatrix} \frac{1}{1 + \left(\tau_2\, a_{T/T_0}\, \dot{\varepsilon}\right)^{-2m_2}} \tag{11.9}$$

In parallel to that, as the extensibility of the chains should be partly ruled by the level of cross linkage of the network, α^2 was assumed to be proportional to$N_c^{\sim}$. Finally, p (power of the disentanglement factor), was found to linearly depend upon strain-rate.

Finally, this phenomenological approach, combined with our novel model, allowed reproducing the behaviour of PMMA from 0.01 to 0.0001 s^{-1}, and from 120°C to 150°C (Fig. 11.3a) and potentially from 10^{-6} to 0.5 s^{-1} in terms of equivalent strain-rate at reference temperature. It was also possible, using the same parameters, to reproduce both uploading-unloading and uploading-relaxation experiments (Fig. 11.3b).

In addition, it was possible to reproduce linear visco elasticity as characterised using DMTA analysis, i.e. storage and loss modulus observed for sinusoidal loading at low strain (10^{-3} in Fig. 11.4) using same type of model.

In conclusion, the new model made it possible to reproduce most of the visco-elastic characteristics of a rubbery PMMA and their dependence upon temperature and strain-rate only defining a few number of parameters.

11.5 Conclusion

An new Visco hyperelastic frame in which mechanical behaviour is not decomposed into different components through an "a priori" combination has been developed and validated. In this model inelastic phenomenon derives from the alteration of internal variables related to the microstructure. Inelastic strain-rate is such as energy of the material remains constant, i.e. energy necessary for changes in the microstructure is balanced by the release in elastic energy and other dissipative effects.

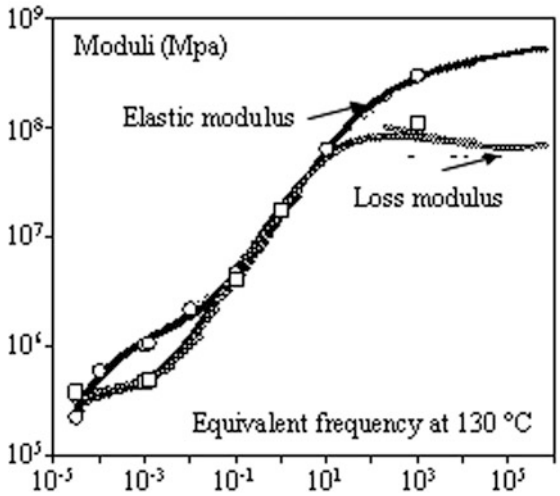

Fig. 11.4 Comparison between model and experimental results. Master curve for the PMMA used in the study. Reference temperature is 130°C; $C_1 = 7.1$; $C_2 = 52.8$. Big symbols (*circle* for elastic modulus, *square* for loss modulus) correspond to calculations with our model

This concept allowed introducing time effects in the rubber elasticity theory, resulting in a visco hyper elastic, visco plastic model consistent with continuum thermodynamics and obeying second principle by construction. The approach has been illustrated with the Edwards Vilgis' theory but could be extended to any other model.

Feasibility of accounting for temperature and strain-rate effects by an "a priori" uses of time temperature superposition principle is clearly demonstrated in this study on the base of a rigorous experimental data base obtained for a PMMA. Further works will be devoted to develop more physically based modelling.

To conclude, the model represents an attractive route for modelling time dependent behaviour of polymers over a wide range of temperature and strain-rate up to of large strains.

Acknowledgements This work was conducted thanks to The European Commission and its support under the Framework 6 Program via the Apt-Pack strep project (STREP 505204-1).

References

1. Chaboche J-L (1997) Int J Solids Struct 34:2239
2. Germain P, Nguyen Q, Suquet P (1983) J Appl Mech 50:1010
3. Arruda E, Boyce M (1993) J Mech Phys Solids 41:389
4. Arruda E, Boyce M, Jayachandran R (1995) Mech Mater 19:193
5. Wu PD, van der Giessen E (1993) J Mech Phys Solids 41:427
6. Septanika EG, Ernst LJ (1998) Mech Mater 30:265
7. Sweeney J (1999) Comput Theor Polym Sci 9:27
8. Ball R, Doi M, Edwards S, Warner M (1981) Polymer 22:1010
9. Edwards SF, Vilgis T (1986) Polymer 27:483
10. Sweeney J, Naz SP, Coates D (2009) J Appl Polym Sci 111:1190
11. Sweeney J, Spares R, Woodhead M (2009) Polym Eng Sci 49:1902
12. Sweeney J, Ward IM (1996) J Mech Phys Solids 44:1033
13. Buckley CP, Jones D (1995) Polymer 36:3301
14. Buckley CP, Jones D (1996) Polymer 37:2403
15. Dooling PJ, Buckley CP, Rostami S, Zahlan N (2002) Polymer 43:2451
16. Gorlier E, Agassant J-F, Haudin J-M, Billon N (2001) Plast Rubber Compos 30:48
17. Sweeney J, Ward IM (1995) J Rheol 39:861
18. Lai D, Yakimets I, Guignon M (2005) Mat Sci Eng A 405:266
19. Drozdov AD, Agarwal S, Gupta R (2004) Comp Mat Sci 29:195
20. Drozdov AD (2006) Compos Sci Technol 66:2648
21. Drozdov AD, de Christiansen JC (2009) Int J Fract 159:63
22. Drozdov AD, de Christiansen JC (2008) Int J Solids Struct 45:4274
23. Drozdov AD, Christiansen J (2009) Int J Solids Struct 46:2298
24. Richeton J, Ahzi S, Vecchio KS, Jiang FC, Makradi A (2007) Int J Solids Struct 44:7938

25. Richeton J, Ahzi S, Daridon L, Rémond Y (2005) Polymer 46:6035
26. Septanika EG, Ernst LJ (1998) Mech Mater 30:253
27. Septanika EG, Ernst LJ (1998) Mech Mater 30:265
28. Baquet E (2011) Ph.D. thesis. Mines-ParisTech, France
29. Billon N (2012) J Appl Polym Sci (in press)

Chapter 12
Solution Approach for Coupled Diffusion-Reaction-Deformation Problems in Anisotropic Materials

R.B. Hall, H. Gajendran, A. Masud, and K.R. Rajagopal

Abstract A capability to model oxidizing carbon-fiber polyimide matrix composites has evolved over the past number of years at Air Force Research Laboratory [1]. Quoting [1] regarding a unidirectional non-woven fibrous layer, without cracks, "The [finite element model] requires mesh sizes in the 1-μm scale and time increments in 1-s steps. A 200-h oxidation simulation with 100-μm oxidation zone size typically requires problem sizes in the order of 100,000 degrees of freedom (DOF) and 720,000 time steps." Because of interest in a number of related problem classes including structural component scales**,** desire to incorporate process restrictions offered by thermodynamics, and the possible involvement of finite deformations, a mixture theory approach was developed by Hall and Rajagopal [2]. The theory is based on two constituents, an anisotropic viscous fluid and an anisotropic hyperelastic solid, which react with each other. The model considers the comparatively simple cases where conversions of species, including the associated masses, linear and angular momenta, energies and entropies, are limited to interchanges between the original fluid and solid.

The theory of [2] can be reduced to seven partial differential equations (PDEs) in the unknown seven components of the fluid and solid velocities and the temperature rate, $(\mathbf{v}^f, \mathbf{v}^s, \dot{\theta})$. The state variables $(\mathbf{F}^s, \rho^f, \rho^s, \theta, \Gamma)$ are the solid deformation gradient, the fluid and solid partial densities, the temperature and the tensorial extent of reaction, the latter reflecting the mass transfer between the constituents as a function of direction in the effective medium. The theory invokes the maximization of the rate of entropy production, which involves a Lagrange multiplier that constrains the entropy production to meet the restrictions imposed by the balance laws of continuum mechanics. Inherent in the described reduction are the following assumptions, which render the Lagrange multiplier a single-valued function of the unknowns and state variables:

1. A single free energy function can replace those of the separate constituents, having separate components governing the individual constituents.
2. Slow diffusion permits neglect of the squared relative kinetic energy terms $\left((\mathbf{v}^f - \mathbf{v}^s) \cdot (\mathbf{v}^f - \mathbf{v}^s)\right)^2$. We retain the dissipation due to the drag force between the constituents, resulting from a combination of viscosity and tortuousity, involving the relative velocity acting through a tensor expressing the drag force.
3. The reaction is slow enough to neglect the squared difference in the chemical potentials of the constituents, and the product of the chemical potential difference with the (unsquared) relative kinetic energy term mentioned previously.

For purposes of developing solution techniques, the system is further reduced to 1-dimension, resulting in three PDEs in the three unknowns $(v_1^f, v_1^s, \dot{\theta})$. It is assumed that the reaction proceeds in the x_1-direction; it is noted that a unidirectional

R.B. Hall (✉)
Materials and Manufacturing Directorate, Air Force Research Laboratory, AFRL/RXBC Bldg 654, 2941 Hobson Way, WPAFB, OH 45433-7750, USA
e-mail: richard.hall@wpafb.af.mil

H. Gajendran • A. Masud
Department of Civil and Environmental Engineering, University of Illinois at Urbana-Champaign, 205 North Mathews Ave, Urbana, IL 61801-2352, USA

K.R. Rajagopal
Department of Mechanical Engineering, Texas A&M University, 3123 TAMU, College Station, TX 77843-3123, USA

B. Antoun et al. (eds.), *Challenges in Mechanics of Time-Dependent Materials and Processes in Conventional and Multifunctional Materials, Volume 2*, Conference Proceedings of the Society for Experimental Mechanics Series 37,
DOI 10.1007/978-1-4614-4241-7_12,

reaction process approximates observations of oxidation in polyimide composites [1]. The following kinematic assumptions are made, where $\mathbf{X}^s$ is the reference position of a solid point, and $\mathbf{x}$ is the present position of a point of the mixture:

$$F^s_{11} = \frac{\partial x_1}{\partial X^s_1} \neq 0, \quad F^s_{iJ} = \frac{\partial x_i}{\partial X^s_J} = 0, \quad iJ \neq 11 \tag{12.1}$$

$$v^f_2 = v^s_2 = v^f_3 = v^s_3 = 0 \tag{12.2}$$

It is additionally assumed that the transverse components of the drag and body forces vanish.

The following Helmholtz free energy function is assumed, which corresponds to the 1-D representation of a transversely isotropic thermoelastic solid permeated by a compressible inviscid fluid which reacts with the solid:

$$\begin{aligned}\Psi[X_1,t] = {} & A^s + (B^s + c^s_2)(\theta - \theta_s) - \frac{c^s_1}{2}(\theta - \theta_s)^2 - c^s_2\theta \ln\left(\frac{\theta}{\theta_s}\right) + \frac{1}{\rho^s_R}\left\{\frac{k^f_1}{q}\theta^p\left(\rho^f\right)^q + k^f_2\rho^f\right\} \\ & + \frac{\rho^s}{\rho}\frac{1}{\rho^s_R}\left\{\begin{array}{l}\frac{1}{2}(\lambda^s_R - \lambda^s_\theta\theta/\theta_R) + (\mu^s_{TR} - \mu^s_{T\theta}\theta/\theta_R) + (\alpha^s_R - \alpha^s_\theta\theta/\theta_R) \\ \quad + 2\left[(\mu^s_{LR} - \mu^s_{L\theta}\theta/\theta_R) - (\mu^s_{TR} - \mu^s_{T\theta}\theta/\theta_R)\right] + \frac{1}{2}(\beta^s_R - \beta^s_\theta\theta/\theta_R)\end{array}\right\}(E^s_{11})^2 + \Lambda\end{aligned} \tag{12.3}$$

where Λ, given below, is a functional that reflects the influence of chemical dissipation on the free energy, see [2]; $\mathbf{\Gamma}^0$ is the extent of reaction referred to the reference configuration; p and q are empirical exponents; $\mathbf{E}^s$ is the solid Lagrangian strain; $\rho = \rho^f + \rho^s$ is the mixture density; and additional symbols are constants. (It is observed that the effective 1-D constants are substantially fewer in number than those displayed, which result from reduction of a transversely isotropic model.) Λ incorporates into the free energy a coupling of the solid strain and extent of reaction, as well as the rate of reaction. In 1-D the expression reduces to ($\bar{K}_1$ and $\overline{A}^{0\Gamma}_{1111}$ are constants):

$$\Lambda = \int \frac{\mu}{2}\{(\Gamma^0_{11})^2\bar{K}_1 E^s{}_{11} + 2\dot{\Gamma}^0_{11}\overline{A}^{0\Gamma}_{1111}\}d\Gamma^0_{11} \tag{12.4}$$

For the 1-d deformation, for the case of $\rho^f << \rho^s$, with $\mathbf{B}^s$ the left Cauchy-Green tensor of the solid, the solid and fluid stresses are approximated by:

$$\begin{aligned}\mathbf{T}^s \approx {} & \frac{\rho^s}{\rho^s_R}\left(\frac{1}{2}\{(\lambda^s + 2\mu^s_T + \alpha^s)(B^s_{11} - 3) + 4\mu^s_T + (\alpha^s + \beta^s + 4(\mu^s_L - \mu^s_T))(B^s_{11} - 1)\} + \rho\frac{\partial\Lambda}{\partial E^s_{11}}\right)B^s_{11}\mathbf{e}_1 \otimes \mathbf{e}_1 \\ & - \rho\rho^s\frac{\partial\Lambda}{\partial\rho^s}\mathbf{I}\end{aligned} \tag{12.5}$$

$$\mathbf{T}^f \approx -\frac{\rho}{\rho^s_R}\left(k^f_1\theta^p(\rho^f)^q + k^f_2\rho^f\right)\mathbf{I} - \rho\rho^f\frac{\partial\Lambda}{\partial\rho^f}\mathbf{I} \tag{12.6}$$

The full field theory has been developed in 1-d, and specific cases will be illustrated.

References

1. Schoeppner G, Tandon GP, Pochiraju K (2008) In: Kwon Y, Allen D, Talreja R (eds) Multiscale modeling and simulation of composite materials and structures, Predicting Thermooxidative Degradation and Performance of High-Temperature Polymer Matrix Composites. Springer, New York, pp. 359–462. doi: 10.1007/978-0-387-68556-4_9
2. Hall RB, Rajagopal KR (2011) Diffusion of a fluid through an anisotropically chemically reacting thermoelastic body within the context of mixture theory. Math Mech Solids. MMS407754 Online First 21 Jun 2011. doi: 10.1177/1081286511407754

Chapter 13
Effect of Crushing Method of Wasted Tire on Mechanical Behavior on PLA Composites

Takenobu Sakai, Takuya Morikiyo, C.R. Rios-Soberanis, Satoru Yoneyama, and Shuichi Wakayama

Abstract Poly Lactic Acid (PLA) is one of the Biodegradable Materials which has excellent mechanical properties. However, PLA is not wasted for the structural materials because of its brittleness. For improvement in the brittleness, the wasted tire was chosen as the reinforcement. On the other hand, wasted tires are a huge problem in terms of health and contamination due to bad disposal. There are many mechanisms to deal with this problem but they still have inconveniences. In this study, we made the wasted tire powder reinforced PLA. The wasted tire powder was crushed by two ways. One is frost shattering method, and the other is thermal shock process. The composites based on PLA were made with these two powders. To investigate the effect of crush method of wasted tire, fracture mechanics were investigated. And the viscoelastic behavior was investigated with the Dynamic Mechanical Analysis. And for impact tests, Split Hopkinson Pressure Bar tests were carried out. As the results of static and impact test, thermal shocked powder composites have the good impact resistance.

Keywords Wasted tire • PLA • Composite • Visco-elasticity • Split Hopkinson pressure bar • Dynamic mechanical analysis

13.1 Introduction

From some decades ago, people were concerned that landfills were rapidly filling to the brim with smelly disposable diapers and plastic junk. There seems to be less public debate on this today, but is assumed that the landfill issue remains largely unresolved. In recent years, much attention has been focused on biodegradable and biocompatible polymers particularly from an ecological point of view. The mechanical properties and degradation rates of biodegradable polymers, in general, depend on their morphology or crystallinity as well as on their chemical structures [1].

Research in biodegradable polymers has gained considerable momentum in recent years due to the increasingly attractive environmental, biomedical and agricultural applications. Current commercial biodegradable polymers are predominantly limited to aliphatic polyesters, polyethers, poly(viny1 alcohol) and polysaccharides. Among these, the more important synthetic biodegradable polymers are aliphatic polyesters, such as polylactic acid (PLA), polyglycolic acid (PGA), poly (c-caprolactone) (PCL) and poly(hydroxy butyrate)(PHB) [2].

PLA is an important biopolymer with a great future. It can be extruded, molded and can also be oriented biaxially. All the processes used for thermoplastics can be essentially used for processing of PLA. However, processing of PLA has certain inherent problems. PLA picks up ambient moisture very rapidly and most of the problems experienced on PLA arise from inadequate drying. Hence, PLA is required to be properly dried before processing. Because it is a condensation polymer, presence of even a very small amount of moisture during melt processing cause degradation of polymer chains and loss of molecular weight and mechanical properties.

T. Sakai (✉) • S. Wakayama
Tokyo Metropolitan University, 1-1, Minami-Osawa, Hachioji, Tokyo 192-0397, Japan
e-mail: t-sakai@tmu.ac.jp

T. Morikiyo • S. Yoneyama
Aoyama Gakuin University, 5-10-1, Fuchinobe, Chuo-ku, Sagamihara, Kanagawa 229-8558, Japan

C.R. Rios-Soberanis
Unidad de Materiales, Centro de Investigación Científica de Yucatán, México, Mexico

B. Antoun et al. (eds.), *Challenges in Mechanics of Time-Dependent Materials and Processes in Conventional and Multifunctional Materials, Volume 2*, Conference Proceedings of the Society for Experimental Mechanics Series 37,
DOI 10.1007/978-1-4614-4241-7_13,

PLA has received much attention in recent years. They are synthesized from renewable resources and are biodegradable. They are degraded by hydrolytic cleavage of the ester bonds to give lactic acid and its low molecular weight oligomers, which can be metabolized by both soil and marine organisms [3]. PLA is synthesized from either lactic acid or its cyclic dimer and is a biodegradable and biocompatible thermoplastic with a melting point around 180 ºC [4]. When exposed to elevated temperatures, PLA is known to undergo thermal degradation, leading to the formation of lactide monomers. It has been suggested that this property may be leveraged for the feedstock recycling of PLA [5].

From the environmental viewpoint, the compostable characteristics of PLA are well suited for many applications where recycling, reuse and recovery of products are not feasible. Since the raw materials for PLA is based on agricultural feedstock, the increased demand for PLA resins will create a positive impact on the global agricultural economy. Nevertheless, there are a number of areas which still need to be improved, especially in applications where PLA is intended to be used as a substitution for existing thermoplastics.

Blends of PLA with various non-degradable polymers have been investigated [6–8]. Some of these blends were found to be immiscible, resulting in fairly poor mechanical properties [9]. To improve the properties of these biodegradable polymers, blending and copolymerization techniques are extremely promising approaches. Additionally PLA has been used as polymeric matrix in composite materials to develop partially biodegradable materials.

Used tires are a major problem in the world. Used tires that have completed their functional life cannot be used on automobiles again. Until recently, they were either buried with other industrial waste in landfill sites or stockpiled in huge dumps that could easily contain millions of tires [10, 11].

When piled, the tires attract rodents and some dangerous reptiles and also create stagnant pools of water, which create the breeding grounds for mosquitoes. If the tire piles catch fire they are virtually impossible to put out. As they burn, the fire emits a rank smell and toxic fumes. Their indiscriminate disposal causes blocking of drainage resulting in urban flooding during the raining season [12, 13].

Currently, there are several means of recovery: reuse, rethreading, recycling, landfill engineering and energy recovery. The scientific community's efforts in finding ways to reduce tire waste has leaded to intense research on rubber that includes the possibility of applying it in concrete, filler in natural rubber vulcanizates and blends with polymers [13–15].

Elastomeric part of the tire has been also analyzed and its powder was used to elaborate composite materials with good mechanical properties [16]. It is an important issue to create new techniques to reuse waste materials such as tires. Tires are classified as thermosetting materials since they present a high degree of crosslink that provide them of great resistant. However they cannot be transformed to be used again. Therefore an option is to be used as fillers in the elaboration of tough materials, conductive materials or semidegradable composites.

In this study, wasted tire and PLA were used to develop new materials such as high-impact composites. There are two types of wasted tire powders as thermal shocked powder and frost shattered powder. The mechanical tests, such as DMA, tensile test and Hopkinson bar impact test were carried out to characterize these materials and to evaluate the impact resistance of each composite.

13.2 Materials

Wasted tire and PLA resin were used to make the composites. PLA resin (PLA polymer 2002D) was made by Cargill Dow LLC. PLA was dried in the oven for 2 h at 70°C. The wasted tire was obtained from Mexican government, and they were powdered with two ways as thermal shock process and frost shattering method. Methodology for tire reduction by thermal and frost shattering techniques consist in applying a rapid change of extreme temperatures in short time as an alternative process for reducing size particles in elastomeric pieces by the following stages:

1-a) Thermal shocked tire reduction
Small elastomeric pieces from tire were placed into a crucible and then heated in a furnace at 400°C during 10 min. After the heating, samples are immersing immediately into liquid nitrogen (N2) for 15 min. When N2 is vaporized completely, residues are pulverized manually in a pestle.

1-b) Frost shattered tire reduction
Small elastomeric pieces from tire were placed into liquid nitrogen (N2) for 5 min and then tire was mixed with rotary blades.

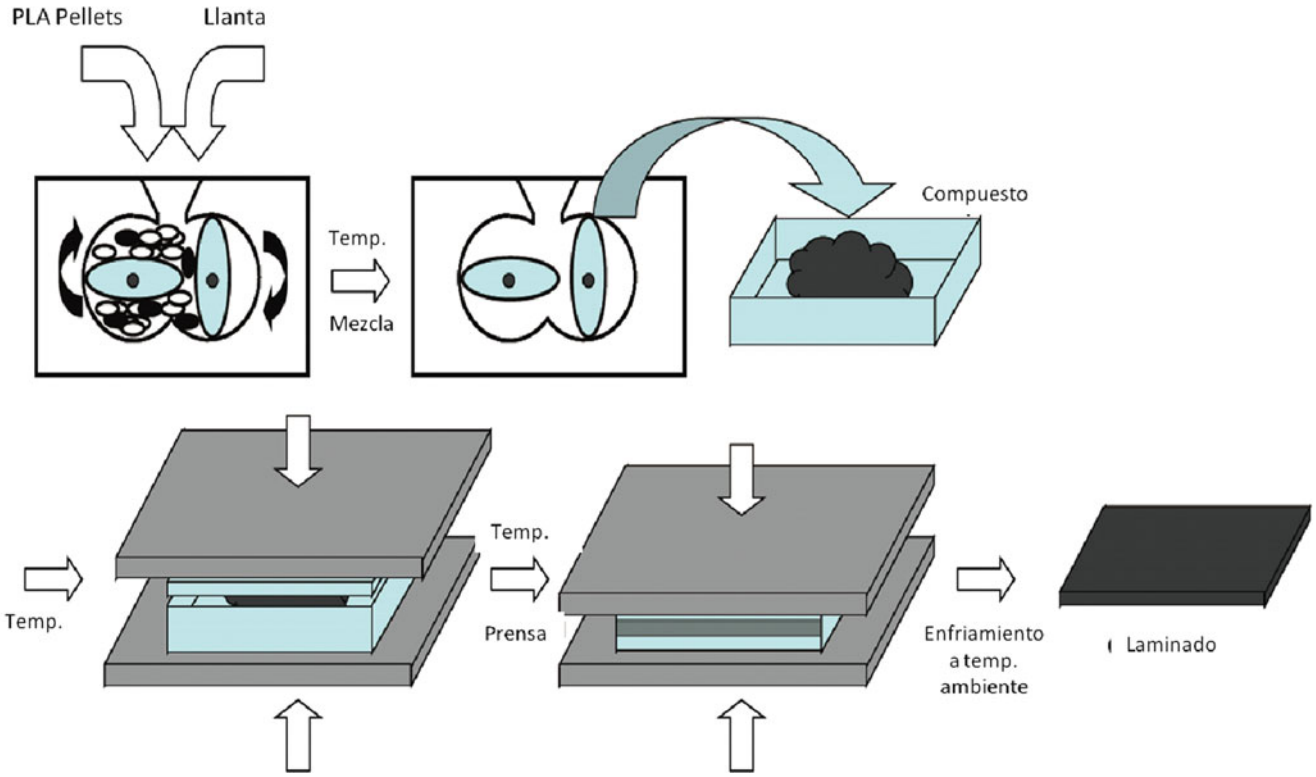

Fig. 13.1 Schematic drawing of b lending of the composite and lamination

2) Powder is obtained and then used to elaborate the composite materials in the brabender 60 cc mixer.
Blends concentrations are shown in Fig. 13.1 that presents the schematics of the mixing and lamination processes. The composite material obtained from the mixing machine is completely amorphous and homogeneous. It was observed a good dispersion of the filler (wasted tire) into the polymer matrix (PLA). Formulations of the composite material were 10, 20 wt.% of filler.

3) The composite materials were placed in a mold to be pressed in order to get laminas.
Composite formulations from 10 and 20 wt.% followed the established process for making the laminas. Coupons were obtained from these laminas to be characterized mechanically. The dimension of specimens is 130 × 15 × 4 (mm).

The specimens for Dynamic Mechanical Analysis (DMA) and tensile test were obtained from these laminas. The specimens for Split Hopkinson Pressure Bar tests were placed in the special mold to be pressed.

13.3 Experimental Conditions

To understand the viscoelasticity of materials, Dynamic Mechanical Testing was carried out with the Rheometrics Solid Analyzer RSA II (Rheometric Scientific Co., Ltd.). RSA II characterizes the viscoelastic properties of solid materials. In this study, the 3-point bending method was used. A servo motor applies an oscillatory strain to the test specimen, and a transducer measures the force required to effect the applied deformation. Heat gun controls the temperature in the environmental chamber through forced convection of either vapor evaporating from liquid nitrogen or air passing over a heating element. We performed strain, temperature, and frequency sweeps. We selected a strain (0.001) such that the specimens deformed within the linear viscoelastic range. The temperature sweep tests varied T between 25 and 45°C (under T_g) on frequencies of from 0.1 to 10 rad/s. stepping the temperature upwards in increments of 5°C. And thermal soaking

times of 3 and 6 min (for temperatures above and below ambient) minimized the effects of thermal transients. The dimension of the specimen is 52 × 10 × 2 mm.

Tensile tests were carried out with the universal testing machine (Servo Pulsar, Shimadzu Co., Ltd.) at room temperature, and crosshead speed was 0.5 mm/min. Strain gage was attached on the middle of specimen. The dimension of the specimens is 13 × 75 × 3 mm.

To understand the effect of strain rate on the specimens, Split Hopkinson Pressure Bar tests were carried out. The dimension of the specimen is Φ14 × 21 mm, and the dimensions of the input and output bars are Φ16 × 2,000 mm. Strain gages were attached at the middle of input and output bars. The materials of input and output bars are S45C, and the lateral wave speed is 5,150 m/s.

13.4 Results of Dynamic Mechanical Analysis

To know the basic visco-elastic behavior, we carried out the dynamic mechanical testing. We measured the phase lag of the input and the response of strain and stress, and the tan δ was calculated by storage modulus E' and loss modulus E'' by following equation.

$$E' = \frac{\sigma}{\varepsilon_0} \cos\delta \tag{13.1}$$

$$E'' = \frac{\sigma}{\varepsilon_0} \sin\delta \tag{13.2}$$

$$\tan\delta = \frac{E'}{E''} \tag{13.3}$$

where, E' is storage modulus, E'' is Loss modulus, E^* is complex modulus, δ is phase difference and tan δ is loss tangent. And, tan δ shows the amount of energy absorption. Figure 13.2 shows the results of tan δ of each specimen at 30°C. On low angular speed, frost shattered powder composite have high tan δ values, but on high angular speed, they have low tan δ values. And the other materials have similar tendency as frost shattered powder composite. That is, tan δ has the dependency on the angular speed on dynamic mechanical analysis. However, tan δ of 20% of thermal shocked powder composite shows little dependency on the angular speed. Therefore, 20% of thermal shocked powder composite has good capacity for the energy absorption at 30°C.

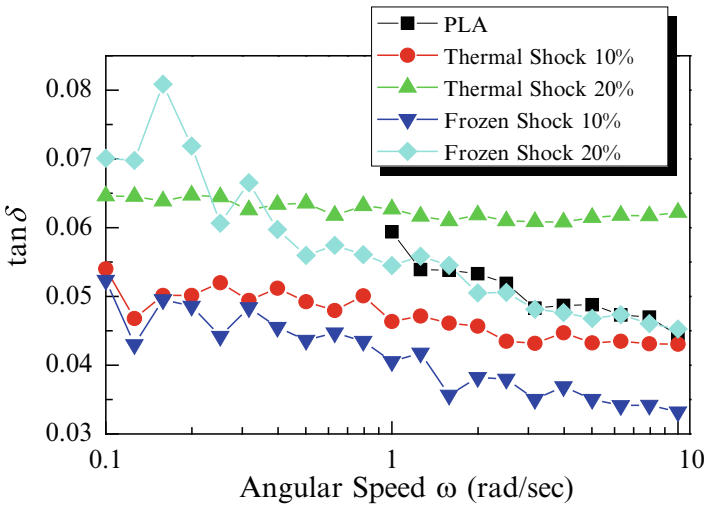

Fig. 13.2 tan delta of PLA and wasted tire composites at 30°C

13.5 Tensile Properties of Composites

To understand the basic mechanical properties of the materials, tensile tests were carried out. Figure 13.2a shows the Stress-Strain diagram of thermal shocked powder composites, and Fig. 13.2b shows the S-S diagram of frost shattered powder composites. As shown in Fig. 13.2a, Young's moduli and tensile strength were decreased with increasing powder contents.

Thermal shocked powder worked as filler of the materials. However, the tensile strain of composites were increased with addition of the powder. Therefore, thermal shocked powder makes the composite more ductile. And as shown in Fig. 13.2b, frost shattered powder worked as filler, too. The difference between thermal shocked powder composite and frost shattered powder composited was observed in the maximum tensile strain (Fig. 13.3).

13.6 Split Hopkinson Pressure Bar Test

To consider the impact resistance, Split Hopkinson Pressure Bar tests were carried out. Figure 13.4 indicates the typical oscilloscope records from the impact tests. The top trace gives the incident and reflected strain pulses, and the bottom trace gives the transmitted strain pulse. As shown in this graph, the output bar's response is much smaller than input bar's. The similar tendencies were observed on the other materials. Especially, frost shattered powder composites shows more decrease in the output bar's response. This is because that the specimens absorbed the energy when the materials were failure.

And the S-S diagrams were shown in Fig. 13.5. PLA resin and thermal shocked powder composites show the same S-S behavior, but frost shattered powder composite show smaller strength than the other materials. These are same results as static tensile behavior.

When thermal shocked powder was made, it was heated at 400°C and then degraded by heat treatment. However, frost shattered powder was not affected the heat treatment, and frost shattered powder still has the tire (rubber) properties. On the static and impact tests, the frost shattered powder behaved as the pore because tire's properties were very poor. Therefore, the static and impact strength are lower than other materials.

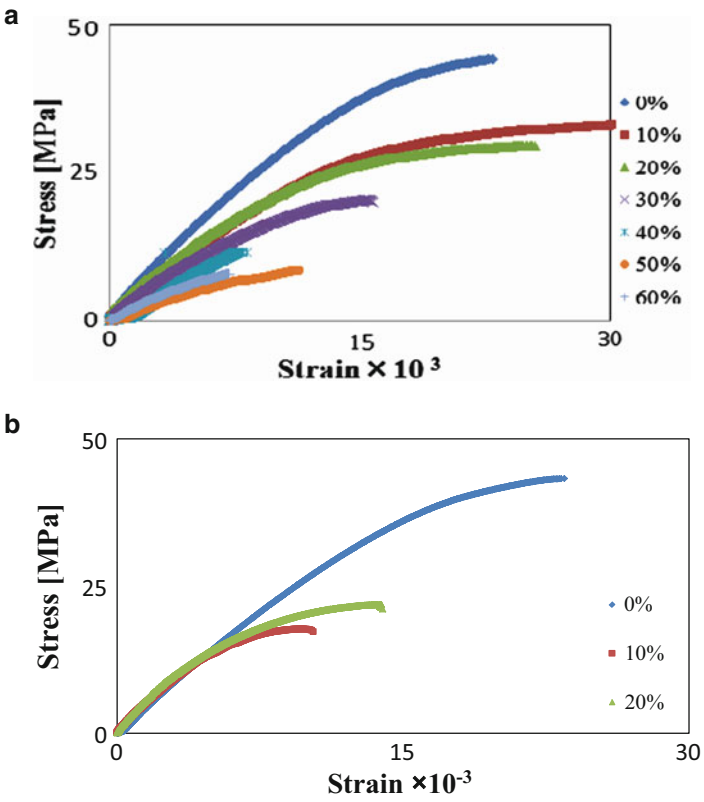

Fig. 13.3 S-S diagrams of (**a**) thermal shocked powder composite and (**b**) frost shattered powder composite

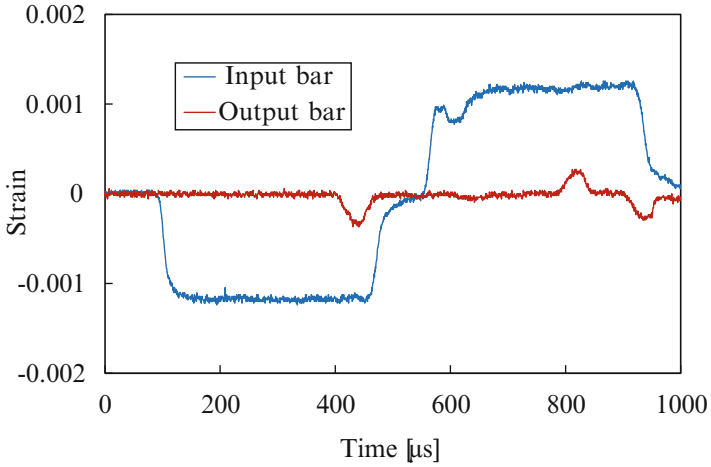

Fig. 13.4 typical oscilloscope records from Split Hopkinson Pressure Bar tests (PLA resin)

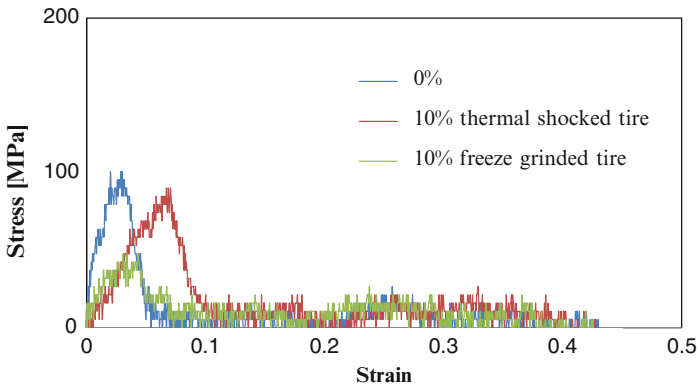

Fig. 13.5 Strain-strain diagram in high strain rate

Table 13.1 Relationship between static strength and strength at high-strain rate

		Static strength (MPa)	Strength at high-strain rate (MPa)	Ratio between static and impact tests
PLA resin	0%	42.2	100.9	2.40
Thermal shocked method	10%	34.4	90.3	2.63
	20%	30.0	–	–
Frost shattering method	10%	21.2	47.8	2.27
	20%	17.6	37.18	2.19

13.7 Evaluation of Impact Resistance

As the results of DMA, thermal shocked powder composite has good ability for energy absorption. To evaluate the impact resistance of the materials, the strain rate dependency for the materials' strength was discussed. Generally, the material with larger strain rate dependency on the mechanical strength has the good impact resistance. In this study, we compared about the strain rate dependency on the strength. Table 13.1 shows the static strength, the strength at high-strain rate and the ratio of static and strength at high-strain rate.

Thermal shocked powder composite's value is higher than the other materials. This value shows the impact resistance, therefore, Thermal shocked powder composite seems to be the highest-impact resistance.

13.8 Conclusions

In this study, it came to be able to make two types of composites using wasted tire and PLA resin. One is thermal shocked powder composite, and the other is frost shattered powder composite. And the static tensile, dynamic mechanical analysis and Split Hopkinson Pressure Bar tests were carried out to evaluate the ability for impact response of the composites. As the results of these tests, it was cleared that thermal shocked powder composites have the highest impact resistance.

References

1. Miyata T, Masukobohse T (1998) Crystallization behaviour of poly(L-lactide). Polymer 39(22):5515–5521
2. Wang L, Ma W, Gross RA, McCarthy SP (1998) Reactive compatibilization of biodegradable blends of poly(lactic acid) and poly (ε-coprolactone). Polym Degrad Stab 59:161–168
3. Zhang L, Goh SH, Lee SY (1998) Miscibility and crystallization behaviour of poly(L-lactide)/poly(p-vinylphenol) blends. Polymer 39 (20):4841–4847
4. Oshkoshi I, Abe H, Doi Y (2000) Miscibility and solid-state structures for blend of poly[(S)-lactide] with atactic poly[(R, S)-3-hydroxybutyrate]. Polymer 41(22):5985–5992
5. Lim T, Auras R, Rubino M (2008) Processing technologies for poly(lactic acid). Prog Polym Sci 33:820–852
6. Nijenhuis AJ, Colstee E, Grijpma DW, Pennings AJ (1996) High molecular weight poly(l-lactide) and poly(ethylene oxide) blends: thermal characterization and physical properties. Polymer 37:5849
7. Ogata N, Jimenez TJ (1997) J Polym Sci, Part B: Polym Phys 35:389
8. Zhang L, Goh SH, Lee SY (1998) Polymer 39:4841
9. Martin O, Averous L (2001) Poly(lactic)acid: plasticization and properties of biodegradable multiphase systems. Polymer 42:6209–6216
10. Shih CJ (1995) Chain-end scission in acid catalyzed hydrolysis of poly(D, L-lactide)in solution. Control Release, Journal of controlled Release 34(1):9–15
11. Colom X, Carrillo F, Canavate J (2007) Composites reinforced with reused tyres: surface oxidant treatment to improve the interfacial compatibility. Compos Part A 38:44–50
12. Aisien FA, Hymore FK, Ebewele RO (2003) Potential application of recycled rubber in oil pollution control. Environ Monit Assess 85:175–190
13. Dierkes WK (2003) Rubber recycling. In: Pandalai SG (ed) Recent research developments in macromolecules, vol 7. Research Signpost, Trivandrum, pp 265–292
14. Bucknall CB (1997) Toughened plastics. Applied Science Publishers, London
15. Kim JI, Ryu SH, Chang YW (2000) Mechanical and dynamic mechanical properties of waste rubber powder/HDPE composite. J Appl Polym Sci 77:2595–2602
16. Mis-Fernandez R, Azamar-Barrios JA, Rios-Soberanis CR (2008) Characterization of the powder obtained from wasted tires reduced by pyrolysis and thermal shock process. J Appl Res Technol 6(2):95–105

Chapter 14
Characteristic Length Scale Investigation on the Nanoscale Deformation of Copper

Joshua D. Gale and Ajit Achuthan

Abstract Variation in the mechanical properties of copper subjected to severe plastic deformation (SPD) is studied experimentally to understand the mechanics of nanoscale deformation. By varying the parameters of SPD process, a set of samples with different levels of damage associated with plastic deformation is obtained. The distribution of the evolving structural features, and possibly its type and nature, may vary according to the amount of damage induced in the sample. The various levels of damage is introduced by varying the duration of electrochemical polishing on mechanically polished samples and also by using surface mechanically attrition treatment (SMAT) technique. Mechanical properties such as microhardness and nanohardness are then obtained in the sample surface. The surface deformation behavior near the indent is also characterized by optical imaging. Based on the experimentally obtained correlations, the characteristic length scale of deformation associated with indentation is discussed.

14.1 Introduction

Mechanical deformation history depending on its severity has a large impact on the properties of metal. Certain techniques such as severe plastic deformation (SPD) have been shown to cause nanorecrystallization [1] and there is evidence to suggest that the deformation mechanisms such as polishing also introduce microstructural changes [2, 3]. This change in microstructure has been shown to lead to an increase in desirable properties of the material such as hardness, strength, and toughness [4]. The large number of nanograins and grain boundaries inhibit the movement of dislocations, and at low temperatures this strengthens the material. Through the use of various instruments such as micro and nanoindenters it is possible to determine this material property change at the appropriate scale.

Indentation size effect (ISE) is an interesting phenomenon were the hardness of a material increases as the indentation load is decreased. ISE has been widely theorized as being the result of geometrically necessary dislocations (GND) [5]. The size effect has been correlated with the characteristic length scale associated with the indentation testing, such as the sample grain size, sample thickness size as in thin films and indentation probe size. At the same time, some studies have attributed the increase in hardness to certain other phenomena such as the effect of mechanical polishing and surface roughness [6].

The present study investigates the effect of deformation history on the hardness of copper through the use of two different length scale instruments. Electrochemical polishing yielded the ability to control the thickness of a mechanically deformed layer by varying the electrochemical polishing duration. Analysis of its properties at varying length scales were then studied with both micro and nanoindentation testing. In addition, the interaction between a SPD produced deformation layer and a polishing produced deformation layer were also studied. A SPD process called Surface Mechanical Attrition Treatment (SMAT) [7, 8] is used in this study. SMAT is accomplished by impregnating kinetic energy by shot peening on the sample surface. The cross-section of SMAT sample is expected to have a gradient in grain sizes and the amount of residual stress through the thickness.

Initial results show the correlation between mechanical polishing and increased hardness readings at both the micro and nanoscales. The difference in hardness behavior observed between micro-indentation and nanoindentation measurements

J.D. Gale • A. Achuthan (✉)
Department of Mechanical & Aeronautical Engineering, Clarkson University, Potsdam, NY 13699, USA
e-mail: aachutha@clarkson.edu

B. Antoun et al. (eds.), *Challenges in Mechanics of Time-Dependent Materials and Processes in Conventional and Multifunctional Materials, Volume 2*, Conference Proceedings of the Society for Experimental Mechanics Series 37,
DOI 10.1007/978-1-4614-4241-7_14,

has also been correlated with the length scale associated with these measurements. Significant difference in the deformation behavior in terms of the density of slip planes on the surface near the intents between the regions those hardened by SMAT and those are relatively far away from the SMAT surface were also observed.

14.2 Experiment

Bar Stock of 25.4 mm diameter 99.99% alloy 101 Copper Alloy was utilized in all cases. The bar was cut into 6 mm pucks, polished and then annealed in a vacuum furnace at 700°C for 1 h. Polishing consisted of varying grits of silicon carbide paper, 120, 340, 800, and 1200 grit respectively. After rough polishing, samples were diamond polished with a 3 and 1 um Buehler Meta-Di diamond suspension. Annealing removed the effects of polishing and any prior mechanical deformation, as well promoted grain growth up to an average size of 100 um. Two sets of samples were then created to study the effect of nanoscale deformation.

14.2.1 Mechanically Polished Sample Preparation

Annealed samples described previously were exposed to various polishing levels. Two samples were used for repeatability at each level of polishing. To establish a base condition of existing deformation all samples were first rough polished using the earlier regime and fine polished with a 3 and 1 micron diamond suspension. Electrochemical polishing was then utilized and time was varied as the independent variable. The samples were categorized according to their immersion time in an 85% ortho-phosphoric acid bath with a steady state voltage of 1.5 V and a bath temperature of −10°C. Removal rate of material in the bath was very low due to the high viscosity and resistance of the acid, so immersion times ranged from 30 to 900 min. The longer time periods experiencing the largest amount of material removed. The time segments used were 30, 60, 180, 480, and 900 min, respectively. After immersion each sample was immediately dipped in distilled water and cleaned with methanol to prevent post immersion etching.

14.2.2 SMAT Treated Sample Preparation

Post annealed samples were subjected to Surface Mechanical Attrition Treatment (SMAT) for 15 min. The SMAT process was accomplished by using a dome shaped vacuum sealed refractory chamber attached to a Labworks Inc. LW-139-40 Electrodynamic Shaker System [9]. Each sample was clamped into the top of the dome refractory chamber and impacted with ten 6 mm tungsten carbide balls at a frequency of 31 Hz. Further details on the SMAT process have been documented in a previous article [9]. Tungsten balls were used in order to deter mechanical alloying of the balls into the specimen. After treatment the samples were cross sectioned using a Buehler Isomet low speed saw with an HC 50 diamond wafering blade. Each cross section was then placed in an epoxy resin and polished using the same technique as in the pre annealed state. Electrochemical polishing was then utilized to remove unwanted effects from mechanically polishing the sample as discussed for the non-SMAT samples. Again, the duration of electrochemical polishing was varied to analyze its effects on indentation results.

14.2.3 Sample Testing

Microindentation test was used to examine the effect of hardness due to the polishing deformation layer, through the use of a LECO M-400 Microindenter with a Knoop tip. A 25 indent rectangular pattern was used on the mechanically polished samples. Whereas, the SMAT cross section samples were indented 50 times in a vertical pattern perpendicular to the treated edge. The indents were produced with a force of 200 gf and a hold time of 15 s to account for thermal expansion and creep. Post micro indentation samples were examined with an Olympus PME optical microscope and Joel SEM for slip line characterization.

Nanoindentation was carried out on the same samples that microindentation had been performed on. A Hysitron Triboindenter 950 nanoindenter was used for indentation along with a Berkovich 150 nm tip. The mechanically polished samples were indented with a 50 indent rectangular pattern on the polished face. The SMAT cross section of each sample was indented a total of 50 times in a vertical pattern oriented laterally from the SMAT treated edge towards the interior untreated edge. Each indent lasted 45 s with a 5 s hold time to account for creep and thermal expansion. This process was repeated three times on each sample for validation of consistent results.

14.3 Results and Discussion

14.3.1 Non-SMAT Samples

Change in micro-hardness with electro chemical polishing duration is shown in Fig. 14.1. Around 25 indents were made on each sample, and the indent number is shown as the x-axis to give an idea of variability in hardness from indent to indent. The annealed sample has an average hardness of around 25 Kg/mm^2, while polishing increased hardness on the surface to an average of 45 kg/mm^2. Thirty minutes of electrochemical polishing didn't produce any significant change in hardness. However, significant hardness change was observed when electrochemical polishing duration reached 60 min. The change in hardness achieved was not as significant for 120 and 180 min of elector-polishing when compared to 60 min. Further reduction in hardness was observed for samples with 480 min of electrochemical polishing. Though significant reduction is obtained with 480 min of electro-polishing, these values were still significantly higher than the hardness of the annealed samples.

The behavior of hardness variation with electro-polishing duration under nanohardness testing showed overall the same trend as in microhardness testing (Fig. 14.2). A nanohardness value of approximately 0.85 GPa was obtained for annealed samples which was increased to approximately 2.0 GPa due to mechanical polishing. Interestingly, this increase in hardness, about 135%, is much larger than increase in hardness obtained in micro-hardness testing, which was about 80%. Similarly, the significant reduction in hardness obtained in samples with 60 min of electrochemical polishing for microindentation was not observed with the nanoindentation. Further increase in electrochemical polishing duration did show continuous reduction of nanohardness with duration. Again, the nanohardness value of about 1.3 GPa obtained for samples subjected to 480 min of electro-polishing was significantly higher than that of the annealed samples by about 53%.

The hardness values of the samples that were annealed after introducing mechanical polishing and various levels of electro-polishing are shown in Figs. 14.3 and 14.4. The hardness values of these annealed samples, which are very close to the original annealed values, show that the plastic deformation can be removed irrespective of various conditions of polishing these samples had before annealing.

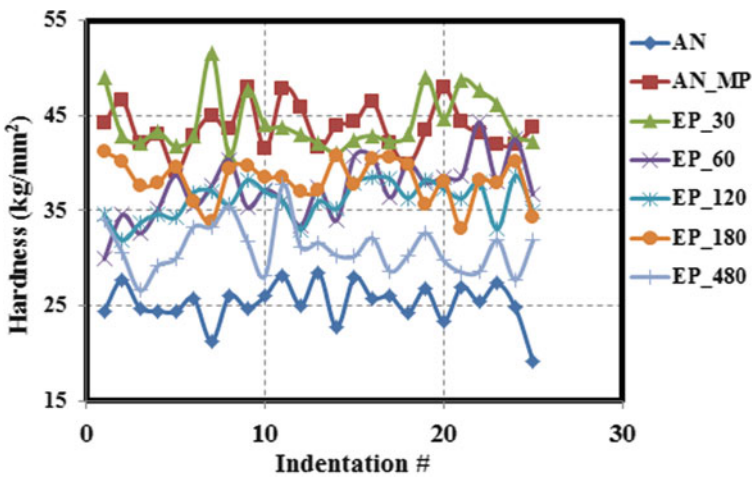

Fig. 14.1 Knoop hardness results of micro indentation on samples subjected to various durations of electrochemcial polishing. Data is shown for about 25 indents in each case. As the duration of electro-polishing increases the hardness value decreases from around 45 kg/mm^2 corresponding to mechanically polished sample

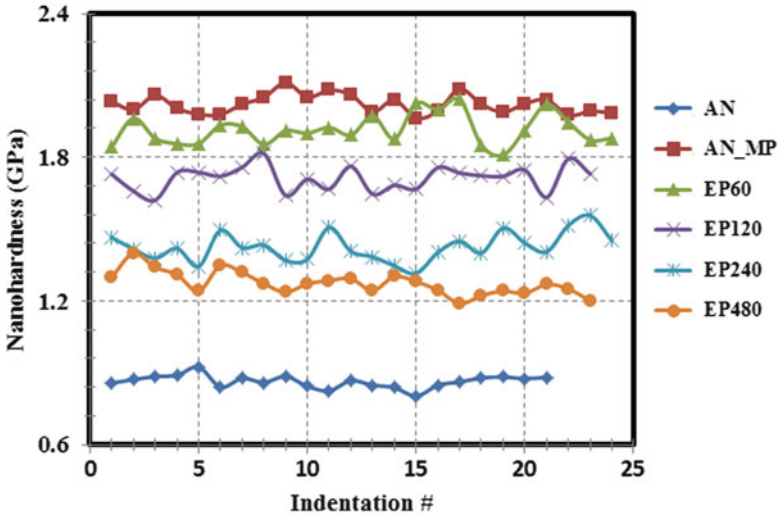

Fig. 14.2 Nanoindentation hardness results on samples subjected to various durations of electro chemical polishing. Data is shown for around 25 indents in each case. As the duration of electro-polishing increases the hardness value decreases from around 2.04 kg/mm^2 corresponding to mechanically polished sample

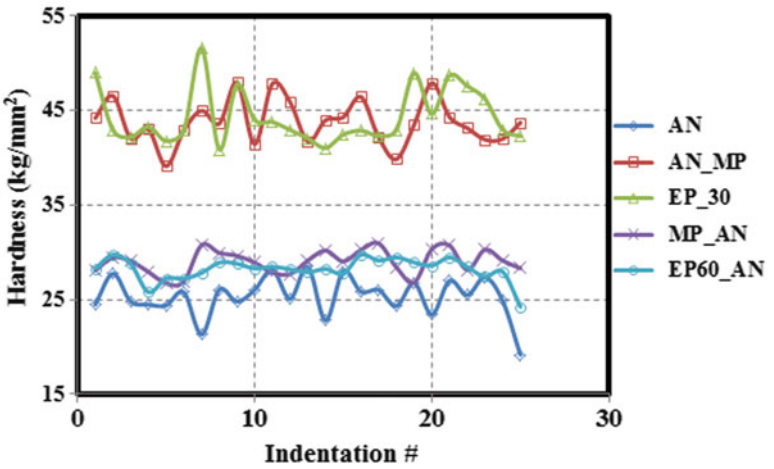

Fig. 14.3 Knoop hardness values of samples annealed after various levels of electro chemical polishing. The results show that the mechanically induced plastic deformation is completely removed due to annealing

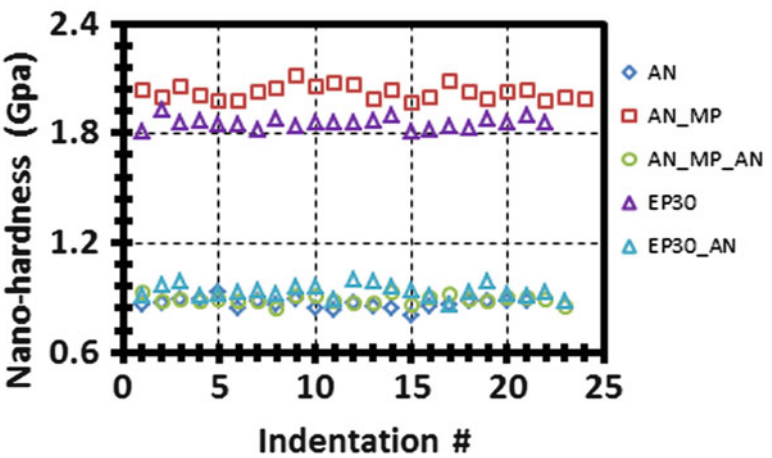

Fig. 14.4 Nanoindentation hardness values of samples annealed after various levels of electrochemical polishing. The results show that the mechanically induced plastic deformation is completely removed due to annealing

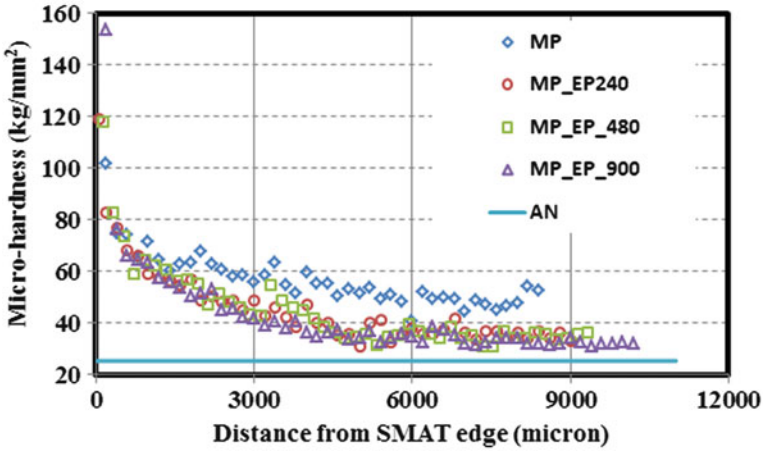

Fig. 14.5 Knoop hardness on the cross section of copper sample subjected to various conditions of polishing. Hardness on SMAT sample decrease with the increase in the distance from the SMAT edge of the sample

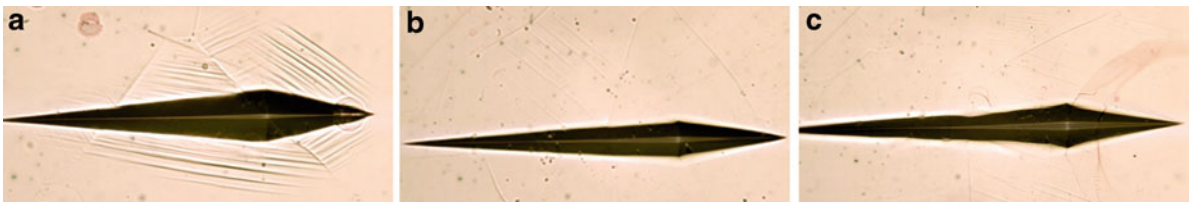

Fig. 14.6 Optical images of the indents from the microindentation testing (**a**) near SMAT surface, (**b**) away from the SMAT surface and (**c**) annealed (non-SMAT) sample

14.3.2 SMAT Samples

The micro-hardness values measured at the cross-section of SMAT samples were plotted against its distance from the SMAT edge as shown in Fig. 14.5. The hardness values of these samples increased significantly when compared to annealed samples. As expected increase in hardness is very high near the SMAT edge, as high as 155 kg/mm^2, which is about 520% increase in hardness. However, as distance from the SMAT edge increases this increase in hardness decreases exponentially, with the majority of the reduction observed in the first 1 micron distance, followed by a gradual reduction between 1 micron and 5 micron distances from the SMAT edge. The hardness of the mechanically polished samples that were not electro-polished reduced to a value of 45 to 50 kg/mm^2 approximately at locations beyond 5 micron distance from the SMAT surface. This value is comparable to the hardness obtained in the mechanically polished non-SMAT samples. As the samples were electrochemically polished the hardness values closer to the SMAT surface increased dramatically, while those away from the SMAT surface decreased moving closer and closer to the annealed hardness values. The samples with 900 min of electrochemical polishing resulted in a hardness of approximately 30 kg/mm^2, compared to 25 kg/mm^2 of the annealed sample.

The optical image analysis of the deformation near the indents of the micro-indentation tests shows significant difference in the deformation behavior in the regions closer to the SMAT surface and away from the SMAT surface. A typical image obtained near the SMAT surface is shown in as Fig. 14.6a, and the one taken away from the SMAT surface is as shown in Fig. 14.6b. The optical image of a non-SMAT annealed sample is shown in Fig. 14.6c for comparison. Near the SMAT surface, large amount of slip activity is visible compared to region far away from the SMAT surface. The relatively low slip activity obtained at locations away from the SMAT surface is comparable with that of an annealed sample.

14.3.3 Discussion

Overall, the results from the present study shows that mechanical polishing increases the hardness significantly at both the microscale and nanoscale. This increase in hardness due to plastic deformation, induced by the mechanical polishing, can be decreased by subjecting the sample to electro-polishing. A complete removal of the induced plastic deformation and recovery of annealed hardness data was not achieved. This could require modifications in the current procedure of electrochemical polishing.

The increase in micro-hardness due to mechanical polishing of non-SMAT samples was about 80% while the increase in nanohardness of these samples was about 130%. This significant difference in the enhancement of hardness can be explained based on the difference in the length scale of activation volume associated with the indentation. Since the activation volume associated with the nanoindentation is much smaller than the activation volume associated with micro-indentation, the corresponding defect density could be very high for nanoindentation. In other words, the activation volume associated with the micro-indentation can go deeper than the volume affected by mechanical polishing, thereby resulting in relatively lower hardness.

The increase in hardness observed on the SMAT samples has the effect of plastic deformation from both the mechanical polishing and the SMAT. In the microindentation tests, in a region closer to SMAT surface the hardness can be considered as independent of the polishing conditions. This could be attributed to the dominance of the effect of plastic deformation due to SMAT relative to the effect of plastic deformation due to mechanical polishing. For the locations away from the SMAT surface, the effect of SMAT decreases and hence, the effect of mechanical polishing dominates.

The significant slip activity near the SMAT surface observed using optical imaging highlights the difference in the deformation mechanisms when compared to an annealed or non-SMAT region which represents relatively defect free material volume. Though further investigation is required for understanding the actual micro/nanoscale deformation mechanism underlying this phenomena, one possible scenario can be envisioned by considering the work-hardening and the difference in the resistance to deformation of a material volume closer to the surface than the volume relatively deeper. In the region where hardness in increased by SMAT, the ratio of the resistance to deformation of material volume in the bulk relative to that at the surface might be larger due to larger work-hardening compared to an annealed sample. Hence the contribution of surface in accommodating the indentation is larger in the hardened region which is realized through significant amount of slipping.

14.4 Conclusion

The effects of severe plastic deformation on copper samples were investigated by introducing various levels of deformation in this study. Various levels of plastic deformation were introduced by polishing the sample surface mechanically followed by partial removal of this polishing effect by subjecting various duration of electro chemical polishing. Samples subjected to surface mechanical attrition treatment (SMAT) were also investigated. Based on the study it was found that surface hardness increases significantly in both the mechanically polished samples and SMAT samples. The amount of hardness attained using severe plastic deformation was found to be a function of the characteristic length scale of the indentation itself. Study of the cross-section of SMAT samples clearly shows variation in hardness with increase in distance from the SMAT surface. Dominance of the effect of SMAT near the SMAT surface and the dominance of mechanical polishing away from the SMAT surface were found. Optical imaging of the indent shows relatively larger slip activity near the SMAT surface compared to region far from SMAT surface or annealed samples.

Acknowledgements The authors would like to thank Center for Advanced Materials and Processing (CAMP) at Clarkson University for the use of their resources and facilities.

References

1. Fecht HJ, Ivanisenko Y (2007) Nanostructured materials, 2nd edn. William Andrew Publishing, Norwich, pp 119–172
2. Turley DM, Samuels LE (1985) The nature of mechanically polished surfaces of copper: polishing with fine diamond abrasives. Metallography 18(2):149–160
3. Turley DM, Samuels LE (1981) The nature of mechanically polished surfaces of copper. Metallography 14(4):275–294

4. Sanders PG, Eastman JA, Weertman JR (1997) Elastic and tensile behavior of nanocrystalline copper and palladium. Acta Mater 45(10):4019–4025
5. Nix WD, Gao H (1998) Indentation size effects in crystalline materials: a law for strain gradient plasticity. J Mech Phys Solids 46(3):411–425
6. Liu Y, Ngan AHW (2001) Depth dependence of hardness in copper single crystals measured by nanoindentation. Scr Mater 44(2):237–241
7. Lu J, Lu K (2003) Comprehensive structural integrity. Pergamon, Oxford, pp 495–528
8. Lu K, Lu J (2004) Nanostructured surface layer on metallic materials induced by surface mechanical attrition treatment. Mater Sci Eng A 375–377:38–45
9. Mao XY, Li DY, Fang F (2010) A simple technique of nanocrystallizing metallic surfaces for enhanced resistances to mechanical and electrochemical attacks. Mater Sci Eng A 527(12):2875–2880

Chapter 15
Rate-Dependent, Large-Displacement Deformation of Vertically Aligned Carbon Nanotube Arrays

Y.C. Lu, J. Joseph, M.R. Maschmann, L. Dai, and J. Baur

Abstract Rate dependent mechanical response of the vertically aligned carbon nanotube arrays (VA-CNTs) has been examined with large-displacement indentation tests. The VA-CNTs are observed to exhibit elastic deformation at small displacement and then plastic deformation at large displacement. Under the cylindrical, flat-ended punch, the nanotube arrays collapse plastically at positions of immediately beneath the indenter face. The plastic zone remains stable at large displacement, because the stress/strain field under a flat cylindrical punch is relatively constant. From the normalized indentation stress-displacement curve, the critical indentation pressure (P_m), a measure of collapsing stress of the CNT arrays, is obtained. The speeds of the indenter have been varied, from 0.5 to 4 μm/s. The large displacement deformation is influenced by the effective strain rate of the material. The critical indentation pressure increases with the increase with the strain rates.

Keywords Carbon Nanotube • Strain Rate • Indentation • Large Displacement

15.1 Introduction

Vertically aligned carbon nanotube arrays (VA-CNTs) have received considerable attention lately due to their unique structures and properties. The VA-CNTs can be grown from various seeded substrates via the chemical vapor deposition (CVD) process. VA-CNTs grown on planar substrates have found applications in areas such as the electrical interconnects [1, 2], thermal interface materials [3, 4], energy dissipation devices [4, 5], and microelectronic devices and microelectromechanical systems [6]. VA-CNTs grown on rounded carbon fibers can be used for improving the fiber-matrix interfaces in composites [7–10], and as flow or pressure sensors used on micro air vehicles (MAVs) [11].

The mechanical properties of these VA-CNTs have been investigated lately, mostly through the nanoindentation technique. In this, an indenter of parabolic or three-face pyramidal shapes is pressed into the specimen to a shallow depth (a few nanometers or microns) and then withdrawn from it, from which the indentation load-depth curves are obtained. Following the standard Oliver-Pharr method, the modulus and hardness of the CNT arrays can be estimated. Most existing studies have been limited to small strain, elastic type deformation of the CNTs [12–14]. The deformation behavior of the VA-CNTs at large strain has drawn great interest recently. Uniaxial compressive tests have been conducted on CNT arrays [15–17]. The CNT array was found to behave as an open-cell foam-like material. The stress–strain curve displays three

Y.C. Lu (✉) • J. Joseph
Department of Mechanical Engineering, University of Kentucky, Lexington, KY 40506, USA
e-mail: chlu@engr.uky.edu

M.R. Maschmann
Air Force Research Laboratory, Materials and Manufacturing Directorate, AFRL/RXBC, Wright-Patterson AFB, OH 45433, USA

Universal Technology Corporation, Dayton, OH 45432, USA

L. Dai
Department of Chemical Engineering, Case Western University, Cleveland, OH 44106, USA

J. Baur
Air Force Research Laboratory, Materials and Manufacturing Directorate, AFRL/RXBC, Wright-Patterson AFB, OH 45433, USA

B. Antoun et al. (eds.), *Challenges in Mechanics of Time-Dependent Materials and Processes in Conventional and Multifunctional Materials, Volume 2*, Conference Proceedings of the Society for Experimental Mechanics Series 37,
DOI 10.1007/978-1-4614-4241-7_15,

distinct stages: a short elastic region, followed by a prolonged plateau region, and finally a densification region. Under compression, the CNT arrays folded themselves in wavelike pattern. The wavelike folding has been observed to always initiate at the bottom of the CNT arrays and then to propagate towards the top. This paper reported the rate-dependent, large-displacement deformation of the VA-CNT arrays through indentation tests.

15.2 Experimentation

15.2.1 Materials

VA-CNTs were synthesized by low pressure chemical vapor deposition (CVD) of acetylene on 15 $\times$ 15 mm^2 SiO_2/Si wafers [20]. A 10-nm thick Al layer was first coated on the wafers before the deposition of 3-nm Fe film in order to enhance the attachment of grown nanotubes on the silicon (Si) substrate. The catalyst coated substrate was inserted into the quartz tube furnace and remained at 450°C in air for 10 min, followed by pumping the furnace chamber to a pressure less than 10 mTorr. Thereafter, the growth of the CNT arrays was achieved by flowing a mixture gases of 48% Ar, 28% H_2, 24% C_2H_2 at 750°C under 10 ~ 100 Torr for 10–20 min. The length of the resultant aligned VA-CNTs could be adjusted by controlling the deposition time and pressure. The VA-CNTs produced were multiwalled carbon nanotubes (VA-MWNTs) and had a narrow uniform diameter distribution between 10 and 15 nm. The carbon nanotube density was approximately: $d_0 = 10^{10}$–10^{11} tubes/cm^2. The microstructure of the carbon nanotube samples were studied using scanning electron microscopy (SEM). SEM was carried out at 15 kV using a field emission Hatachi S800 SEM unit.

15.2.2 Indentation Tests

Large-displacement indentation tests were performed on a conventional nanoindentation tester (Agilent Nano Indenter XP) for rate-dependent experiments. A flat cylindrical tip geometry was used for the indenter, since the stress analysis under a tip of this form had been extensively modeled [18, 19]. Compared to indenters of parabolic and three-face pyramidal shapes, the contact area of a cylindrical flat indenter does not change with displacement, and the extent of the stress field scales with the diameter of the indenter. The commercially-made indenter has a nominal diameter of 100 μm at the end. The resolutions for load and displacement are 50 nN and 0.01 nm, respectively. The Agilent XP style actuator has a large travel distance up to 1 mm thus could be configured for conducting large-displacement indentation tests. The continuous stiffness measurement (CSM) function was used for large displacement indentation. The indenter was oscillated at a frequency of 50 Hz and amplitude of 2 nm. For most experiments, the indenter was driven into the CNT samples to a depth of 150 μm (three times of the indenter radius).

The large displacement indentation test has been a proved method for examining the plastic deformation of materials in small volumes, and has been used on isotropic polymers [21–24], and oriented polymers [25, 26]. The test is run typically to an indentation depth (d) greater than at least one indenter radius (d/a $>$ 1), where a is the indenter radius. Under a cylindrical, flat-ended punch, the deformation zone at large penetration becomes fully developed surrounding the indenter and then remains relatively constant in size. Because of this stable plastic zone, the resultant load-depth curve at large displacement is linear. The small, finite slope of the curve at large displacement arises from the frictional force on the lateral surface of the indenter, due to the elastic compression from the surrounding materials. At some cases (brittle amorphous polymers), the load–displacement curves at large strain exhibit a series of distinctive load-drops, which are due to the microcracking formed in front of the indenter face [21].

15.3 Results and Discussion

15.3.1 Morphology of the VA-CNT Arrays

The surface morphology of the present nanotube specimens was examined by the SEM. Figure 15.1 shows the side and top views of the specimen under various magnifications. As can be seen, the nanotubes are well-aligned perpendicularly to the

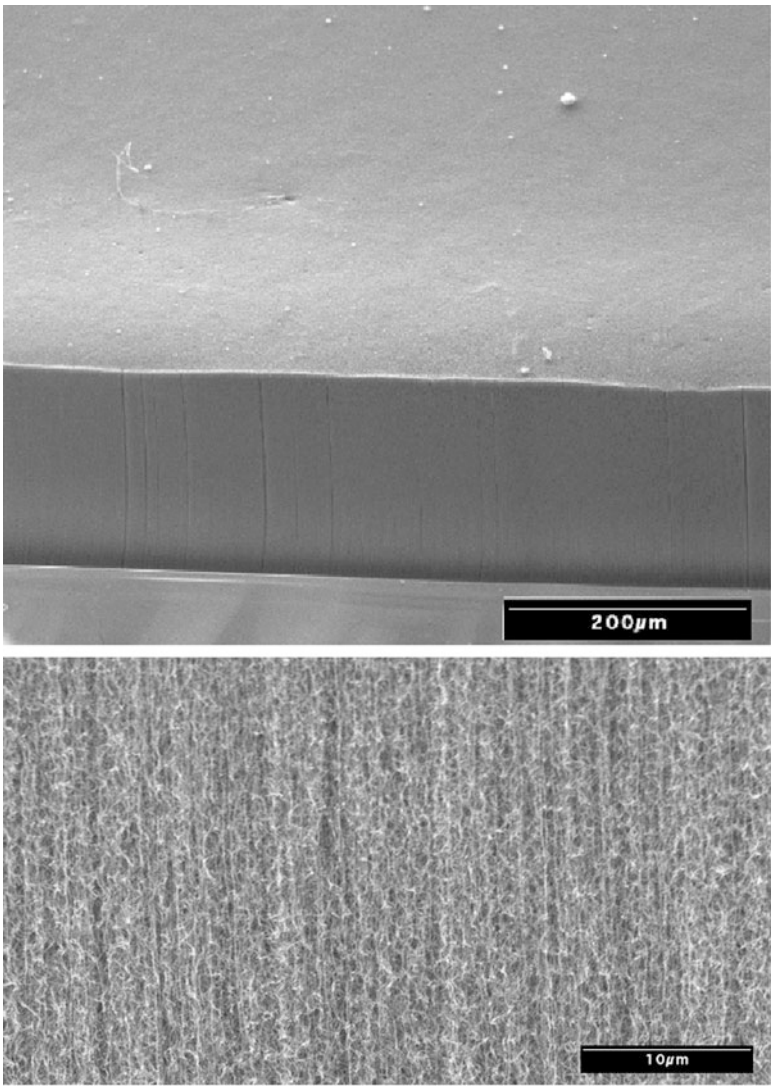

Fig. 15.1 SEM images showing the morphology of the side surface of the vertically-aligned carbon nanotube array (thickness = 500 μm)

substrate. The high magnification SEM image shows that the constituent individual nanotube is somewhat zigzag-like along the nanotube length with some entanglements between the nanotubes as a result of the growth process. However, the specimens have a quite smooth top surface suitable for the nanoindentation tests. No material pile-up is observed around the indentation, indicating that the present nanotube array exhibits negligible strain hardening.

15.3.2 Large-Displacement Indentation Tests

The large-displacement deformation of the VA-CNTs has been recently examined through conventional axial compressive test. Such test often requires special sample preparation technique. For example, the photolithography method is needed to grow cylindrical CNT pillars to be fitted at small testing platens [13, 16]. Here we examined the large-displacement deformation of the CNT arrays by conducting indentation directly on the as-grown samples. Under a cylindrical, flat-faced indenter, the contact area does not change with depth. Thus, the indentation stress (P) is simply the force applied (L_{total}) divided by the cross-sectional area of the indenter (πa^2). The deformation under the indenter tip is clearly not uniform, and a reasonable measure of the mean indentation strain under this type of indenter can be obtained following the suggestion by Hill [27], in which the indentation depth (d) is normalized with respect to the diameter (2a).

Figure 15.2 shows a typical indentation stress-displacement curve of the vertically aligned carbon nanotube arrays. The sizes (heights) of the specimens were chosen carefully to avoid the influence of rigid substrates. The present test was

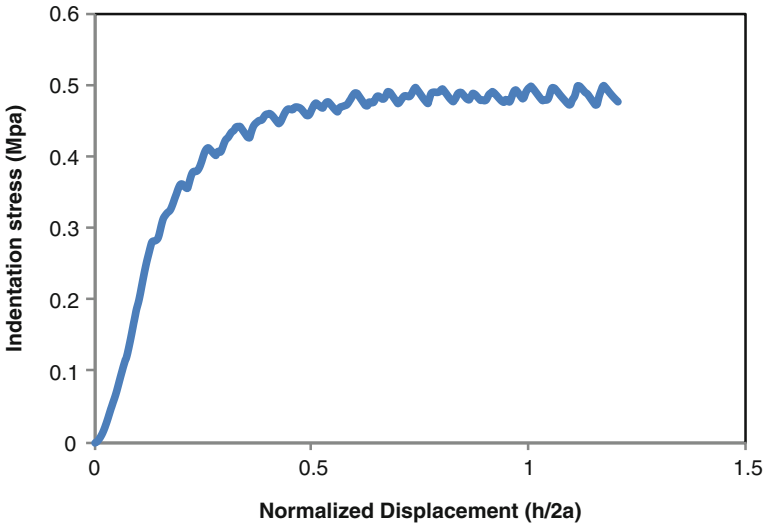

Fig. 15.2 Indentation stress-displacement curve of a vertically aligned carbon nanotube array with cylindrical, flat-faced indenter (Equipment: conventional nanoindentation, sample height: 1,100 μm, indenter diameter: 100 μm)

conducted at a rate of 0.1 μm/s. By using a cylindrical geometry rather than a conical or three-faced pyramidal (Berkovich) indenter, the applied stress measured by the indenter at this steady state is constant. The achievement of this steady state can be observed in the stress-displacement curve. Two distinctive regimes can be observed in the indentation stress-displacement curves of the CNT arrays: a short elastic region and a plateau-like region (Fig. 15.2). The plateau region indicates the plastic collapses of carbon nanotubes beneath the indenter face. Such collapse allows the strain increase while the stress stays approximately constant. A series of "load-drops" in the plateau regions is observed, which corresponds to the folding of additional carbon nanotubes. If further penetration is permitted until all folding is completed, a third region would appear: the densification region. In that region, the folding of all nanotubes under the indenter face has been completed and the compression of the folded/collapsed materials has started. As a result, the stress would start to rise sharply. Alternatively, the densification response can be observed by indenting a shorter specimen. Overall, the stress-displacement response of the CNT arrays is identical to that of an open-cell foam-like material [15–17].

The normalized stress-displacement curve could then be used to estimate the critical indentation stress (P_m), which is a measure of the collapsing stress of the foam-like CNT structure. The critical indentation stress, P_m, is then determined by extrapolating the large-strain indentation stress-displacement curve back to zero displacement, where the frictional load vanishes. The magnitude of P_m so obtained for the present CNT arrays is approximately 0.56 MPa, from Fig. 15.2. The same CNT array has been tested under uniaxial compression using the same in-situ testing apparatus. The yield strength is taken as the maximum stress at the peak: $\sigma_y = 0.48$ MPa. A comparison with the indentation test shows that the critical value of the indentation stress, P_m, is very close to the uniaxial yield stress (σ_y) for the CNT arrays: $P_m/\sigma_y \approx 1.16$. The critical indentation stress (P_m) is proportional to the uniaxial yield stress (σ_y) for a material. The mean indentation contact pressure beneath an indenter is larger than the uniaxial compressive yield stress of the material because of the confining pressure generated by the surrounding elastically strained material in the indentation stress field. The ratio between the mean indentation pressure and the uniaxial yield stress is referred as the constraint factor (C) [28]. For ductile metals, a value of $C \approx 3$ is generally considered to be appropriate [28, 29]. For soft polymers, the value of C is slightly smaller [21–24]. For foam-like materials, the value of C often approaches to unity [30–32]. For the foam-like CNT arrays with a plastic Poisson's ratio near zero, the large indentation has resulted in very little lateral spreading of the CNT fibers under the indenter. Thus, the constraint factor becomes unity.

15.3.3 Strain Rate Dependent Effects

The mechanical properties of carbon nanotube arrays have been reported as rate-dependent, again due to their open-cell foam-like structures [5, 17]. The CNT sample under a high speed impact loading has developed a much higher stress than that under a low speed compression test [5]. The loss stiffness (modulus) of the CNT arrays increases as the frequency (rate) increases [17]. The influence of strain rate on large displacement deformation of the CNTs was examined in the present study. The speed of the indenter was varied from 0.5 to 4 μm/s. Figure 15.3 shows the indentation stress-displacement curves obtained at various speeds. As expected, higher loading velocity has resulted in higher stress. As the indenter velocity

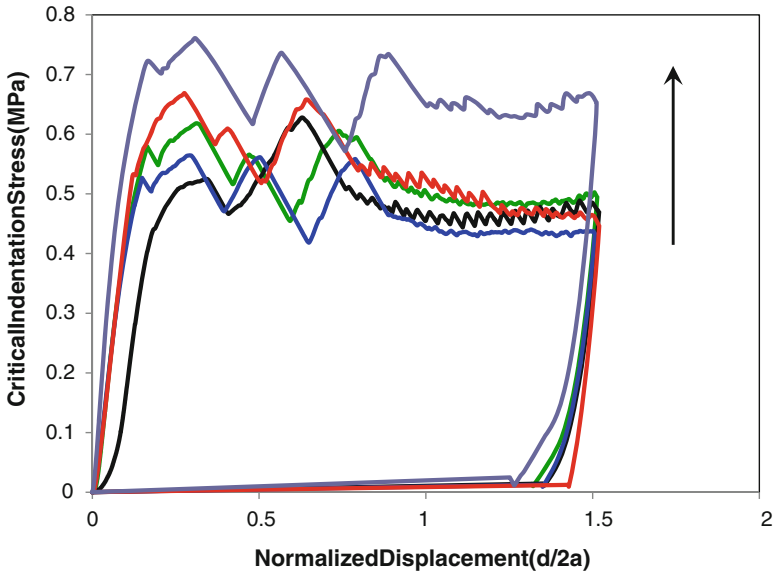

Fig. 15.3 Variation of indentation stress-displacement responses with strain rate for the CNT arrays. The strain rate ranges from 0.005 to 0.05 s^{-1}, increasing in the direction of the *arrow* (Equipment: conventional nanoindentation, sample height: 630 μm, indenter diameter: 100 μm)

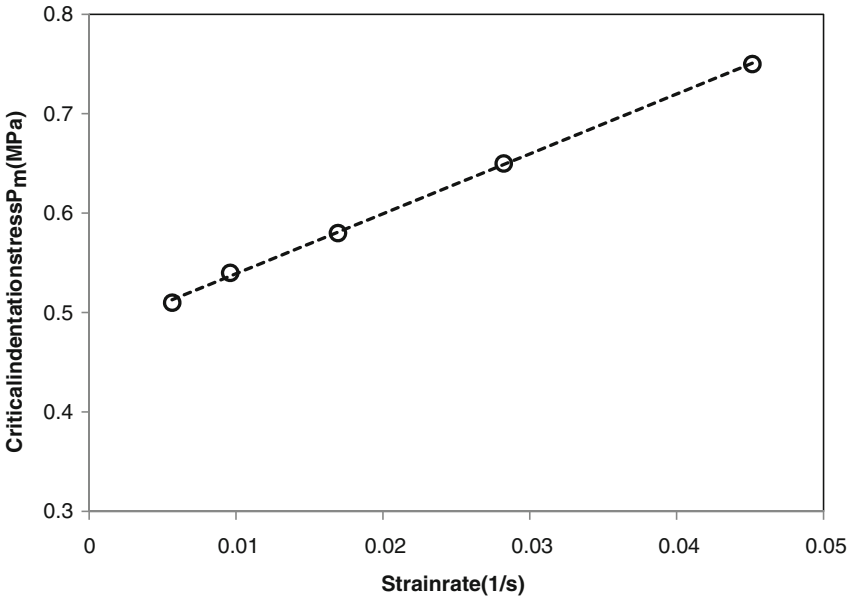

Fig. 15.4 Variation of critical indentation pressure (P_m) as a function of indentation strain rate

changes, the strain rate in the penetrated material changes. The effective strain rate under a flat-faced indenter was estimated using the approximation of Sargent and Ashby: $\dot{\varepsilon} = v/\sqrt{A}$, where v is the indenter velocity and A the indenter cross-sectional area [33]. The relationship between the critical indentation stress (P_m) and effective strain rate ($\dot{\varepsilon}$) is seen in Fig. 15.4. As strain rate increases, the stress required for nanotube collapsing also increases. In this experiment, the beginning of the indentation stress-displacement curves at plateau regions are characterized with a few large "load humps". Those large load drops are resulted from the initiation of nanotube array folding/buckling. In some cases the formation of folding/buckling can be so dramatic that the indenter head can momentarily lose contact with the specimen [16]. It was observed that not all CNT samples exhibited such dramatic load drops. Therefore, the appearance of such load humps may be random, depending upon the testing condition (loading speed), and the structure and properties of each individual CNT sample being tested.

15.4 Conclusions

Large-displacement deformation of the vertically aligned carbon nanotube arrays have been studied through indentation tests. Under the indenter, the vertically aligned carbon nanotube arrays exhibit a transient elastic deformation at small displacement and then plastic deformation at large displacement. The critical indentation pressure (P_m) can be extrapolated from the indentation stress-displacement curve, which is a measure of the collapsing stress of CNT arrays. The magnitude of P_m at the end of the indenter is approximately equal to the collapsing stress of the same carbon nanotube array under uniaxial compression, indicating that there is negligible interfacial friction between the nanotubes and the indenter sidewall. The large displacement indentation tests were performed at various indenter velocities. The critical indentation pressure (P_m) is found to be proportional to the effective strain rate.

References

1. Fan S, Chapline MG, Franklin NR, Tombler TW, Cassell AM, Dai H (1999) Self-oriented regular arrays of carbon nanotubes and their field emission properties. Science 283(5401):512–514
2. Kreupl F, Graham AP, Duesberg GS, Steinhogl W, Liebau M, Unger E, Honlein W (2002) Carbon nanotubes in interconnect applications. Microelectron Eng 64:399–408
3. Xu J, Fisher TS (2006) Enhancement of thermal interface materials with carbon nanotube arrays. Int J Heat Mass Transfer 49:1658–1666
4. Cola BA, Xu J, Fisher TS (2009) Contact mechanics and thermal conductance of carbon nanotube array interfaces. Int J Heat Mass Transfer 52(15–16):3490–3503
5. Misra A, Greer JR, Daraio C (2008) Strain rate effects in the mechanical response of polymer-anchored carbon nanotue foams. Adv Mater 21:334–338
6. Liu Y, Qian WZ, Zhang Q, Cao AY, Li ZF, Zhou WP, Ma Y, Wei F (2008) Hierarchical agglomerates of carbon nanotubes as high-pressure cushions. Nano Lett 8:1323
7. Ci L, Suhr J, Pushparaj V, Zhang X, Ajayan PM (2008) Continuous carbon nanotube reinforced composites. Nano Lett 8(9):2762–2766
8. Zhang S, Zhu L, Wong C-P, Kumar S (2009) Polymer-infiltrated aligned carbon nanotube fibers by in situ polymerization. Macromol Rapid Commun 30(22):1936–1939
9. Ma W, Liu L, Zhang Z, Yang R, Liu G, Zhang T (2009) High strength composite fibers: realizing true potential of carbon nanotubes in polymer matrix through continuous reticulate architecture and molecular level couplings. Nano Lett 9(8):2855–2861
10. Patton ST, Zhang Q, Qu L, Dai L, Voevodin AA, Baur J (2009) Electromechanical characterization of carbon nanotube grown on carbon fibers. J Appl Phys 106:104313
11. Zhang Q, Lu YC, Du F, Dai L, Baur J, Foster DC (2010) Viscoelastic creep of vertically aligned carbon nanotubes. J Phys D: Appl Phys 43:315401
12. Mesarovic SD, McCarter CM, Bahr DF, Radhakrishnan H, Richards RF, Richards CD, McClain D, Jiao J (2007) Mechanical behavior of a carbon nanotube turf. Scr Mater 56:157–160
13. McCarter CM, Richards RF, Mesarovic SD, Richards CD, Bahr DF, McClain D, Jiao J (2006) Mechanical compliance of photolithographically defined vertically aligned carbon nanotube turf. J Mater Sci 41:7872–7878
14. Pathak S, Cambaz ZG, Kalidindi SR, Swadener JG, Gogotsi Y (2009) Viscoelasticity and high buckling stress of dense carbon nanotube brushes. Carbon 47(8):1969–1976
15. Cao A, Dickrell PL, Sawyer WG, Ghasemi-Nejhad MN, Ajayan PM (2005) Super-compressible foamlike carbon nanotube films. Science 310 (5752):1307–1313
16. Hutchens SB, Hall LJ, Greer JR (2010) In situ mechanical testing reveals periodic buckle nucleation and propagation in carbon nanotube bundles. Adv Funct Mater 20(14):2338–2346
17. Maschmann MR, Zhang Q, Wheeler R, Du F, Dai F, Baur J (2011) In situ SEM observation of column-like and foam-like CNT array nanoindentation. ACS Appl Mater Interfaces 3:648–653
18. Sneddon IN (1946) Boussinesq's problem for a flat-ended cylinder. Proc Cambridge Philos Soc 42:29
19. Barquins M, Maugis D (1982) Adhesive contact of axisymmetric punches on an elastic half-space-the modified Hertz-Hubers stress tensor for contacting spheres. J Mech Theor Appl 1:331–57
20. Bajpai V, Dai L, Ohashi T (2004) Large-scale synthesis of perpendicularly aligned helical carbon nanotubes. J Am Chem Soc 126:5070–5071
21. Wright SC, Huang Y, Fleck NA (1992) Deep penetration of polycarbonate by a cylindrical punch. Mech Mater 13:277
22. Lu YC, Shinozaki DM (1998) Deep penetration microindentation testing of high density polyethylene. Mater Sci Eng A 249:134–144
23. Lu YC, Shinozaki DM (2008) Characterization and modeling of large displacement micro-/nano-indentation of polymeric solids. ASME J Eng Mater Technol 130:041001
24. Lu YC, Kurapati S, Yang F (2008) Finite element analysis of cylindrical indentation for determining plastic properties of materials in small volumes. J Phys D: Appl Phys 41:115415
25. Lo JCW, Lu Y, Shinozaki DM (2005) Kink band formation during microindentation of oriented polyethylene. Mater Sci Eng A 396(15):77–86
26. Shinozaki DM, Lo JCW, Lu YC (2008) Depth-dependent displacement modulated indentation in oriented polypropylene. Mater Sci Eng A 491:182–191
27. Hill R (1950) The mathematical theory of plasticity. Oxford University Press, Clarendon
28. Tabor D (1951) The hardness of metals. Oxford University Press, Clarendon

29. Johnson KL (1985) Contact mechanics. Cambridge University Press, Cambridge
30. Wilsea M, Johnson KL, Ashby MF (1975) Indentation of foamed plastics. Int J Mech Sci 17:457–460
31. Olurin OB, Fleck NA, Ashby MF (2000) Indentation resistance of an aluminum foam. Scr Mater 43:983–989
32. Flores-Johnson EA, Li QM (2010) Indentation into polymeric foams. Int J Solids Struct 47:1987–1995
33. Sargent P, Ashby MF (1992) Indentation creep. Mater Sci Technol 8:594

Chapter 16
Characterization and Analysis of Time Dependent Behavior of Bio-Based Composites Made Out of Highly Non-Linear Constituents

Liva Rozite, Roberts Joffe, Janis Varna, and Birgitha Nyström

Abstract The objective of this investigation is to predict mechanical behavior of bio-based composites and their constituents by generalizing existing models to capture their time-dependent behavior. In order to identify and quantify parameters needed for the modeling, extensive damage tolerance tests as well as creep experiments are carried out.

Keywords Bio-based composites • Time dependent behavior • Flax fibers • Regenerated cellulose fibers • Creep

16.1 Introduction

Currently there is compelling motivation from industries and society for development of materials from renewable resources. Fairly recently a number of bio-based thermosetting resins and high quality natural fibers (e.g. flax, hemp) became available which promoted development of entirely bio-based high performance composites for structural applications. However, there are still weaknesses related to the natural fibers, such as limited fiber length, sensitivity to moisture, temperature etc. But probably major drawback of these fibers is variability of their properties. Therefore, another type of reinforcement with high cellulose content and of natural origin has attracted attention—regenerated cellulose fibers (RCF). RCF are continuous and it is easy to arrange them into fabrics with stable orientation and geometry. But RCF are highly non-linear and the performance of bio-based resins is also of similar kind. Therefore, performance of the composite with such constituents is non-linear with presence of very significant vicsco-elastic/plastic component.

In the present study, new combinations of fibres and resins from renewable resources are used as constituent materials in composites with an attempt to develop structural materials. Fibres made from regenerated cellulose and high quality spun flax fibres are combined with two types of bio-based thermosetting resins.

Preliminary results from tests of composite laminates with RCF show that damage modes in these materials are very similar to that of synthetic composites (like glass and carbon fiber composites). However, these results also show that stress-strain curves for these materials are very non-linear and loading-unloading experiments demonstrate that the shape of the stress-strain curve has the form of a hysteresis loop. Therefore, these materials have to be treated as highly non-linear with presence of visco-elastic and/or visco-plastic effects.

L. Rozite • J. Varna
Luleå University of Technology, Luleå S-97187, Sweden

R. Joffe (✉)
Luleå University of Technology, Luleå S-97187, Sweden

Swerea SICOMP AB, Piteå S-94126, Sweden
e-mail: roberts.joffe@ltu.se

B. Nyström
Swerea SICOMP AB, Piteå S-94126, Sweden

B. Antoun et al. (eds.), *Challenges in Mechanics of Time-Dependent Materials and Processes in Conventional and Multifunctional Materials, Volume 2*, Conference Proceedings of the Society for Experimental Mechanics Series 37,
DOI 10.1007/978-1-4614-4241-7_16,

16.2 Mechanical Characterization

16.2.1 Materials

Two types of fibers were used in this study—regenerated cellulose fibers "Cordenka 700 Super 3" (Cordenka, Germany) and unbleached high quality flax fibers produced by Linificio e Canapificio Nazionale, Spain, supplied by eXtreme in Italy. Tribest and EpoBioX were used as bio-based resins. Tribest is acrylated, epoxidized soy oil based resin (Cognis, Germany). As a curing agent 2.25% peroxide Benox L40LV (Syrgis Performance Initiators AB) was used. EpoBioX is epoxidised pine oil based resin (Amroy, Finland). As a curing agent for EpoBioX Ca35Tg hardener with mixing ratio 100:27 was used. Tribest resin and EpoBioX base are approximately 75% bio-based.

16.2.2 Composite Manufacturing

Fiber roving was winded on steel plates using a filament winding machine (two layers for unidirectional composites (UD)). Afterwards fiber preforms were impregnated using vacuum infusion with resin heated to 50°C. Composites with Tribest resin were cured for 8 h at 80°C. Composites with EpoBioX resin were cured for 2 h at 80°C. The final composite laminates were with fiber volume fractions of approximately 40–50%.

16.2.3 Tensile Tests

16.2.3.1 Composite and Neat Resin

Composite plates were cut into rectangular shaped specimens and then polished (up to the 1,200 grit sand paper). Specimens did not have end tabs but grinding paper (roughness 240) was used to wrap the ends of the specimens in order to prevent material crashing in the grips.

Tensile tests of composites and neat resins were performed on Instron 3366 machine equipped with 10 kN load cell, pneumatic grips and extensometer (Instron 2630-111) with a gauge length of 50 mm. Specimen was clamped in the grips (25 mm from each end) in such a way that gauge length was set to 100 mm. In all quasi-static tensile tests the speed of the tensile machine's cross-head was 5 mm/min which roughly corresponds to a strain rate of 5%/min. Load and displacement was registered by data acquisition unit and stored on PC. Tensile tests were performed at room temperature and relative humidity (RT ~ 22°C, RH ~ 25%).

16.2.3.2 Cordenka Bundle

Tensile tests of Cordenka bundles were performed on Instron 4411 equipped with 500 N load cell and mechanical grips. Every bundle was fitted with wooden end tabs by gluing bundle ends in between flat pieces of wood (Araldite 2011 two-component epoxy resin was used as glue).

The average diameter of single Cordenka fiber is $d_f = 12.5$ μm (this value is used to calculate stress). The number of single fibers in the yarn is 1,350. The diameter and filament count were determined experimentally and verified from a product data sheet supplied by manufacturer.

16.2.4 Creep Tests

16.2.4.1 Composite and Neat Resin

Tensile creep tests were performed using a creep rig with dead weights. Creep load is applied in steps and in every step k stress is applied instantly at t_k and kept constant for time interval t_{k+1}–t_k. The duration of strain recovery interval was at least

five times longer than the loading interval. Creep strains (measured using extensometer) were recorded during the loading and also during the following interval of strain recovery after load removal.

The irreversible strains at the end of the recovery period (if present) were analyzed as viscoplastic. All creep tests used for determination of time and load dependence of viscoplastic strains were carried out in multiple steps over shorter time intervals of 10, 20, 30 and 60 min.

16.2.4.2 Cordenka Bundles

Bundle specimens for creep tests were prepared in the same way as for simple tensile tests, but in this case specimens with a gauge length of 100 mm were prepared. Creep tests were performed on Instron 3366 with same set-up as in simple tensile tests.

16.2.5 Accumulation of Microdamage and Resulting Stiffness Degradation

After material has been subjected to high stress levels the elastic properties of the material may be degraded. The elastic modulus dependence on the previously applied maximum strain/stress level was measured to evaluate the significance of microdamage developing at high stresses.

16.3 Results and Discussion

It is important to be able to predict long term behavior of materials under investigation. One of the most general approaches is thermodynamically consistent theory for nonlinear viscoelastic and nonlinear viscoplastic materials developed by Schapery [1, 2]. The constitutive equation was further modified to account for microdamage in [3]. The final form of the material model (for one-dimensional case) is

$$\varepsilon = d(\sigma_{\max})\left[\varepsilon_0 + g_1 \int_0^t \Delta S(\Psi - \Psi') \frac{d(g_2\sigma)}{d\tau} d\tau + \varepsilon_{pl}(t,\sigma)\right] \tag{16.1}$$

This model has been successfully applied to randomly oriented bio-based composites [4, 5] and continuous glass fiber composites [6].

This model can be used to predict behavior of composite as well as constituents (fiber and/or resin). However, this requires a great number of input parameters and, therefore a substantial number of experiments must be performed. Considering that a huge variety of different compositions of constituents is possible, a more efficient way to predict the behavior of composite would be based on constitutive modeling. This means that once constituents (fibers and resins) are fully characterized, the long term properties for resulting composites can be analytically predicted based on this information.

16.3.1 Mechanical Behaviour of Regenerated Cellulose Fibers

Stress-strain curves for Cordenka bundles with and without twist are presented in Fig. 16.1. Average mechanical properties are presented in Table 16.1. Stress-strain curves from loading-unloading tests of regenerated cellulose bundles are presented in Fig. 16.2.

In Fig. 16.1 it is possible to distinguish two linear regions and one transformation region on the stress-strain curve. Both fiber types of bundles exhibit similar trends, but stress-strain curves for twisted bundles are slightly shifted to the right on the strain axis. This is somewhat different from the behavior of other manmade fibers (e.g. glass and carbon) where the load-displacement curve has a bell-like shape and it can be used to identify parameters of Weibull strength distribution. In the case of synthetic fibers, filaments in the bundle fail progressively and therefore failure of the bundle is not sudden as for Cordenka

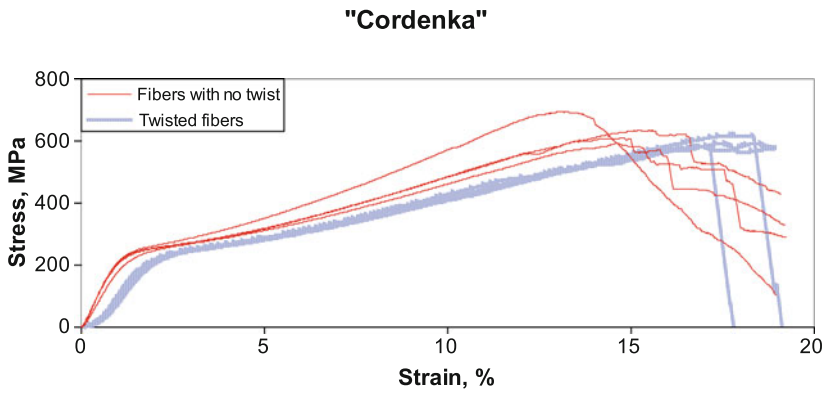

Fig. 16.1 Stress-strain curves for regenerated cellulose fiber bundles with and without twist

Table 16.1 Average mechanical properties for fiber bundles

Bundle type	Elastic modulus (GPa)	Strain at maximum stress (%)	Maximum stress (MPa)
Twisted	15.68 ± 0.93	18.61 ± 1.94	602.8 ± 17.8
Without twist	23.71 ± 2.51	14.45 ± 0.82	633.2 ± 45.1

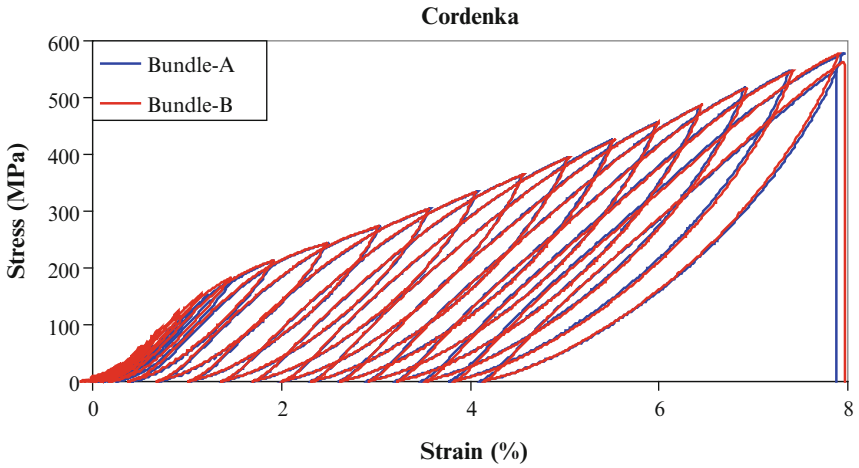

Fig. 16.2 Stress-strain curves from loading-unloading tests for twisted regenerated cellulose fiber bundles

bundles. Thus it can be stated that strength of Cordenka fibers cannot be described by the Weibull strength distribution, because these fibers are not brittle material for which this distribution was introduced. Moreover, in the case of twisted bundles fiber are very tightly squeezed together and friction between fibers is very high.

Figure 16.2 shows well defined hysteresis loops, this is typical phenomenon for visco-elastic materials. The overall behavior of specimens is similar to that in simple tensile tests, but bundles fail at significantly lower strains of 8%, whereas in simple tensile tests bundles failed around 15%. Stress-strain curves for two tested bundles are almost identical which indicates very good repeatability of experimental results.

16.3.2 Mechanical Behavior of Composites and Neat Resin

Stress-strain curves for neat Tribest resin are presented in Fig. 16.3. All experimental curves almost coincide with each other showing excellent repeatability. At the beginning stress-strain curves show linear behavior, but after approximately stress level of 3 MPa curves have non-linear trend.

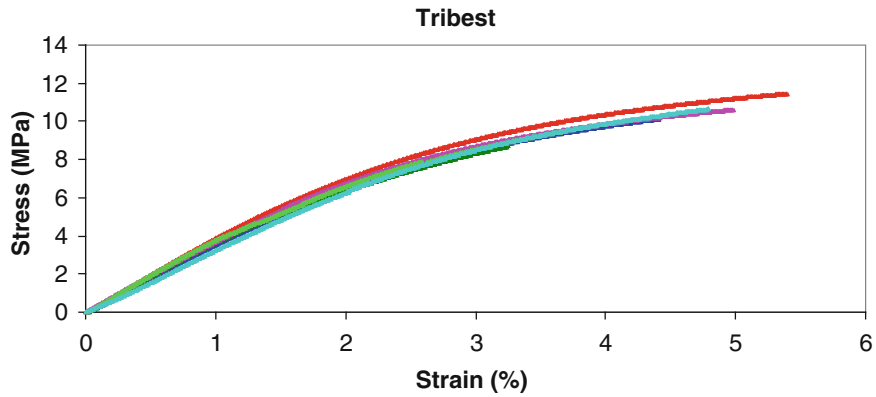

Fig. 16.3 Stress-strain curves for neat Tribest resin

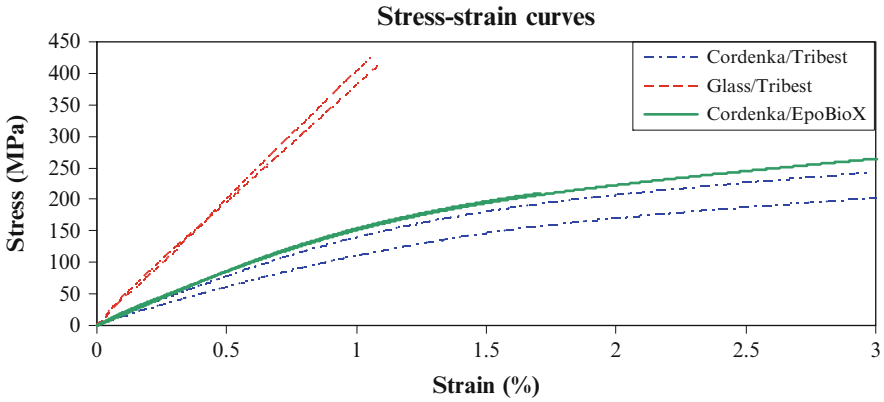

Fig. 16.4 Stress-strain curves for GF and cellulose composites with Tribest and EpoBioX resins

Table 16.2 Measured elastic modulus for nest Tribest resin and composites

Material	Elastic modulus (GPa)
Neat Tribest resin	0.53
Glass/Tribest UD	43.0
Cordenka/Tribest UD	15.0
Cordenka/EpoBioX UD	17.4
Flax/EpoBioX UD	22.0

Stress strain curves for UD composites are presented in Fig. 16.4 (for more convenient comparison only part of the curves is presented). It is obvious that glass fiber (GF) composites have higher stiffness than regenerated cellulose fiber composites. GF composite curves are linear, whereas regenerated cellulose fiber composite exhibit non-linear behavior. Comparison of stress-strain curves for GF and Cordenka fiber composites with the same matrix (Tribest) leads to conclusion that non-linear behavior of composites is mostly defined by fibers. Stress-strain curves for composites with regenerated cellulose fibers but different matrices have similar shape. Composite with EpoBioX has slightly higher modulus. Measured elastic modulus of neat resin and composites are presented in Table 16.2.

16.3.2.1 Tensile Creep Tests

Several step creep tests for neat Tribest resin were performed at three stress levels: 4, 5 and 6 MPa (Fig. 16.5). Visco-plastic strains for resin at stress levels 4 and 5 MPa are similar, however, increase of applied stress from 5 to 6 MPa doubles level of visco-plastic strain.

Several step creep tests for Cordenka fiber bundles are presented in Fig. 16.6. At relatively low stress levels 50 and 100 MPa viscoplastic and viscoelastic strains are low, but with increase of stress level amount of strain dramatically increases.

Several step creep test for GF/Tribest composite is presented in Fig. 16.7. As expected, GF composite exhibits linear elastic behavior also in creep. There are no significant viscoelastic strains and even at high stress levels there are only very small viscoplastic strains.

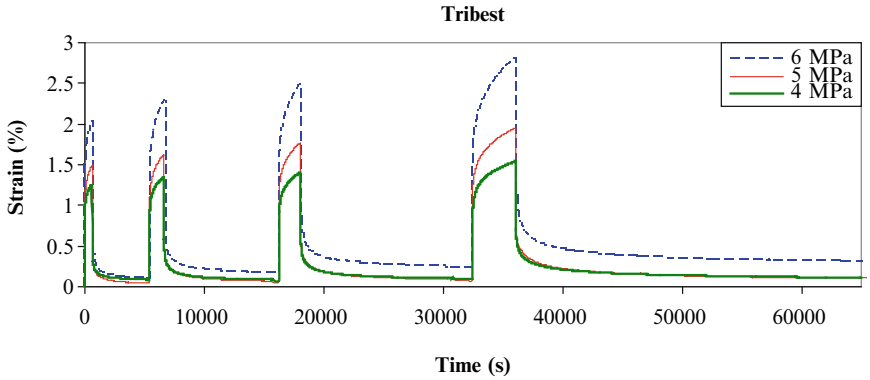

Fig. 16.5 Several step creep test results for neat Tribest resin

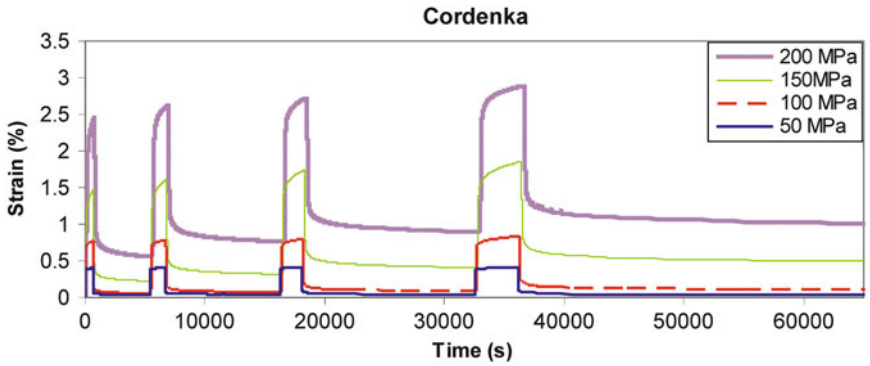

Fig. 16.6 Several step creep test results for Cordenka fibers bundles

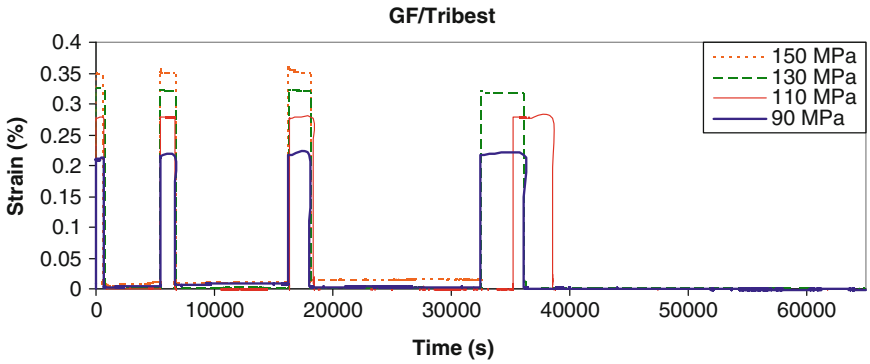

Fig. 16.7 Several step creep tests results for GF/Tribest composite

Several step creep tests for Cordenka/EpoBioX composites are presented in Fig. 16.8. It can be seen in Fig. 16.8 that viscoplastic and viscoelastic strains at 160 MPa stress increases twice as much as at lower stress levels with 20 MPa stress increase. This stress level is close to the point when slope of stress-strain curve from tensile tests of bundle is changing (see Fig. 16.1). It is obvious that around this "transformation region" composites, similarly as in case of fibers, are behaving differently than at lower stress levels.

16.4 Summary

The highly non-linear behavior of Cordenka bundles was demonstrated via quasi-static and creep tensile tests. At high stresses (>150 MPa) Cordenka bundles exhibit very significant creep, whereas at low applied stress (<100 MPa) evolution of strain during the creep test is not excessive and almost no residual strain has developed. Two types of bundles, with and without twist, were tested. Bundles without twist perform slightly better than those with twist. Moreover, use of untwisted

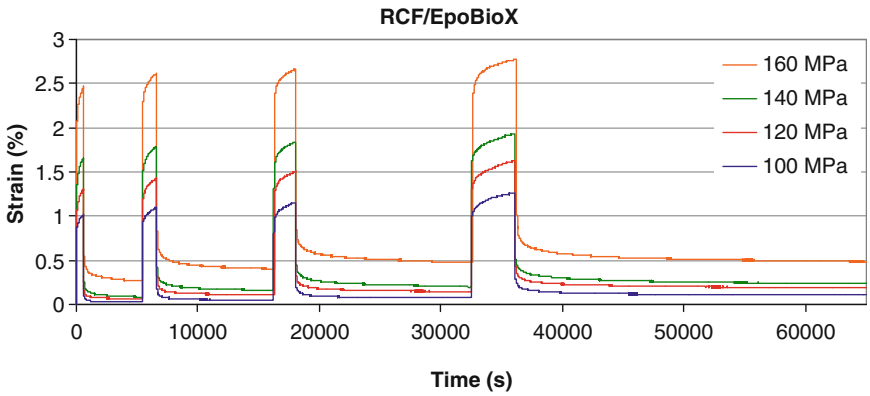

Fig. 16.8 Several step creep tests results for Cordenka/EpoBioX composite

bundles is mush more beneficial for manufacturing of composites: fibers are dispersed more homogeneously throughout the material.

Tensile tests of composites show that GF/Tribest behaves linearly with elastic modulus of 43 MPa. It should be noted that this value is rather close to the stiffness of commonly used GF/Epoxy UD prepreg composite with high volume content of fibers (value of 45–47 GPa has been reported). But the composites made out of Cordenka fibers with Tribest resin behave non-linearly and show much lower stiffness. However, it should be noted that stiffness of Cordenka fibers is 3.6 times lower than that of GF but stiffness of composite based on Cordenka fibers is only 2.9 lower than elastic modulus of GF composites. This means (assuming similar volume fractions of fibers in GF and Cordenka laminates) that properties of Cordenka are well utilized due to homogeneous fiber distribution and well controlled fiber orientation in the material.

There is small difference between stiffness of Tribest and EpoBioX resin based composites (with Cordenka fibers): EpoBioX composite has 15% higher modulus than composite with Tribest. This of course can be explained by difference in properties of matrix (stiffness of Tribest is <1 GPa, whereas stiffness of EpoBioX is 3.0–3.5 GPa) and possible small deviations in fiber content.

Neat Tribest resin showed highly viscoelastic and viscoplastic response in creep tests, whereas GF/Tribest composites did not creep at all. The strain developed in GF composite during the creep were 2.5 times smaller than for Cordenka composites but it can be explained by difference in stiffness. In general, it can be stated that at small applied stresses (<100 MPa) Cordenka composite does not exhibit extreme creep.

The results accumulated in this investigation facilitate understanding of behavior of composites with highly non-linear fibers. It will promote development of these materials as well as help in validation of models for prediction of performance of such composites. This knowledge will be further used to design materials with new compositions (and properties) tailored according to the particular applications.

Acknowledgments Part of this study was financially supported by Interreg IVA Nord project ANACOMPO (funding by EC and regional government of Norrbotten). Manufacturing of composites was financially supported by VINNOVA/project Nanofibre.

Authors would like to acknowledge Fanny ROOS (EEIGM, LTU) for performing part of experiments and Runar Långström (Swerea SICOMP) for composite manufacturing.

References

1. Lou YC, Schapery RA (1971) Viscoelastic characterization of a nonlinear fiber-reinforced plastic. J Compos Mater 5:208–234
2. Schapery RA (1997) Nonlinear viscoelastic and viscoplastic constitutive equations based on thermodynamics. Mech Time Depend Mater 1:209–240
3. Marklund E, Eitzenberger J, Varna J (2008) Nonlinear viscoelastic viscoplastic material model including stiffness degradation for hemp/lignin composites. Compos Sci Technol 68:2156–2162
4. Varna J, Rozite L, Joffe R, Pupurs A (2012) Nonlinear behavior of PLA based flax composites. Plast Rubber Compos 41:49–60
5. Varna J, Sparnins E, Joffe R, Nättinen K, Lampinen J (2012) Time dependent behavior of flax/starch composites. *Mech Time-Depend Mater*, 16(1):47–70.
6. Giannadakis K, Mannberg P, Joffe R, Varna J (2011) The sources of inelastic behaviour of glass fiber/vinylester non-crimp fabric $[\pm 45]_s$ laminates. *J Reinf Plast Compos*. 30(12):1015–1028.

Chapter 17
Combined Effects of Moisture and UV Radiation on the Mechanics of Carbon Fiber Reinforced Vinylester Composites

Chad S. Korach, Heng-Tseng Liao, Derek Wu, Peter Feka, and Fu-pen Chiang

Abstract Fiber reinforced polymer resin composites are used in infrastructure, structural, and foam core sandwich structure applications. When exposed to environmental factors degradation initiates in the composite matrix due to stress, radiation, moisture and chemical effects, causing overall weakening. Combined exposure of UV radiation and moisture creates synergistic degradation mechanisms. Here, accelerated aging of carbon fiber-reinforced vinylester composites is performed using UV radiation and moisture exposure with environmental chambers to ascertain the effect on the composite mechanical response over time. Composite coupons are characterized for mass and surface volume changes, and mechanical characterization is used to assess the effects of combined environments on strength. The significant physical and chemical mechanisms of the composite performance loss for combined exposure conditions will be discussed in the context of accelerated aging.

Keywords Carbon fiber • Vinylester • Composites • Degradation • Moisture • Ultraviolet light • Accelerated aging

17.1 Introduction

Infrastructure and structural applications are increasingly moving towards the use of polymer composite materials for components of structures and structural repairs. Polymer composites are attractive due to the high strength-to-weight ratio and the corrosion resistance. Though polymer composite materials have been successfully used in application, the long-term durability of the materials is still an open question, and effects wide-spread implementation. This is partly due to the multitude of conditions composite materials can be exposed to in application [1]. The effect of environmental exposure of vinylester resin composites has shown detrimental effects on long-term residual mechanical properties [2]. Combined effects of ultraviolet radiation and moisture at elevated temperatures have shown an increased degradation of mechanical properties for epoxy resin composites [3]. Similar combined exposures have not been addressed for vinylester resin composites, and here the combination of UV radiation and moisture-temperature are studied for carbon fiber/vinylester composites.

17.2 Materials and Methods

17.2.1 Materials

Carbon-fiber reinforced vinylester unidirectional composite laminates (Graphtek LLC) were used for all experiments and conditions. Composite laminate sheets with nominal thickness of 1.4 mm were machined using a diamond wet saw into two sizes: (1) 12.5 × 77 mm (width × length) for flexural testing with two fiber directions [0°] and [90°], and (2) 25 × 152 mm with [0°] fiber direction in the length for fracture testing. Two 5 mm notches were machined in specimen size (2) at the midpoint of the length with a diamond saw to create double edge notch (DEN) fracture specimens.

C.S. Korach (✉) • H.-T. Liao • D. Wu • P. Feka • Fu-pen Chiang
Department of Mechanical Engineering, Stony Brook University, Stony Brook, NY 11974, USA
e-mail: chad.korach@stonybrook.edu

B. Antoun et al. (eds.), *Challenges in Mechanics of Time-Dependent Materials and Processes in Conventional and Multifunctional Materials, Volume 2*, Conference Proceedings of the Society for Experimental Mechanics Series 37,
DOI 10.1007/978-1-4614-4241-7_17,

Fig. 17.1 Environmental exposure performed in the laboratory (with accelerated aging chambers) (*left*, QUV/se ultraviolet radiation and condensation chamber) (*right*, Tenney BTRS temperature and humidity chamber)

17.2.2 Exposure Conditions

Samples were exposed to ~800 h of combined and individual accelerated aging before characterization using two chambers: (1) Moisture and heat in a Tenney Benchmaster BTRS temperature and humidity chamber, and (2) UV radiation/condensation in a Q-Lab QUV/se accelerated weathering chamber (Fig. 17.1). UV radiation simulates natural sunlight using fluorescent UV bulbs at a 340 nm wavelength. Intensity is monitored by real-time UV irradiance sensors. Temperature is controlled using a blower. Condensation is provided by water evaporation which condenses on the sample surfaces. Three to five specimens per condition were placed in the chambers. Sample mass is monitored every 48 h with a precision balance by removing specimens from the temperature and humidity chamber. Samples are blotted with sterile paper tissue (kimwipe) to remove surface moisture if present and then immediately weighed.

One-half the samples are rotated between the two chambers every 24 h to create a combined effect between controlled constant temperature and humidity and the cyclic UV radiation/condensation condition. The conditions in the chambers remained constant for the duration of the exposure. In the temperature and humidity chamber, moisture was set at 85% relative humidity (RH) and temperature at 35°C. In the QUV chamber, the UV radiation and condensation conditions cycled every 3 h. For the UV cycle, the UV irradiance was set at 0.6 W/m^2 at 60°C, and the condensation cycle was set at a temperature of 50°C.

17.2.3 Surface Microscopy and Chemical Analysis

Composite coupons surfaces were examined by high resolution digital optical microscopy (Keyence VHX-500). Samples were mounted beneath the microscope objective with two orientations to image the edges and surfaces. Specimens from all exposure conditions as well as unconditioned samples were imaged. Fourier transform infrared (FTIR) photoacoustic spectroscopy was performed on 1 × 1 cm samples cut from the unconditioned and exposed specimens. Absorption spectra were obtained for wavenumbers from ~700 to 3,700 cm^{-1}.

17.2.4 Mechanical Testing

Three point bending tests were performed on the composite samples following the ASTM D790 standard using a screw-driven mechanical loading frame (TiraTest 26005) with a 0.5 kN load cell. The tests determined flexural strength and modulus of the composites. Specimen sizes were 77 × 12.5 × 1.4 mm (L × W × H). Support geometry followed ASTM D790, with the support span set for 60 mm resulting in a span/thickness ratio of ~43. A crosshead rate of 4.25 mm/min was used to give a strain rate of 0.01 mm/mm/min.

Energy release rate was determined using the DEN specimens in a hydraulic mechanical loading frame (Instron 8501). A gage length of ~102 mm was used with the edge notches in the center of the gage. A crosshead rate of 2 mm/min was used,

and load at first failure was recorded. Tensile modulus of an un-notched specimen was measured with the recorded load and instrumenting with strain gages to compute the tangent modulus.

17.3 Results and Discussion

17.3.1 Specimen Weight Changes as a Function of Duration

Mass changes of all samples have been tracked for the environmental chambers. The results indicate that samples exposed to the conditions all had mass gain, which is due to moisture uptake. Only the large fracture specimens showed a significant difference between the combined humidity-UV and constant humidity conditions. This observed phenomenon is being investigated.

17.3.2 Surface Morphology

Surface changes due to environmental exposure of the composites were characterized by high-resolution microscopy (Keyence VHX-500), to determine the effects on the vinylester resin. Images provided evidence of micro-cracking and potential matrix erosion for samples exposed to combined UV conditions (Fig. 17.2). Surface cracking observed on the edges was more extensive than on the surface. There was no micro-cracking observed for specimens exposed to only constant humidity.

17.3.3 Chemical Changes Due to Exposure Conditions

Surface effects govern the environmental degradation of the composites and were characterized by photoacoustic FTIR, to determine photodegradation processes of the vinylester resin. The vinylester spectrum was acquired for all specimen conditions, with several peak magnitude and spectral changes identified by FTIR (not shown). Changes were most prominent for the combined UV condition, with peak suppression at 3,040 cm^{-1} and 2,180 cm^{-1}, and attenuation of multiple peaks, most notably at 1,730 cm^{-1}. The peak at 3,040 cm^{-1} is associated with the C-H bond on the benzene ring, where side groups may be disrupted, and the peak at 1,730 cm^{-1} is related to changes in the carbonyl content. The O-H stretching and carbonyl are indications of hydrolysis [4], and carbonyl an indicator of photodegradation.

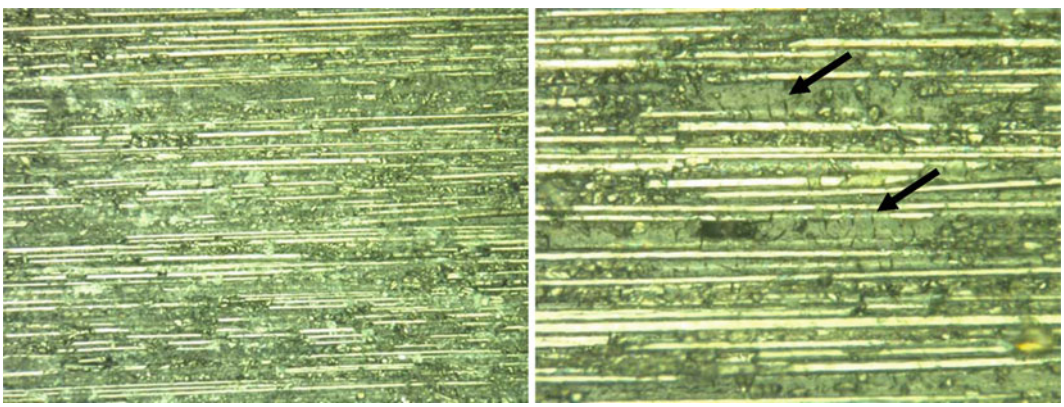

Fig. 17.2 Optical microscopy of unexposed (*left*) and 768 h combined UV-moisture exposed (*right*) carbon fiber/vinylester composite edges; micro-cracking observed in right image marked by arrows

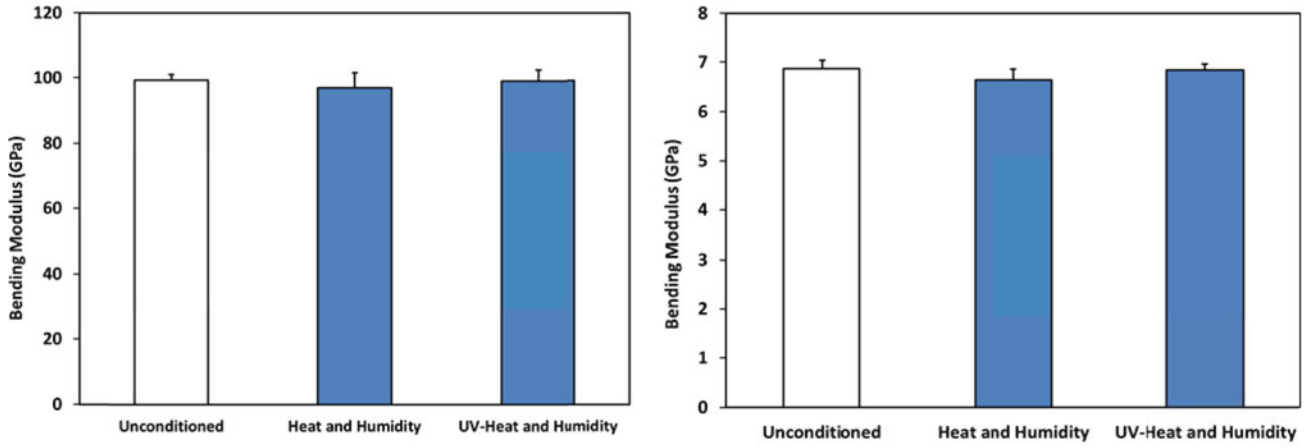

Fig. 17.3 Bending modulus of carbon fiber/vinylester composites determined from three point bending tests; 0° specimens (*left*), 90° specimens (*right*)

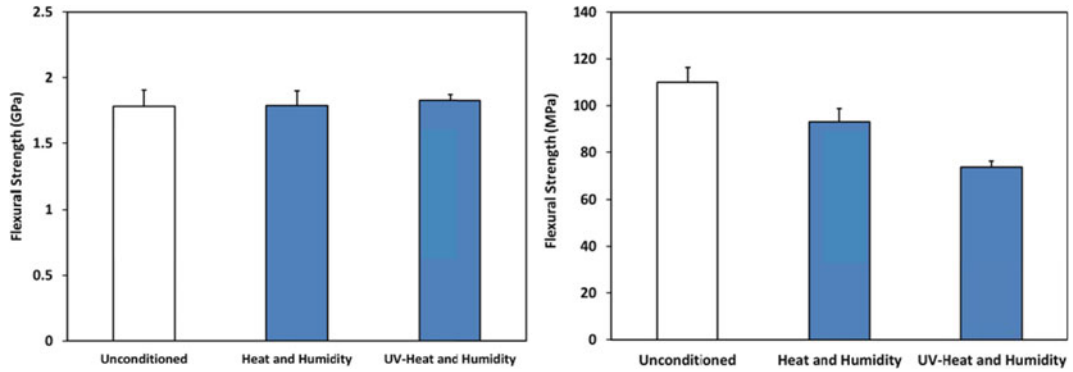

Fig. 17.4 Flexural strength of carbon fiber/vinylester composites determined from three point bending tests; 0° specimens (*left*), 90° specimens (*right*)

17.3.4 Mechanical Flexural Response

Samples exposed to 768 h of combined environments have been characterized by three point bending to determine flexural modulus and residual strength (ASTM D790) [5]. Samples with [0°] and [90°] fiber orientations were characterized after exposure. All exposure conditions showed an insignificant difference in the flexural modulus when compared to the unconditioned specimens, and within experimental error (Fig. 17.3). Modulus results in the [0°] fiber direction (not shown) were an order of magnitude larger than the [90°] fiber samples, due to the fiber driven versus matrix driven mechanical response, respectively. Results showed the residual flexure strength to have minimal change within the experimental error for the [0°] fiber direction samples when compared with the unconditioned samples (Fig. 17.4). The result is consistent with previous data on carbon fiber/epoxy composites. Residual strength in the [90°] fiber direction demonstrated sensitivity to the exposure conditions, with all conditions decreasing compared to the unconditioned control (Fig. 17.4). The conditions involving the UV radiation exhibited the most significant reduction in the residual strength, decreasing by 21% for the combined Humidity-UV case. The exposure to the UV radiation demonstrates a synergistic degradation effect which leads to a decrease in the vinylester composite mechanical strength attributed to surface micro-cracking.

17.3.5 Fracture Strength

Energy release rate of longitudinal fractures for samples exposed to 768 h of combined environments were characterized with the method of Nairn [6] that utilizes the shear-lag model. Samples were all 0° composites with double-edge notches

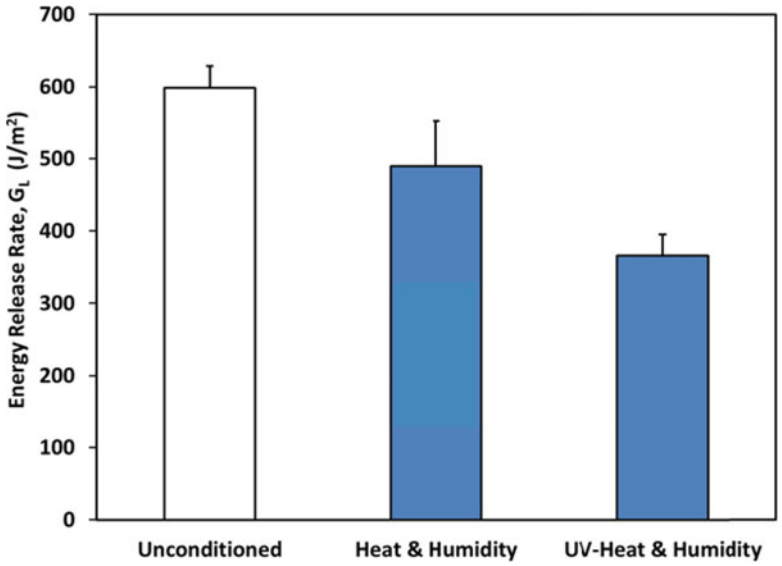

Fig. 17.5 Energy release rate of carbon fiber/vinylester composites determined from double edge notched tensile specimens

(DEN) machined across the fibers with a diamond saw. All exposure conditions showed a decrease in the energy release rate compared with the unconditioned specimens (Fig. 17.5). To compute the energy release rate, the tensile modulus of an un-notched specimen was measured by instrumenting with strain gages then computing the tangent modulus, which was found to be 152 GPa. The combined exposures showed a decrease in the energy release rate of ~25% for the UV-Humidity condition. This difference is attributed to the surface micro-cracking observed on the edges of the samples, which lead to a more efficient path for crack initiation.

17.4 Conclusions

Carbon fiber-reinforced vinyleseter unidirectional composite laminates were characterized for their time-dependent mechanical behavior as a function of exposure to UV radiation and temperature-humidity conditions. Samples were exposed to two sets of conditions, one which exposed samples to continuous temperature and humidity, and a second where samples were exposed to cyclic UV radiation and temperature-humidity conditions. Exposure to the condition containing UV radiation which mimics naturally occurring sunlight was found to cause micro-cracking in the composite surfaces and edges, and chemical changes in the vinylester matrix. Mechanically, samples were tested by three point bending in two fiber orientations, 0° and 90°, where bending modulus was found unchanged, though flexural strength was found to decrease for the 90° fiber orientation, the largest change occurring for the condition containing cyclic UV and moisture. The energy release rate was computed for 0° DEN samples in tension, where the a decrease in energy release rate was found to occur for the samples exposed to the environmental chambers, with the UV radiation and temperature-humidity case causing the largest decrease.

Acknowledgements The authors respectfully acknowledge the support from Drs. Yapa D.S. Rajapakse and Airan J. Perez from the Office of Naval Research through grant #N000141110816. We also acknowledge the assistance of Prof. G. Halada and Mr. M. Cuiffo from Stony Brook University with the FTIR photoacoustic spectroscopy and analysis.

References

1. Chin JW, Nguyen T, Aouadi K (1997) Effects of environmental exposure on fiber-reinforced plastic (FRP) materials used in construction. J Compos Technol Res 19(4):205
2. Weitsman YJ (2006) Anomalous fluid sorption in polymeric composites and its relation to fluid-induced damage. Compos A 37:617

3. Kumar BG, Singh RP, Nakamura T (2002) Degradation of carbon fiber-reinforced epoxy composites by ultraviolet radiation and condensation. J Compos Mater 36:2713
4. Chin JW, Aouadi K, Haight MR, Hughes WL, Nguyen T (2001) Effects of water, salt solution and simulated concrete pore solution on the properties of composite matrix resins used in civil engineering applications. Polym Compos 22(2):282
5. ASTM D790 (2000) Standard test method for flexural properties of unreinforced and reinforced plastics and electrical insulating materials, West Conshohocken, PA
6. Nairn JA (1988) Fracture mechanics of unidirectional composites using the shear-lag model model II: experiment. J Compos Mater 22:589

Chapter 18
Long Term Life Prediction of CFRP Laminates Under Wet Condition

Masayuki Nakada and Yasushi Miyano

Abstract A general and rigorous advanced accelerated testing methodology (ATM-2) for the long-term life prediction of polymer composites exposed to an actual loading having general stress and temperature history has been proposed. The tensile and compressive static strengths in the longitudinal and transverse directions of unidirectional CFRP under wet condition are evaluated using ATM-2. The applicability of ATM-2 can be confirmed for these static strengths. The effect of water absorption on the time and temperature dependence of these static strengths can be characterized by the viscoelastic behavior of matrix resin.

Keywords CFRP • Life prediction • Water absorption • Time-temperature superposition principle

18.1 Introduction

Carbon fiber reinforced plastics (CFRP) are now being used for the primary structures of airplanes, ships and others, in which the high reliability should be kept during the long-term operation. Therefore, it would be expected that the accelerated testing methodology for the long-term life prediction of CFRP structures exposed under the actual environments of temperature, water, and others must be established.

We have proposed a general and rigorous advanced accelerated testing methodology (ATM-2) which can be applied to the life prediction of CFRP exposed to an actual load and environment history based on the three conditions. One of these conditions is the fact that the time and temperature dependence on the strength of CFRP is controlled by the viscoelastic compliance of matrix resin [1]. The formulations of creep compliance and time-temperature shift factors of matrix resin are carried out based on the time-temperature superposition principle (TTSP). The formulations of long-term life of CFRP under an actual loading are carried out based on the three conditions.

In this paper, the tensile and compressive static strengths in the longitudinal and transverse directions of unidirectional CFRP under wet condition are evaluated using ATM-2. The applicability of ATM-2 and the effect of water absorption on time and temperature dependence of these static strengths are discussed.

18.2 ATM-2

ATM-2 is established with following three conditions: (a) the failure probability is independent of time, temperature and load history [2]; (b) the time and temperature dependence of strength of CFRP is controlled by the viscoelasticity of matrix resin. Therefore, the TTSP for the viscoelasticity of matrix resin holds for the strength of CFRP; (c) the strength degradation of CFRP holds the linear cumulative damage law as the cumulative damage under cyclic loading.

The long-term fatigue strength exposed to the actual loading where the temperature and load change with time can be shown by the following equation based on the conditions (a), (b) and (c).

M. Nakada (✉) • Y. Miyano
Materials System Research Laboratory, Kanazawa Institute of Technology, 3-1 Yatsukaho, Hakusan, Ishikawa 924-0838, Japan
e-mail: nakada@neptune.kanazawa-it.ac.jp

B. Antoun et al. (eds.), *Challenges in Mechanics of Time-Dependent Materials and Processes in Conventional and Multifunctional Materials, Volume 2*, Conference Proceedings of the Society for Experimental Mechanics Series 37,
DOI 10.1007/978-1-4614-4241-7_18,

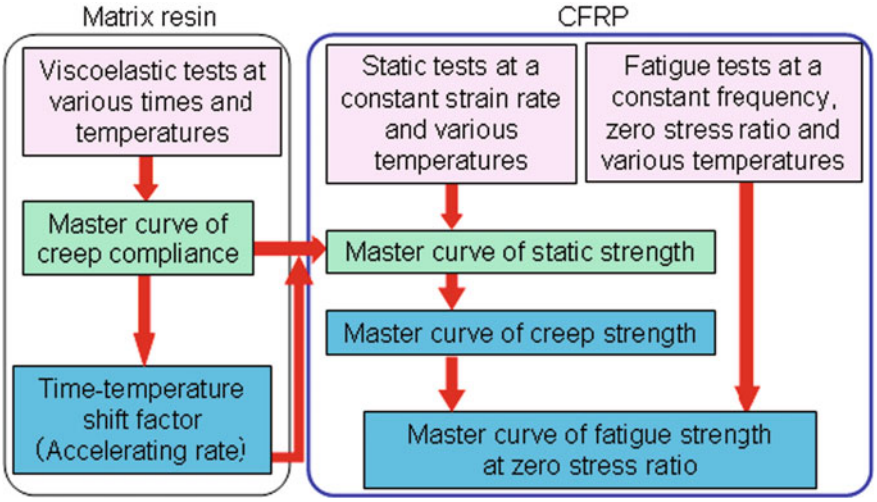

Fig. 18.1 Procedure of ATM-2

$$\log \sigma_{\mathrm{f}}(t', T_0, N_{\mathrm{f}}, R, P_{\mathrm{f}}) = \log \sigma_{\mathrm{f0}}(t_0', T_0) + \frac{1}{\alpha} \log[-\ln(1 - P_{\mathrm{f}})] - n_{\mathrm{r}} \log \left[\frac{D^*(t', T_0)}{D_{\mathrm{c}}(t_0', T_0)}\right] - \frac{(1 - R)}{2} n_{\mathrm{f}} \log(2N_{\mathrm{f}}) + n_{\mathrm{f}}^* \log(1 - k_{\mathrm{D}}) \tag{18.1}$$

The first term of right part shows the reference strength (scale parameter for the static strength) at reduced reference time t_0' under the reference temperature T_0.

The second term shows the scatter of static strength as the function of failure probability P_{f} based on condition (a). α is the shape parameter for the strength.

The third term shows the variation by the viscoelastic compliance of matrix resin which depend on temperature and load histories. n_{r} is the material parameter. The viscoelastic compliance D^* in (18.1) can be shown by the following equation:

$$D^*(t', T_0) = \frac{\varepsilon(t', T_0)}{\sigma(t', T_0)} = \frac{\int_0^{t'} D_{\mathrm{c}}(t' - \tau', T_0) \frac{d\sigma(\tau')}{d\tau'} d\tau'}{\sigma(t', T_0)}, \quad t' = \int_0^t \frac{d\tau}{a_{T_0}(T(\tau))}, \tag{18.2}$$

where D_{c} shows the creep compliance of matrix resin and $\sigma(\tau')$ shows the stress history. t' is the reduced time at T_0, $a_{T\mathrm{o}}$ shows the time-temperature shift factor of matrix resin and $T(\tau)$ shows the temperature history.

The fourth and fifth terms show the degradation by the cumulative damage under cyclic load. The N_{f} and R show the number of cycles to failure and the stress ratio at the final step, respectively. n_{f} and n_{f}^* are the material parameters. The k_{D} shows the accumulation index of damage defined as the following equation based on the condition (c).

$$k_{\mathrm{D}} = \sum_{i=1}^{n} \frac{n_i}{N_{\mathrm{f}i}} < 1, \tag{18.3}$$

where n_i and N_{fi} are the number of cycles and the number of cycles to failure at the loading of step i, respectively.

The procedure for determining the materials parameters in the formulation is illustrated in Fig. 18.1. In this paper, we conduct the viscoelastic tests for matrix resin and the static tests for unidirectional CFRP. The master curves of static strengths can be shown by simplifying (18.1) as

$$\log \sigma_{\mathrm{f}}(t', T_0, N_{\mathrm{f}}, R, P_{\mathrm{f}}) = \log \sigma_{\mathrm{f0}}(t_0', T_0) + \frac{1}{\alpha} \log[-\ln(1 - P_{\mathrm{f}})] - n_{\mathrm{r}} \log \left[\frac{D^*(t', T_0)}{D_{\mathrm{c}}(t_0', T_0)}\right] \tag{18.4}$$

where the viscoelastic compliance D^* in (18.4) can be shown by the following equation assumed the stress history under constant deformation rate loading (static loading) as the step loading shown in Fig. 18.2.

$$D^*(t', T_0) = D_{\mathrm{c}}(t'/2, T_0) \tag{18.5}$$

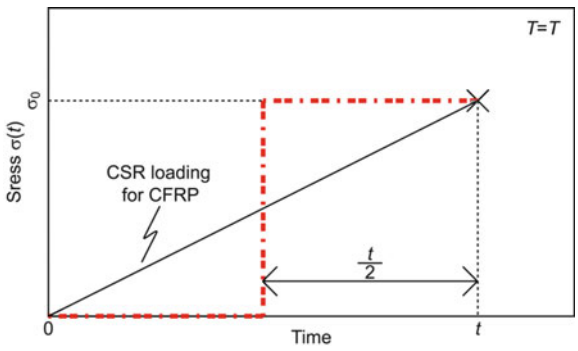

Fig. 18.2 Stress history under constant deformation rate loading (static loading) for determination of the viscoelastic compliance D^*

18.3 Experimental Procedures

Unidirectional CFRP laminates which consist of carbon fiber T300 and epoxy resin 2500 were molded by autoclave technique. The CFRP laminates were cured at 135°C for 2 h and then post-cured at 160°C for 2 h. The aging treatment for post-cured specimen was conducted at 110°C for 50 h. The Wet specimens by soaking the aged specimen (Dry specimen) in hot water of 95°C for 121 h for 1 mm thick specimen in longitudinal direction, 95°C for 144 h for 2 mm thick specimen in longitudinal direction and 95°C for 121 h for 2 mm thick specimen in transverse direction were respectively prepared. The water content of all of wet specimen was 1.9 wt.%

The dynamic viscoelastic tests for the transverse direction of unidirectional CFRP were carried out at various frequencies and temperatures to construct the master curve of creep compliance for matrix resin. The static tests for typical four directions of unidirectional CFRP were carried out at various temperatures to construct the master curves of static strength for unidirectional CFRP. Longitudinal tension tests were carried out according with SACMA 4R-94. Longitudinal bending tests under static and fatigue loadings were carried out according with ISO 14125 to get the longitudinal compressive static strengths. Transverse bending tests were carried out according with ISO 14125 to get the transverse tensile static strengths. Transverse compression tests under static and fatigue loadings were carried out according with SACMA 1R-94.

18.4 Results and Discussion

18.4.1 Viscoelastic Behaviour of Matrix Resin

The left side of Fig. 18.3a shows the loss tangent tan δ for the transverse direction of unidirectional CFRP (Dry specimen) versus time t, where time t is the inverse of frequency. The right side shows the master curve of tan δ which is constructed by shifting tan δ at various constant temperatures along the logarithmic scale of t until they overlapped each other, for the reduced time t' at the reference temperature $T_0 = 25°C$. Since tan δ at various constant temperatures can be superimposed so that a smooth curve is constructed, the TTSP is applicable for tan δ for the transverse direction of unidirectional CFRP. The master curve of tan δ for Wet specimens can be also constructed as shown in Fig. 18.3b. The TTSP is also applicable for tan δ under wet condition. The master curve of tan δ is shifted to the left side by water absorption as shown in Fig. 18.3b.

The left side of Fig. 18.4a shows the storage modulus E' for the transverse direction of unidirectional CFRP (Dry specimen) versus time t. The right side shows the master curve of E' which is constructed by shifting E' at various constant temperatures along the logarithmic scale of t using the same shift amount for tan δ and logarithmic scale of E' until they overlapped each other, for the reduced time t' at the reference temperature $T_0 = 25°C$. Since E' at various constant temperatures can be superimposed so that a smooth curve is constructed, the TTSP is applicable for E' for the transverse direction of unidirectional CFRP. The master curve of E' for Wet specimens can be also constructed as shown in Fig. 18.4b. The TTSP is also applicable for E' under wet condition.

The time-temperature shift factor $a_{To}(T)$ which is the horizontal shift amount shown in Fig. 18.5a can be formulated by the following equation:

$$\log a_{T_0}(T) = \frac{\Delta H_1}{2.303G}\left(\frac{1}{T}-\frac{1}{T_0}\right)\mathrm{H}(T_g - T) + \left[\frac{\Delta H_1}{2.303G}\left(\frac{1}{T_g}-\frac{1}{T_0}\right) + \frac{\Delta H_2}{2.303G}\left(\frac{1}{T}-\frac{1}{T_g}\right)\right]\left(1 - \mathrm{H}(T_g - T)\right) \tag{18.6}$$

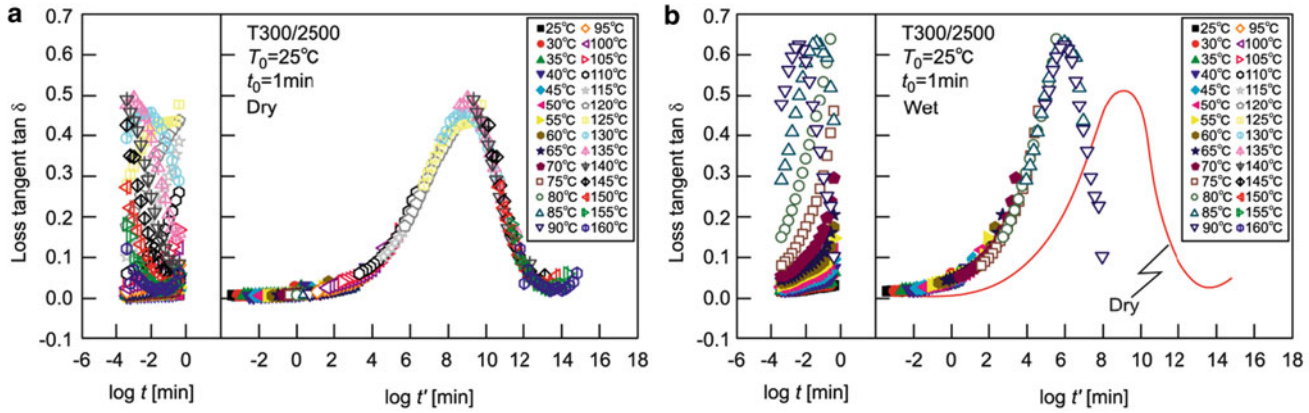

Fig. 18.3 Master curves of loss tangent for transverse direction of unidirectional CFRP

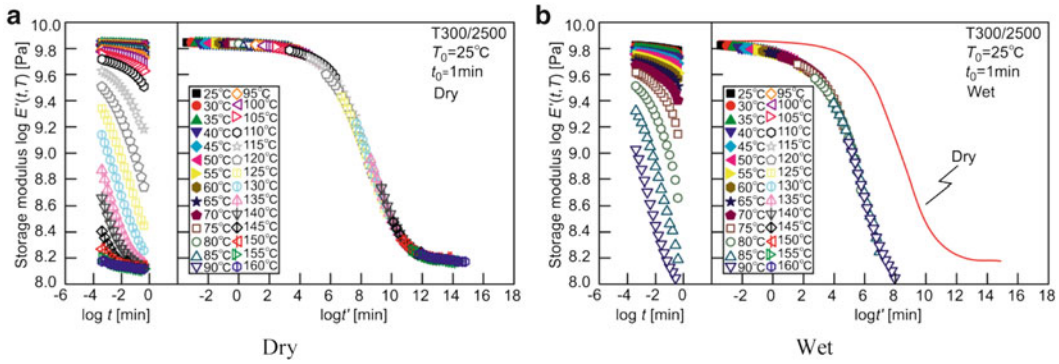

Fig. 18.4 Master curves of storage modulus for transverse direction of unidirectional CFRP

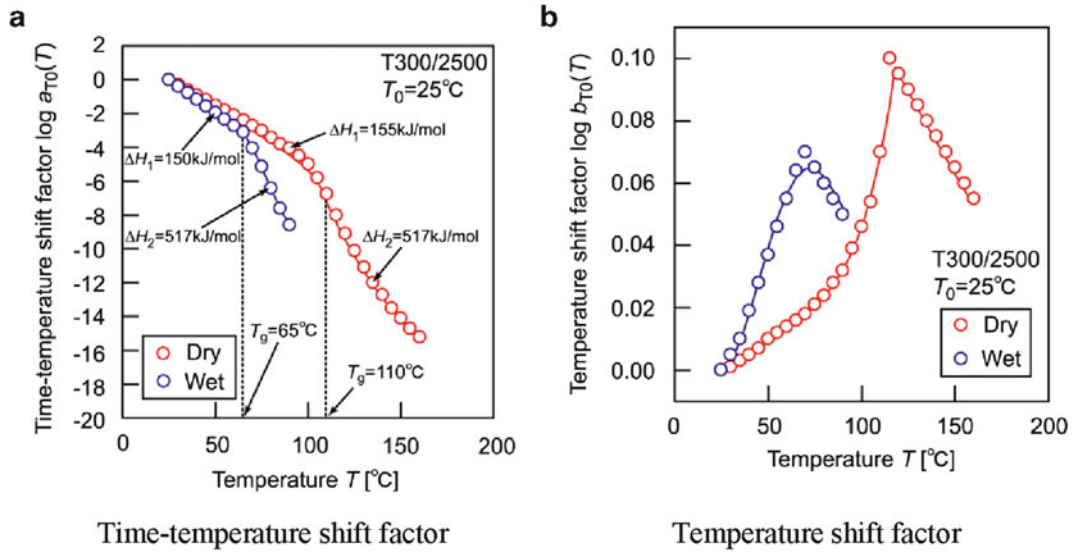

Fig. 18.5 Shift factors of storage modulus for transverse direction of unidirectional CFRP

where G is the gas constant, 8.314×10^{-3} [kJ/(K•mol)], ΔH_1 and ΔH_2 are the activation energies below and above the glass transition temperature T_g, respectively. H is the Heaviside step function.

The temperature shift factor $b_{To}(T)$ which is the amount of vertical shift shown in Fig. 18.5b can be fit with the following equation:

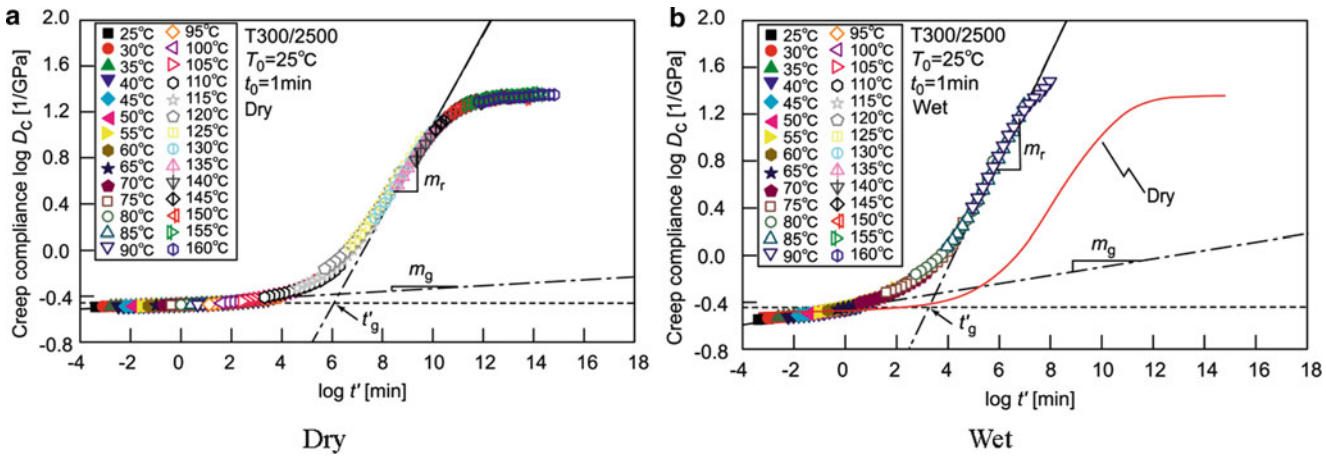

Fig. 18.6 Master curves of creep compliance for matrix resin calculated from the storage modulus for the transverse direction of unidirectional CFRP

Table 18.1 Parameters for master curve and shift factors of creep compliance for matrix resin

	Dry	Wet		Dry	Wet
T_0 (°C)	25	25	ΔH_1 (kJ/mol)	155	150
T_g (°C)]	110	65	ΔH_2 (kJ/mol)	517	547
D_{c0} (1/GPa)	0.337	0.351	b_0	1.65E-02	0.150
t'_0 (min)	1	1	b_1	3.81E-09	1.73E-08
t'_g (min)	1.54E-06	2.34E-03	b_2	−8.29E-07	−4.71E-06
m_g	0.0101	0.0348	b_3	6.64E-05	4.26E-04
m_r	0.405	0.466	b_4	−1.86E-03	−1.39E-02

$$\log b_{T_0}(T) = \left[b_4(T-T_0)^4 + b_3(T-T_0)^3 + b_2(T-T_0)^2 + b_1(T-T_0) + b_0\right]\mathrm{H}(T_g - T) + \left[b_4(T_g-T_0)^4 + b_3(T_g-T_0)^3 + b_2(T_g-T_0)^2 + b_1(T_g-T_0) + b_0 + \log\frac{T_g}{T}\right]\left(1-\mathrm{H}(T_g-T)\right) \quad (18.7)$$

where b_0, b_1, b_2, b_3 and b_4 are the fitting parameters.

The creep compliance D_c of matrix resin was back-calculated from the storage modulus E' for the transverse direction of unidirectional CFRP using [3]

$$D_c(t) \sim 1/E(t),\ E(t) \cong E'(\omega)|_{\omega \to 2/\pi t} \quad (18.8)$$

and approximate averaging method by Uemura and Yamada [4].

The master curve of back-calculated D_c of matrix resin is shown in Fig. 18.6. The master curve of D_c can be formulated by the following equation:

$$\log D_c = \log D_{c,0}(t'_0, T_0) + \log\left[\left(\frac{t'}{t'_0}\right)^{m_g} + \left(\frac{t'}{t'_g}\right)^{m_r}\right] \quad (18.9)$$

where $D_{c,0}$ is the creep compliance at reduced reference time t'_0 and reference temperature T_0, and t'_g is the glassy reduced time on T_0, and m_g and m_r are the gradients in glassy and rubbery regions of D_c master curve. Parameters obtained from the formulations for $a_{To}(T)$, $b_{To}(T)$, and D_c are listed in Table 18.1.

18.4.2 Master Curves of Static Strengths for Unidirectional CFRP

Figures 18.7 and 18.8 show the master curves of static strengths for longitudinal tension X, longitudinal compression X', transverse tension Y and transverse compression Y' for Dry and Wet specimens of unidirectional CFRP obtained from the

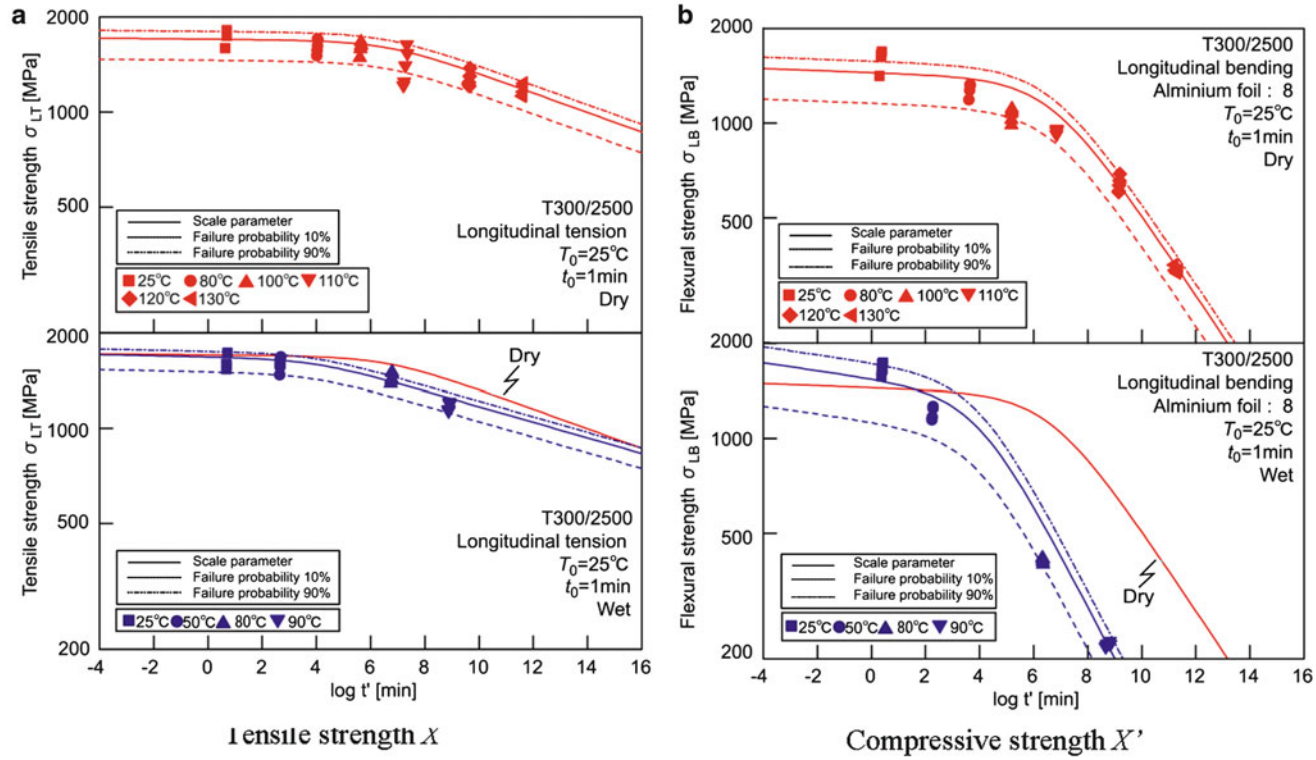

Fig. 18.7 Master curves of tensile and compressive strengths in the longitudinal direction of unidirectional CFRP

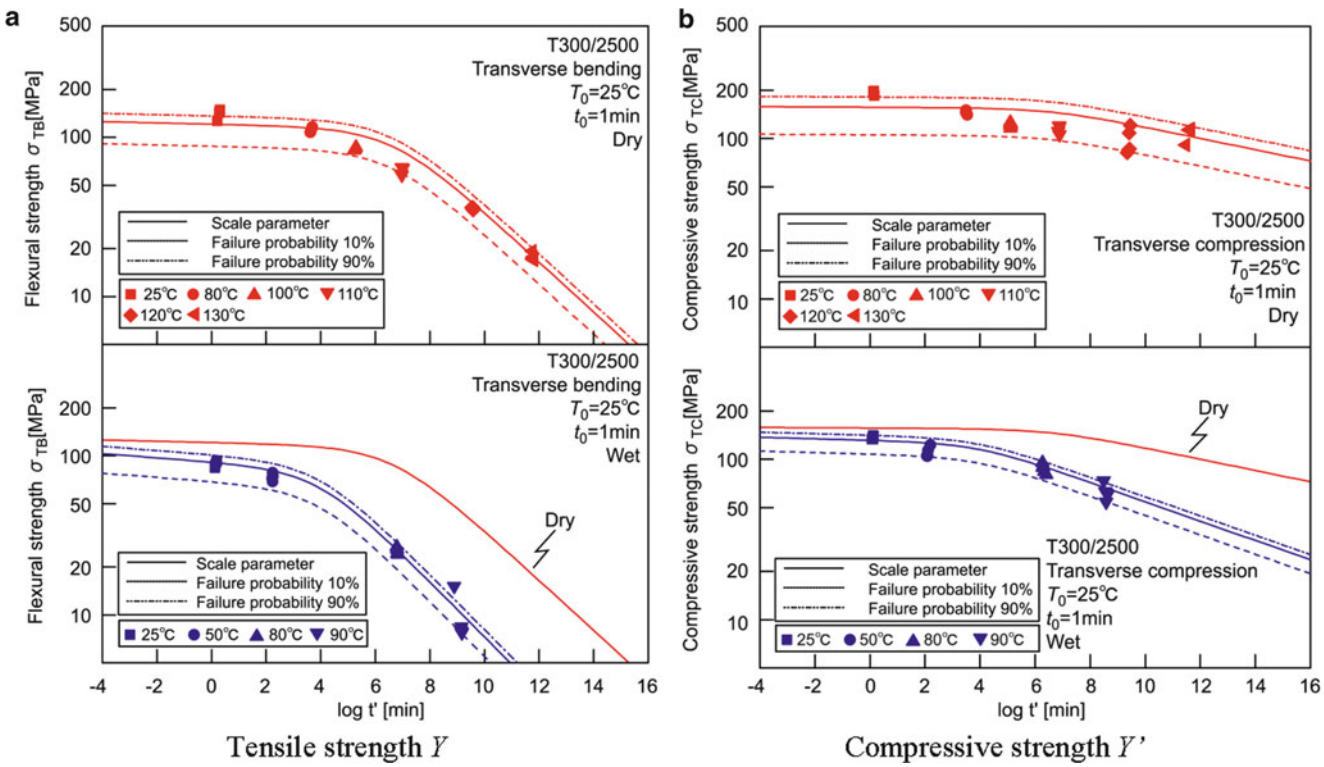

Fig. 18.8 Master curves of tensile and compressive strengths in the transverse direction of unidirectional CFRP

Table 18.2 Parameters for master curve of fatigue strength of unidirectional CFRP

	X		X'		Y		Y'	
	Dry	Wet	Dry	Wet	Dry	Wet	Dry	Wet
σ_{s0} (MPa)	1,700	1,675	1,446	1,535	121	90.6	156	131
n_r	0.0762	0.0528	0.316	0.356	0.387	0.371	0.0868	0.130
α	14.7	20.7	10.0	7.18	7.04	7.97	5.68	11.4

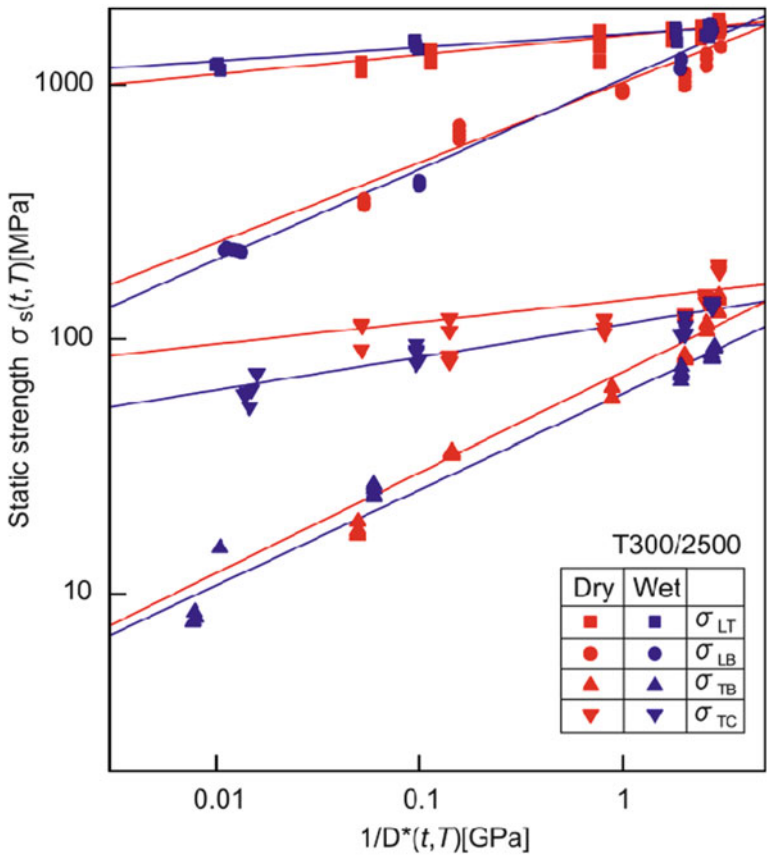

Fig. 18.9 Static strength of unidirectional CFRP versus viscoelastic compliance D^* of matrix resin

strength data at various temperatures by using the time-temperature shift factors a_{To} shown in Fig. 18.5a. The solid and dotted curves in these figures show the fitting curves by (18.4) using the master curves of creep compliance of matrix resin in Fig. 18.6. The parameters obtained by formulation are shown in Table 18.2.

From Figs. 18.7 and 18.8, the static strengths of unidirectional CFRP decrease with increasing time, temperature and water absorption. The time, temperature and water absorption dependencies of static strength of unidirectional CFRP are different with the loading direction. Figure 18.9 shows the relationship between the static strength of unidirectional CFRP and the viscoelastic compliance of matrix resin. The slop of this relation corresponds to the parameter n_r in Table 18.2. The slop depends on the loading direction while that changes scarcely with water absorption. It is cleared from these facts that the time, temperature and water absorption dependencies of static strength of unidirectional CFRP can be determined by the viscoelastic behavior of matrix resin.

18.5 Conclusion

A general and rigorous advanced accelerated testing methodology (ATM-2) for the long-term life prediction of polymer composites exposed to an actual loading having general stress and temperature history has been proposed. The tensile and compressive static strengths in the longitudinal and transverse directions of unidirectional CFRP under wet condition are

evaluated using ATM-2. The applicability of ATM-2 can be confirmed for these static strengths. The time, temperature and water absorption dependencies of static strength of unidirectional CFRP can be determined by the viscoelastic behavior of matrix resin.

Acknowledgements The authors thank the Office of Naval Research for supporting this work through an ONR award with Dr. Yapa Rajapakse as the ONR Program Officer. Our award is numbered to N000140611139 and titled "Verification of Accelerated Testing Methodology for Long-Term Durability of CFRP laminates for Marine Use". The authors thank Professor Richard Christensen, Stanford University as the consultant of this project.

References

1. Miyano Y, Nakada M and Cai H (2008) Formulation of Long-term Creep and Fatigue Strengths of Polymer Composites based on Accelerated Testing Methodology, J. Composite Materials, 42, 1897
2. R.M. Christensen and Y. Miyano, "Stress Intensity Controlled Kinetic Crack Growth and Stress History Dependent Life Prediction with Statistical Variability", Int. J. Fracture, 137, 77 (2006).
3. Christensen RM (1982) Theory of viscoelasticity, 2nd edn. Dover, Mineola, p 142
4. Christensen RM and Miyano Y (2006) Stress Intensity Controlled Kinetic Crack Growth and Stress History Dependent Life Prediction with Statistical Variability, Int. J. Fracture, 137, 77

Chapter 19
Nonlinear Behavior of Natural Fiber/Bio-Based Matrix Composites

Roberts Joffe, Liva Rozite, and Andrejs Pupurs

Abstract The rising concern about the dependence on synthetic polymers and oil has motivated research on competitive bio-based replacement materials. Some of the often considered bio-based thermoplastics are starch, polylactic acid (PLA) and rather recently, lignin. These bio-plastics in combination with natural fibers (flax, hemp, wood) are used to manufacture whole bio-based composites. Although there are certain direct benefits to use natural fibres in composites, their performance is often very nonlinear. Moreover, properties of these materials are very sensitive to moisture and temperature. The behavior of these composites has to be studied and mechanisms occurring during the loading must be identified. The effect of temperature and relative humidity on mechanical behavior of natural fiber reinforced bio-based matrix composites subjected to the tensile loading was investigated. Time dependent behavior of these materials is analyzed. Testing methodology is suggested to identify sources of nonlinearities observed in stress-strain curves. It was found that microdamage accumulation and stiffness reduction is significant for some of the composites but the major nonlinear phenomena are related to nonlinear viscoelasticity and viscoplasticity. Material models accounting for these effects are proposed and their predictive capability is demonstrated.

Keywords Bio-based composites • Viscoepastic and viscoplastic strain • Flax fibers • PLA • Lignin • Creep

19.1 Introduction

The lignin is one of the most common organic molecules found in nature, it accounts for more than one quarter of the non-fossil organic carbon in various biomasses. This material is obtained in vast quantities worldwide as by-product derivative in the pulp and paper industrial processes and it is often used as fuel to power paper mills. Only recently lignin has been considered for applications in composite materials along with other known bio-based polymers. Whereas polylactic acid (PLA) is used not only as neat polymer but also as thermoplastic matrix in composites. The PLA is biodegradable, aliphatic polymer, which can be obtained from renewable resources, such as corn, sugarcane, by fermentation of sugar (in various forms) and is mainly used in medical applications. Nowadays PLA is entering also the packaging market due to its good barrier properties. When used in composites, in combination with reinforcement, such as various types of fibers, these materials exhibit rather decent mechanical properties. In order to maintain advantages of natural origin of the bio-based polymers, it makes sense to use natural fibers as reinforcement to develop wholly bio-based composites. Not only ecologically friendlier material is obtained in this way but reinforcement with natural fibers such as wood or agrofibers gives acceptable performance in terms of mechanical properties. The stiffness of some of the natural fibers (e.g. bast fibers) in longitudinal direction is comparable to that of glass fibers (for example flax fibers have stiffness 50–100 GPa vs. 72 GPa for E-glass fibers) [1–3]. Undoubtedly there are direct benefits of use of natural fibers in composites, such as light weight, reduced wear on the processing equipment and lower impact on the environment. Nevertheless, there are also certain disadvantages of bio-based materials, for example, their high sensitivity to moisture and temperature changes.

R. Joffe (✉) • L. Rozite • A. Pupurs
Luleå University of Technology, S-97187 Luleå, Sweden
e-mail: Roberts.Joffe@ltu.se

B. Antoun et al. (eds.), *Challenges in Mechanics of Time-Dependent Materials and Processes in Conventional and Multifunctional Materials, Volume 2*, Conference Proceedings of the Society for Experimental Mechanics Series 37,
DOI 10.1007/978-1-4614-4241-7_19,

Common processing methods and products of natural fiber composites include injection molding of packages, extrusion of beams for decking, and compression molding of panels for automotive use.

Basic mechanical behavior of natural fiber composites (elastic modulus, strength, strain to failure, impact resistance etc.) has been studied by numerous researchers, an overview of some results can be found in [4–6]. Whereas inelastic and time-dependent properties are not as often considered, some work is done on polypropylene and starch reinforced with flax fibers [7–9], also pulp fiber/formaldehyde composite is investigated [10]. These studies showed that in natural fiber composites the mechanical properties of fibers and the matrix are inherently nonlinear and the composite exhibits complex time dependent stress-strain behavior with loading rate effects and hysteresis loops. The phenomena dominating mechanical behavior may also include evolving microdamage (cracks, debonds etc.) resulting in elastic properties degradation and development of irreversible strains. Therefore, models for these materials should account for viscoelasticy and viscoplasticity accompanied with microdamage.

Generally speaking, the viscoelastic behavior may be nonlinear with respect to stress. Moreover, the irreversible strains even in a simple high stress creep test depend on loading time and the stress level.

This paper is intended as an overview of number of studies [11–13] on mechanical properties of the flax fiber based composite with lignin and PLA matrices. The identified material models for the description of viscoelastic, viscoplastic and stiffness reduction effects are presented here. Optimized set of experiments needed to determine the stress dependent functions in the material model and reliable methodology for data reduction are briefly described.

19.2 Theoretical Background

The modeling approach used to predict behavior of materials used in this study is based on the theory of nonlinear viscoelastic materials developed by Schapery and co-authors [14, 15]. More detailed description about derivation and use of model for one-dimensional case is given in [11]:

$$\varepsilon = d(\sigma_{\max})\left(\varepsilon_0 + g_1\int_0^t \Delta S(\Psi - \Psi')\frac{d(g_2\sigma)}{d\tau}d\tau + \varepsilon_{VP}(\sigma, t)\right) \tag{19.1}$$

where $d(\sigma_{max})$ accounts for microdamage, and the members in brackets are: (1) elastic strain ε_0; (2) the time dependent part of the viscoelastic response (integral in equation); (3) viscoplastic component of strain ε_{VP}. Other functions/constants in (19.1): $\Delta S(\Psi)$—transient component of the linear viscoelastic creep compliance which does not depend on the stress level; g_1 and g_2 are stress dependent material properties; τ—dimensionless time; Ψ—"reduced time" (time normalized with shift factor dependent on stress).

In order to obtain all constants/functions needed to perform modeling, the following tests have to be performed: (a) tensile tests with loading/unloading program to obtain elastic properties of composites and also amount of microdamage introduced by load application; (b) creep/recovery tests at different stresses and time intervals to evaluate viscoelastic strains, obtain stress dependent material constants and estimate accumulation of viscoplastic strains as a function of time and stress.

19.3 Experimental

19.3.1 Materials and Manufacturing of Specimens

Loose 1 mm long flax fibers supplied by Ekotex Kotonia were used as reinforcement for thermoplastic lignin and PLA matrices. Specimens were produced and delivered by Tecnaro GmbH (Germany). The processing procedure was as follows: (1) mixing of the raw materials: matrix, fibers, processing aids, flame retardants; (2) lignin based composite was directly pelletized without heating to produce granules, while PLA based composite was compounded by extruder; (3) granules processed in an injection molding machine in order to produce dog-bone specimens. The specimen thickness was about 3.8–3.9 mm, and width in working zone 10.0–10.1 mm (length of working zone ≈70 mm). Total length (together with clamping part) of specimen was 150 mm and grip separation distance was 100 mm. Specimens were conditioned to obtain materials with different moisture content, they were kept in desiccators at fixed relative humidity (RH) for 2–3 weeks before

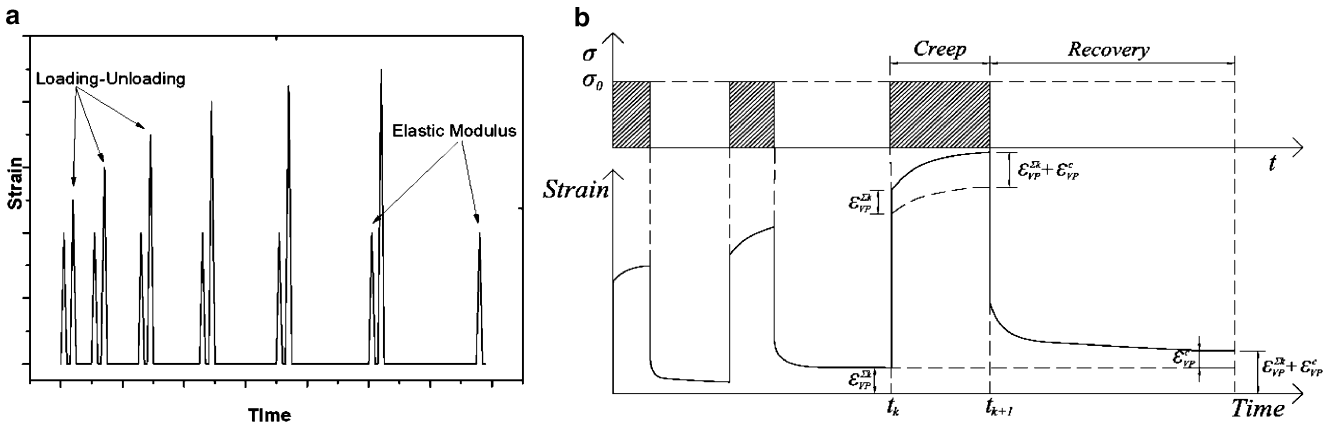

Fig. 19.1 Schematic representation of loading-unloading tensile test (**a**) and multi-step creep experiment (**b**)

testing. The weight of specimens was regularly measured in order to ensure saturation of moisture uptake. Two RH values were used for conditioning: 34% and 66%.

19.3.2 Simple Tensile Tests

Tensile tests were carried out on Instron 3366 testing machine equipped with 10 kN load cell and Instron extensometer with 50 mm base. Tests were performed in displacement controlled mode with the crosshead speed of 5 mm/min, which roughly corresponds to strain rate of 5%/min. All the tests were performed at room temperature. Specimens were loaded until the failure and load, displacement and axial strain were recorded during the test. Later on stress-strain curves were constructed in Excel and the following values determined: (a) maximum stress σ_m and corresponding strain ε_m (called 'strain at maximum stress'); (b) strain and stress to failure σ_f and ε_f; E(3) initial elastic modulus. Elastic modulus was determined in a loading–unloading cycle with the maximum strain value slightly above 0.2%, expecting that no damage and other irreversible phenomena will develop at such low strains. The elastic modulus was defined by the slope of the stress–strain curve in the strain region of 0.05–0.2% strain.

19.3.3 Damage Accumulation in Tension

After specimen is subjected to high stress levels the elastic properties of composite may be degraded. The elastic modulus dependence on the applied maximum stress was measured to evaluate the significance of microdamage developing at high stresses. It consists of a sequence of steps each containing: (a) loading/unloading in low stress region for elastic modulus determination, duration of this step is t_1; (b) recovery for a time $5t_1$; (c) loading up to certain high strain level with following unloading to almost zero stress, the duration of this step is t_2; (d) recovery at almost zero stress level for decay of all viscoelastic effects during time $5t_2$. Then the same sequence (a)–(d) was repeated for a higher level of applied maximum strain in step c). The schematic representation of the damage accumulation cycle is shown in Fig. 19.1a.

19.3.4 Creep and Recovery

Tensile creep tests were performed using a creep rig with dead weights. In Fig. 19.1b the picture on the top represents the load application sequence: creep load is applied in steps and in step k+1 stress is applied instantly at t_k and kept constant for time interval $t_{k+1}-t_k$. The bottom part of picture (Fig. 19.1b) shows creep strain during loading interval and also strain recovery after load removal. The duration of strain recovery interval was at least five times longer than the loading interval.

Creep strains (measured using extensometer) were recorded during the loading and also during the following interval of strain recovery after load removal.

The irreversible strains at the end of the recovery period (if present) are considered in analysis as viscoplastic (VP). Creep tests used for determination of time and load dependence of VP-strains were in multiple steps over time intervals of 10, 20 and 30 min.

19.4 Results and Discussion

It should be noted that due to limitation of space only selected results are presented in this section, more details can be found in [11–13].

The tensile stress-strain curves for flax/PLA (with 10 wt.% of fibers) and flax/lignin (with 30 wt.% of fibers) composites conditioned at different relative humidity (RH = 34 and 66%) are presented in Fig. 19.2. Since fiber content is higher in lignin based than in PLA based composite, flax/lignin is stiffer than flax/PLA, although higher maximum stress was achieved by PLA based material. Results show very significant influence of relative humidity (and resulting moisture content) on mechanical performance of both materials. This influence is rather expected and similar for both, PLA and lignin, composites: stiffness and strength is decreased with increased moisture content. Table 19.1 shows the average mechanical properties of composites obtained at different moisture contents and temperatures (standard deviation is given in brackets). These results show that temperature also affects mechanical properties of composites similarly to the moisture, the properties are decreased.

Damage accumulation curves for PLA and lignin composites conditioned at RH = 34% are shown in Fig. 19.3. It is rather obvious that stiffness reduction is very small in PLA based composite, as a matter of fact, there is almost no decrease

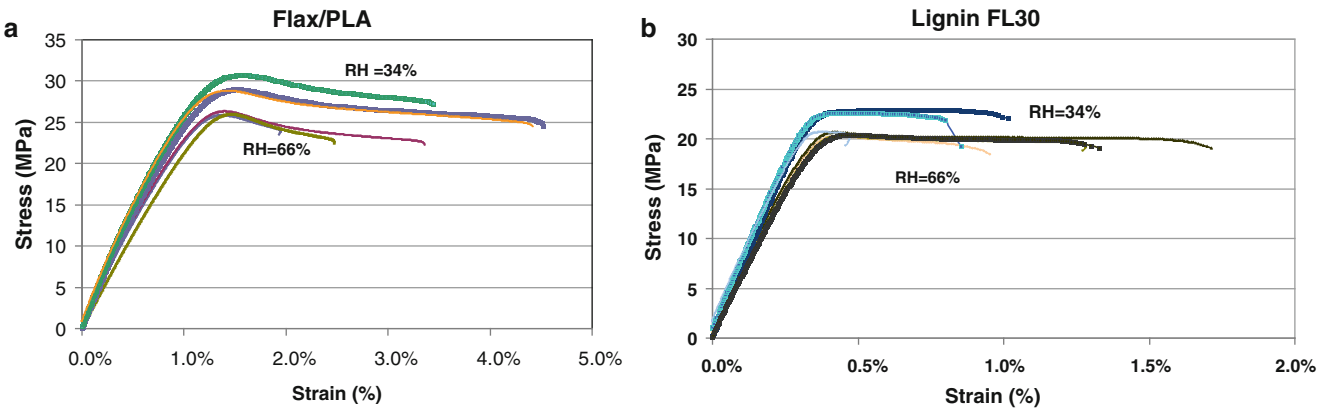

Fig. 19.2 Stress-strain curves for flax/PLA (**a**) and flax/lignin (**b**) composites conditioned at different relative humidity

Table 19.1 Average mechanical properties of composites conditioned at different relative humidity (RH = 34% and 66%) and tested at different temperature (T = 22°C, 30°C and 35°C)

		Flax/PLA			Flax/lignin		
RH (%)	T (°C)	E (GPa)	ε_{max} (%)	σ_{max} (MPa)	E (GPa)	ε_{max} (%)	σ_{max} (MPa)
34	22	6.54 (0.41)	0.40 (0.01)	22.1 (1.2)	3.05 (0.11)	1.50 (0.05)	29.5 (1.0)
	30	6.88 (0.14)	0.40 (0.02)	21.5 (1.9)	2.89 (0.20)	1.48 (0.02)	28.1 (0.2)
	35	6.56 (0.28)	0.39 (0.02)	21.8 (0.7)	2.84 (0.14)	1.30 (0.05)	25.3 (0.4)
66	22	5.99 (0.16)	0.41 (0.01)	20.3 (0.1)	2.60 (0.24)	1.40 (0.03)	26.1 (0.2)
	30	5.69 (0.13)	0.44 (0.03)	18.7 (1.1)	2.56 (0.10)	1.34 (0.03)	23.8 (0.3)
	35	4.86 (0.48)	0.43 (0.02)	16.2 (3.0)	2.59 (0.19)	1.29 (0.03)	22.2 (0.3)

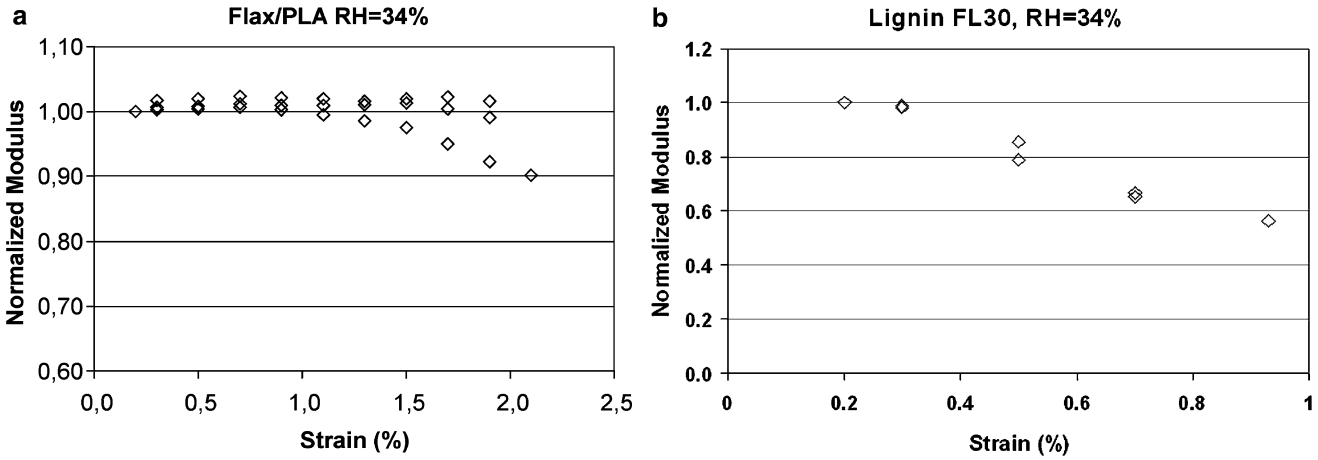

Fig. 19.3 Reduction of stiffness for flax/PLA (**a**) and flax/lignin (**b**) composites conditioned at RH = 34%

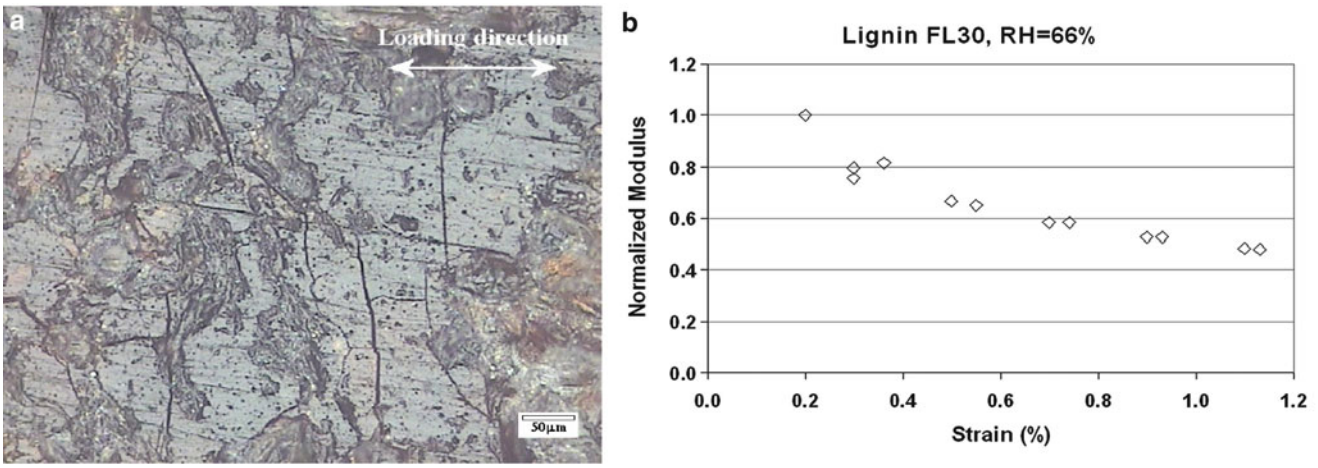

Fig. 19.4 Micrograph of flax/lignin composite (**a**) showing microdamage and reduction of stiffness (**b**) for this material conditioned at RH = 66%

of modulus at all, except for one specimen. On the other hand, in lignin based material the decrease of modulus with increasing load is very significant. This means that damage accumulation will not affect strain calculated by (19.1) and the $d(\sigma_{max}) = 1$. However, damage effects cannot be neglected for flax/lignin composite. The micrograph which shows microcracks in flax/lignin composite is shown in Fig. 19.4a, along with stiffness degradation for material conditioned at RH = 66%. The creep results for flax/PLA composite along with viscoplastic strains are presented in Fig. 19.5. The strain development for flax/lignin composite during the creep tests at different stress levels and for different moisture contents are presented in Fig. 19.6. As expected, material with higher moisture content exhibits more creep.

The results obtained in the presented experiments are used to obtained material constants and functions (see [11]) needed for simulation of creep curves as well as stress-strain curves for the studied composites. The results of these simulations are presented in Figs. 19.7 and 19.8.

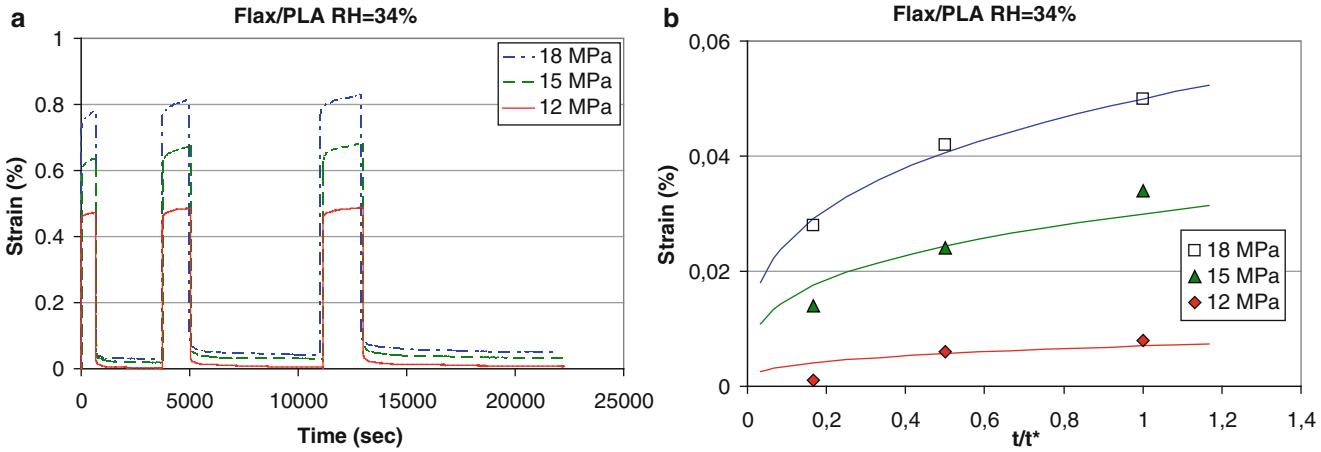

Fig. 19.5 Creep results for flax/PLA composite (**a**) accumulation of viscoplastic strain (**b**)

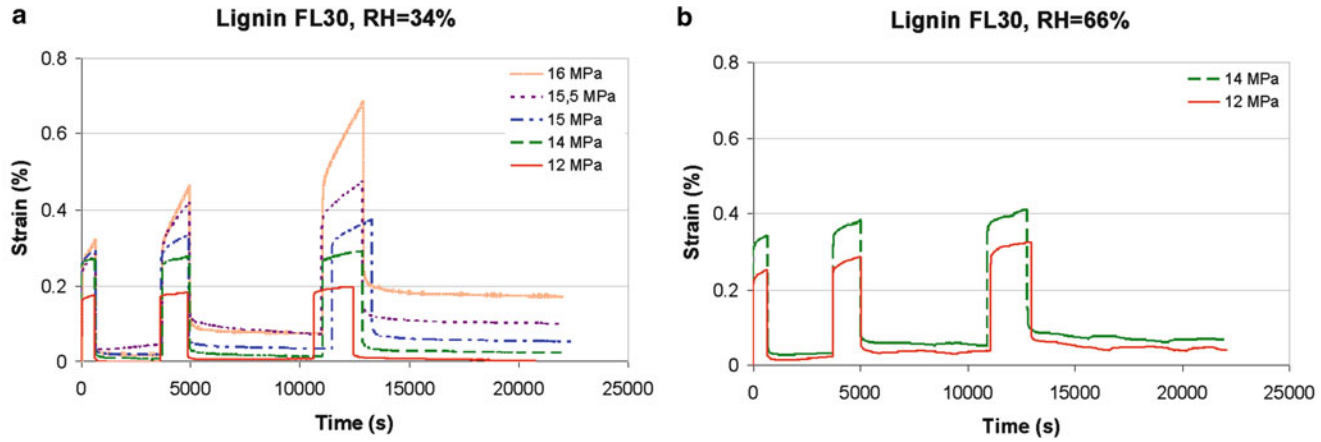

Fig. 19.6 Creep results for flax/lignin composite for different relative humidity, 34% (**a**) and 66% (**b**)

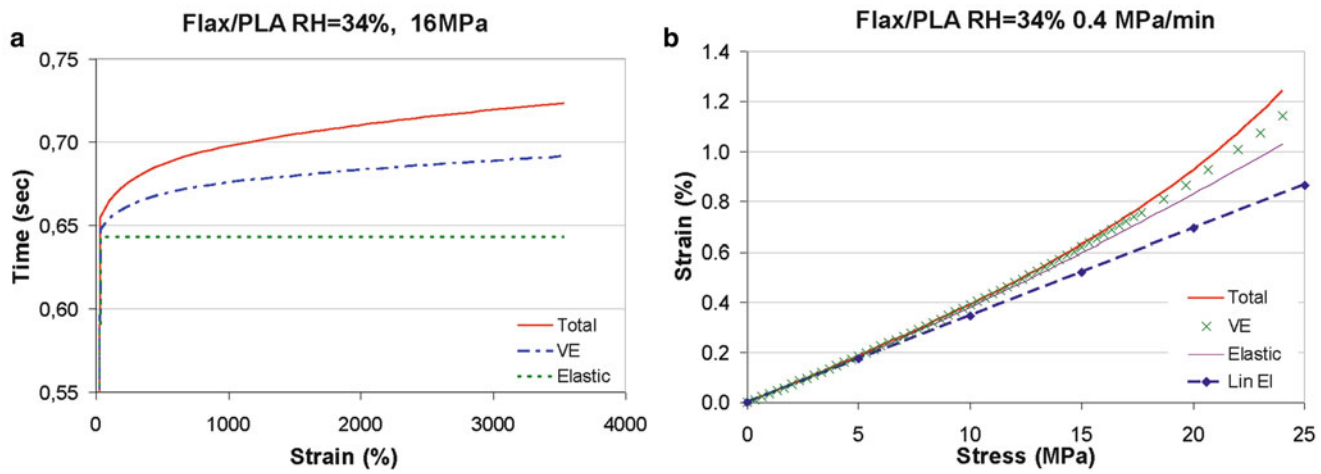

Fig. 19.7 Simulation results for: (**a**) creep tests, (**b**) constant stress rate tensile test for flax/PLA

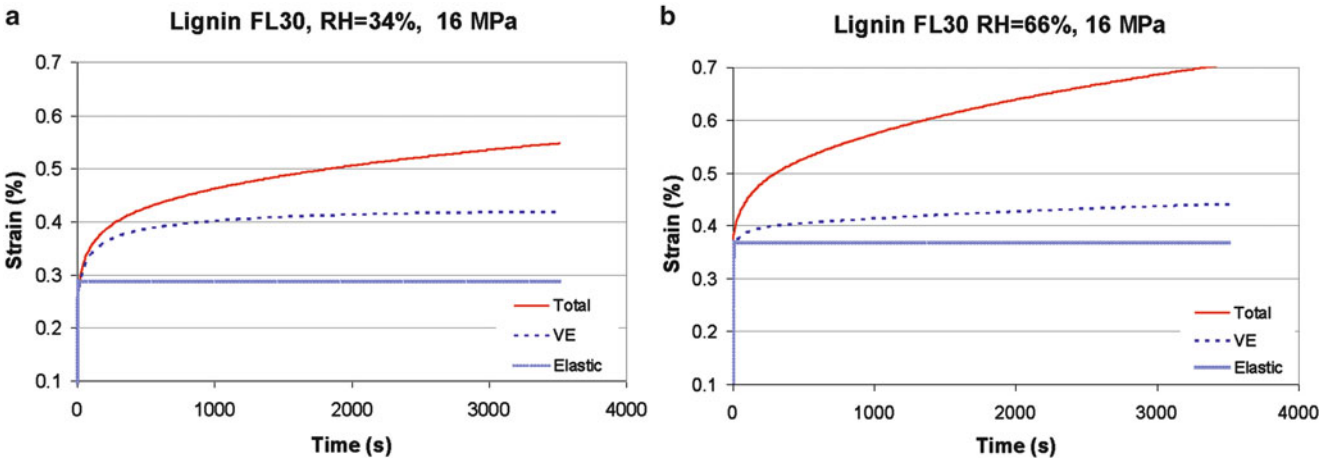

Fig. 19.8 Simulation for creep tests of flax/lignin composite conditioned at 34% (**a**) and 66% (**b**) RH

19.5 Summary

Comprehensive characterization of flax/PLA and flax/lignin composite mechanical properties in tension has been carried out. Simple tensile tests, loading-unloading experiments as well as creep with recovery were done. The effect of moisture and temperature on the mechanical performance of these materials has been demonstrated. As expected, moisture as well as temperature have very strong effect on mechanical properties of bio-based composites. Stiffness and strength are reduced by presence of moisture and development of strain in creep is significantly increased (roughly by 50% in flax/lignin composite). The initiation (and accumulation) of micro-damage and its effect on material stiffness depends on the bio-polymer used in composite. This is because the damage is in the form of matrix cracks and their initiation and propagation depends on fiber/matrix adhesion as well as on ductility of polymer. It was shown that stiffness reduction in flax/PLA composite is very small and therefore its effect on the performance of these composites can be neglected. However, stiffness was very significantly affected (reduced by up to 55%) by loading (and resulting micro-damage) in flax/lignin composites. Higher moisture content in lignin based material promoted larger drop in stiffness, modulus was reduced by 45% and 55% for the materials conditioned at RH = 34% and RH = 66% respectively.

Input parameters obtained from mechanical characterization were used in simulations of creep curve and also stress-strain curve in tension.

References

1. Lilholt H, Lawther JM (2000) Natural organic fibres, comprehensive composite materials, vol 1. Oxford, Elsevier Science, pp 303–325
2. Joffe R, Andersons J, Wallstrom L (2003) Strength and adhesion characteristics of elementary flax fibres with different surface treatments. Compos Appl Sci Manuf 34A:603–612
3. Andersons J, Sparnins E, Joffe R, Wallstrom L (2005) Strength distribution of elementary flax fibres. Compos Sci Technol 65:693–702
4. Bledzki AK, Gassan J (1999) Composites reinforced with cellulose based fibres. Prog Polym Sci 24:221–274
5. Nabi Saheb D, Jog JP (1999) Natural fiber polymer composites: a review. Adv Polym Technol 18(4):351–363
6. Pandey JK, Ahn SH, Lee CS, Mohanty AK, Misra M (2010) Recent advances in the application of natural fiber based composites. Macromol Mater Eng 295(11):975–989
7. Marklund E, Varna J, Wallstrom L (2006) Nonlinear viscoelasticity and viscoplasticity of flax/polypropylene composites. J Eng Mater Technol 128(4):527–536
8. Sparnins E, Pupurs A, Varna J, Joffe R, Nattinen K, Lampinen J (2011) The moisture and temperature effect on mechanical performance of flax/starch composites in quasi-static tension. Polym Compos 32(12):2051–2061
9. Sparnins E, Varna J, Joffe R, Nattinen K, Lampinen J (2012) Time dependent behavior of flax/starch composites. Mech Time-Depend Mater 16(1):47–70
10. Nordin L-O, Varna J (2005) Nonlinear viscoelastic behavior of paper fiber composites. Compos Sci Technol 65:1609–1625
11. Varna J, Rozite L, Joffe R, Pupurs A (2012) Nonlinear behavior of PLA based flax composites. Plast Rubber Compos 41(2):49–60
12. Varna J, Rozite L, Joffe R, Pupurs A (2012) Nonlinear behavior of PLA and lignin based flax composites subjected to tensile loading. J Thermoplast Compos Mater. Available on-line prior to publication.
13. Rozite L, Varna J, Joffe R, Pupurs A (2012) Analysis of nonlinear behavior of lignin based flax composites. Mech Compos Mater (submitted)
14. Lou YC, Schapery RA (1971) Viscoelastic characterization of a nonlinear fiber-reinforced plastic. J Compos Mater 5:208–234
15. Schapery RA (1997) Nonlinear viscoelastic and viscoplastic constitutive equations based on thermodynamics. Mech Time-Depend Mater 1(2):209–240

Chapter 20
A Pressure-Dependent Nonlinear Viscoelastic Schapery Model for POM

D. Tscharnuter, S. Gastl, and G. Pinter

Abstract The nonlinear viscoelastic behavior of POM was characterized in tensile and compression tests. Digital image correlation strain measurements were used the determine the axial and transverse strain, thus providing the necessary data for three-dimensional modeling. The nonlinear viscoelastic model of Schapery was chosen to describe the time-dependent mechanical behavior. A parameter identification procedure using nonlinear optimization is presented. It is shown that the Schapery model is capable of describing the nonlinear viscoelastic relaxation behavior in tension and compression.

20.1 Introduction

Polyoxymethylene (POM) is used in components such as gears, hinges or rolls, which may experience complex stress states, including compression or bending, over extended periods of time during their service life. An accurate simulation of the mechanical performance of such componentes thus requires a model for the nonlinear viscoelastic behavior that can account for general stress states. Thermoplastics exhibit a strong dependence on the hydrostatic pressure of the elastic properties [1], time-dependence [2] and yield behavior [3, 4]. This effect can be analysed in compression tests (e.g. [5]), but in comparison to tensile testing, compression testing requires a much greater effort in specimen preparation and care in conducting the experiments. For a typical specimen height of 10 mm, a strain of 0.1% corresponds to a length change of 10 μm. This illustrates the high precision requirements on the load transmission and specimen manufacture, in particular for precise measurements at low strains. Due to the simplicity of tensile testing, mechanical characterization is often based on tensile testing and consequently models are built on tensile data only. For a more generally applicable model, the effect of the hydrostatic pressure should be accounted for.

The model of Schapery has been widely used to model the nonlinear viscoelastic behavior of polymers. Numerous studies rely on 1d data and the Schapery model is taken in its 1d form. The model has been derived [6] and applied [7, 8] in a 3d form, but its application is apparently somewhat limited by the lack of 3d data. In his pioneering work, Schapery presented parameter identification strategies using creep and creep recovery tests [9]. In these methods, step loading is assumed to simplify the model equation in order to obtain simple equations for calculating the model parameters. Nordin and Varna [10] have discussed the errors that can arise from the step loading idealization and developed an improved method. When the model is to be applied to arbitrary load histories, a technique to solve the model equation without assumptions on the type of load history is needed. A general recursive strategy for this purpose has been developed for use in FE simulations [11]. In a previous work [12], we have used such a recursive strategy within a nonlinear optimization algorithm for parameter identification by fitting the model to experimental data. The generality of this method enables the use of an arbitrary set of data without restricting mathematical assumptions that need to be satisfied in the mechanical tests.

With the aim of defining a model that can be applied in the tensile as well as the compressive regime, we investigate the applicability of the 3d Schapery model for modeling the response to various uniaxial compressive and tensile load histories. Digital image correlation is used for optical strain measurement to provide axial as well as transverse strains for a complete

D. Tscharnuter (✉) • S. Gastl
Polymer Competence Center Leoben GmbH, Roseggerstrasse 12, 8700 Leoben, Austria
e-mail: tscharnuter@pccl.at

G. Pinter
Institute of Materials Science and Testing of Plastics, Otto-Glöckel-Strasse 2, 8700 Leoben, Austria

B. Antoun et al. (eds.), *Challenges in Mechanics of Time-Dependent Materials and Processes in Conventional and Multifunctional Materials, Volume 2*, Conference Proceedings of the Society for Experimental Mechanics Series 37,
DOI 10.1007/978-1-4614-4241-7_20,

description of the stress-strain behavior. The paper is organized as follows. In Sect. 20.2 we give a brief account of the experimental procedures. In Sect. 20.3, we introduce the pressure-dependent formulation of the model and the algorithm for solving the model equation. Finally, we discuss optimization techniques for the determination of parameters in Sect. 20.4 and present results in Sect. 20.5.

20.2 Experimental

20.2.1 Material

The investigated polyoxymethylene is Tenac 3010 produced by Asahi Kasei. ISO 3176 type B specimens were injection-molded.

20.2.2 Tensile Tests

Tensile relaxation tests were performed using an electro-mechanical testing machine (Zwick Z250; Zwick-Roell, Ulm, Germany) equipped with an extensometer to control strain rate and target strain. Axial and transverse strain were measured using the digital image correlation system ARAMIS (GOM mbH, Germany). Details are given in Ref. [13]. For this study, the measurement was performed in 3d mode using 105 mm lenses. The true longitudinal strain $\varepsilon_{t,\,l}$ and transverse strain $\varepsilon_{t,\,t}$ are calculated from the respective engineering strains, $\varepsilon_{e,\,l}$ and $\varepsilon_{e,\,t}$ by

$$\varepsilon_{t,l} = \ln(\varepsilon_{e,l} + 1) \tag{20.1}$$

and

$$\varepsilon_{t,t} = \ln(\varepsilon_{e,t} + 1) \tag{20.2}$$

The true stress is defined as

$$\sigma_t = \frac{F}{A_0} \frac{1}{(1 + \varepsilon_{e,t})^2} \tag{20.3}$$

where F is the force and A_0 the cross-sectional area of the unstrained specimens.

20.2.3 Compression Tests

Compression tests were carried out on an electro-mechanical testing machine (Instron 5500; Instron, Norwood, USA). The setup utilizes a compression tool with highly accurate aligning bars and ball linings and polished compression plates. The axial strain is controlled by an LVDT. This is setup is presented in detail elsewhere [14].

Compression specimens with a length of 10 mm were machined from the multipurpose specimens, thus the exact same material is used for tensile and compression tests. Before each test a preload of 10 N was applied before zeroing the LVDT. PTFE spray was used to lubricate the compression plates to reduce friction. To avoid the cumbersome calibration procedure for 3d measurements in the confined space of the compression tool axial and transverse strain were measured with ARAMIS in 2d mode using telecentric lenses (S5LPJ0625, Sill Optics, Germany). Compared to standard lenses telecentric lenses are significantly less sensitive to out of plane-errors [15]. Despite this, the obtained lateral strain was fairly high, giving Poisson's ratio values in excess of 0. 5. The reasons for the erroneous transverse strain results have yet to be determined. We suspect an effect of the non-rectangular specimen cross-section due the sink mark along the length of the specimen. Because of the limited number of available compression specimens, this could not be investigated within this study. Instead, two stress relaxation and two creep tests were analysed with a 3d setup with 50 mm lenses. The two optical setups yielded consistent axial data, but much smaller lateral strain values were measured with the 3d setup.

20.3 Schapery Model

In this section, we outline the Schapery model equation and the recursive solving method. The equations are expressed in Voigt notation and summation is implied for repeated indices. The Schapery equation is written as

$$\varepsilon_i(t) = g_0 D_{ij}^{(0)} \sigma_j(t) + \left(\frac{\partial g_1}{\partial \sigma_i} \sigma_j + g_1 \delta_{ij} \right) \int_0^t \Delta S_{jk}(\psi(t) - \psi(\tau)) \frac{dg_2 \sigma_k(\tau)}{d\tau} d\tau \tag{20.4}$$

Here, $D^{(0)}$ is the initial and ΔS the transient compliance matrix and g_i are nonlinearizing functions. The shifted time ψ is defined by

$$\psi(t) = \int_0^t \frac{1}{a_\sigma} d\tau \tag{20.5}$$

with the nonlinearizing time-shift function a_σ. We assume a Prony series is for transient part of the compliance. The M-term Prony series is expressed with inverse retardation times $\lambda^{(m)} = 1/\tau^{(m)}$ as

$$\Delta S_{jk}(t) = \sum_{m=1}^{M} S_{jk}^{(m)} \left(1 - \exp(-\lambda^{(m)} t) \right) \tag{20.6}$$

The compliance matrices $S^{(m)}$ reflect the material symmetry, see e.g. Ref. [8] for orthotropic material properties. For the unfilled POM we assume isotropic behavior, i.e.

$$S_{jk}^{(m)} = J^{(m)} \begin{pmatrix} 1 & -\nu^{(m)} & -\nu^{(m)} & 0 & 0 & 0 \\ -\nu^{(m)} & 1 & -\nu^{(m)} & 0 & 0 & 0 \\ -\nu^{(m)} & -\nu^{(m)} & 1 & 0 & 0 & 0 \\ 0 & 0 & 0 & 2(1+\nu^{(m)}) & 0 & 0 \\ 0 & 0 & 0 & 0 & 2(1+\nu^{(m)}) & 0 \\ 0 & 0 & 0 & 0 & 0 & 2(1+\nu^{(m)}) \end{pmatrix} \tag{20.7}$$

where $J^{(m)}$ and $\nu^{(m)}$ are compliance and Poisson coefficients. Lévesque et al. [6] have introduced nonlinearizing functions depending on the stress via invariants of the stress tensor. We follow this isotropic approach and account for the pressure dependence by defining

$$g_z = g_z(h^{(z)}(\sigma)) = g_z\left(\alpha^{(z)} I_1 + \sqrt{J_2} \right) \tag{20.8}$$

where $z = 0...3$ indexes the nonlinearizing functions and $z = 3$ refers to a_σ. g_0, g_1, g_2 and $1/a_\sigma$ are chosen as polynomial functions of $h^{(z)}$.

The model equation is efficiently solved using a recursive procedure based on a Prony series model for the compliance [11]. The 2RA algorithm [16] is an algorithm of this type and will be used in this study. In what follows the superscript $n+1$ denotes evaluation at time t^{n+1}, e.g. $g_0^{n+1} = g_0(h^{(0)}(\sigma(t^{n+1})))$. Substituting Eq. (20.6) into Eq. (20.4) gives

$$\varepsilon_i^{n+1} = g_0^{n+1} D_{ij}^{(0)} \sigma_j^{n+1} + g_{1,ij}^{n+1} \sum_{m=1}^{M} S_{jk}^{(m)} g_2^{n+1} \sigma_k^{n+1} - g_{1,ij}^{n+1} \sum_{m=1}^{M} S_{jk}^{(m)} q_k^{(m),n+1} \tag{20.9}$$

where

$$g_{1,ij} = \frac{\partial g_1}{\partial \sigma_i} \sigma_j + g_1 \delta_{ij} \tag{20.10}$$

and

$$q_k^{(m),n+1} = \int_0^{t_{n+1}} \exp\left(-\lambda^{(m)} \left(\psi^{n+1} - \psi(\tau) \right) \right) \frac{dg_2(\tau)\sigma_k(\tau)}{d\tau} d\tau \tag{20.11}$$

This integral is split into integrals up to time step t_n and from t_n to t_{n+1} to derive the recursive relation [16]

$$q_k^{(m),n+1} = q_k^{(m),n} \exp(-\lambda^{(m)} \Delta\psi^{n+1}) + (g_2^{n+1}\sigma_k^{n+1} - g_2^n \sigma_k^n)\, \Upsilon^{(m),n+1} \tag{20.12}$$

The incremental reduced time is calculated by

$$\Delta\psi^{n+1} = \psi^{n+1} - \psi^n = \frac{\Delta t}{2}\left(\frac{1}{a_\sigma^{n+1}} + \frac{1}{a_\sigma^n}\right) \tag{20.13}$$

and

$$\Upsilon^{(m),n+1} = \exp\left(\frac{-\lambda^{(m)}\Delta t}{2\, a_\sigma^{n+1}}\right) \frac{1 - \exp\left(\dfrac{-\lambda^{(m)}\Delta t}{2\, a_\sigma^n}\right)}{\dfrac{-\lambda^{(m)}\Delta t}{2\, a_\sigma^n}} + \frac{1 - \exp\left(\dfrac{-\lambda^{(m)}\Delta t}{2\, a_\sigma^{n+1}}\right)}{\dfrac{-\lambda^{(m)}\Delta t}{2\, a_\sigma^{n+1}}} \tag{20.14}$$

with $\Delta t = t^{n+1} - t^n$.

20.4 Determination of Model Parameters

We examine nonlinear optimization techniques to identify the model parameters, specifically the compliance and Poisson coefficients of the Prony series, the polynomial coefficients of the nonlinearizing functions, and the weights $\alpha^{(z)}$ for the first invariant of the stress tensor. The following procedure is the 3d formulation of the method we introduced in one dimension [12].

For the j-th test, the i-th strain component $\hat{\varepsilon}_i^{(j),n}$ is calculated using the experimentally measured stress history and Eqs. (20.9)–(20.14) for all time points t_n. The obtained values depends on the set of parameters,

$$\hat{\varepsilon}_i^{(j),n} = \hat{\varepsilon}_i^{(j),n}(J, \nu, g_0, g_1, g_2, 1/a_\sigma, \alpha) \tag{20.15}$$

The bold symbols denote vectors of the parameters belonging to the symbol, e.g. g_0 denotes the polynomial coefficients of g_0. For each test a measure of the error between the measured strain and the model strain is computed by

$$E_l = \sum_{n=1}^{N} \sum_{i=1}^{3} \left(\varepsilon_i^{(j),n} - \hat{\varepsilon}_i^{(j),n}\right)^2 \tag{20.16}$$

where $\varepsilon_i^{(j),n}$ is the measured strain at time t_n of test l. The best set of parameters minimizes the total error

$$E = \sum_l E_l \tag{20.17}$$

where the sum extends over all considered tests. Thus, in this least-squares problem, we seek the best fit of the model to all input data from several tests. Constraints on the parameters are imposed due to physical requirements [6]. First, all polynomial coefficients of the nonlinearizing functions are positive to enforce monotonic behavior. This ensures that the material becomes more compliant with increasing stress in accordance with the experimentally determined material response. The constant term of the polynomial equals unity for linear viscoelastic limiting behavior. Second, the Prony series coefficients are positive to guarantee a monotonic time dependence. The retardation times $\lambda^{(m)}$ were prescribed to reduce the number of parameters for the optimization. Additionally, the constraints $\alpha^{(z)} \geq 0$ are imposed, which implies that a negative hydrostatic stress leads to a less pronounced nonlinearity, which is consistent with the experimental observations. Prior to the optimization of the viscoelastic parameters, the data points are mapped to 250 logarithmically spaced time points by linear interpolation to provide an even contribution of all data points regardless of the rate of data acquisition.

A substantial number of optimization algorithms have been proposed [17], for a variety of problems and with varying performance. In the context of parameter identification of material models, performance is not only determined by the computational effort of the parameter identification, but also by the effort involved in understanding, implementing and

applying the algorithm. The understanding of state-of-the-art algorithms may be hard and time-consuming work for researchers or engineers of different fields, but when commercial software is used this effort is substantially reduced. Implementation and application of the algorithm is facilited by manuals and examples. Several optimization algorithms are e.g. provided by the MATLAB Optimization Toolbox (The MathWorks, Inc.) or the optimization tool LS-Opt (LSTC Inc.).

20.5 Results

20.5.1 Stress Relaxation in Tension and Compression

Stress relaxation tests in tension and compression were carried out with axial strains below 2.5% (Fig. 20.1), which was identified as a limiting strain in a series of strain recovery tests performed as described in Ref. [18]. We emphasize that these tests establish load limits for viscoelastic behavior only for the specific monotonic loading tested. Hence, we must assume that no viscoplastic strain is generated during the stress relaxation. With regard to this consideration and the amount of time needed to conduct experiments, the testing time was typically limited to 3 h or roughly 10^4 s.

20.5.2 Identification of Model Parameters from Relaxation Tests

In this study, we use the trust-region reflective algorithm (*lsqnonlin*, MATLAB) to find the best parameters. This algorithm is local, i.e. it finds a minimum close to a starting guess for the parameters. In general, nonlinear optimization problems may have several local minima and hence the choice of the initial value can be crucial for the success of the optimization. Finding a suitable initial guess may require a number of parametric studies and trial and error-computations to establish rough values. We choose fourth degree polynomials for the nonlinearizing functions g_0, g_2 and a_σ and a quadratic polynomial for g_1. Including the pressure weights $\alpha^{(z)}$, this amounts to 20 parameters for the nonlinear behavior. With this relatively large number of parameters, many trial and error calculations are needed. Including a N-term Prony series, the total number of parameters is $22 + 2 * N$. We found that optimization in this high dimensional parameter space does not lead to satisfactory results. In the following section, we discuss a strategy using optimization runs in subspaces for finding a suitable minimum, thus avoiding trial and error runs. We will use a data set of five tensile and five compression relaxation tests for the parameter identification. As we formulate the model with stress as the independent variable, the strain controlled relaxation tests constitute complex load histories.

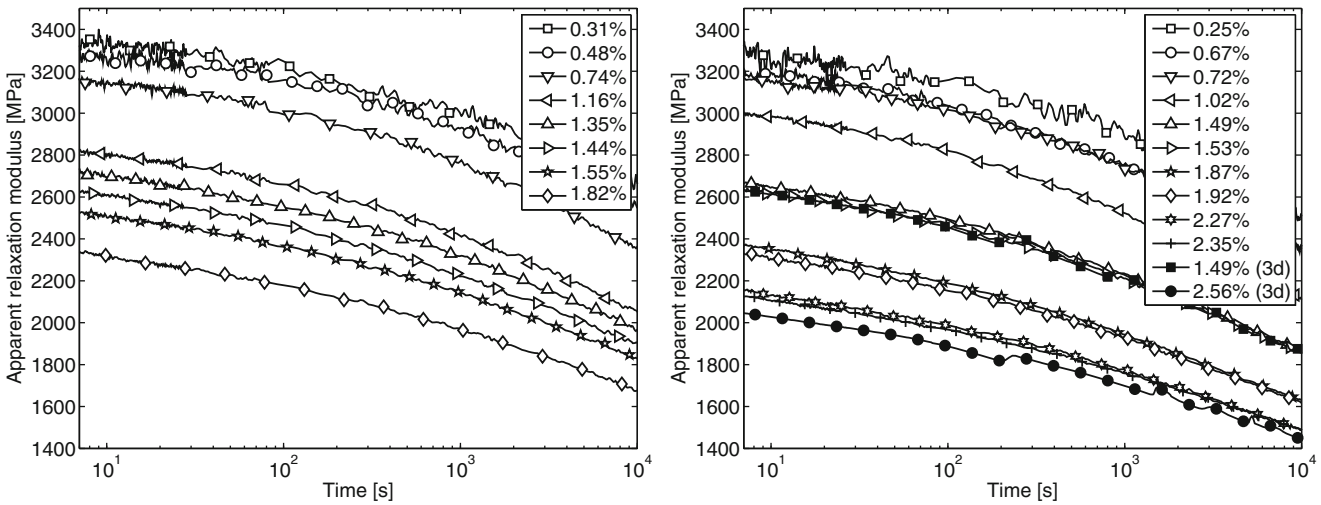

Fig. 20.1 Apparent tensile (*left*) and compressive (*right*) stress relaxation modulus for various strains. The legend refers to the mean strain in the relaxation phase

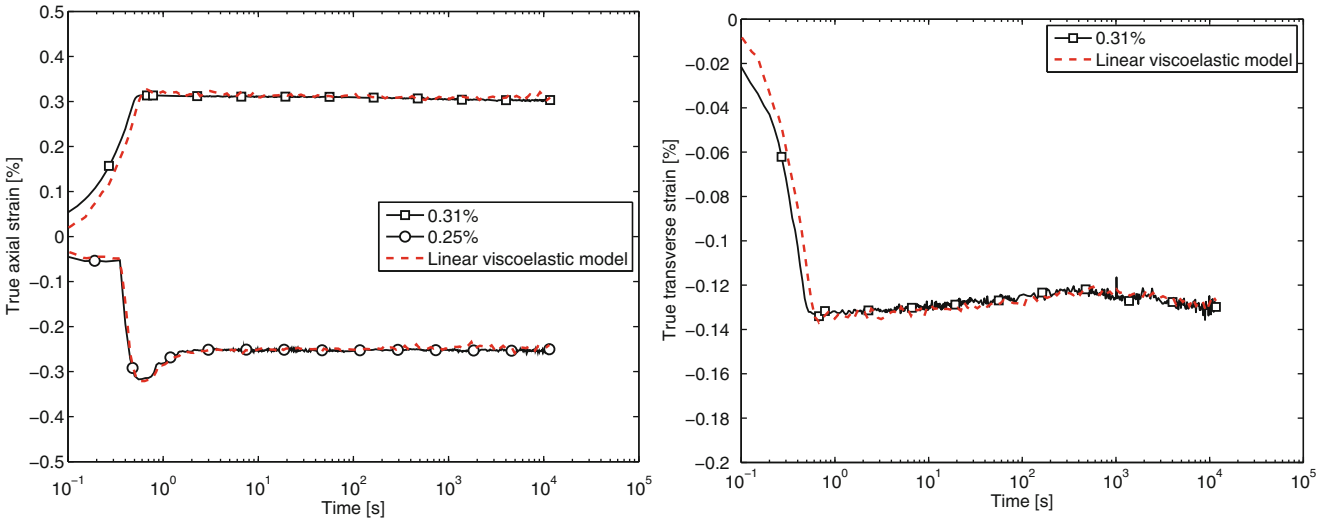

Fig. 20.2 LVE model fit to low strain data. *Left*: Axial strain. *Right*: Transverse strain. The legend refers to the mean strain during the relaxation phase

Table 20.1 Prony series parameters

n	τ (s)	J (MPa $^{-1}$)	ν (1)
1	∞	3. 02e − 004	0. 40
2	1. 58e + 002	1. 84e − 005	1. 5e − 008
3	3. 98e + 003	6. 69e − 005	0. 49
4	1. 00e + 005	2. 35e − 005	0. 49

20.5.2.1 Identification of Linear Viscoelastic Parameters

As illustrated by the experimental data shown in Fig. 20.1, we do not observe linear viscoelastic behavior in the measured strain range. Nevertheless, we treat the data from the lowest strain levels of 0.3% and − 0.25% as linear viscoelastic for fitting the Prony series parameters. To fit the linear viscoelastic (LVE) model, we set the polynomial coefficients of the nonlinearizing functions to zero. We prescribe the retardation times and optimize the remaining compliance and Poisson parameters (Eq. 20.7). Three terms are sufficient for a good fit to the low strain data (Fig. 20.2). The parameters are given in Table 20.1.

20.5.2.2 Identification of the Nonlinearizing Function Parameters

In the next step, we identify a preliminary nonlinear model by fixing the Prony series parameters to the previously obtained LVE values and optimizing the values of the parameters of the nonlinearizing functions. As initial guess we choose $\alpha^{(z)} = 0.\ 1$ and zero values for all polynomial coefficients, i.e. we start from the LVE model. We refer to this model as preliminary because even for the lowest strains the nonlinearizing functions are greater than unity by design, thus the use of the LVE Prony series implies a small inconsistency. We obtain a nonlinear model with rather large errors (Figs. 20.3 and 20.4, Model #1).

20.5.2.3 Refining the Parameters

The preliminary model is built using the LVE prony series and an estimate for the nonlinearizing functions that was determined by starting from the LVE model. This model can be improved by two additional optimizations, optimizing the Prony series parameters and subsequently optimizing the nonlinearizing functions again. In the first step, the Prony series

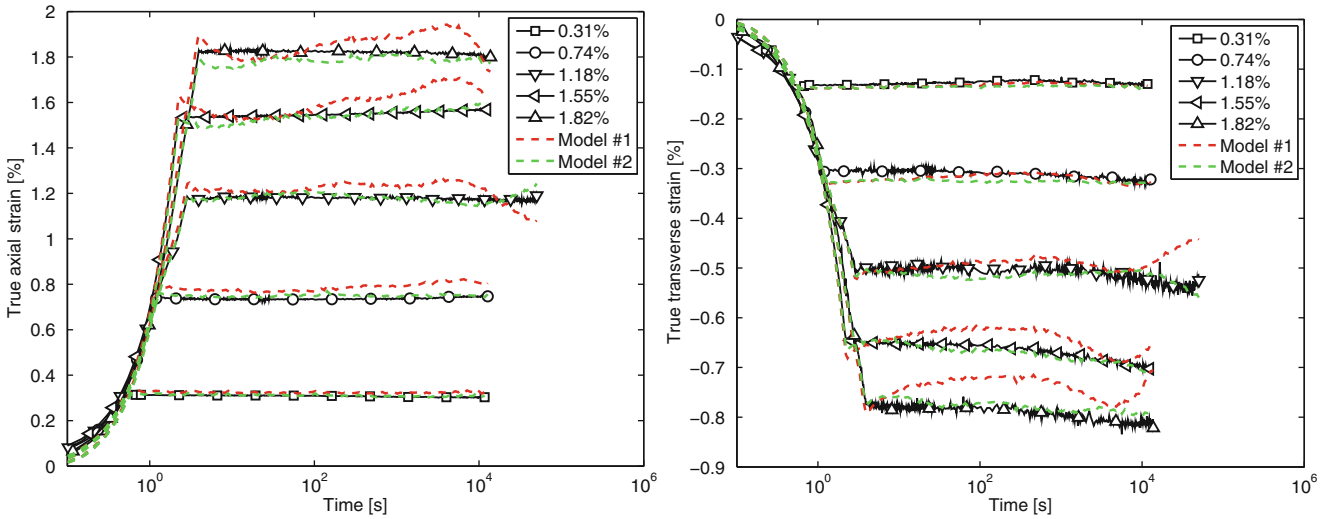

Fig. 20.3 Preliminary and improved nonlinear model: tensile relaxation

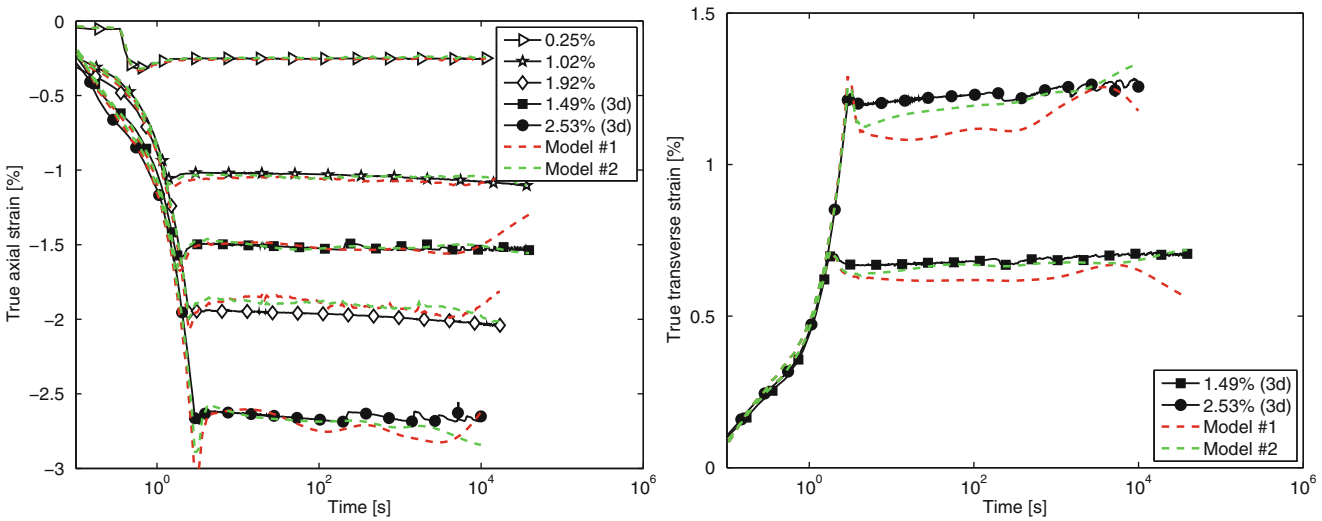

Fig. 20.4 Preliminary and improved nonlinear model: compression relaxation

parameters are adjusted to account for the non-unity nonlinearizing functions. In the second step, the nonlinearizing functions are once again refined. The parameters of this improved model (Figs. 20.3 and 20.4, Model #2) are given in Tables 20.2 and 20.3.

20.5.3 On the Uniqueness of the Parameters

We have mentioned before that there may be several minima in this optimization problem. Thus, a different choice of initial values may lead to very different model parameters. For example, in the LVE model, Prony series with different numbers of terms or different retardation times can yield practically identical fits to the input data. Thus, the parameters are not unique. We have conducted a substantial number of trial calculations to find alternate solutions and we identified a different set of parameters, which yields an improved fit to the relaxation data. The results of this model #3 are compared with model #2 in Figs. 20.5 and 20.6 and the parameters are given in Tables 20.4 and 20.5.

Table 20.2 Model #2: polynomial coefficients of the nonlinearizing functions and the respective weights for the effect of the hydrostatic pressure

Degree	0(1)	1(MPa $^{-1}$)	2(MPa $^{-2}$)	3(MPa $^{-3}$)	4(MPa $^{-4}$)	$\alpha^{(z)}$(1)
g_0	1	1. 88e − 008	3. 08e − 004	9. 01e − 007	2. 49e − 007	1. 88e − 002
g_1	1	7. 21e − 007	5. 19e − 004			2. 80e − 002
g_2	1	5. 78e − 007	2. 26e − 013	1. 06e − 011	3. 13e − 007	7. 44e − 001
$1/a_\sigma$	1	1. 42e − 013	7. 05e − 009	4. 67e − 004	1. 03e − 005	0. 00e − 000

Table 20.3 Model #2: prony series parameters

n	τ (s)	J (MPa $^{-1}$)	ν (1)
1	∞	2. 98e − 004	0. 43
2	1. 58e + 002	2. 08e − 005	0. 43
3	3. 98e + 003	4. 37e − 005	0. 44
4	1. 00e + 005	2. 00e − 004	0. 49

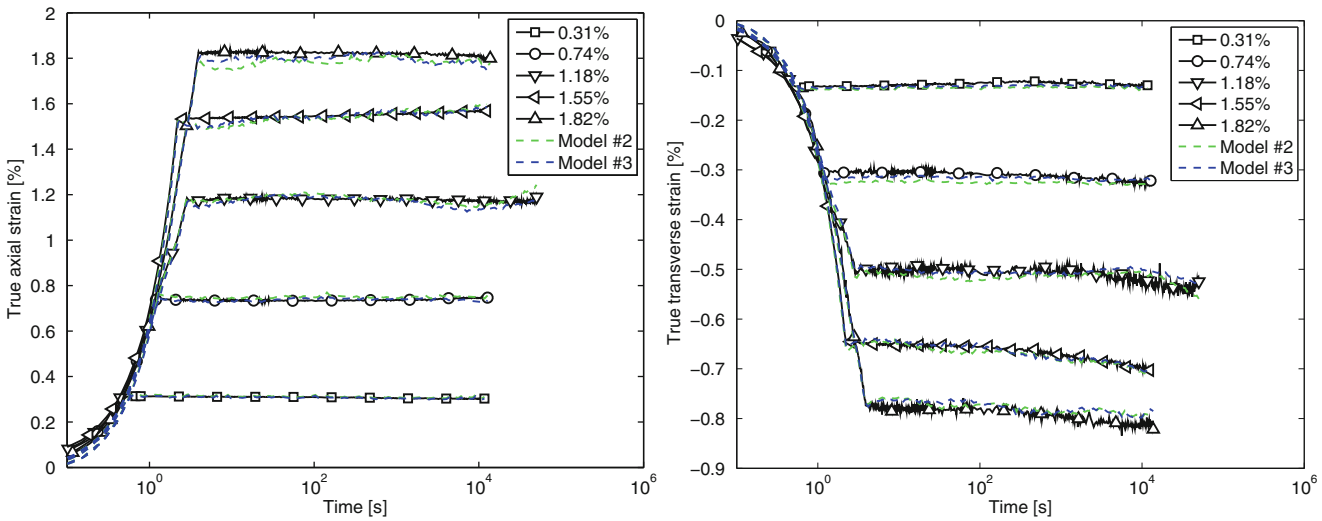

Fig. 20.5 Nonlinear models: tensile relaxation

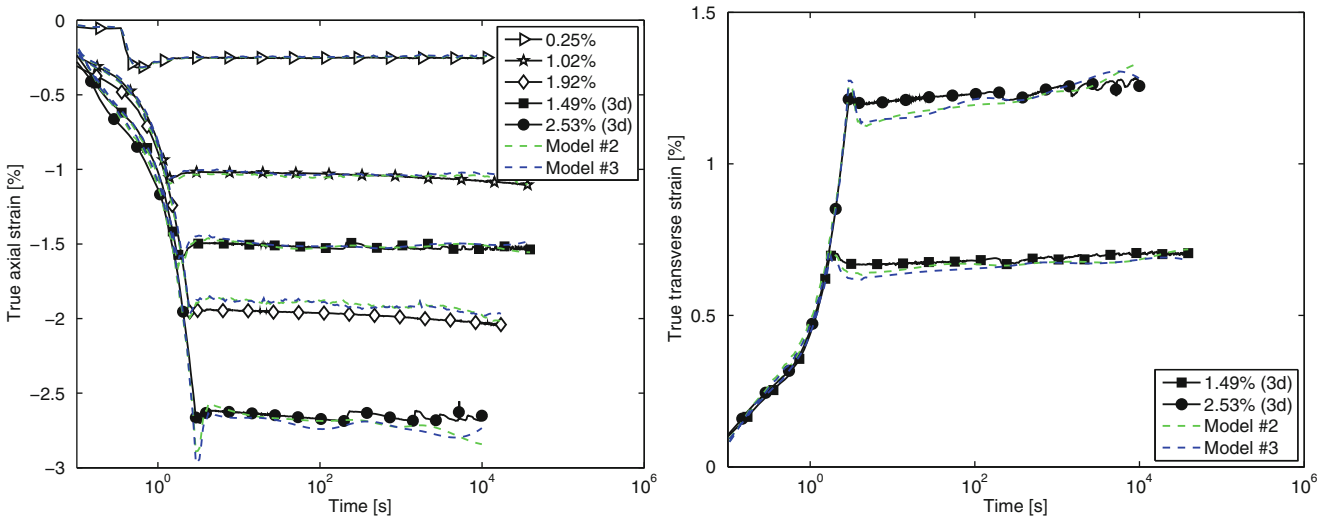

Fig. 20.6 Nonlinear models: compression relaxation

Table 20.4 Model #3: polynomial coefficients of the nonlinearizing functions and the respective weights for the effect of the hydrostatic pressure

Degree	0 (1)	1 (MPa^{-1})	2 (MPa^{-2})	3 (MPa^{-3})	4 (MPa^{-4})	$\alpha^{(z)}$ (1)
g_0	1	9. 34e − 004	7. 06e − 005	6. 92e − 006	3. 22e − 007	2. 79e − 002
g_1	1	7. 72e − 004	4. 57e − 004			2. 84e − 002
g_2	1	6. 99e − 005	5. 94e − 007	1. 76e − 008	5. 33e − 009	6. 42e − 001
$1/a_\sigma$	1	1. 11e − 002	8. 79e − 007	1. 22e − 005	6. 25e − 005	0. 00e − 000

Table 20.5 Model #3: prony series parameters

n	τ (s)	J (MPa^{-1})	ν (1)
1	∞	2. 94e − 004	0. 43
2	1. 58e + 002	2. 17e − 005	0. 31
3	3. 98e + 003	4. 17e − 005	0. 50
4	1. 00e + 005	1. 62e − 004	0. 50

20.6 Conclusion

Uniaxial tensile and compression stress relaxation tests of polyoxymethylene at several strains were performed. Optical strain measurement using digital image correlation provided the axial and transverse strain, which is essential for the complete characterization of the deformation. The Schapery nonlinear viscoelastic model was formulated for a 3d isotropic material. Based on the relaxation test data, a nonlinear optimization technique was used to identify the parameters of the model. An optimization strategy based on searches in subspaces of the parameter space was presented and it was shown that a good agreement between model and experiment could be achieved for both tension and compression.

Acknowledgements The research work of this paper was performed at the Polymer Competence Center Leoben GmbH (PCCL, Austria) within the framework of the COMET-program of the Austrian Ministry of Traffic, Innovation and Technology with contributions by the University of Leoben. The PCCL is funded by the Austrian Government and the State Governments of Styria and Upper Austria.

References

1. Silano A, Pae K, Sauer J (1977) Effects of hydrostatic pressure on shear deformation of polymers. J Appl Phys 48(10):4076–4084
2. Jerabek M, Tscharnuter D, Major Z, Ravi-Chandar K, Lang R (2010) Relaxation behavior of neat and particulate filled polypropylene in uniaxial and multiaxial compression. Mech Time Depend Mater 14(1):47–68
3. Rabinowitz S, Ward I, Parry J (1970) The effect of hydrostatic pressure on the shear yield behaviour of polymers. J Mater Sci 5:29–39
4. Pae K (1977) The macroscopic yielding behaviour of polymers in multiaxial stress fields. J Mater Sci 12:1209–1214
5. Qvale D, Ravi-Chandar K (2004) Viscoelastic characterization of polymers under multiaxial compression. Mech Time Depend Mater 8(3):193–214
6. Lévesque M, Derrien K, Baptiste D, Gilchrist M (2008) On the development and parameter identification of schapery-type constitutive theories. Mech Time Depend Mater 12(2):95–127
7. Nordin L-O, Varna J (2005) Nonlinear viscoelastic behavior of paper fiber composites. Compos Sci Technol 65(10):1069–1625
8. Sawant S, Muliana A (2008) A thermo-mechanical viscoelastic analysis of orthotropic materials. Compos Struct 83(1):61–72
9. Schapery R (1969) On the characterization of nonlinear viscoelastic materials. Polym Eng Sci 9(4):295–310
10. Nordin L-O, Varna J (2005) Methodology for parameter identification in nonlinear viscoelastic material model. Mech Time Depend Mater 9(4):57–78
11. Henriksen M (1984) Nonlinear viscoelastic stress analysis – a finite element approach. Comput Struct 18(1):133–139
12. Tscharnuter D, Jerabek M, Major Z, Pinter G (In Press) Uniaxial nonlinear viscoelastic viscoplastic modeling of polypropylene. Mech Time Depend Mater
13. Jerabek M, Major Z, Lang R (2010) Strain determination of polymeric materials using digital image correlation. Polym Test 29(3):407–416
14. Jerabek M, Major Z, Lang R (2010) Uniaxial compression testing of polymeric materials. Polym Test 29(3):302–309

15. Sutton M, Yan J, Tiwari V, Schreier H, Orteu J (2008) The effect of out-of-plane motion on 2d and 3d digital image correlation measurements. Opt Lasers Eng 46(10):746–757
16. Crochon T, Schönherr T, Li C, Lévesque M (2010) On finite-element implementation strategies ofschapery-type constitutive theories. Mech Time Depend Mater 14:359–387
17. Rao S (1996) Engineering optimization – theory and practice, 3rd edn. Wiley, New York
18. Tscharnuter D, Jerabek M, Major Z, Pinter G (2011) Irreversible deformation of isotactic polypropylene in the pre-yield regime. Eur Polym J 47(5):989–996

Chapter 21
Viscoelastic Creep Compliance Using Prony Series and Spectrum Function Approach

Jutima Simsiriwong, Rani W. Sullivan, and Harry H. Hilton

Abstract The objective of this study is to compare the viscoelastic material property of a vinyl ester (VE) resin using (1) the generalized 3-D viscoelastic constitutive equation with a Prony series representation and (2) a spectrum function model. The Prony series representation of the Generalized Kelvin model (GKM) is used to determine the Prony series coefficients through the linear least squares (LSQ) method. The Elastic-Viscoelastic Correspondence Principle (EVCP) and the Laplace transform are used in the spectrum function approach, which utilizes a carefully selected distribution function that has the potential to describe a wide range of materials. Short-term unidirectional tensile creep experiments are conducted at two stress levels and at four temperatures below the glass transition temperature of the VE polymer. Experimental strains in both the longitudinal and transverse directions and the applied stress are measured using the digital image correlation (DIC) technique. The measured data is subsequently used to determine the creep compliance function for each test configuration. The potential and limitations of each modeling approach are discussed.

Keywords Viscoelasticity • Constitutive viscoelastic relations • Spectrum function • Material property characterizations • Creep

21.1 Introduction

The exponential Prony series representation has been widely used to describe the viscoelastic response and material functions of polymers. An attractive feature of using the Prony series representation is that the viscoelastic functions can be easily manipulated mathematically and used in a recursive algorithm for the convolution integral of the viscoelastic constitutive relation [1–3]. Although most studies describe the behavior of time-dependent materials by a power law or a Prony series representation, the spectral approach can also be used. In a spectrum representation, a continuous distribution function is used to describe the viscoelastic behavior. Essentially, using a spectrum distribution is equivalent to using a series with an infinite number of terms. In this study, the spectrum function approach to describe the behavior of time-dependent materials developed by Sullivan [4–7] is explored. In [4], the analytical model for a spectral representation of linear viscoelastic materials is developed using a carefully selected distribution function that mimics the behavior of viscoelastic materials. The model is extended to include the flexure creep behavior of viscoelastic composite beams in [5] and also used in the development of a viscoelastic continuum damage model for a polymer matrix composite subject to cyclic loading in [6].

In this study, the primary objectives are to study and compare the viscoelastic creep compliance functions of a vinyl ester resin polymer (Derakane 441-400), obtained from the generalized 3-D viscoelastic constitutive equation with a Prony series representation and the spectrum function model. An analytical methodology to determine creep compliance functions using both approaches is given in Sect. 21.2 followed by experimental methods in Sect. 21.3. Section 21.4 discusses the results of the experimental and analytical studies, and the advantages and limitations of each approach are presented in Sect. 21.5.

J. Simsiriwong (✉) • R.W. Sullivan
Department of Aerospace Engineering, PO Box A, Mississippi State, MS 39762-5501, USA
e-mail: js319@msstate.edu

H.H. Hilton
Department of Aerospace Engineering, College of Engineering and Private Sector Program Division, National Center for Supercomputing Applications, University of Illinois at Urbana-Champaign, Urbana, IL 61801-2935, USA

B. Antoun et al. (eds.), *Challenges in Mechanics of Time-Dependent Materials and Processes in Conventional and Multifunctional Materials, Volume 2*, Conference Proceedings of the Society for Experimental Mechanics Series 37,
DOI 10.1007/978-1-4614-4241-7_21,

21.2 Analytical Methodology

Although the most accurate representation of creep data is a plot of strain vs. time for various stresses and temperatures, many theoretical and empirical models have been suggested for representing viscoelastic behavior and properties. In this paper, the creep compliance of an isothermal linear viscoelastic material is obtained using the generalized 3-D viscoelastic constitutive equation with a Prony series representation and a spectrum function model. A brief development of both approaches is given in the following section.

21.2.1 Creep Compliance Analysis Using Prony Series Representation

The deformation response of different viscoelastic materials can be simulated by mechanical models comprising of linear spring elements (Hooke) for elastic behavior and viscous damper elements (Newton) for viscous behavior. The Generalized Kelvin model (GKM), uses a number of Kelvin elements connected in series to describe the creep compliance (C(t)) as [8]

$$C(t) = C^0 + \sum_{n=1}^{Npr} C^n \left[1 - \exp\left(-\frac{t}{\tau_n}\right)\right] \tag{21.1}$$

where C_n and τ_n are the Prony series coefficients and retardation times, respectively. One of the challenges of using a Prony series representation is to determine the appropriate Prony series coefficients and relaxation (or retardation) times that produce a good fit of the data. Several techniques to fit a Prony series representation to a linear viscoelastic constitutive response from the experimental creep/relaxation data are found in the literature [1–3, 9–13]. Although the methods developed in earlier years such as Schapery (1961) [9, 10] or Cost and Becker (1970) [12] present straightforward techniques for determining the Prony series coefficients, these methods produce both positive and negative values. The negative coefficients are physically unrealistic and create oscillations in the fitted curve [13]. However, the sign control method which is based on the multidata method [12] uses mathematical constraints which allow only positive values for the Prony series coefficients (longitudinal C_n). This technique also allows the user to select the retardation times in the evenly spaced log time over the range of data, which simplifies the analysis to a linear system of equations. Once the retardation times are chosen, the Prony series coefficients are obtained to optimally match the experimental data [11]. Due to the afore mentioned reasons, the sign control method [11] is used.

First, the constitutive relation for an isothermal isotropic linear viscoelastic material with Prony series representation is stated as [2]

$$\varepsilon_{\underline{ii}}(t) = \sum_{j=1}^{3} \left\{ C^0_{\underline{iijj}} \sigma_{jj}(t) + \sum_{n}^{N_{pr}} \left[\frac{C^n_{\underline{iijj}}}{\tau_n} \int_0^t e^{-\frac{t-t'}{\tau_n}} \frac{\partial \sigma_{jj}(t')}{\partial t'} dt' \right] + \frac{C^{Npr+1}_{\underline{iijj}}}{\tau_{Npr+1}} \int_0^t \sigma_{jj}(t') dt' \right\}. \tag{21.2}$$

In (21.2) the first term describes the instantaneous elastic response, the second term represents the secondary viscoelastic creep, and the long-time response is described by the last term. Since only short-term creep is considered here, the long-time response is not considered and therefore, the last term in (21.2) is neglected. Additionally, the importance of including the starting transients in the viscoelastic analysis is recognized. Therefore, the loading conditions for the loading phase and the steady-state creep are described as [3]

$$\sigma_{11}(t) = \begin{cases} f_\sigma(t) & 0 \le t \le t_1 \text{ (loading phase)} \\ \sigma_0 H(t - t_1) & t \ge t_1 \text{ (steady - state phase)} \end{cases} \tag{21.3}$$

In (21.3) for the creep phase, the Heaviside unit step function is often used in the loading function description, but it does not satisfy the physical interpretation of the actual loading phase, i.e., zero slope at $t = 0$ and $t = t_1$. Therefore, the loading condition in (21.4) is selected as it is mathematically admissible and physically realistic.

$$f_\sigma(t) = \sum_{q=0}^{Q} \sigma_m t^m \quad 0 \le t \le t_1 \tag{21.4}$$

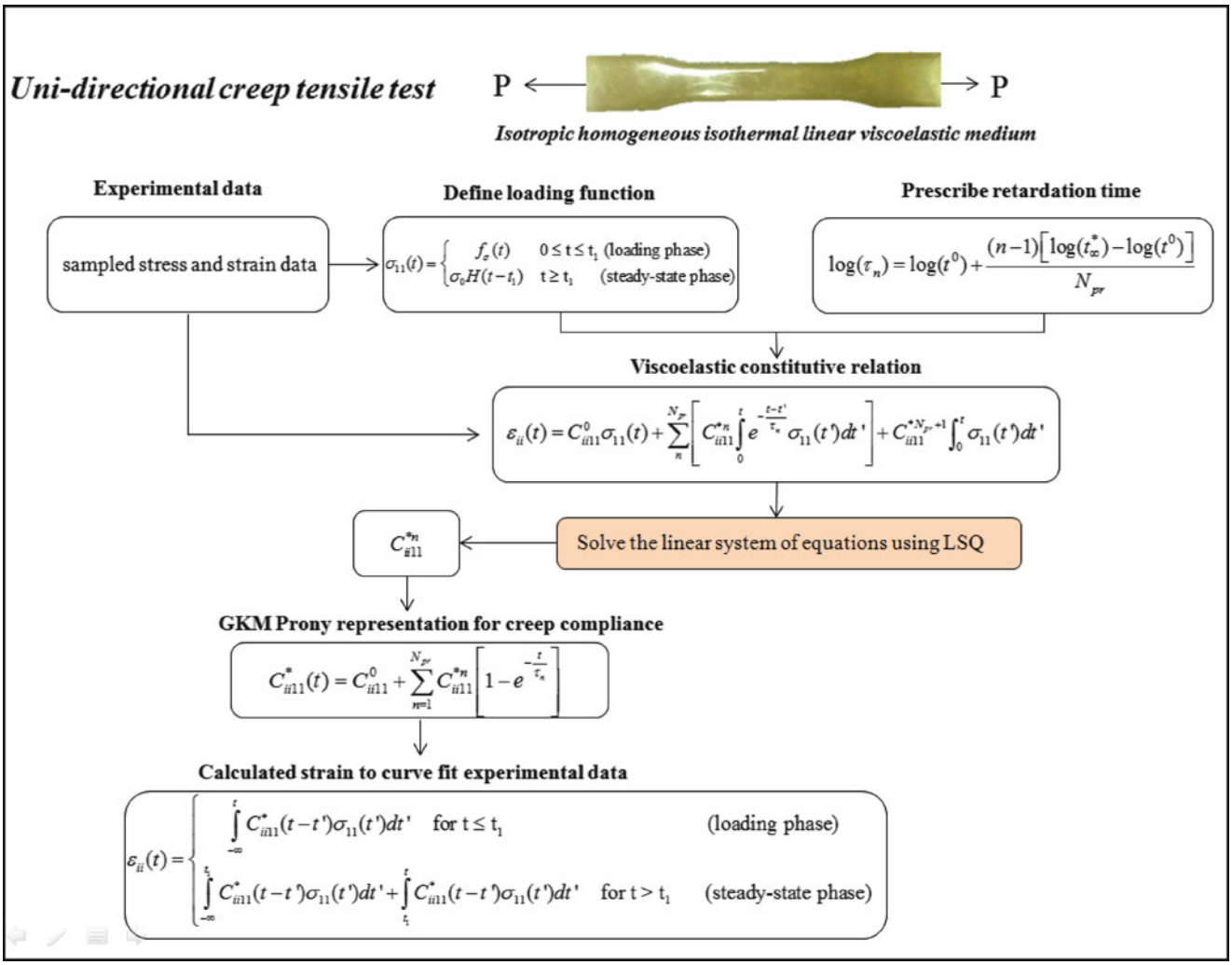

Fig. 21.1 Procedure to calculate creep compliance using Prony series representation

The procedure to obtain creep compliances using the Prony series method which utilizes the linear least squares (LSQ) method is shown in Fig. 21.1. Here, the loading function is first determined from the experimental stress and strain data. By prescribing the approximate values for the retardation times (τ_n), the Prony series coefficients (C_{ii}^n) are the only unknown variables in the viscoelastic constitutive equation. Using the LSQ technique with the mathematical constraints imposed on the Prony series coefficients, the linear system of equations is solved and the coefficients are determined. The analytical creep strain is then calculated and compared to the experimental strain data [2].

21.2.2 Creep Compliance Analysis Using the Spectrum Function Method

The spectral approach used here, follows Sullivan's model [7], in which a spectrum function is carefully selected to represent a generalization of a discrete distribution inherent in a natural system. The spectrum function is used to develop the fundamental material functions, which are later incorporated through the Elastic-Viscoelastic Correspondence Principle (EVCP) to obtain the material response and properties. A thorough discussion of the spectrum approach used in this study is given in [4, 7]; for completeness, a brief overview follows.

The constitutive equation describing an anisotropic, linear viscoelastic material with multi-axial inputs and responses can be written as

$$\varepsilon_{ij}(t) = \int_{-\infty}^{t} C_{ijkl}\,(t-t')\ \frac{d\sigma_{kl}(t')}{dt'}dt' \tag{21.5}$$

where C_{ijkl} are the creep compliances and i, j = 1, 2, 3. These creep compliances can be written as [14–16]

$$C_{ijkl}(t) = C_{ijkl_0} + \alpha \int_{0}^{\infty} \varphi_{ijkl}\,(t')\left[1 - e^{\frac{-t}{t'}}\right]dt'\ C_{ijkl_0} = \lim_{t\to 0} C_{ijkl} \tag{21.6}$$

where $\varphi(t')$ is the spectrum function, selected as

$$\varphi(\alpha) = \frac{n}{\pi\left(1 + n_0^2\alpha^2\right)} \tag{21.7}$$

with material constants n and n_o having dimension of [1/s].

Using the spectrum function in (21.7), for the case of a constant one-dimensional loading, the strain (using EVCP and Laplace transform) is given by the integral equation [4] as

$$\varepsilon_{11}(t) = \frac{\sigma_o}{E_e} + \frac{m}{\pi}\int_{0}^{t} \varepsilon_{11}(t-t')\psi(t')d\,t' \tag{21.8}$$

where,

$$\psi(t) = \int_{n_o t}^{\infty} \frac{\cos(z - n_o t)}{z}dz. \tag{21.9}$$

In (21.8), σ_o is the constant stress applied for creep loading. The two viscoelastic parameters n and n_o (which appear in (21.8) and (21.9)) are determined from the experimental data and used to form all other time-dependent properties such as compliances or moduli. The Volterra equation in (21.8) is solved through a numerical iterative technique [17] and the resulting relaxation modulus from the spectral approach is determined as [4–7]

$$E(t) = E_0\left[\left(1 - \frac{m}{2}\right) + \frac{m}{\pi}\int_{n_0 t}^{\infty} \frac{\sin(z - n_0 t)}{z}dz\right], \quad m = \frac{n}{n_o} \tag{21.10}$$

Once the relaxation modulus is obtained, the creep compliance is determined through the interrelation of the linear viscoelastic material functions, described by the convolution integral as [18, 19]

$$\int_{-\infty}^{t} E(t-\tau)C(\tau)d\tau = \int_{-\infty}^{t} E(\tau)C(t-\tau)d\tau = t \tag{21.11}$$

The analytical inversion of (21.11) to obtain C(t) can be performed by using an appropriate numerical integration technique. The range of the integral is divided into a finite number of subintervals, with the creep compliance function assumed to be constant in each subinterval, so that (21.11) can be expressed in a recursive form as

$$\sum_{i=1}^{I} \frac{C(t_i) + C(t_{i-1})}{2}\,\frac{E(t_I - t_i) + E(t_I - t_{i-1})}{2}(t_i - t_{i-1}) = t_I \tag{21.12}$$

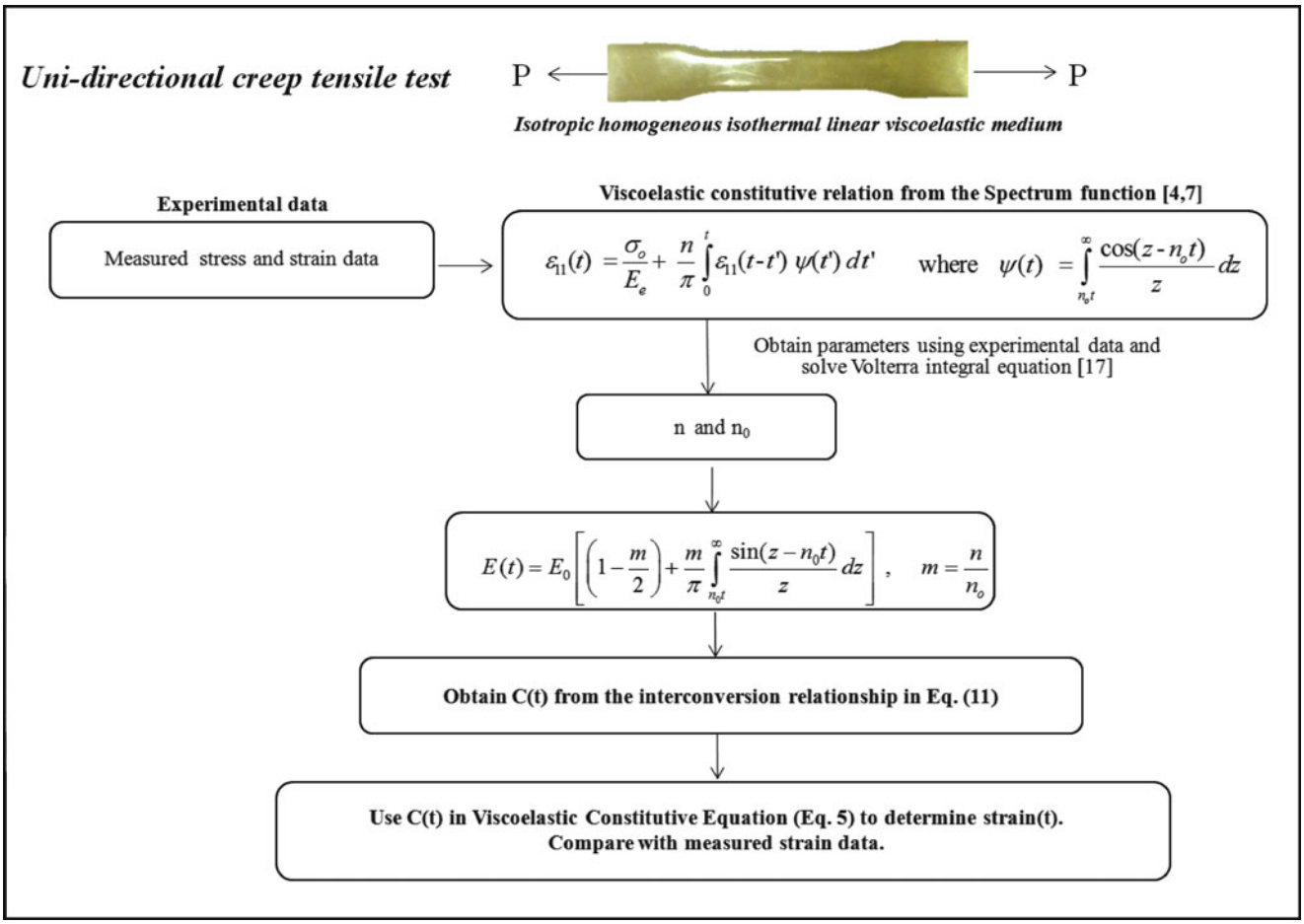

Fig. 21.2 Procedure to calculate creep compliance using the spectrum function model

The procedure to obtain the relaxation modulus using the spectrum function model is shown in Fig. 21.2. Following the analytical analysis as described in (21.5, 21.6, 21.7, 21.8, 21.9, 21.10), the analytical strains in the longitudinal and transverse directions are determined and compared to the experimental data.

21.3 Experimental Method

21.3.1 Materials and Specimen Preparation

Vinyl ester (VE) resins are commonly used as an alternative to epoxy or unsaturated polyester resins because of their excellent toughness, as well as their improved fatigue and chemical resistance [20]. These resins are inexpensive and widely used in structural applications for automotive parts. In this study, a thermoset VE resin, Derakane 441-400 by Ashland Co., with styrene content of 33 wt.% is selected. The curing agent and curing promoter are Cobalt naphthenate 6% solution (North American Composites Co.) and methyl ethyl ketone peroxide, MEKP (U.S. Composites Inc.), respectively. The curing promoter is used to facilitate the reaction between the VE resin and the hardener. To remove air bubbles trapped during mixing, a combination of two air release additives, BYK-A 515 and BYK-A 555 (BYKChemie GmbH), are used. The formulation, which is based on 100 parts of the resin or phr, is shown in Table 21.1.

At ambient temperature, the curing promoter and the air release agents are added to the VE resin. The mixture is then blended manually before the curing agent (hardener) is added. Air bubbles introduced during mixing are removed by using a vacuum pump operating at a pressure of 8–10 kPa. The mixture is then poured in a mold that is sprayed with a semi-permanent

Table 21.1 Formulation components of test specimens

Ingredient	Weight (g)
Derakane 441-400 (VE resin)	100
Cobalt naphthenate 6% (curing promoter)	0.20
BYK-A 515 (air release agent)	0.20
BYK-A 555 (air release agent)	0.20
MEKP (curing agent)	1.00

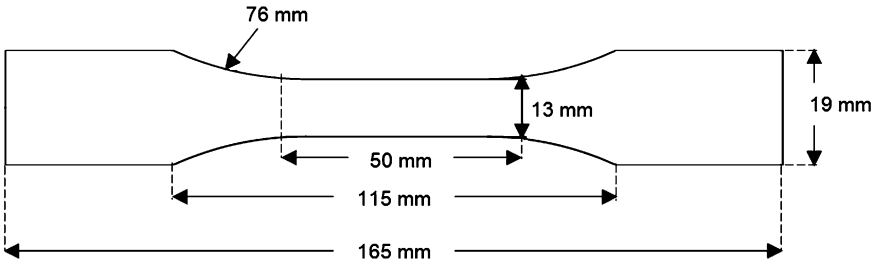

Fig. 21.3 Specimen configurations

mold release agent (Frekote® by Henkel). The specimens are oven-cured under nitrogen atmosphere for 5 h at 60°C and post-cured for 2 h at 120°C. A total of seven specimens are fabricated each time.

The mold and specimen configurations in this study are based on the ASTM D638 standard test method for tensile properties of plastics [21]. The configuration and dimensions of the dog-bone specimen used in this study are shown in Fig. 21.3. After specimen fabrication, a process of sanding and polishing is performed on each specimen using the Labopol-2 Polisher machine.

21.3.2 Mechanical Instruments

An INSTRON Model 5869 compression/tension electromechanical testing system is used to conduct the tensile and creep tests. A 50-kN load cell is mounted to the load frame to measure the applied load. To reduce specimen slippage, the grips of the test specimens are wrapped with a small piece of sandpaper prior to being clamped in the wedge grips.

The digital image correlation (DIC) technique is used to obtain strain measurements through the LaVisionStrainMaster system. This technique allows the user to obtain strains in both the longitudinal and transverse directions simultaneously, thus eliminating the need to obtain the stress-time histories-dependent Poisson's ratio in linear viscoelasticity [22]. The selected camera system is a high resolution 14-bit charge-coupled device camera that has up to 16 million pixel spatial resolution. The camera has a recording capacity of 29 frames/s. The images of the specimen are taken over the complete duration of the test at the sample rate of 24 Hz. By comparing at least two images of the area of interest on the test piece at two different times, the strain contours around microstructural and geometrical heterogeneities are quantified. In addition to the DIC system, an axial extensometer with a gage length of 25.44 mm is used to verify the DIC-measured longitudinal strain, as shown in Fig. 21.4.

21.3.3 Quasi-Static Tensile and Creep Tests

The ultimate tensile stress (σ_u) is determined from uniaxial quasi-static tensile tests performed at the selected temperatures. The tensile tests are conducted according to ASTM D638 at a constant strain rate of 0.001/s [21]. These tests are performed at ambient temperature and at three elevated temperatures (40°C, 60°C, 80°C) lower than the glass transition temperature T_g (120°C–130°C) of the VE resin [23]. The higher temperature tests are performed inside an environmental chamber with an optical quality viewing window that is mounted to an electromechanical test system. Heating parameters are set and monitored using a programmable controller with an accuracy to ±0.5%.

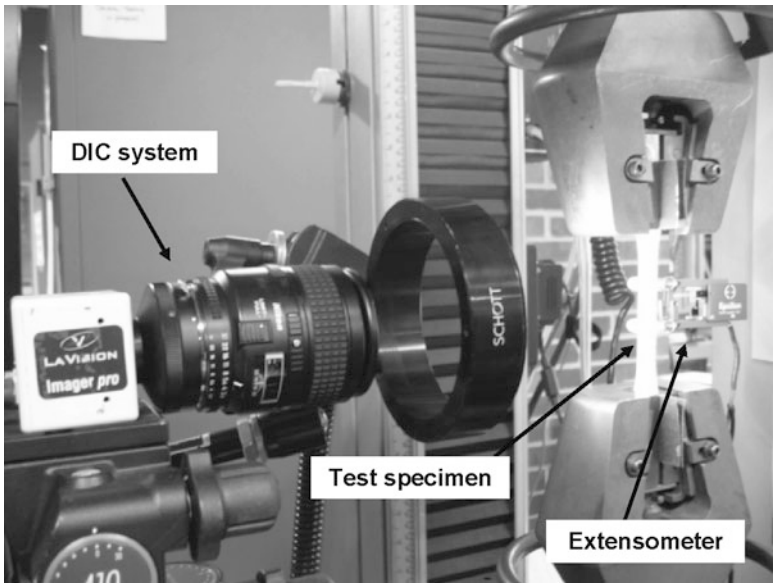

Fig. 21.4 Room temperature tensile test setup

Table 21.2 Quasi-static tensile test results

Temperature (°C)	Ultimate tensile stress (σ_u) (MPa)	Elongation (%)
23.8	75	2.64
40	70.2	2.83
60	59>	3.0
80	46.4	4.1

Table 21.3 Test matrix for creep test

	Stress level (MPa)	
Temperature (°C)	60% σ_u	70% σ_u
23.8	45	52.5
40	42.1	49.1
60	35.4	41.3
80	27.8	32.5

Five tensile tests are performed at each temperature and the averaged values of the data are used. The ultimate tensile stress and percent of elongation obtained from the quasi-static tensile tests are shown in Table 21.2. As expected, the results indicate that at a constant strain rate, the deformation increases whereas the ultimate tensile stress of the VE polymer decreases with increasing temperature.

Following the determination of the ultimate tensile stress σ_u of the VE resin, constant-stress creep tests are performed in accordance with ASTM D2990 [24] at two stress levels (60% and 70% σ_u) and four temperatures (RT, 40°C, 60°C, 80°C). The test matrix for the creep test is shown in Table 21.3. The constant stress is applied for 2 h, followed by 1 h of recovery. A total of ten creep tests are conducted for each test configuration and the average strain values of ten tests are used to obtain the creep compliance function.

21.4 Results

21.4.1 Longitudinal and Transverse Strains

The DIC creep strain histories for both the longitudinal and transverse directions for the VE polymer at constant stresses of 60% and 70% σ_u and temperatures of 23.8°C, 40°C, 60°C are shown in Figs. 21.5 and 21.6, respectively. The primary creep

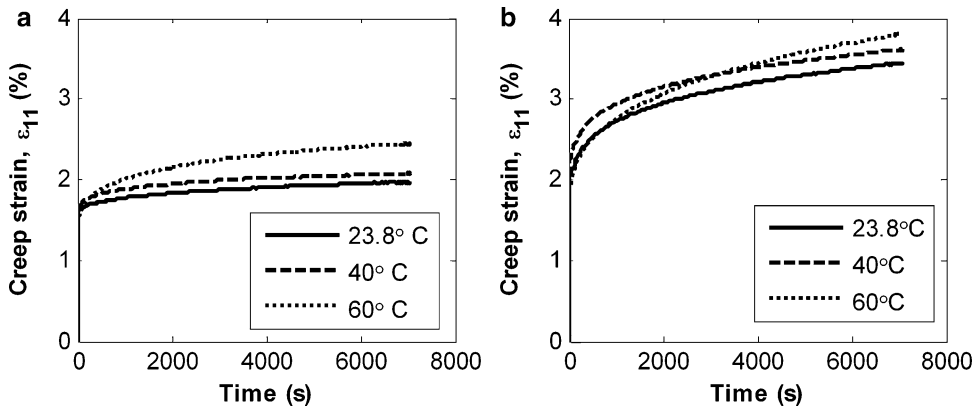

Fig. 21.5 Comparison of creep strain in (**a**) longitudinal and (**b**) transverse directions at 60% σ_u

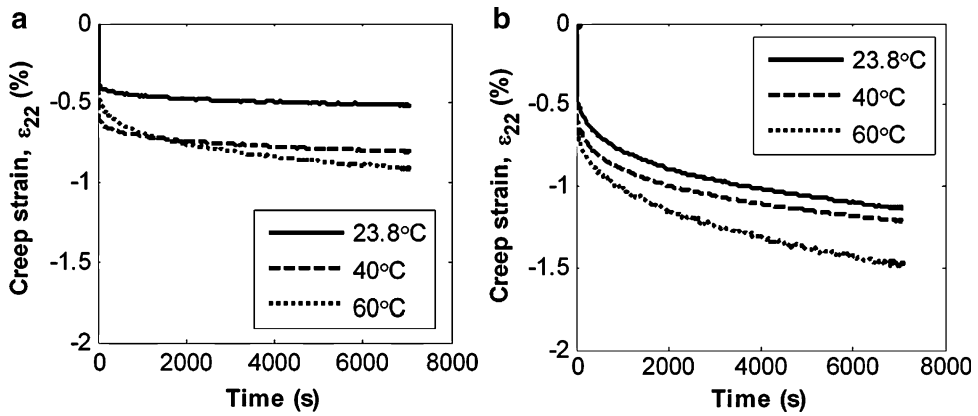

Fig. 21.6 Comparison of creep strain in (**a**) longitudinal and (**b**) transverse directions at 70% σ_u

and secondary (steady-state) creep stages are observed. As expected, at a constant holding stress, the creep deformation increases as the temperature level increases. Since non-linear visocoelastic behavior was observed for the creep tests at 80°C, it has not been included in this study.

21.4.2 Prony Series

Using the measured strains in the longitudinal and transverse directions, the creep compliances are calculated using the Prony series method, as outlined in Fig. 21.1. By applying the mathematical constraints to the Prony series coefficients and the retardation times as shown in (21.13), a good quality of the LSQ fit is obtained. The number of Prony terms is chosen by trial and error. As illustrated in Fig. 21.7, 30 Prony coefficients are selected as this number produced a good convergence of the LSQ fit of the data.

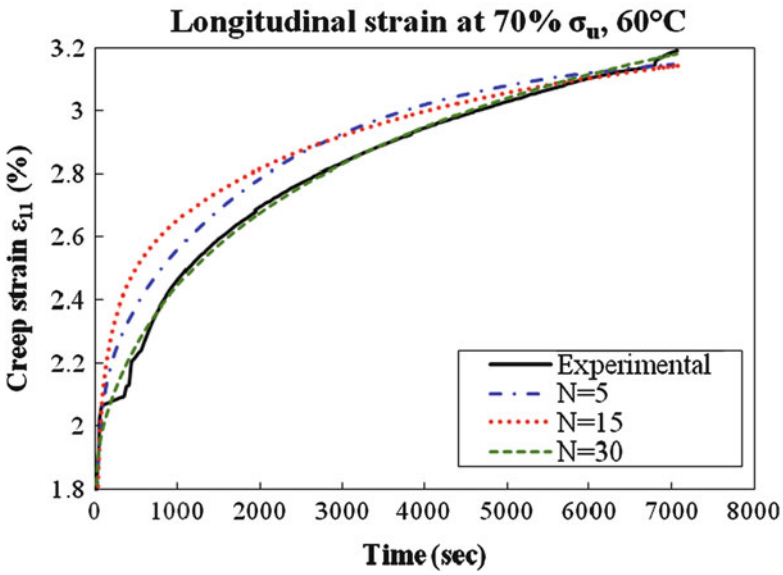

Fig. 21.7 Comparison of longitudinal strain at 70% σ_u, 60°C with various numbers of Prony series terms, N

$$\begin{aligned} C_{1111}(t) > 0, \quad & C_{1122}(t) < 0 \\ C^0_{1111} > 0, \quad & C^n_{1111} > 0 \\ C^0_{1122} < 0, \quad & C^n_{1122} < 0 \\ \tau_n > 0 & \end{aligned} \tag{21.13}$$

21.4.3 Spectrum Function

The measured strain data is also used in the spectrum function model to obtain the material constants n and n_0 which are subsequently used in (21.10) for each test configuration. The relaxation modulus as a function of time is then converted to the creep compliance function using (21.12). The comparison of normalized creep compliance functions, $C_{11}(t)$, computed from the Prony series method and the spectrum function model, and percent difference between the models are shown in Figs. 21.8 and 21.9.

Once the creep compliances are obtained from both methods, the creep strain is computed using the constitutive relation in (21.2). Figure 21.10 shows the computed and measured, longitudinal and transverse creep strain for the 60% σ_u tests at the various temperatures. Table 21.4 lists the percent errors in the longitudinal creep strain at 60% σ_u between the Prony series and spectrum methods and the measured data at discrete times for the three test temperatures.

21.5 Discussion and Conclusion

A comparison of the two approaches with regards to the determination of the creep compliance function is summarized in Table 21.5.

For properly characterizing the viscoelastic behavior of the polymer in this study, a total of 30 Prony constants were necessary. The number of parameters required by the spectrum approach is dependent on the choice of the spectrum function and for the present work, the selected distribution function required only two parameters to represent the secondary creep behavior. Analytically, a series formulation is proposed for the material functions when using the Prony series representation. In the spectrum approach, the modulus is developed from applying the correspondence principal to the elastic solution and the time-dependent modulus is obtained from the Laplace inversion. Once the parameters have been obtained from the

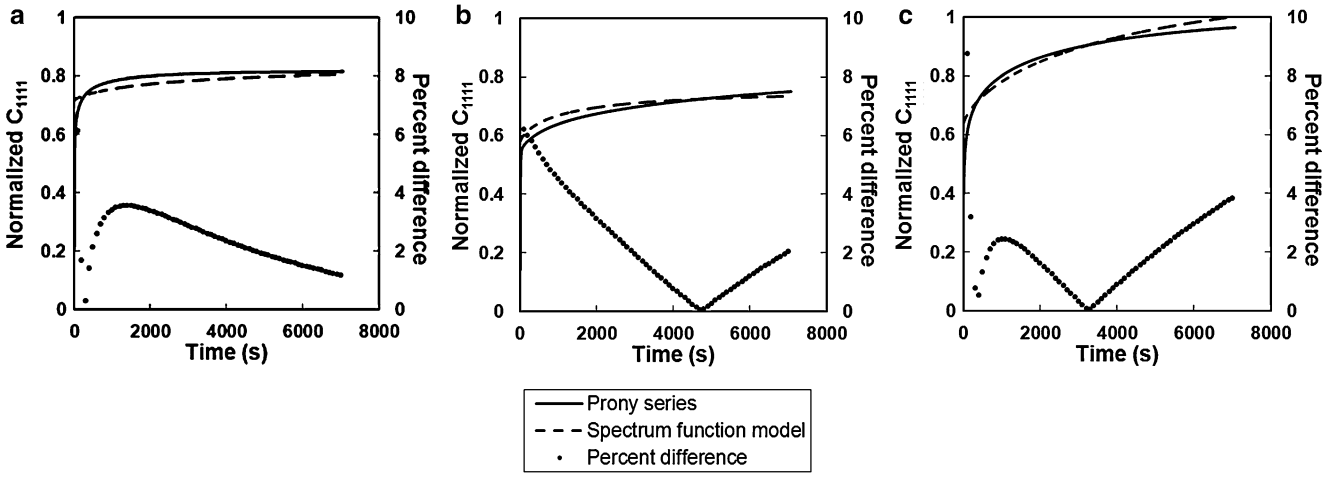

Fig. 21.8 Comparison of normalized creep compliances, C_{1111}, obtained from the spectrum function model and the Prony series representation for creep tests at 60% σ_u at (**a**) 23.8°C, (**b**) 40°C, and (**c**) 60°C

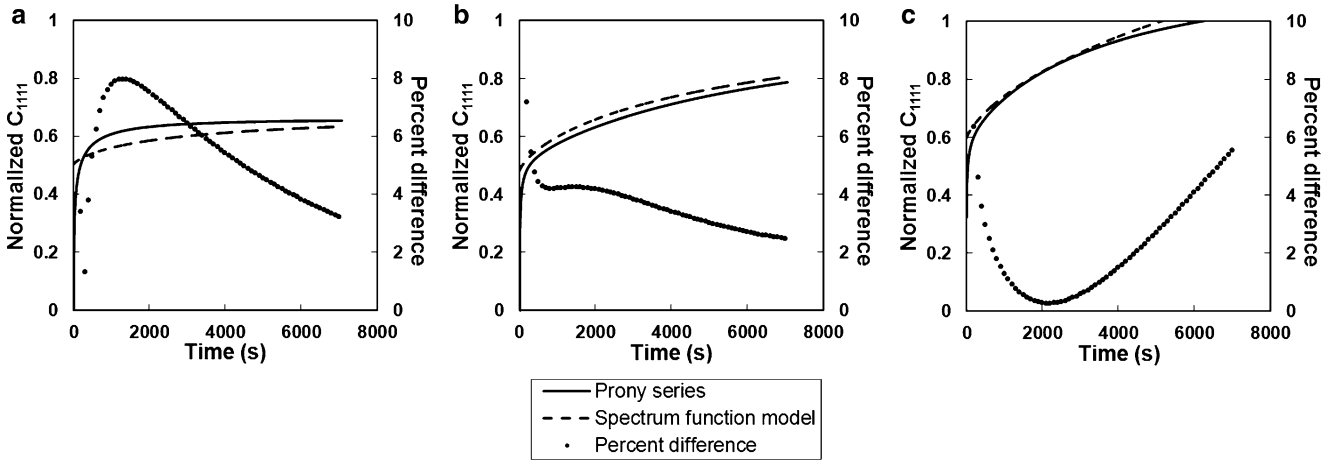

Fig. 21.9 Comparison of normalized creep compliances, C_{1111}, obtained from the spectrum function model and the Prony series representation for creep tests at 70% σ_u at (**a**) 23.8°C, (**b**) 40°C, and (**c**) 60°C

strain data, the material function is solved directly. The resulting creep compliance from each method is shown in Figs. 21.8 and 21.9, which show good agreement (less than 0.8% difference) between the two methods. The final comparison is obtained when using the material functions in the constitutive equation to obtain the strain which is subsequently compared to the experimental data. As seen by Fig. 21.10 and 21.11, both methods correlate well with the experimental data, with the largest differences between the methods and the measured data being at the beginning of the creep tests. The initial deviations between the two approaches and the experimental data can be due to the different starting conditions for the two methods, i.e., starting transients are not included for the spectrum approach. Also, only two parameters are used for the selected spectrum function; a more general function that includes additional parameters should improve the accuracy of the prediction. During secondary creep, both techniques produce good agreement with the experimental data, which is substantiated by the low percent error at discrete times listed in Table 21.4. Errors may also be due to (a) the inaccuracy of the instantaneous modulus/compliance used in the models, (b) the approximate technique used for interconversion from modulus to compliance, and (c) the use of averaged creep strain data. Ongoing work includes formulation of statistical descriptions of the data due to the large scatter obtained in creep testing of viscoelastic polymers as well as including the starting transients for both approaches.

Overall, the Boltzmann superposition principle provides the mathematical and physical modeling of viscoelastic behavior and it is typically represented by the traditional Prony series approach which uses a finite number of discrete terms. However, the spectrum function approach can also be used, which is essentially the series approach with an infinite number

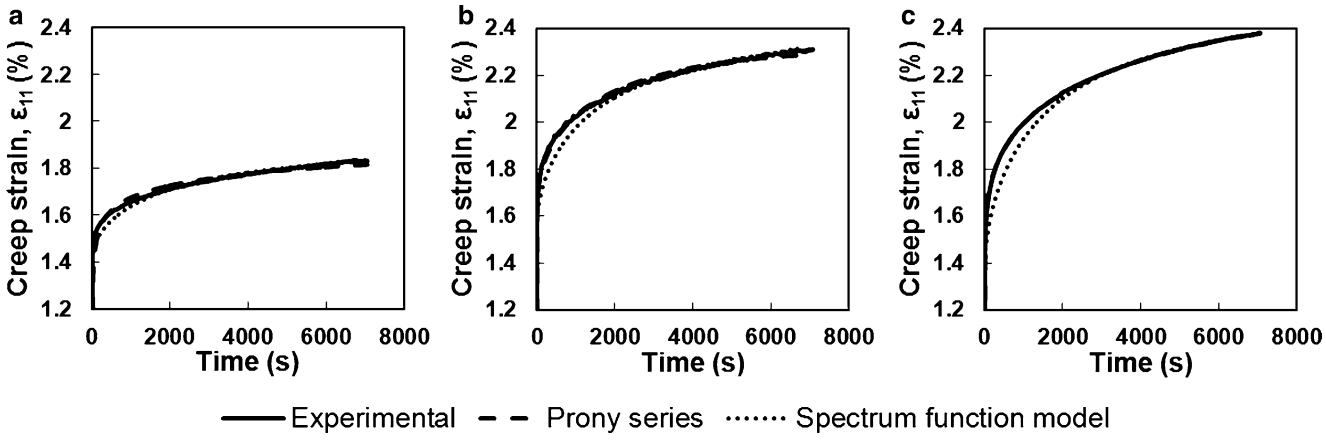

Fig. 21.10 Comparison of experimental and analytical creep strain in longitudinal direction at 60% σ_u at (**a**) 23.8°C, (**b**) 40°C, and (**c**) 60°C

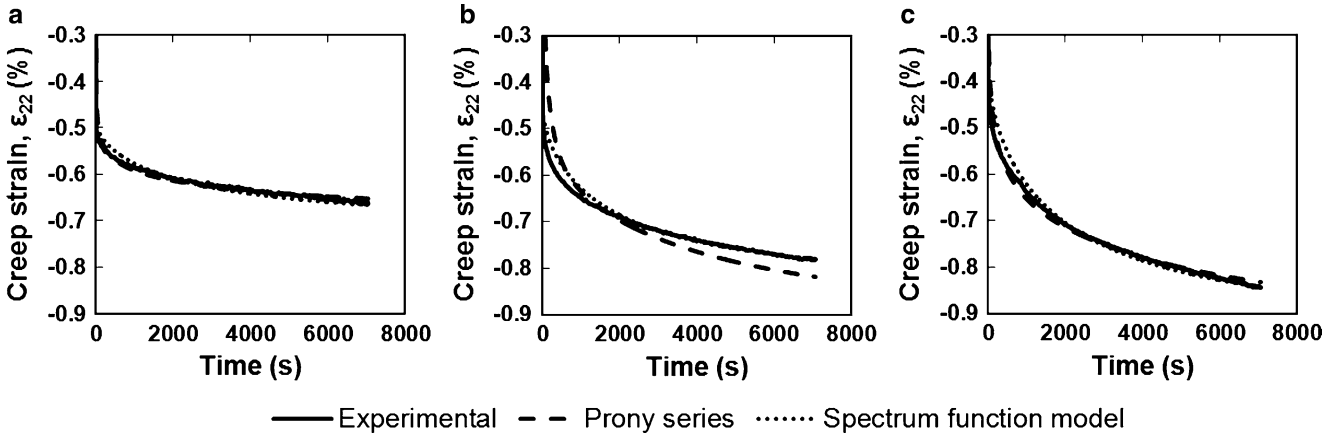

Fig. 21.11 Comparison of experimental and analytical creep strain in (transverse direction at 60% σ_u at (**a**) 23.8°C, (**b**) 40°C, and (**c**) 60°C

Table 21.4 Comparison of the percent error of creep strain at 60 % σ_u

	60% σ_u, 23.8°C				60% σ_u, 40C				60% σ_u, 60°C			
	% error ε_{11}		% error ε_{22}		% error ε_{11}		% error ε_{22}		% error ε_{11}		% error ε_{22}	
Time (s)	Prony	Spectrum	Prony	Spectrum	Prony	Spectrum	Prony	Spectrum	Prony	Spectrum	Prony	Spectrum
1,000	1.09	1.11	1.04	1.62	0.13	2.32	2.26	3.31	0.08	3.32	2.33	2.63
3,000	0.60	0.47	0.81	1.11	0.36	0.31	2.46	0.14	0.06	0.15	0.52	0.76
4,000	0.05	0.37	0.46	1.48	0.47	0.23	3.32	0.28	0.00	0.15	0.20	0.75
5,000	0.32	0.28	0.13	1.38	0.20	0.35	4.08	0.35	0.02	0.12	0.26	0.95
6,000	0.80	0.04	0.62	1.21	0.51	0.01	4.34	0.00	0.01	0.02	0.62	0.65
7,000	0.74	0.11	1.55	0.49	0.86	0.02	4.80	0.05	0.08	0.05	1.31	0.06

of terms. Mathematically, the Prony series approach is simpler as it mainly involves the LSQ technique whereas the spectrum approach utilizes the Correspondence Principle and Laplace transforms and inversions. Although the Prony series approach implements the history, it models the material functions in a general fashion, providing no information about the specific forms of these functions. The spectrum method, as implemented in this study is a more physics-based approach in that a distribution function which mimics viscoelastic behavior is utilized and fundamental material functions are developed using the selected spectrum. Of the two methods, the inherent formulation of the spectrum approach facilitates descriptions of statistical processes such as the scatter in the data encountered in creep experiments of viscoelastic materials. From the results of this study, both methods are successful in describing the viscoelastic response of solids.

Table 21.5 Comparison of Prony series and spectrum function for viscoelastic behavior representation

		Prony series representation	Spectrum function model
		$\varepsilon_{\underline{ii}}(t) = \sum_{j=1}^{3} \left\{ \begin{array}{l} C^0_{\underline{ijj}}\sigma_{jj}(t) + \\ \sum_{n}^{N_{pr}} \left[\frac{C^n_{\underline{ijj}}}{\tau_n} \int_0^t e^{-\frac{t-t'}{\tau_n}} \frac{\partial \sigma_{jj}(t')}{\partial t'} dt' \right] + \\ \frac{C^{Npr+1}_{\underline{ijj}}}{\tau_{Npr+1}} \int_0^t \sigma_{jj}(t')dt' \end{array} \right\}$ Eq. 21.2	$\varepsilon_{11}(t) = \frac{\sigma_o}{E_e} + \frac{m}{\pi} \int_0^t \varepsilon_{11}(t-t')\psi(t')dt'$ where $\psi(t) = \int_{n_o t}^{\infty} \frac{\cos(z-n_o t)}{z} dz$ Eqs. 21.8 and 21.9
Parameters	Number of parameters	In this study, 30 retardation times, τ_n, and 30 Prony series coefficients, C^n are chosen by trial and error to improve the convergence and quality of the LSQ fits	Two material parameters, n and n_0, for selected spectrum function (21.10)
	Constraints	Mathematical constraints for both retardation time, τ_n, and Prony series coefficients, C^n, as shown in (21.13)	Specified by the selected function
Analytical	Function	$C(t) = C^0 + \sum_{n=1}^{Npr} C^n \left[1 - \exp\left(-\frac{t}{\tau_n} \right) \right]$ Eq. 21.1	$E(t) = E_0 \left[\left(1 - \frac{m}{2}\right) + \frac{m}{\pi} \int_{n_0 t}^{\infty} \frac{\sin(z-n_0 t)}{z} dz \right]$ Eq. 21.10
	Mathematical method of solution	Solve analytically and LSQ to experimentally data	Solve for Volterra integral of convolution iterative method
	Result	Creep compliance, C(t)	Relaxation modulus, E(t)

References

1. Beldica, CE, Hilton, HH (1999) Analytical and computational simulations of experimental determinations of deterministic and random linear viscoelastic constitutive relations. In: Proceedings of the 12th International Conference on Composite Materials
2. Michaeli M, Shtark A, Grosbein H, Steevens AJ, Hilton HH (2011) Analytical, experimental and computational viscoelastic material characterizations absent Poisson's ratios. In: Proceedings of the 52nd AIAA/ASME/ASCE/AHS/ASC structures, structural dynamics, and materials conference. American Institute of Aeronautics and Astronautics Inc., 23–26 Apr 2007
3. Shtark A, Grosbein H, Sameach G, Hilton HH (2007) An alternate protocol for determining viscoelastic material properties based on tensile tests without use of Poisson ratios. In: Proceedings of ASME International Mechanical Engineering Congress and Exposition
4. Sullivan RW (2006) On the use of a spectrum-based model for linear viscoelastic materials. Mech Time-Depend Mater 10(3):215–228
5. Sullivan RW (2010) Using a spectrum function approach to model flexure creep in viscoelastic composite beams. Mech Time-Depend Mater 19 (1–3):39–47
6. Sullivan RW (2008) Development of a viscoelastic continuum damage model for cyclic loading. Mech Time-Depend Mater 12(4):329–342
7. Sullivan RW (2003) An analytical method to determine the mechanical properties of linear viscoelastic solids. Mississippi State University
8. Prony R, Prony R (1795) Essai experimental et analytique. J Ec Polytech (Paris) 2:24–76
9. Schapery RA (1961) A simple collocation method for fitting viscoelastic models to experimental data. Rep. GALCIT SM 61-23A
10. Schapery RA (1967) Stress analysis of viscoelastic composite materials. J. Compos. Mater. 1:228–267
11. Bradshaw R, Brinson L (1997) A sign control method for fitting and interconverting material functions for linearly viscoelastic solids. Mech Time-Depend Mater 1(1):85–108
12. Cost TL, Becker B (1970) Multidata method of approximate Laplace transform inversion. Int J Numer Methods Eng 2(2):207–219
13. Park S, Kim Y (2001) Fitting Prony-series viscoelastic models with power-law presmoothing. J Mater Civil Eng 1(3):26
14. Betten J (2008) Creep mechanics. Springer-Verlag, Berlin
15. Christensen RM (1982) Theory of viscoelasticity: an introduction. Academic Press, New York
16. Eringen AC (1980) Mechanics of continua, vol 1. Robert E. Krieger Publishing Co., Huntington, p 606
17. Sullivan RW, Razzaghi M, Simsiriwong J (2011) Numerical iterative method for Volterra equations of the convolution type. Math Method Appl Sci 34(2):140–146
18. Lakes RS (1999) Viscoelastic solids. CRC, Boca Raton
19. Park S, Kim Y (1999) Interconversion between relaxation modulus and creep compliance for viscoelastic solids. J Mater Civil Eng 1(1):76
20. Goodman SH (1998) Handbook of thermoset plastics. William Andrew, New York
21. ASTM Standard D 638M-89 (1998) Standard test methods for tensile properties of plastics, Vol 08.01. American Society of Testing and Materials, West Conshohocken, PA
22. Hilton HH (2011) Clarifications of certain ambiguities and failings of Poisson's ratios in linear viscoelasticity. J Elast. 104(1–2):303–318
23. Nouranian S (2011) Vapor-grown carbon nanofiber/vinyl ester nanocomposites: designed experimental study of mechanical properties and molecular dynamics simulations. Mississippi State University
24. ASTM Standard D 2990-77 (1998) Standard test methods for tensile, compressive, and flexural creep and creep-rupture of plastics, Vol 08.01. American Society of Testing and Materials, West Conshohocken, PA

Chapter 22
Viscoelastic and Viscoplastic Behavior of GF/VE $[\pm 45]_s$ Laminates

J. Varna, K. Giannadakis, and R. Joffe

Abstract The nonlinear and time dependent stress-strain response of non-crimp fabric (NCF) $[\pm 45]_s$ laminates in tension is studied. Testing methodology is suggested to separate and quantify the effect on the inelastic response of damage development, nonlinear viscoelastic effects and viscoplasticity. Material model based on Schapery's work on viscoelasticity and Zapas viscoplastic functional with added damage terms is used. Simulation is performed and validated with constant stress rate tensile tests, identifying the nonlinear viscoelasticity and viscoplasticity as the major sources of the nonlinear response.

Keywords Viscoplasticity • Viscoelasticity • Material model • GF non-crimp fabric

22.1 Introduction

Fiber composites in transverse tension and in in-plane shear present complex stress-strain behaviour, hysteresis loops and loading rate effects [1–6]. In case of angle-ply laminates the nonlinear shear response is responsible for the non-linear performance of the laminate. Several researchers have tried to describe the nonlinear shear response as combination of elastic response and plasticity [1, 6]. In [6] the elastic response is changing due to compliance degradation and the plasticity is for both shear and transverse stress. In [1] the plastic yielding of the matrix is included using Mohr-Coulomb criterion. These approaches can be successful describing the stress-strain curves during monotonously increasing loading but they are unable to deal with unloading and loading rate effects. The nonlinearity in tension in the transverse direction of the UD composite was analyzed and material model was developed in [7] using Schapery's model [8] for nonlinear viscoelastic analysis. Authors used power lower for viscoelastic compliance and this seems to be the limitation to achieve good fitting.

One of the most complete analysis of strain development in angle ply [45/−45]s is given in [2] where the laminate's response to tensile load is simulated using laminate theory type of analysis based on UD composite material model which accounts for all above phenomena except the effect of damage. Methodology for decoupled experimental analysis of damage effect, nonlinear viscoelasticity and viscoplasticity in composites has been developed in [3–5] for short fibre composites where nonlinear effects are pronounced.

The objective of this paper is to investigate the inelastic behaviour of a GF/VE $[\pm 45]_s$ laminates. The sources of the inelastic behaviour are analysed by studying the strain response in tensile tests and creep-strain recovery tests. The significance of the following phenomena is quantified and included in the material model: (a) reduction of elastic properties due to microdamage development in layers at high stresses; (b) viscoelastic composite material behaviour, which may be nonlinear with respect to stress; (c) viscoplastic (irreversible) strain development with time at high loads; (d) nonlinearity of the elastic response. In contrast to papers referred above the damage in the presented model is affecting not only the elastic but also the viscoelastic and viscoplastic responses.

J. Varna (✉) • K. Giannadakis • R. Joffe
Lulea University of Technology, SE 971 87, Luleå, Sweden
e-mail: janis.varna@LTU.SE

B. Antoun et al. (eds.), *Challenges in Mechanics of Time-Dependent Materials and Processes in Conventional and Multifunctional Materials, Volume 2*, Conference Proceedings of the Society for Experimental Mechanics Series 37,
DOI 10.1007/978-1-4614-4241-7_22,

22.2 Material

Knitted biaxial ±45 glass fiber non-crimp fabric (surface weight 1,800 g/m^2) was used as reinforcement in $[45/-45]_s$ laminate. Bundle width was very large and therefore the bundle mesostructure, was difficult to be seen. The resin used was bisphenol-A epoxy-vinylester, Dow Derakane 411-C50. Plates were manufactured using vacuum infusion with stiff mould base and flexible top (polyamide film). After completed infusion the plates were in-mould cured at room temperature, approximately 22°C for 12 h. Then, the specimens were subjected to a post-cure at 80°C for 9 h.

The material has high fibre content, fibers are homogeneously distributed and void content is rather low.

All experiments were performed at room temperature (22–23 C) and at a relative humidity (RH) of about 20–30%. For the current experiments, an Instron 3366 equipped with a 10 kN load cell and a 50 mm Instron extensometer with ±5 mm of travel length was used. The elastic modulus was determined in a range between 0.05% and 0.2% of the axial strain during increasing loading.

22.3 Material Model

The assumptions in the material model that includes the desired features are: (a) the viscoelastic and viscoplastic responses may be decoupled, (b) although both, viscoelastic, ε_{VE} and viscoplastic,ε_{VP} strains are affected by micro-damage $d(\sigma_{\max})$. We rely on the model introduced using thermodynamic treatment by Schapery [8]. In one-dimensional case the model can be written as

$$\varepsilon = d(\sigma_{\max}) \cdot \left(\varepsilon_0 + g_1 \int_0^t \Delta S(\Psi - \Psi') \frac{d(g_2\sigma)}{d\tau} d\tau + \varepsilon_{VP}(\sigma, t) \right) \tag{22.1}$$

In (22.1) integration is over "reduced time" introduced as,

$$\psi = \int_0^t \frac{dt'}{a_\sigma} \text{ and } \psi' = \int_0^\tau \frac{dt'}{a_\sigma} \tag{22.2}$$

ε_0 represents the nonlinear elastic strain, $\Delta S(\psi)$ is the transient component of the linear viscoelastic creep compliance

$$\Delta S(\psi) = \sum_i C_i \left(1 - \exp\left(-\frac{\psi}{\tau_i} \right) \right) \tag{22.3}$$

In (22.3) C_i are stress level independent constants and τ_i are called retardation times, g_1 and g_2 are stress invariant dependent material properties. a_σ is the shift factor, which in fixed conditions is a function of stress only.

The viscoplastic strains ε_{VP} in angle-ply laminates develop at high stresses and they increase with time at fixed stress. For many materials the development of viscoplastic strains may be described by a functional presented by Zapas and Crissman [9]

$$\varepsilon_{VP}(\sigma, t) = C_{VP} \left\{ \int_0^{\frac{t}{t^*}} \left(\frac{\sigma(\tau)}{\sigma^*} \right)^M d\tau \right\}^m \tag{22.4}$$

In (22.4) $\frac{t}{t^*}$ represents normalised time, C_{VP}, M and m are constants to be determined, and t^*, $\sigma^*$are characteristic time and stress constants.

22.4 Stiffness Degradation Due to High Stress

The function $d(\sigma_{\max})$in (22.1) was incorporated to account for microdamage. The values of this function depend on the maximum (most damaging) strain/stress state experienced during the previous service life and its meaning is the reduced elastic compliance of the composite

$$d(\sigma_{\max}) = \frac{E_0}{E(\sigma_{\max})} \tag{22.5}$$

where E_0 is the initial elastic modulus and $E(\sigma_{\max})$ is the current elastic modulus. The elastic modulus and Poisson's ratio dependence on the previously applied maximum stress level was measured to evaluate the significance of the modulus degradation.

The results are presented in Fig. 22.1 showing about 10% reduction of the elastic modulus. The reduction of the normalized stiffness was fitted by

$$d(\sigma_{\max}) = \frac{1}{1 - 0.2\left(\dfrac{\sigma_{\max} - \sigma_0}{3\sigma_0}\right)^2} \text{ for } \sigma_{\max} > \sigma_0 \; \sigma_0 = 30MPa \tag{22.6}$$

For all specimens a small increase in Poisson's ratio was observed. Acoustic events indicating formation of intra-laminar cracks in layers at high loads were also detected.

22.5 Accumulation of Viscoplastic Strain

In the case of creep test at fixed stress $\sigma(t) = \sigma_0$ the integration in (22.4) is trivial and the VP-strain accumulated during the time interval $t \in [0; t_1]$ is

$$\varepsilon_{VP} = A\left(\frac{t}{t^*}\right)^m \; A = C_{VP}\left(\frac{\sigma_0}{\sigma^*}\right)^{Mm} \tag{22.7}$$

In other words, according to the model the VP-strains in creep test grow according to power law with respect to time and with stress. According to (22.4) an interruption of the constant stress test for an arbitrary time t_a has no effect on VP-strain development: since stress during the unloaded state is zero, only the total time under loading is of importance. Hence, instead of testing at stress σ_0 for time $t_\Sigma = t_1 + t_2$continuously, one could perform the testing in two steps: (1) creep at stress σ_0 for

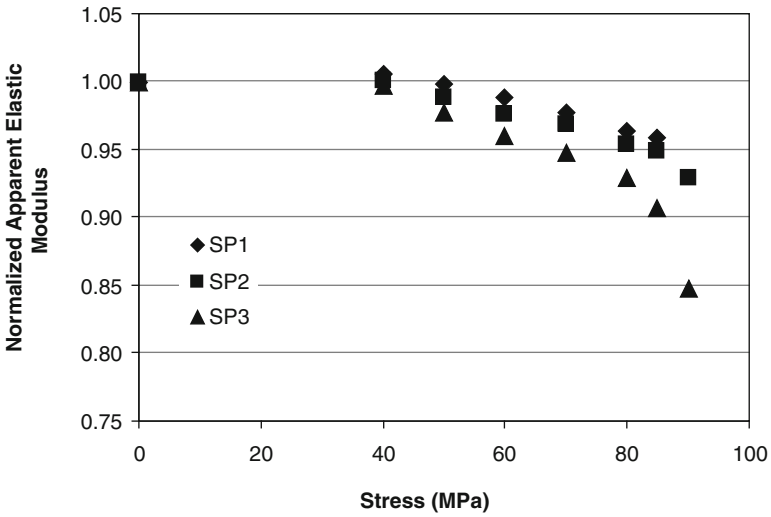

Fig. 22.1 Axial modulus reduction at high stress due to intralaminar cracking in $[\pm 45]_S$ laminate

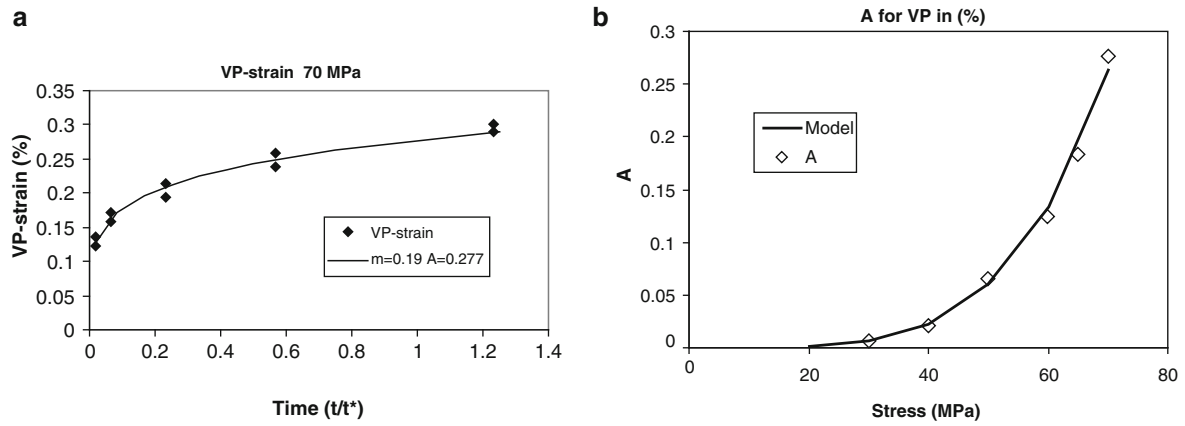

Fig. 22.2 Axial viscoplastis strain development (**a**) with time; (**b**) as a function of stress in creep test (22.7)

time t_1; unloading the specimen and measuring the permanent strain ε_{VP}^1 developed during this step (it has to be done after the recovery of viscoelastic strains); (2) then the stress $\sigma_0$is applied again for interval $t_2$and after strain recovery the new VP-strain $\varepsilon_{VP}^2$is measured which has developed during the second creep test. The sum of two viscoplastic strains corresponding to two tests of length $t_1$and t_2 will be equal to the viscoplastic strain that would develop in one creep experiment of length $t_\Sigma = t_1 + t_2$.

This conclusion was used to construct the VP-test (development of VP-strains with time). A fixed level of stress was defined and a sequence of creep and strain recovery tests were performed on the same specimen. The strain recovery time after the load application was eight times the length of the loading step. The test was performed for several stress levels to evaluate whether the shape of the time dependence is changing and how the strain values depend on the stress level. According to the model (22.7), the time dependence is not stress level dependent, whereas the magnitude A is.

The viscoplasticity development is demonstrated in Fig. 22.2a. All tests corresponding to different stress levels can be fitted with power function with the same exponent m. The A versus stress is plotted in Fig 22.2b.

22.6 Nonlinear Viscoelasticity

22.6.1 Data Reduction Methodology

Creep tests for viscoelastic characterisation lasted 40 min. After the load was removed, the sample was allowed to recover. When the stress is removed, the strain recovery period begins according to $\sigma = \sigma[H(t) - H(t - t_1)]$, where $H(t)$ is the Heaviside step function.

The material model (22.1) may be applied separately to the creep interval $t \in [0, t_1]$and to the strain recovery interval after the creep test $t>t_1$. The expression for strain development during the creep test is [6]

$$\varepsilon_{creep} = d(\sigma_{\max})\left\{\varepsilon_0 + g_1 g_2 \sigma \sum_i C_i\left(1 - \exp\left(-\frac{t}{a_\sigma \tau_i}\right)\right)\right\} + d(\sigma_{\max})\varepsilon_{VP}(\sigma, t). \quad 0<t<t_1. \tag{22.8}$$

The time dependence of strain in the recovery region follows expression

$$\varepsilon_{rec} = d(\sigma_{\max})\left\{g_2 \sigma \sum_i C_i\left(1 - \exp\left(-\frac{t_1}{a_\sigma \tau_i}\right)\right)\exp\left(-\frac{t - t_1}{\tau_i}\right)\right\} + d(\sigma_{\max})\varepsilon_{VP}(\sigma, t_1) \quad t>t_1 \tag{22.9}$$

Constants C_i $i = 1,\ldots, I$ (stress independent), and ε_0, a_σ, g_1 and g_2 (stress dependent) are found as result of fitting. The retardation times $\tau_i$in Prony series are chosen arbitrary, but the largest τ_i should be at least a decade larger than the length of the conducted creep test and they are all spread more or less uniformly over the logarithmic time scale, typically with a factor of about ten between them.

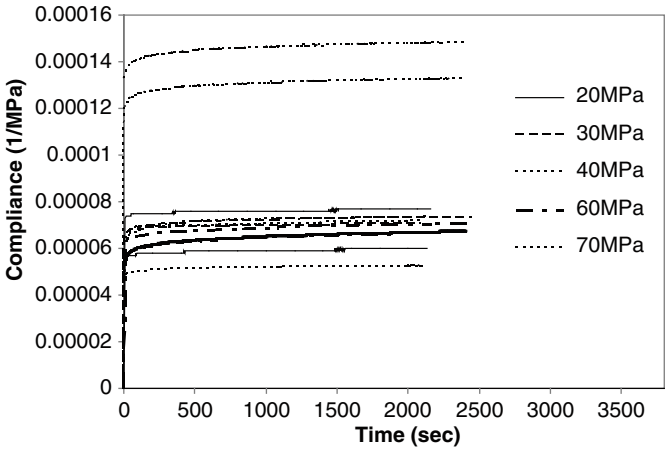

Fig. 22.3 Nonlinear viscoelastic compliance of $[\pm 45]_S$ laminate as a function of stress

The stress and time dependent VP-strains enter (22.8) and (22.9). The term $\varepsilon_{VP}(\sigma, t_1)$ is the VP-strain developed during the creep test and it comes directly from the test as the last data point at the end of strain recovery. However, in the creep strain expression in (22.8), the time dependence of the VP-strain during this test is required. It has to be subtracted from the total strain during the creep test with the rest being a pure nonlinear viscoelastic strain.

In the first loading step for the specimen the expression is very simple and follows from (22.7).

$$\varepsilon_{VP}(t) = \varepsilon_{VP}(\sigma, t_1)\left(\frac{t}{t_1}\right)^m \tag{22.10}$$

The steps to determine coefficients a_σ, g_1, g_2 and ε_0 are summarized below:

1. Creep and strain recovery data in low stress region (expected linear response) assuming $g_1 = g_2 = a_\sigma = 1$ are used to determine C_i by fitting simultaneously the reduced creep and strain recovery data using method of least squares (LSQ) and (22.8), (22.9). Average values of C_i for all specimens are calculated.
2. Nonlinear viscoelastic analysis is performed using obtained C_m, τ_m and fitting (22.17), (22.18) to find a_σ, g_1, g_2 and ε_0. The following routine can be suggested: initial (small) value of a_σ is assigned and then increased with a selected step. For each value the method of LSQ is used to find the best g_1, $g_2$and ε_0. For each set of a_σ, g_1, g_2 and ε_0 the misfit function (sum of squares of deviations with test data) is calculated. The set of a_σ, g_1,g_2 that gives the minimum of the misfit function is considered as the best fit.

22.6.2 Creep Compliance

The viscoelastic compliance was calculated to check for linear/non-linear behaviour. Usually, the first indication of linear behaviour is independence of compliance curves of stress level. However, differences may appear during recovery. If for a higher stress level the creep compliance curve leaves the "common cloud" it is a proof of a non-linear behaviour at this stress level. The results are presented in Fig. 22.3.

Analysing Fig. 22.3, we see that all creep levels between 20 and 40 MPa give approximately the same compliance curves and they all belong to the "linear region". It has to be noted that there is NO LINEAR region for this material. The values of nonlinearity parameters in the "linear region" ARE NOT equal to 1. It becomes clear comparing creep and strain recovery curves: the strain rate in recovery is much lower.

22.7 Validation

Simulations were performed using incremental form of the nonlinear viscoelastic part of (22.2) given in [3] and numerically integrating (22.5) for VP-strains. Tensile tests using constant stress rate 1.5 MPa/min were performed reaching 75 MPa after 3,000 s. Experimental data from this test and simulations are shown in Fig. 22.4a.

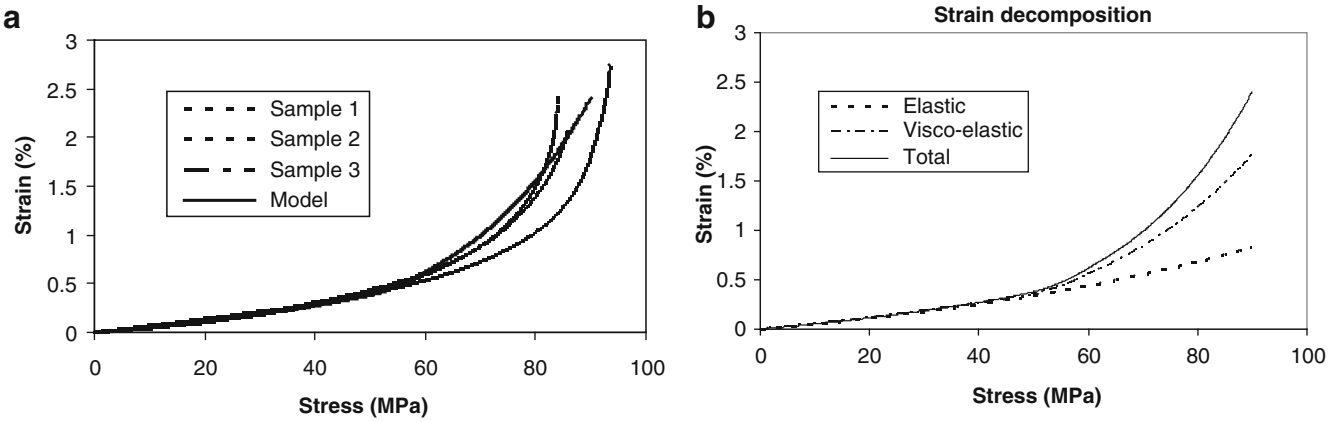

Fig. 22.4 Constant stress rate test: (**a**) experimental and simulated stress-strain curves; (**b**) strain constituents

In Fig. 22.4b the significance of each term in the constitutive model in this test is demonstrated (the total strain is a sum of elastic, visco- and visco-plastic responses). Until 50 MPa the viscoelastic and visco-plastic effects may be neglected. At failure the three strain components have approximately the same significance, but the rate of increase of viscoplasticity is the highest.

22.8 Conclusions

Effect of microdamage development, viscoelasticity and viscoplasticity on inelastic, time dependent behaviour of GF/VE [45/−45]s angle-ply laminate was analyzed experimentally performing stiffness reduction and creep tests with strain recovery. Testing methodology for stress dependent parameter identification in material model was suggested and verified. The elastic response of the angle-ply laminate is slightly nonlinear.

Empirical material model based on Schapery's nonlinear viscoelasticity and Zapas et al. viscoplasticity representation was generalised by including effect of microdamage.

Numerical simulations of slow constant stress rate loading ramp were performed using the developed material model in incremental form. It was found that the nonlinear viscoelasticity becomes very important at high stresses whereas viscoplastic effects are the most important just before failure. Intralaminar cracking in off-axis plies was observed. Simulations show that the effect of damage on the overall inelastic behaviour is rather limited.

References

1. Totry E, Gonzales C, LLorca J, Molina-Aldareguina JM (2009) Mechanisms of shear deformation in fiber-reinforced polymers: experiments and simulations. Int J Fract 158:197–209
2. Guedes RM, Marques AT, Cardon A (1998) Analytical and experimental evaluation of non-linear viscoelastic-viscoplastic composite laminates under creep, creep-recovery, relaxation and ramp loading. Mech Time-Depend Mater 2:113–128
3. Marklund E, Varna J, Wallström L (2006) Nonlinear viscoelasticity and viscoplasticity of flax/polypropylene composites. J Eng Mater Technol 128:527–536
4. Nordin L-O, Varna J (2006) Nonlinear viscoplastic and nonlinear viscoelastic material model for paper fiber composites in compression. Compos A: Appl Sci Manuf 37(2):344–355, ISSN 1359-835X
5. Marklund E, Eitzenberger J, Varna J (2008) Nonlinear viscoelastic viscoplastic material model including stiffness degradation for hemp/lignin composites. Compos Sci Technol 68:2156–2162, ISSN 0266-3538
6. Flatscher T, Schuecker C, Pettermann HE (2009) Prediction of plastic strain accumulation in continuous fiber reinforced laminates by constitutive model. Int J Fract 158:145–156
7. Zaoutsos SP, Papanicolaou GC, Cardon AH, Cardon AH (1998) On the non-linear viscoelastic behaviour of polymer-matrix composites. Compos Sci Technol 58(6):883–889, ISSN 0266-3538
8. Schapery RA (1997) Nonlinear viscoelastic and viscoplastic constitutive equations based on thermodynamics. Mech Time-Depend Mater 1:209–240
9. Zapas LJ, Crissman JM (1984) Creep and recovery behaviour of ultra-high molecular weight polyethylene in the region of small uniaxial deformations. Polymer 25(1):57–62, ISSN 0032-3861